UNIVERSITY OF CALIFORNIA SAN DIEGO

High-Fidelity and Reduced-Order Models of Contacting Structures

A dissertation submitted in partial satisfaction of the
requirements for the Degree Doctor of Philosophy

in

Structural Engineering

by

Patrick J. Hughes

Committee in charge:

Gilberto Mosqueda, Chair
Jiun-Shyan Chen
Joel P. Conte
Veronica Eliasson
Robert J. Kuether
Peter Shearer

2020

The dissertation of Patrick J. Hughes is approved, and it is acceptable in quality and form for publication on microfilm and electronically:

_____

_____

_____

_____
Co-chair

_____
Chair

University of California San Diego

2020

DEDICATION

To Arnold, for reminding me to stop working and go for a walk.

And to Lady Gaga's album *Chromatica*, which I listened to countless times while working on this dissertation.

EPIGRAPH

Seek simplicity…and distrust it.

Alfred North Whitehead

I have a dream, a fantasy

To help me through reality,

And my destination makes it worth the while.

Pushing through the darkness, still another mile.

I'll cross the stream - I have a dream.

ABBA

It's a long way to the top

If you wanna rock 'n' roll

AC/DC

TABLE OF CONTENTS

LIST OF FIGURES

LIST OF TABLES

LIST OF ALGORITHMS

ACKNOWLEDGEMENTS

Were it not for the love, patience, and support of the following people, this dissertation would have never been written.

I would first like to acknowledge my graduate advisor, Professor Gilberto Mosqueda. From day one, you treated me as your intellectual equal. You provided the guidance I needed, and the space I wanted. I am a better, more confident researcher because of you.

I also want to acknowledge Dr. Robert J. Kuether, for being my constant mentor and friend. You gave me the tools to succeed in a new and intimidating field.

A special thanks to Lindsay Walton – I have never known a more patient and considerate listener. Thanks also to Natalie Chen, Julie Storing, and Yvonne Wollman, for making me feel welcome in the Structural Engineering department.

Of course, I could not have made it this far without the enduring support of my parents. Through the years, I counted on you many times for your help, and never doubted that you would be there for me. Even during hard times, I can rest easy knowing that you'll always have a spare bed waiting for me at home.

I am also extremely grateful for my best friends Lamec and Kristen Fletez. You were my connection to a world outside the constant stress of graduate school. Nothing is rarer than a true friend, so I am doubly lucky to have both of you in my life.

Finally, thanks most of all to Morgan. Your endless love and patience make me a better man every day. I can't envision completing this journey, nor living my life, without you.

Chapter 3 is, in part, a reprint of the material as in appears in "Evaluation of Uniaxial Contact Models for Moat Wall Pounding Simulation," Hughes, P. J., Mosqueda, G. *Earthquake Engineering and Structural Dynamics* (2020). The dissertation author was the primary investigator and author of this paper.

Chapters 3 and 4 use numerical models and data from prior research conducted by Dr. Armin Masroor. Chapter 5 uses a finite element model of a building structure that was developed by Mr. Tianhao Yu. Section A1 of the Appendix contains derivations that were developed with the assistance of Dr. Robert J. Kuether. I would like to thank Dr. Masroor, Dr. Kuether, and Mr. Yu for their contributions.

Research documented in Chapters 3, 4, and 5 of this dissertation was supported by the Korea Atomic Energy Research Institute. Research documented in Chapters 6 and 7 of this dissertation was supported by Sandia National Laboratories. Sandia National Laboratories is a multimission laboratory managed by National Technology and Engineering Solutions of Sandia, LLC., a wholly owned subsidiary of Honeywell International, Inc., for the U.S. Department of Energy's National Nuclear Security Administration.

Any opinions, findings, conclusions, or recommendations expressed in this dissertation are those of the author, and do not necessarily reflect those of the Korea Atomic Energy Research Institute, Sandia National Laboratories, National Technology and Engineering Solutions of Sandia, Honeywell International, the U.S. Department of Energy, the National Nuclear Security Administration, or the Regents of the University of California.

VITA

2015 Bachelor of Science, University of Arizona

2018 Master of Science, University of California San Diego

2020 Doctor of Philosophy, University of California San Diego

ABSTRACT OF THE DISSERTATION

High-Fidelity and Reduced-Order Models of Contacting Structures

by

Patrick J. Hughes

Doctor of Philosophy in Structural Engineering

University of California San Diego, 2020

Gilberto Mosqueda, Chair

Manmade structures can be described as a collection of smaller substructures joined together at contacting interfaces. Contact nonlinearities present at these interfaces can cause computational bottlenecks in large, high-fidelity finite element models. Consequently, different techniques of model order reduction have emerged, wherein the number of degrees of freedom (DOF), particularly at nonlinear interfaces, is decreased to a manageable level. In the analysis of civil structures, so-called “macro” elements are often employed, which represent entire contact surfaces using uniaxial spring and dashpot elements. Mechanical and aerospace systems, on the

other hand, more often use projection-based model order reduction, which transform interface deformations onto a low-dimensional subspace.

This research develops high-fidelity and reduced-order models of contacting structures, from large-scale building structures down to small-scale mechanical components. Moat wall pounding, a phenomenon where base-isolated buildings collide with their retaining walls during seismic shaking, is examined as a case study for reduced-order models of civil structures. In the first half of the dissertation, new and existing macro impact elements are verified against experimental data, and then statistically examined in a large parametric study. Following that, two different high-fidelity models of moat wall pounding are developed and compared with corresponding experimentation. Results from these studies indicate that most macro models provide sufficient accuracy for moat wall pounding simulations. Their high-fidelity counterparts, while more difficult to calibrate to experimental data, reveal dynamic behavior that cannot be ascertained with macro elements alone.

The second half of the dissertation develops a novel family of methods to reduce the nonlinear interface DOF for preloaded bolted structures. Five such methods are applied to a bolted beam assembly and compared in terms of accuracy and computational savings. Results show that the interface reduction methodology is capable of capturing often-neglected interface kinematics, including transient contact area and joint slip. Furthermore, the methods are tunable to the desired combination of accuracy and computational effort.

Chapter 1 Introduction

Almost all manmade structures can be described as an assembly of smaller substructures connected at discrete interfaces. Every building is a combination of beams, columns, walls, and floors. An airplane can be divided into a fuselage, cockpit, wings, engines, and rudders – each of which can be subdivided into its own assembly of plates, bolts, and other mechanical parts. Indeed, a structure may be defined as an "organization of parts as dominated by the general character of the whole" [1].

In most engineering fields, the finite element method (FEM) is the preferred tool for analyzing structures subjected to some type of loading [2]. The complexity of structures that can be analyzed by FEM has increased proportionately to the growing power and availability of computing resources. As a result, analysts are no longer limited to simplified, monolithic structural models, and each component of a structure can be modeled in rich detail. Consequently, many modern finite element models consist of numerous parts connected at contact interfaces. And while the modeling of constitutive parts is a more straightforward endeavor, numerical treatment of contact remains an ongoing research problem.

Contact between structural components represents a boundary nonlinearity, where interface forces and displacements are unknown. In the context of finite element analysis, contact can be viewed as a multi-body constraint. The displacement field of each component must minimize its respective potential energy, while also satisfying equilibrium and compatibility at the contacting surfaces [3]. Multi-body contact presents a number of numerical challenges because the contact boundary is unknown (displacement nonlinearity) and the interface forces can change abruptly (discontinuous loading). Accurate determination of contact areas also requires a high mesh resolution, potentially increasing model sizes to the point of computational intractability. Nonetheless, inter-component contact strongly influences system-level stiffness and damping [4], so the computational bottlenecks must be tolerated or reduced in some way.

Numerical contact models can vary greatly between different engineering disciplines. Civil structures are typically so large that detailed joint representations would result in computationally untenable finite element models. Accordingly, structural connections in building and bridges are often assumed to be rigid, and the effect of the joint compliance can be handled by adjusting the viscous damping values. Due to the frequency mismatch between joints (typically associated with high resonant frequencies) and the dynamic loading of civil structures (low frequency, e.g. seismic shaking), this simplification remains physically sound. In certain cases, however, explicit consideration of contact is unavoidable. For example, earthquake ground motion can induce impact between bridge segments [5] or adjacent buildings [6]. Base isolated buildings, which allow large relative displacements at the ground level [7], can pound against the surrounding retaining wall during seismic events [8]. Inter-component contact is an essential part of the loading in these cases, and must be directly modeled in some way. Due to the size of civil structures, the primary

concern is determining the scale and fidelity at which contact must be considered in order to preserve overall model accuracy.

Mechanical and aerospace structures, on the other hand, are normally subjected to high-frequency loading (e.g. turbomachinery vibration, wing flutter), and so must be modeled at the component level with high mesh resolution. Individual components are evaluated separately through compatible interface loads [9], or they are combined into superelements by truncating vibration modes of each component [10,11]. In either case, numerical models of these structures frequently face computational bloat due to the very high number of interface degrees of freedom. This can be alleviated by employing whole-joint macro models [12], or by mathematical projection of interface deformations onto a lower-order subspace [13].

For any structure large or small, accurate and efficient modeling of substructure contact is critically important. This research presents new methods of modeling contacting substructures, demonstrated on systems of different size and application. The first half of the dissertation studies different modeling methods in low-velocity, high-inertia impacts in civil structures, and the second half considers reduced-order models of mechanical structures with bolted joints.

1.1. Research Objective and Scope

The goal of this study is to develop, verify, and evaluate numerical models of contacting substructures across different physical scales and applications. Specifically, this research considers two classes of structures: (1) base-isolated building structures, which will be evaluated using high-fidelity finite element models, as well as macro element-based reduced-order models; and (2) small mechanical assemblies, which will be evaluated using projection-based reduced-order models.

Base-isolated buildings, when subjected to extreme ground shaking, may exceed the provided clearance and impact the retaining wall – a phenomenon known as moat wall pounding. Though certainly a rare event, moat wall pounding has been documented in past earthquakes [14], and may significantly contribute to the overall collapse probability [15]. Sudden contact between the superstructure base and moat wall induces high-frequency loading for which building structures are typically not designed. This can lead to increased floor accelerations and interstory drifts, eroding the benefits of implementing base isolation in the first place. This study will examine the pounding response of base-isolated buildings using state-of-the-art macro contact elements (Chapter 3). Following this, two base-isolated building specimens are modeled using high-fidelity finite elements: one tested at the University at Buffalo (Chapter 4), and another at the E-Defense testing facility in Kobe, Japan (Chapter 5). Each model is benchmarked against experimental measurements.

Structures with mechanical joints are often modeled in very fine detail, in order to capture the interface kinematics through node-to-node, surface-to-surface, or node-to-surface contact elements. Model order reduction is usually necessary to decrease the number of degrees of freedom (DOF) to something manageable on a typical personal computer, and the first step in this reduction is typically the Hurty/Craig-Bampton (HCB) transformation [10,11]. The HCB method reduces interior DOF while preserving all nonlinear DOF at the boundary interfaces. This process produces a so-called HCB superelement, which, in many cases, may still be of a substantial size due to the high number of interface DOF. This research develops and tests interface reduction strategies specifically tailored to HCB superelements with contact nonlinearities. This is accomplished by exploring different interface basis vectors computed from the HCB superelement system matrices (Chapter 7).

The specific objectives of this research are:

- Investigate uniaxial contact models and their effect on the moat wall pounding response, including local effects at the contact interface and global effects on the superstructure.
- Generate high-fidelity finite element models of moat wall pounding in base-isolated buildings, and benchmark the models against experimental data.
- Develop interface reduction methods for pre-assembled Hurty/Craig-Bampton superelements with contact nonlinearities, and examine their efficiency and accuracy in the time domain.

1.2. Overview of the Dissertation

This dissertation is divided into eight chapters, as follows.

- Chapter 2 is a review of the scientific literature related to numerical models of civil structures subjected to impact loading, as well as projection-based model order reduction of mechanical structures with contact nonlinearities.
- Chapter 3 examines how the phenomenon of moat wall pounding can be modeled using low-dimensional macro elements. Commonly used contact models are compared to show how each model affects the response of a base-isolated building.
- Chapter 4 details efforts in the first of two high-fidelity finite element models of base-isolated buildings subjected to moat wall pounding. Based on a quarter-scale building specimen, this model ignores the upper floors of the superstructure and limits simulation

time to a single impact event. Impact force time histories are compared with experimental data.

- Chapter 5 describes the second high-fidelity model of moat wall pounding. This model considers a complete, three-dimensional earthquake time history analysis of a realistic 4-story building. Response time histories of the superstructure and moat wall are compared with experimental data.
- Chapter 6 provides a rich theoretical background for dynamic time history analyses of Hurty/Craig-Bampton (HCB) superelements with nonlinear interface reduction. The HCB transformation is derived in detail, followed by a generalized introduction to the modal reduction of nonlinear interface degrees of freedom (DOF). A new contact element is shown, followed by strategies for explicit dynamic preloading of structures with bolted joints. Finally, all the pieces are brought together in a unified methodology for response time history analysis of HCB superelements with preloaded bolted joints and nonlinear interface reduction.
- Chapter 7 describes how to reduce the number of interface DOF in HCB superelements. The interface DOF are projected onto low-dimensional modal subspaces using novel adaptations of system-level characteristic constraint (SCC) modes, Gram-Schmidt interface (GSI) modes, or joint interface (JI) modes. Following this, the reduction bases are enriched using approximate residual interface (ARI) modes and interface modal derivatives (IMDs). A mechanical beam assembly is used as a case study to demonstrate the performance of the interface reduction methods, in terms of time-domain accuracy and computational savings.

- Chapter 8 summarizes the research contained in this dissertation, reviews key results and contributions to the body of knowledge, and provides recommendations for future work.

References

1. Merriam-Webster Dictionary 2020. https://www.merriam-webster.com/.

2. Tenek LT, Argyris J. A brief history of FEM. *Finite Element Analysis for Composite Structures. Solid Mechanics and Its Applications; vol 59.*, Springer, Dordrecht; 1998. DOI: https://doi.org/10.1007/978-94-015-9044-0_2

.

3. Wriggers P. *Computational Contact Mechanics*. 2006.

4. Gaul L, Nitsche R. The role of friction in mechanical joints. *Applied Mechanics Reviews* 2002; **54**(2): 93–106.

5. Malhotra PK. Dynamics of seismic pounding at expansion joints of concrete bridges. *Journal of Engineering Mechanics* 1998; **124**(7): 794–802. DOI: 10.1061/(ASCE)0733-9399(1998)124:7(794).

6. Abdel Raheem SE. Seismic pounding between adjacent building structures. *Electronic Journal of Structural Engineering* 2006; **6**: 66–74.

7. Christopoulos C, Filiatrault A. Principles of Passive Supplemental Damping and Seismic Isolation. *IUSS Press* 2006.

8. Komodromos P, Polycarpou PC, Papaloizou L, Phocas MC. Response of seismically isolated buildings considering poundings. *Earthquake Engineering and Structural Dynamics* 2007. DOI: 10.1002/eqe.692.

9. Wijker JJ. Coupled Dynamic Loads Analysis. *Spacecraft Structures*, 2008. DOI: https://doi.org/10.1007/978-3-540-75553-1_20.

10. Hurty W. Vibrations of Structural Systems by Component Mode Synthesis. *Transactions of the American Society of Civil Engineers* 1960.

11. Craig RR, Bampton MCC. Coupling of substructures for dynamic analyses. *AIAA Journal* 1968. DOI: 10.2514/3.4741.

12. Segalman DJ. Modelling joint friction in structural dynamics. *Structural Control and Health Monitoring* 2006; **13**(1): 430–453. DOI: 10.1002/stc.119.

13. Krattiger D, Wu L, Zacharczuk M, Buck M, Kuether RJ, Allen MS, Tiso, P, Brake MRW. Interface reduction for Hurty/Craig-Bampton substructured models: Review and improvements. *Mechanical Systems and Signal Processing* 2019; **114**: 579–603. DOI: 10.1016/j.ymssp.2018.05.031.

14. Gavin HP, Nigbor RL. Performance of the base-isolated Christchurch women's hospital in the Sep. 4 2010 Dar field earthquake and the Feb.22 2011 Christchurch earthquake. *20th Analysis and Computation Specialty Conference - Proceedings of the Conference* 2012(4): 554–563. DOI: 10.1061/9780784412374.049.

15. Masroor A, Mosqueda G. Assessing the collapse probability of base-isolated buildings considering pounding to moat walls using the FEMA P695 methodology. *Earthquake Spectra* 2015; **31**(4): 2069–2086. DOI: 10.1193/092113EQS256M.

Chapter 2 Background and Literature Review

This chapter presents the technical background and relevant literature review of topics discussed in this dissertation. First, a thorough history of the numerical modeling of seismic impact in civil structures is discussed, followed by specific developments in moat wall pounding research. A survey of analyses in mechanical structures with intermittent contact is then shown, with a subsequent review of projection-based reduced order modeling methods.

2.1. Seismic Pounding

Seismic pounding is a phenomenon in which adjacent structures or structural components collide with one another during earthquake ground motion. Occurrences of seismic pounding have been observed between adjacent buildings, bridge segments, bridge-abutment interfaces, and between base isolated buildings and their surrounding retaining walls. Seismic pounding typically constitutes a low-velocity, high-inertia impact event, which can induce high-frequency forces to which the structure was not designed to withstand. This often results in localized damage at the

point of contact, as well as high accelerations that can be damaging to both structural and nonstructural components.

One of the earliest recorded incidents of seismic pounding happened in the 1971 San Fernando earthquake, where the main building of the Olive View hospital collided with a free-standing stairway structure [1]. The pounding was severe enough to cause residual tilting of the more flexible stairway tower, as shown in Figure 2.1.

Figure 2.1. Permanent tilting in a stairway tower caused by seismic pounding in the 1971 San Fernando earthquake [1].

After the 1985 Mexico City earthquake, reconnaissance efforts showed that, of the 330 buildings that were severely damaged or collapsed, 132 (40%) involved earthquake-induced structural pounding [2]. It was also estimated that 15% of all building collapses were directly

caused by pounding [3]. An example of adjacent buildings damaged by pounding is shown in Figure 2.2.

Figure 2.2. Pounding-induced damage in adjacent buildings following the 1985 Mexico City earthquake. Photo credit: Walter Hays, Global Institute for Energy and Environmental Systems.

Pounding damage was documented in many earthquakes since then, including the 1989 Loma Prieta earthquake [4,5], the 1994 Northridge earthquake [6,7], the 1995 Kobe earthquake [8,9], and the 1999 Chi-Chi earthquake [10]. The SSK Hospital in Izmit showed significant damage due to pounding between its constitutive parts during the 1999 Kocaeli earthquake [11]. Reports following the Athens earthquake of 1999 showed that different components of the same school building collided with each other [12]. Intra-building pounding was also observed after the 2010 Darfield earthquake [13]. In all of these cases, disparities in the vibrational characteristics of adjacent buildings was shown to be the major cause of pounding. When two adjacent buildings

vibrate at a different fundamental period, they are likely to collide when their oscillations are out of phase, as shown in Figure 2.3 below.

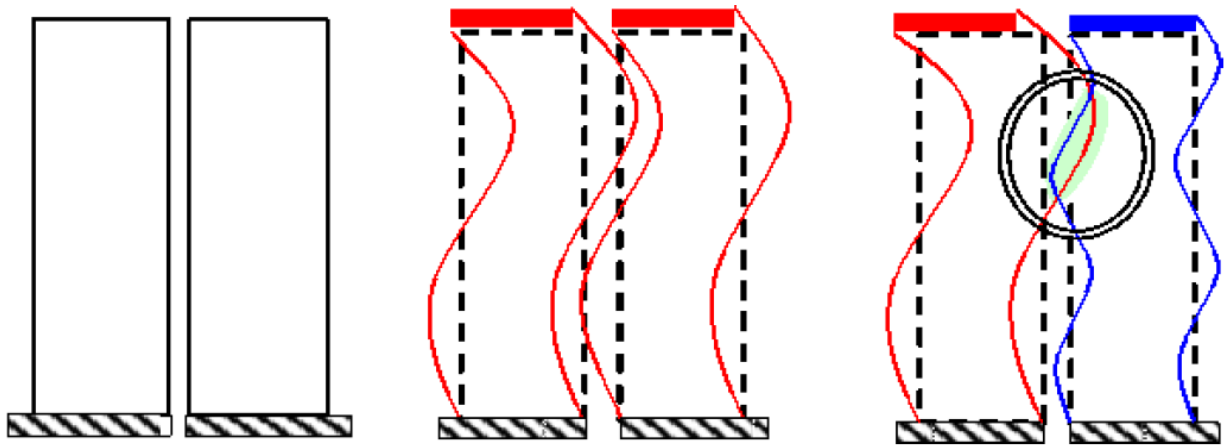

Figure 2.3. Adjacent buildings (left) before the earthquake, (middle) during in-phase vibration, (right) during out-of-phase vibration [14].

Seismic pounding in bridges has also been observed multiple times in post-earthquake reconnaissance. During the Loma Prieta earthquake of 1989, several impact were recorded between different components of the China Basin viaduct [4]. Expansion joints and abutments suffered impact damage during the 1994 Northridge earthquake [6]. Reports following the 1995 Kobe earthquake indicate that pounding was a major cause of bridge segment collapses, illustrated in Figure 2.4.

Earthquake-induced structural pounding is a complex phenomenon that involves inelastic deformations like cracking, crushing, and fracture. At the point of contact, forces are applied over a very short duration, introducing high-frequency stress waves. In a modeling environment, this represents multiple sources of nonlinearity: material nonlinearity due to the severe inelastic deformations, geometric nonlinearity due to large structural displacements, and contact

nonlinearity from the colliding bodies coming in and out of contact. Despite these myriad challenges, recent research efforts have focused on accurate and efficient numerical models of the seismic pounding phenomenon.

Figure 2.4. Collapsed bridge segment where pounding was a contributing factor (1995 Kobe earthquake).

2.2. State-of-the-Art in Modeling Seismic Pounding

The classical theory of impact is the simplest way to represent two bodies undergoing inelastic collision. Sometimes referred to as stereomechanics, this theory focuses on the state of two colliding bodies before and after an inelastic impact, without monitoring the contact forces and deformations during the contact time history [15]. This concept is easily demonstrated by considering two bodies with masses m_1 and m_2, initial velocities $\dot{u}_1^0$ and $\dot{u}_2^0$, and final velocities $\dot{u}_1^f$ and $\dot{u}_2^f$. Such a system is shown in Figure 2.2.

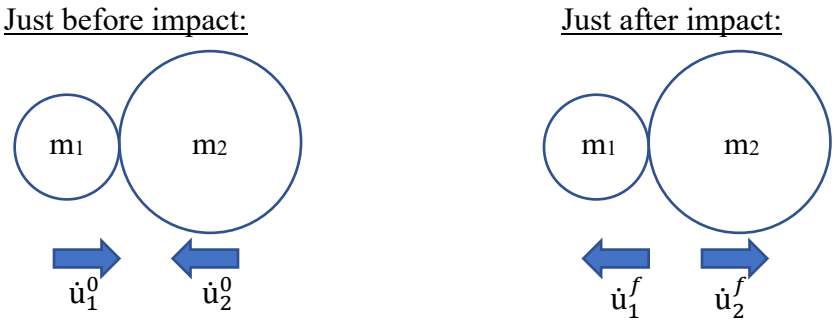

Figure 2.5. Initial (left) and final (right) stereomechanical states of two colliding masses.

Enforcing conservation of momentum and conservation of energy to the system shown in Figure 2.2. yields

$$\dot{u}_1^f = \dot{u}_1^0 - (1+e)\frac{m_2(\dot{u}_1^0 - \dot{u}_2^0)}{m_1 + m_2} \tag{2.1a}$$

$$\dot{u}_2^f = \dot{u}_2^0 + (1+e)\frac{m_1(\dot{u}_1^0 - \dot{u}_2^0)}{m_1 + m_2} \tag{2.1b}$$

where e is the coefficient of restitution, given by

$$e = -\frac{\dot{u}_2^f - \dot{u}_1^f}{\dot{u}_2^0 - \dot{u}_1^0} \tag{2.2}$$

The energy loss during impact ΔE is computed as

$$\Delta E = \frac{1}{2}\frac{m_1 m_2}{m_1 + m_2}(1 - e^2)(\dot{u}_1^0 - \dot{u}_2^0)^2 \tag{2.3}$$

Equations (2.1) and (2.3) are useful for judging the approximate global behavior of bodies undergoing impact. However, its applicability is limited to systems that can be represented single degree of freedom (SDOF) lumped masses. Furthermore, this approach assumes a negligibly short contact duration and cannot compute the interface forces or deformations during impact. As a result, stereomechanical treatment of contact is not commonly used for seismic pounding analyses, particularly when operating in a finite element environment.

The contact element approach is a more popular method of modeling seismic pounding. In this method, interface forces are computed from uniaxial springs and dashpots that relate the indentation (relative deformation between colliding bodies) to corresponding contact forces. These models take the form

$$f_c(t) = f(\delta(t)) \tag{2.4}$$

where f_c is the contact force, δ is the indentation, and t is time. Using the two-mass system as an example, the indentation can be written in terms of the uniaxial body displacements u_1 and u_2 as

$$\delta(t) = u_2 - u_1 \tag{2.5}$$

In the case of velocity-dependent models, Equation (2.3) is rewritten as

$$f_c(t) = f\left(\delta(t), \dot{\delta}(t)\right) \tag{2.6}$$

where $\dot{\delta}$ is the indentation velocity, given in terms of the uniaxial body velocities $\dot{u}_1, \dot{u}_2$, as

$$\dot{\delta}(t) = \dot{u}_2(t) - \dot{u}_1(t) \tag{2.7}$$

In this formulation, the colliding bodies shown in Figure 2.5 can be analyzed using contact elements, as shown in Figure 2.6 below.

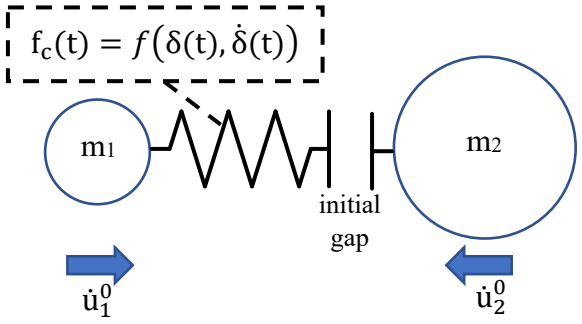

Figure 2.6. Two-mass system analyzed using a contact element.

The contact element approach reformulates the stereomechanics method such that the contact forces are monitored through the constitutive law $f_c(t) = f\left(\delta(t), \dot{\delta}(t)\right)$. Stereomechanical

analysis is limited to lumped masses, whereas contact elements can be applied to any multiple-degree-of-freedom (MDOF) system. In a response time history analysis, the interface forces are tracked at every timestep, so the contact elements can be added to existing finite element models with relative ease. Indeed, force-based contact elements have become a standard simulation tool for seismic pounding models.

Experimental studies of impact [15–18] show that the impact force between two colliding bodies is a function of their masses, contact surface geometries, material properties, loading histories, and pre-impact relative velocities. As such, robust contact elements must consider these features in the constitutive law given by $f_c(t) = f\left(\delta(t), \dot{\delta}(t)\right)$. Many contact elements also separately model the approach (loading) and restitution (unloading) phases of impact. The approach phase begins when the two objects come into contact and ends when the indentation is maximum (and the indentation velocity is zero). The restitution phase begins immediately after the approach phase and ends when the structures come out of contact. Depending on contact model, the approach phase does not necessarily end when the impact force reaches its maximum. Such a case is shown in Figure 2.7.

The simplest contact element is a linear elastic spring, with the force-indentation relationship

$$f_c(t) = k\delta(t) \tag{2.8}$$

where the linear spring stiffness is the sole parameter, given by k. Though this model has been used extensively [19–24], it does not include any energy dissipation or rate effects. The force-indentation (f_c-δ) relationship is shown in Figure 2.8.

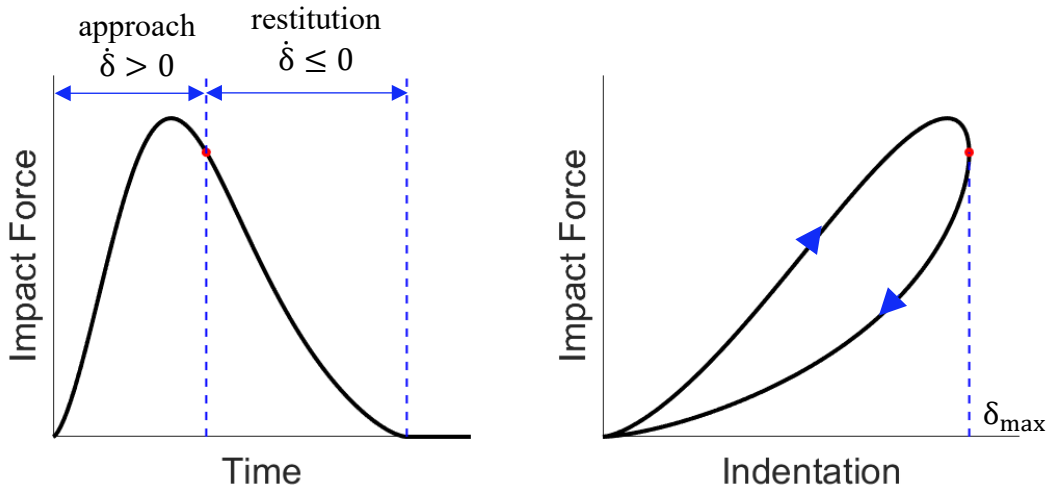

Figure 2.7. Approach and restitution phases of impact. Transition between the two phases, when the indentation is maximum and the indentation velocity changes sign, is marked with a red dot. Note that the phase transition does not necessarily occur when the impact force is maximum.

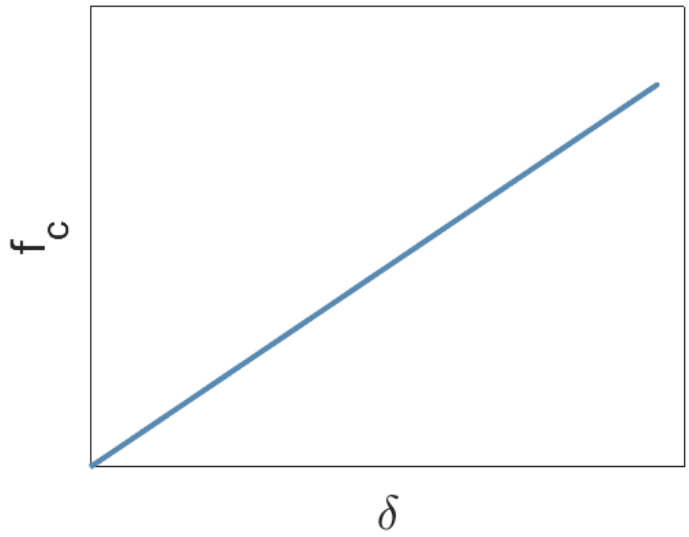

Figure 2.8. Linear elastic impact model.

The linear viscoelastic or Kelvin-Voigt impact element [25–29] is obtained by adding a linear dashpot to Equation (2.8):

$$f_c(t) = k\delta(t) + c\dot{\delta}(t) \tag{2.9}$$

where c is the damping coefficient, given as

$$c = 2\xi_{KV}\sqrt{m_{eff}k} \tag{2.10}$$

The effective mass m_{eff} depends on the mass of each colliding body:

$$m_{eff} = \frac{m_1 m_2}{m_1 + m_2} \tag{2.11}$$

A suitable implicit relationship between the coefficient of restitution (e) and the Kelvin-Voigt damping coefficient (ξ_{KV}) was determined by Brogliato [30] as

$$\ln\left(\frac{1}{e}\right) = \frac{2\xi_{KV}}{\sqrt{1-\xi_{KV}^2}}\arctan\left(\frac{\sqrt{1-\xi_{KV}^2}}{\xi_{KV}}\right) \tag{2.12}$$

A typical force-indentation curve for the linear viscoelastic model is shown in Figure 2.9.

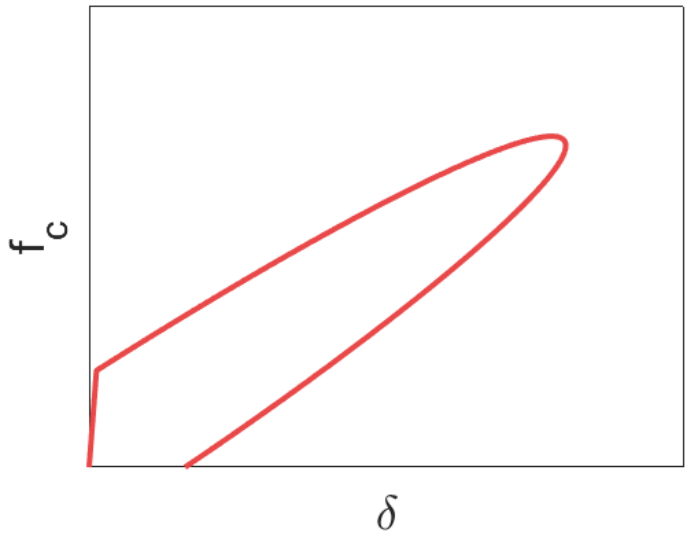

Figure 2.9. Linear viscoelastic (Kelvin-Voigt) impact model.

As shown in Figure 2.9, the linear viscoelastic model will produce a negative, non-physical impact force at the end of the restitution phase. This is because, when the indentation is zero, the indentation velocity is nonzero, so the viscous term in Equation (2.8) generates a negative contact force. Typically, this fictitious tensile force is negligibly small, but its presence has spurned the development of other models that do not have this drawback.

One such model is the Jankowski impact element [31–33], sometimes referred to as the nonlinear viscoelastic model. This model has the form

$$f_c(t) = \begin{cases} k_h \delta(t)^{\frac{3}{2}} + c_J(t)\dot{\delta}(t) & , \quad \dot{\delta}(t) > 0 \quad (approach) \\ k_h \delta(t)^{\frac{3}{2}} & , \quad \dot{\delta}(t) \leq 0 \quad (restitution) \end{cases} \tag{2.13}$$

where k_h is the nonlinear Hertz stiffness [15] and c_J is the Jankowski damping coefficient, given by

$$c_J(t) = 2\xi_J \sqrt{m_{eff} k_h \sqrt{\delta(t)}} \tag{2.14}$$

This expression is indentation-dependent, so the contact force will never be negative, even when the indentation velocity is nonzero. The Jankowski damping ratio (ξ_J) is computed as a function of the coefficient of restitution (e), as

$$\xi_J = \frac{9\sqrt{5}}{2} \frac{1 - e^2}{e(e(9\pi - 16) + 16)} \tag{2.15}$$

The force-indentation relationship for the Jankowski model is shown in Figure 2.10.

Another contact model that eliminates the tensile forces associated with the Kelvin-Voigt model is the Hertzdamp element [34–36]. This model originated from the classical Hertzian contact law [37,38], which relates the impact force to indentation by a simple power law:

$$f_c = k_h \delta(t)^{\frac{3}{2}} \tag{2.16}$$

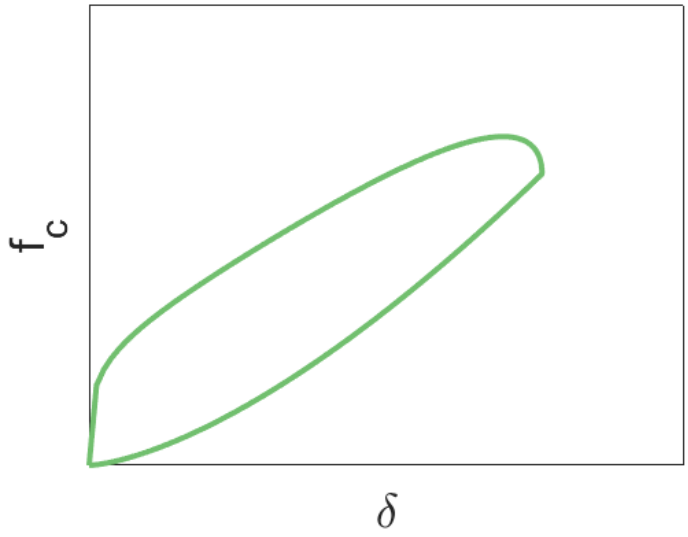

Figure 2.10. Jankowski impact model.

The Hertzdamp contact model adds a quasi-viscous component to this expression:

$$f_c(t) = k_h \delta(t)^{\frac{3}{2}} + c_h \dot{\delta}(t) \tag{2.17}$$

The Hertz damping coefficient $c_h(t)$ is computed as

$$c_h(t) = \xi_h \frac{k_h}{\dot{\delta}_0} \delta(t)^{\frac{3}{2}} \tag{2.18}$$

where $\dot{\delta}_0$ is the relative velocity of the colliding bodies just before impact, and the Hertz damping ratio (ξ_h) is

$$\xi_h = \frac{8}{5} \cdot \frac{1 - e}{e} \tag{2.19}$$

Like the Jankowski model, the Hertz damping coefficient is proportional to the indentation, so that the contact force is zero when the indentation is zero. The impact hysteresis of the Hertzdamp model is shown in Figure 2.11. A visual comparison of the damping ratio-coefficient of restitution relationships for the Kelvin-Voigt, Jankowski, and Hertzdamp models is shown in Figure 2.12.

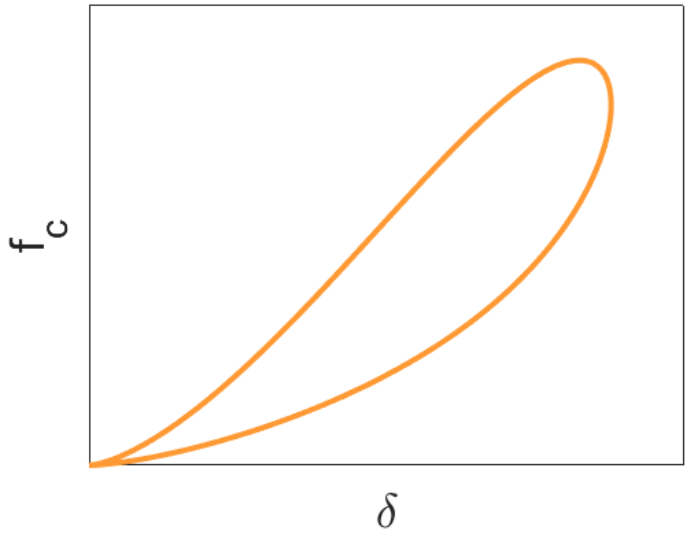

Figure 2.11. Hertzdamp impact model.

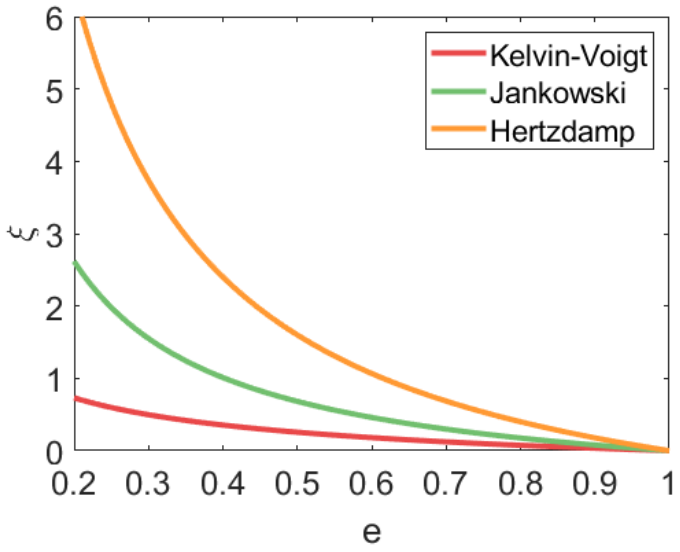

Figure 2.12. Relationship between impact damping ratio (ξ) and coefficient of restitution (e) for three impact models.

Despite the relative simplicity of the contact models shown thus far, their implementation into existing finite element codes may depend on the flexibility of the program being used. Except

for the linear elastic model, all models require some consideration of the rate of indentation, which may or may not be an available function of a given finite element program. Most programs, however, allow the user to define a rate-independent hysteresis backbone curve. As a result, the Muthukumar element [39] was developed as a bilinear approximation Hertzdamp model. The Muthukumar model is summarized as

$$f_c(t)=\begin{cases} k_1\delta(t) & , \ \dot{\delta}(t)>0 \ \text{and} \ \delta(t)\le\delta_y & (\textit{approach 1}) \\ k_1\delta_y+k_2\left[\delta(t)-\delta_y\right] & , \ \dot{\delta}(t)>0 \ \text{and} \ \delta(t)>\delta_y & (\textit{approach 2}) \\ f_m-k_1[\delta_m-\delta(t)] & , \ \dot{\delta}(t)\le 0 \ \text{and} \ \delta_m-\delta_y<\delta(t)\le\delta_m & (\textit{restitution 1}) \\ f_m-k_1\left(\delta_m-\delta_y\right)-k_2\left[\delta_m-\delta_y-\delta(t)\right] & , \ \dot{\delta}(t)\le 0 \ \text{and} \ \delta(t)<\delta_m-\delta_y & (\textit{restitution 2}) \end{cases} \tag{2.20}$$

where δ_y is the yield indentation, determined as a fraction of the maximum expected indentation (δ_{me}) as

$$\delta_y = a\delta_{me} \tag{2.21}$$

The yield indentation ratio (a) must satisfy $0 < a < \frac{2}{5}(1-e^2)$ for the Muthukumar model to be valid. The initial and secondary stiffnesses are, respectively,

$$k_1 = \left(1+\frac{2}{5}\cdot\frac{1-e^2}{a}\right)k_h\sqrt{\delta_{me}} \tag{2.22a}$$

$$k_2 = \left(1-\frac{2}{5}\cdot\frac{1-e^2}{1-a}\right)k_h\sqrt{\delta_{me}} \tag{2.22b}$$

The maximum force (f_m) and maximum indentation (δ_m) occur at the transition between approach and restitution, i.e. when $\dot{\delta}=0$. Note that the actual maximum indentation is not necessarily equal to the maximum expected indentation ($\delta_m \neq \delta_{me}$). A typical force-indentation curve for the Muthukumar model is shown in Figure 2.13.

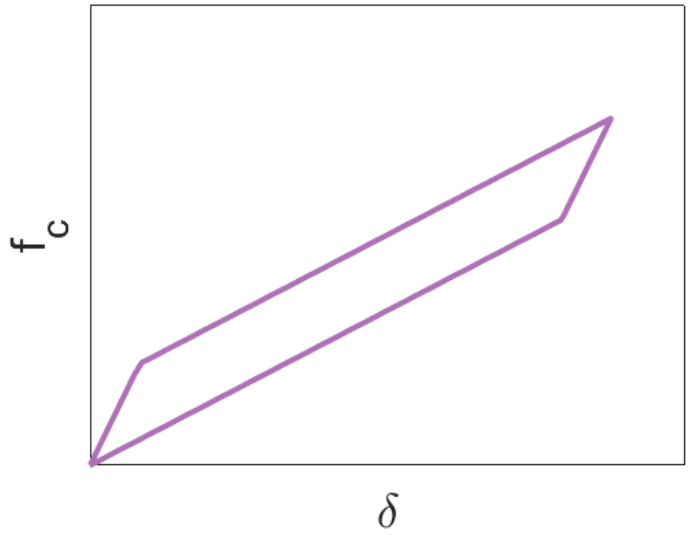

Figure 2.13. Muthukumar impact model.

All contact models summarized here are hypothetically capable of capturing global impact metrics like the overall impact force time history envelope and peak impact force. Indeed, these models are sometimes referred to as "macro" elements because they are limited to capturing response at a macro, or global, scale. In a real seismic pounding event, the colliding bodies will interact in three dimensions, with normal and tangential (i.e. frictional) force components. It is possible to use macro impact elements in series to represent a three-dimensional contact surface [40], but this approach requires cumbersome element calibration per unit length or unit area. Macro models can generate a force-indentation curve at one or more contact points, but material indentation can be extremely difficult or impossible to measure. As a result, some researchers have moved towards high-fidelity models of seismic pounding using two- or three-dimensional finite element models.

High-fidelity pounding models refers to a class of finite element (FE) models where shell and/or solid elements are used to model the colliding bodies, without the use of simplified macro

elements. An early example of this type of analysis is from a study by Papadrakakis et al. [41], where each floor of a building structure was represented by a single linear elastic plane stress shell element. Leibovich et al. [42] extended this work to symmetric buildings subjected asymmetric and torsional poundings. Jankowski [43] developed a three-dimensional model of the Olive View Hospital [1] that included pounding between the main structure and freestanding stairway tower (see Figure 2.14). This work incorporated nonlinear material models for concrete and embedded reinforcing steel, including degradation of strength and stiffness under cyclic loading. Results from this study showed that the response of the flexible stairway tower was strongly influenced by the number and nature of pounding events, while the stiffer main building was relatively unaffected. Bi et al. [44] used three-dimensional finite elements to evaluate the pounding response of a bridge subjected to spatially varying ground motions. In this work, the authors showed that use of a high-fidelity model was necessary to predict realistic responses, especially when examining features near the contact interfaces.

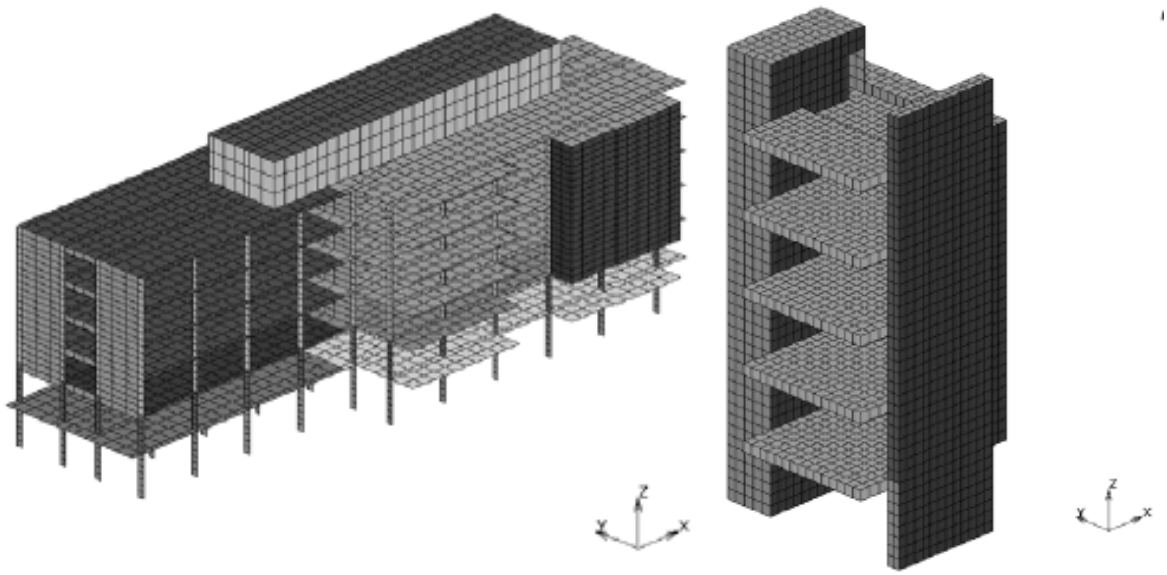

Figure 2.14. FE model of the Olive View hospital (left) and stairway tower (right) [43].

Jameel et al. [45] conducted a comprehensive analysis of two multi-story buildings subjected to seismic pounding (see Figure 2.15). The authors showed that, even if the buildings are modeled using linear elastic elements, the frequencies and mode shapes of the coupled two-building system can change dramatically. This effect was more pronounced in the higher modes. Overall, they demonstrated that pounding between adjacent buildings increases the system stiffness, which reduced displacements and increased accelerations at the colliding floors. Furthermore, they showed that the level of damage in a pounded building is inversely proportional to its mass – the lighter building suffered heavy damage, while the heavier building was less affected. Crucially, this study showed that the level of model fidelity is very important for capturing the pounding response. A simpler model of the buildings that did not include the slabs underestimated the story deformations. A more sophisticated model with direct consideration of the slabs, beams, and columns exhibited larger deformations and story shear forces.

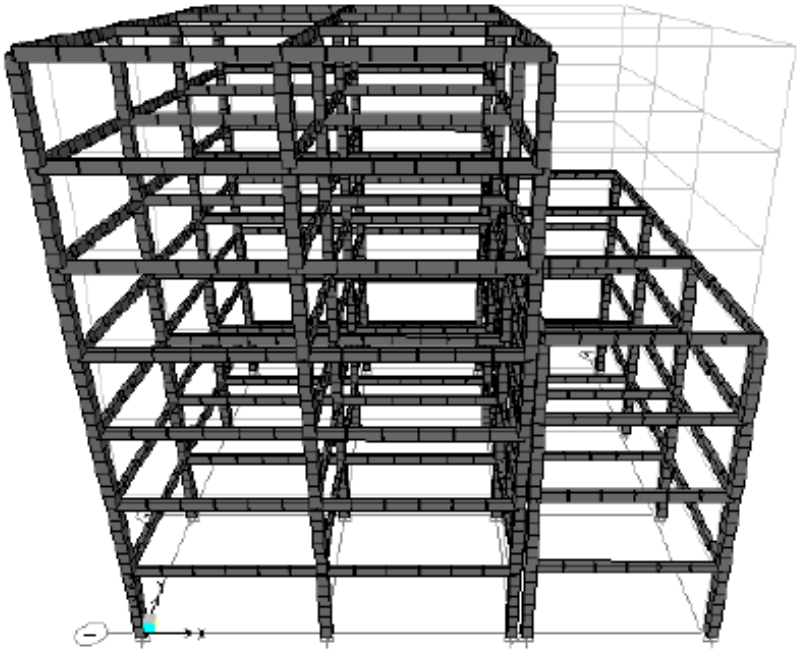

Figure 2.15. FE model of adjacent buildings subjected to seismic pounding [45].

Past research work clearly demonstrates that high-fidelity finite element models can reveal information that is impossible to obtain with simplified macro models. Still, the analyst must weigh the advantages against the increased computational cost. The first few chapters of this dissertation will examine how well different macro and high-fidelity models can capture the phenomenon of moat wall impact in base isolated buildings – a specific type of earthquake-induced pounding. In particular, the response will be compared against data from moat wall pounding experiments. Before that, however, the next section will review the key concepts of base isolation and moat wall pounding.

2.3. Base Isolation and Moat Wall Pounding

Seismic isolation is a proven technique to mitigate the harmful effects of horizontal earthquake shaking [46]. The effectiveness of seismic isolations is derived from two key principles: (1) period elongation, which reduces accelerations at the cost of amplified displacements, and (2) increased damping, which alleviates the displacement demand. This concept is illustrated spectrally in Figure 2.16.

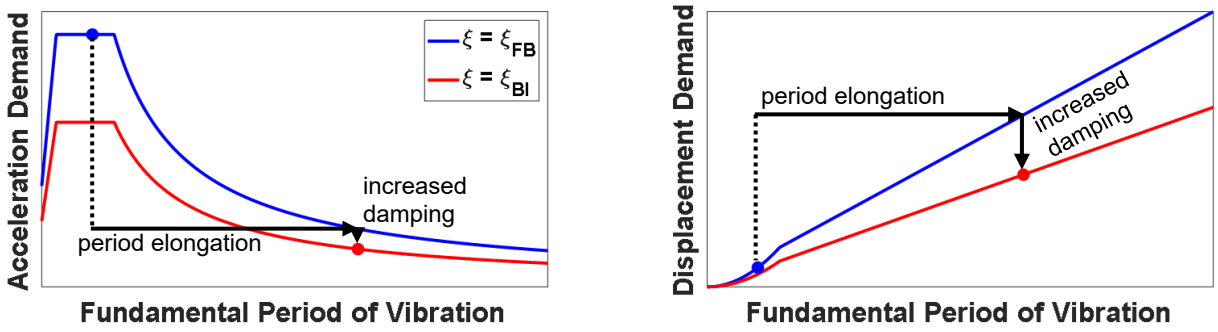

Figure 2.16. Seismic isolation elongates the fundamental vibration period and increases damping. ξ = damping ratio. ξ_{FB} = damping ratio for a fixed-base building. ξ_{BI} = damping ratio for a base-isolated building.

In a building structure, period elongation is achieved by installing a layer of flexible isolation devices with some inherent features to accommodate the large displacements. The location of the isolation layer can be chosen by the designer. By far the most common, base isolation targets the first mode of vibration by weakening the coupling between the building and the ground. In a high-rise building, however, the fixed-base period may be too long for base isolation to be effective. In this case, the isolation devices can be installed between two of the upper floors, which elongates the second or third mode of the building [47,48]. The research contained in this dissertation is limited to base-isolated buildings.

The goal of base isolation is to concentrate most of the displacements at the isolation plane, allowing the superstructure (everything above the isolation plane) to vibrate like a rigid body (see Figure 2.17). A seismic gap is provided at the base level to allow for large displacements, and a retaining wall (or moat wall) is constructed around the seismic gap.

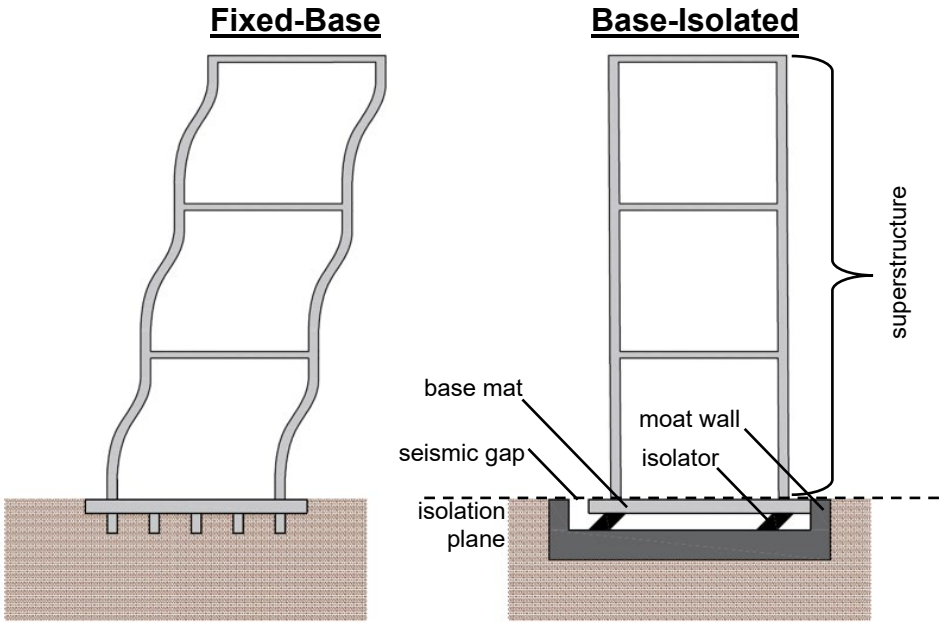

Figure 2.17. *Left:* Fixed-base building deformation pattern. *Right:* Base-isolated building deformation pattern with component labels.

Despite its modern prevalence as a powerful seismic protection tool, the concept of base isolation dates as far back as 1870 [49]. Jules Touaillon of San Francisco, California was issued a U.S. patent [50] for an "improvement in buildings", in which the superstructure would rest on a bed of rigid spheres between oppositely concave rolling surfaces. Several other patents and ideas for base isolation followed from engineers in Germany [51], Italy [52,53], and England [54]. The first implementation of the base isolation concept was probably Frank Lloyd Wright's 1921 design of the Imperial Hotel in Tokyo, Japan [55]. The hotel was supported by short piles driven to the top of a layer of soft mud, which acted as an isolating layer during the 1923 Great Kantō earthquake. Nonetheless, the Imperial Hotel eventually starting sinking into the mud layer and was demolished in 1968 [56].

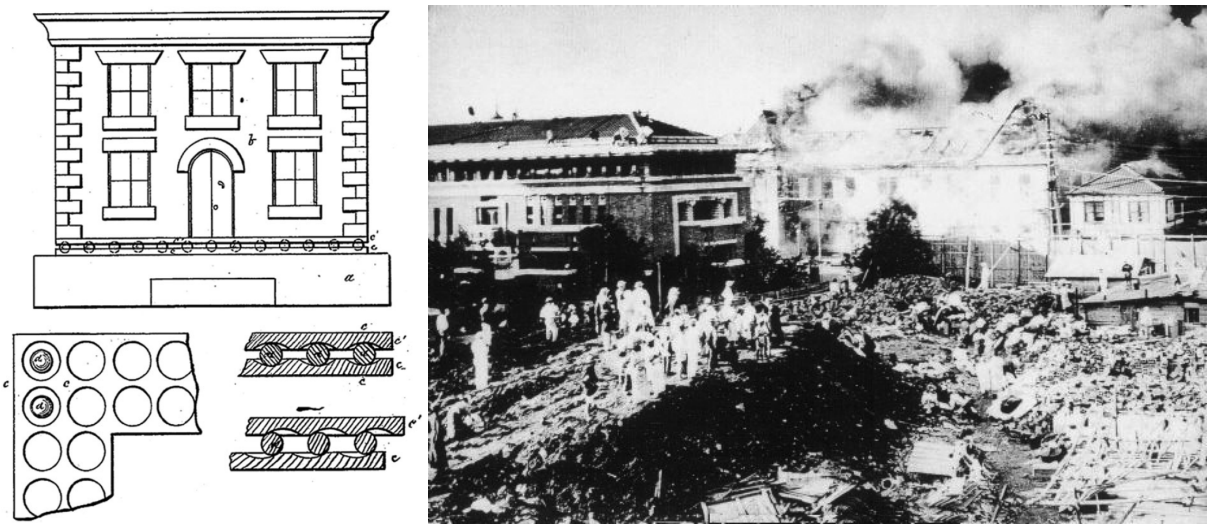

Figure 2.18. *Left:* Jules Touaillon's 1870 concept of base isolation [50]. *Right:* Frank Lloyd Wright's Imperial Hotel immediately after the 1923 Great Kantō earthquake (Tokyo, Japan).

Base isolation technology rapidly evolved in the late 20th and early 21st centuries. Currently, the most common types of isolation hardware are elastomeric (i.e. natural rubber) bearings, high damping rubber bearings, lead rubber bearings, flat slider bearings, friction pendulum bearings, and ball & roller bearings. All isolation devices share three common features: high initial stiffness to prevent large displacements during low excitation events (e.g. wind gusts), low secondary stiffness to provide the period elongation duration seismic shaking, and some form of energy dissipation mechanism. Figure 2.19 shows a lead rubber bearing and triple friction pendulum bearing alongside their respective force-displacement hysteresis loops.

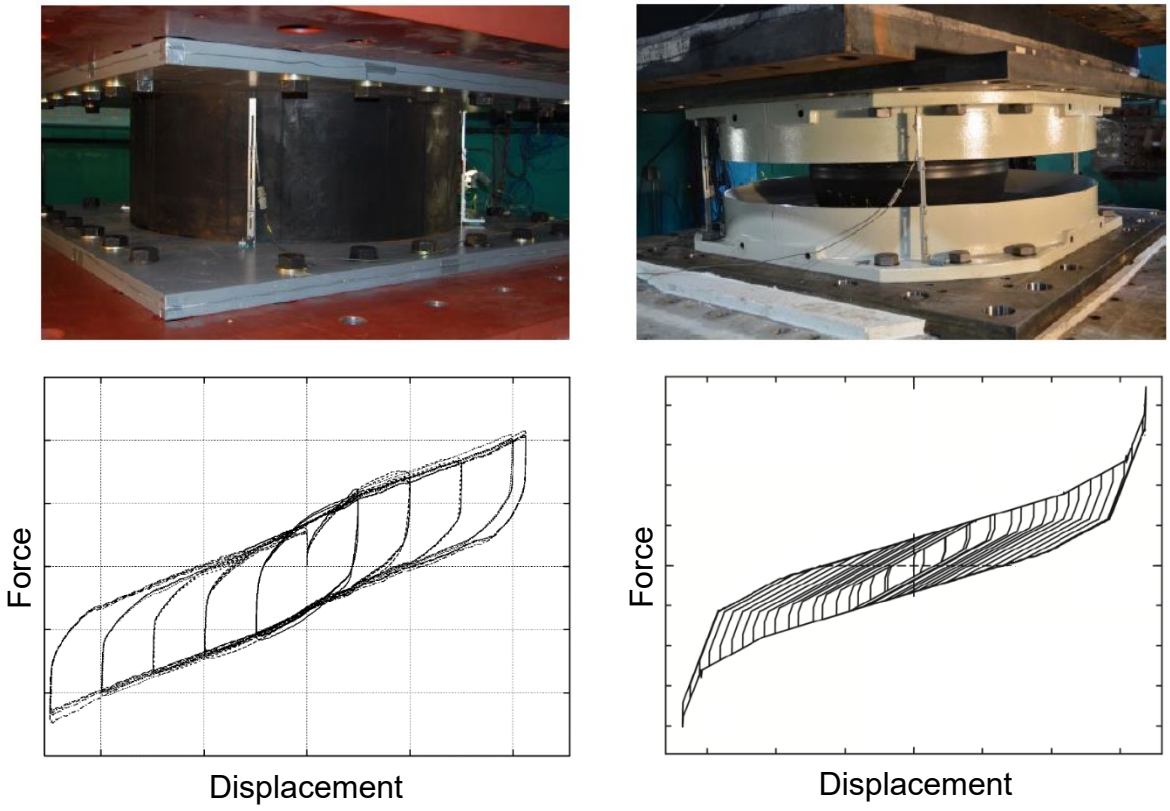

Figure 2.19. Lead rubber bearing (left) and triple friction pendulum bearing (right) [57], with typical force-displacement hysteresis curves [58,59].

During extreme earthquake shaking, the base mat of a base-isolated building may displace beyond the allotted seismic gap and impact the surrounding moat wall. This is referred to as moat wall pounding. While adjacent building pounding is caused by a frequency mismatch between the colliding buildings, moat wall pounding is caused by a frequency mismatch between the base-isolated superstructure and moat wall. Moat wall pounding is a concerning problem because it can amplify floor accelerations and interstory deformation during impact. In many cases, the increased demand from pounding can cause the isolated building to perform worse than an identical building fixed at its base [60].

Moat wall pounding is rare, but it has been documented in past earthquakes. The base-isolated Fire Command and Control (FCC) building in Los Angeles, California pounded against its moat wall during the 1994 Northridge earthquake. Nagarajaiah and Sun [7] determined that, besides the impact event, the FCC building performed well, and that impact reduced the overall effectiveness of the isolation system. The 2010 Darfield earthquake and 2011 Christchurch earthquake caused damage to the seismic moat cover of an isolated women's hospital [61,62], shown in Figure 2.20 below.

Figure 2.20. Damage to a seismic gap cover as a result of moat wall pounding during the 2010 Darfield earthquake [61].

Tsai [63] was among the first to study moat wall pounding using the framework of numerical modeling. In his study, Tsai represented a typical base-isolated building using a continuous inelastic shear beam. The isolators were modeled using linear and bilinear models, while the moat walls were modeled as uniaxial springs with linear elastic, nonlinear elastic, or elastoplastic behavior. The shear beam exhibited normal acceleration demands (except at the base) if it was permitted to yield, but showed very high accelerations if it remained elastic. Furthermore, the type of moat wall macro model had little effect on the superstructure response.

Malhotra [64] conducted a similar study that analyzed a linear elastic model of the superstructure, isolators, and moat wall. The fully linear characteristics permitted closed-form analytical solutions to be obtained, which showed several intriguing results. Firstly, the base shear generated by impacts can be greater than the weight of the entire building. The level of base shear was proportional to the moat wall stiffness, as well as the mass and stiffness of the superstructure. Secondly, the moat walls absorbed a significant portion of the impact energy, and the level of dissipation was proportional to the wall stiffness, overall system damping, and superstructure mass.

Komodromos et al. [65] surveyed three different contact models in a landmark parametric study of moat wall pounding. They determined that impact to the moat wall induces higher-mode vibrations, which amplifies interstory displacements and eliminates the pseudo-rigid body vibration that is the objective of base isolation. Additionally, they concluded that the impact stiffness strongly affects the acceleration response at the base, but weakly affects displacements and upper-floor accelerations.

Masroor and Mosqueda [66] were perhaps the first to conduct large-scale experiments that directly tested moat wall pounding in base-isolated buildings. They constructed a quarter-scale,

three-story building specimen (see Figure 2.21) and subjected it to impact-inducing ground motions. Results from numerous tests concluded that the initial gap distance, impact velocity, and wall flexibility controlled the impact force magnitudes. In extreme pounding cases, the superstructure specimen yielded at reduced beam section locations.

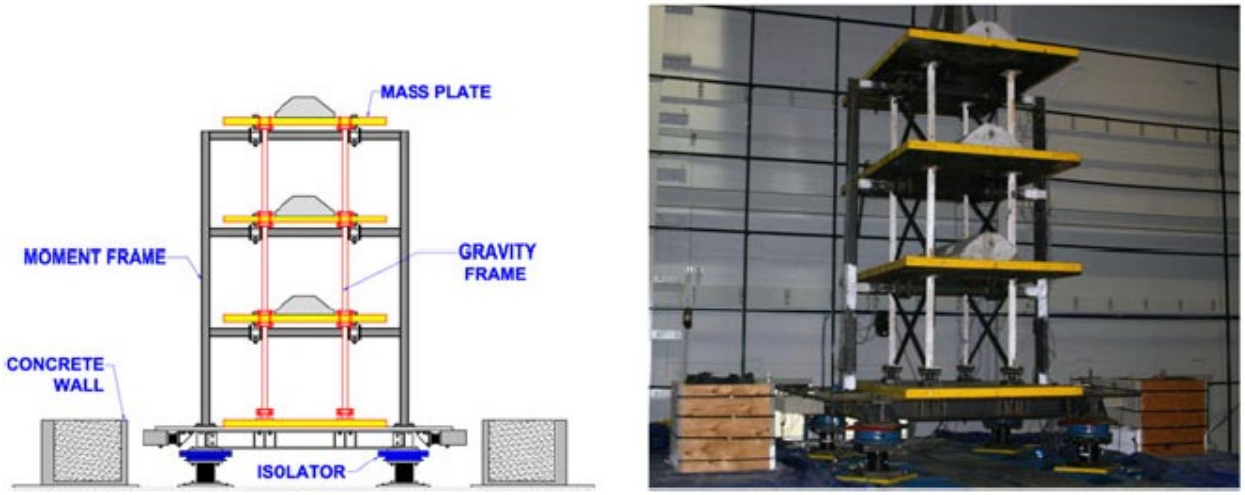

Figure 2.21. Illustration (left) and photograph (right) of a moat wall pounding experiment [66].

Sasaki et al. [67] included moat wall pounding test as part of a broader study on a four-story base-isolated building tested at the E-Defense facility in Kobe, Japan. The building had an asymmetric floor plan, and included realistic nonstructural items like a staircase, garage door, and furniture. Post-impact inspection revealed that the moat walls failed in shear, while the superstructure remained relatively unscathed (see Figure 2.22).

Figure 2.22. *Left:* Overview of base-isolated building specimen. *Right:* Moat walls damaged from pounding events. Photo credit: Hirohisa Fukui, E-Defense.

Kitayama and Constantinou [68] rigorously assessed the collapse probability of base-isolated buildings designed according to ASCE/SEI 7-10 and ASCE/SEI 7-16 specifications. Using multiple nonlinear models and a large suite of ground motions, they showed that current design standard for base-isolated buildings can lead to unacceptably high probabilities of collapse. In fact, "displacement restrainers" such as moat walls may be necessary to limit isolator displacement and put isolated buildings at an acceptable seismic performance level.

Moat wall pounding is a topic of growing interest in the earthquake engineering community. Many numerical studies have been conducted, but very few consider the range of nonlinearities present in the isolation system, moat wall, and superstructure itself. Moreover, little research on pounding is supported by experimental data. The first half of this dissertation will develop moat wall pounding models using simplified contact elements (Chapter 3) and high-fidelity finite element simulations (Chapters 4 and 5). In both cases, the models are verified using experimental data. The following sections review relevant literature for the second half of the dissertation, which will focus on reduced-order models of mechanical structures with bolted joints and intermittent contact.

2.4. Intermittent Contact and Bolted Joints

Intermittent contact refers to a phenomenon where components of a multi-body system come in and out of contact with one another during dynamic loading. Such problems regularly appear in the aerospace and mechanical industries. Turbomachinery, like hydraulic pumps and airplane engines, contain internal rotating components that change contact states several thousand times a second [69]. Changing gears on a bicycle requires contact between the chain and gear cassette [70]. Mechanical joints, which are sometimes assumed to rigidly connect multiple substructures, undergo contact area changes and stick-slip transitions during vibration [71,72].

Figure 2.23. Examples of structural systems with intermittent contact. *Clockwise from top left:* Brake-Reuss beam with a mechanical joint (photo credit: Matthew Brake), vehicle impact (IIHS), turbine with bladed disks (International Turbomachinery Magazine), bicycle gear-chain system (Level Nine Sports).

Intermittent contact can also occur on a limited-time scale, such as automobile impact [73,74], where the car will briefly contact another object. Self-contact of vehicle components within the crush zone is also likely to happen during impact. The seismic pounding problems discussed in the previous sections are example of intermittent contact: adjacent buildings (or a base-isolated building and a moat wall) will come in and out of contact during earthquake ground motion. A few of these examples are summarized in Figure 2.23.

The second half of this dissertation focuses on intermittent contact in dynamic substructures with bolted joints and reduced-order modeling methods to alleviate their associated computational bloat. Many engineering structures are comprised of elements joined by bolts, rivets, welds, adhesives, and the like. It has been shown that the stiffness and damping traits of metallic structures is dominated by the location its joints and the level of bolt preload [71,75–77]. Consequently, accurate dynamic models require rigorous numerical representation of bolted joints. The ensuing discussion reviews the diverse family of joint models used for various applications in structural dynamics. Following that, the final section of this literature review will provide an overview of relevant reduced-order modeling techniques to address the prohibitive size of bolted joint models.

2.5. Joint Models in Structural Dynamics

In a rough sense, joint modeling in structural dynamics can be divided into two groups: whole-joint models [78] and node-to-node (or surface-to-surface) [79,80] models. Whole-joint models rigidize the joint and characterize its macro-level behavior using constitutive laws. Node-to-node and surface-to-surface models are common in finite element software, and pair opposite

sides of an interface with one another and apply contact forces proportional to the relative deformation between the pair.

Owing to the complex dynamic environment at the interior of a joint, whole-joint models have become a staple in structural dynamics analysis. Whole-joint models represent the joint force-displacement relationship with a single function or curve. This is akin to the previously discussed "macro" impact models, which can only capture total contact forces, without considering their distribution in a three-dimensional domain. Whole-joint approximations begin with the assumption that each half of an interface moves as a rigid body. This is typically achieved by constraining the interface degrees of freedom to a single node with only six degrees of freedom (three translational, three rotational), as shown in Figure 2.24 below.

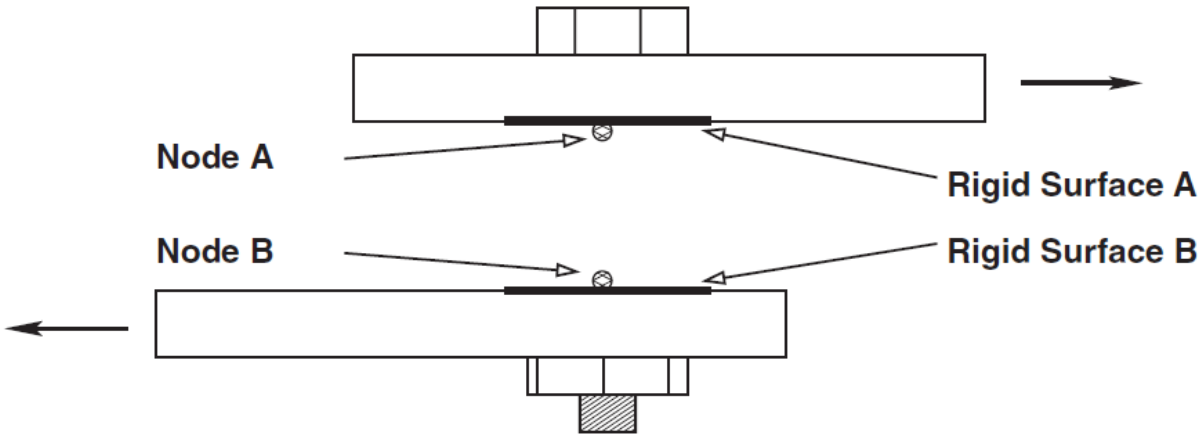

Figure 2.24. Whole-joint models constrain interface motion to a single node [78].

Constitutive models of metallic materials are often applied as whole-joint models because their hysteresis curves resemble that of an entire joint. For example, the Ramberg-Osgood [81] and Valanis [82] plasticity models have both been used to model joint behavior. Iwan studied

material plasticity using infinite Jenkins elements with statistically distributed input parameters [83,84]. Iwan's original method has been refined into a four-parameter model [85], which has become a standard joint analysis tool. In any case, whole-joint models rigidize the interface, which prevents meaningful stress computation from a finite element analysis. Whole-joint models are popular for their ability to reduce large interfaces to just a few degrees of freedom, but any detailed consideration of interior joint mechanics is neglected.

Node-to-node and surface-to-surface contact models, however, are capable of predicting dynamic responses within a joint. These models assign pairs of nodes or surfaces at an interface, and apply forces based on the relative deformation between the nodes. In general, node-to-node models assume small displacements at the interface, such that node pairs never change during dynamic loading. The benefit of this assumption is that a contact element can be attached between each node pair, without having to change location or properties of the element based on the contact state. Surface-to-surface models, however, apply contact forces based on overlapping volumes, which must be updated at every timestep of a dynamic simulation. The following discussions are limited to node-to-node contact models.

The simplest model of a joint considers two masses connected in the normal direction by a "penalty" spring [72], and in the tangential direction by a Jenkins element [86]. Both the penalty and Jenkins elements relate relative displacements to contact forces. For example, the relative normal displacement between two masses with initially coincident coordinates is

$$g_N(t) = u_{N1}(t) - u_{N2}(t) \tag{2.23}$$

and the relative tangential displacement is

$$g_T(t) = u_{T1}(t) - u_{T2}(t) \tag{2.24}$$

where u is a total displacement and g is a relative displacement. Subscripts 1 and 2 refer to the mass or node in question, and subscripts N and T refer to the normal and tangential directions, respectively. The force-displacement relationship of a penalty element is

$$f_N(t) = \begin{cases} k_N g_N(t) & , \quad g_N(t) < 0 \quad (contacting) \\ 0 & , \quad g_N(t) \geq 0 \quad (gapping) \end{cases} \tag{2.25}$$

where f_N is the normal contact force and k_N is the normal contact stiffness. Typically, k_N is determined heuristically – it should be large enough to keep nodal overlap to a minimum, but small enough to ensure a numerically stable solution.

Jenkins elements consist of a spring and frictional slider in series, where sticking behavior is controlled by the tangential contact stiffness k_T, and slipping behavior is governed by the friction coefficient μ. The force-displacement relationship of a Jenkins element is

$$f_T(t) = \begin{cases} k_T g_T(t) & , \quad g_N(t) < 0 \quad \& \quad |k_T g_T(t)| < f_{CL}(t) \quad (sticking) \\ f_{CL}(t) & , \quad g_N(t) < 0 \quad \& \quad |k_T g_T(t)| \geq f_{CL}(t) \quad (slipping) \\ 0 & , \quad g_N(t) \geq 0 \quad (gapping) \end{cases} \tag{2.26}$$

where $f_T(t)$ is the tangential contact force, and $f^{CL}(t)$ is the Coulomb limit force, defined as

$$f^{CL}(t) = |\mu f_N(t)| \tag{2.27}$$

The tangential contact stiffness is usually defined as a fraction of the normal contact stiffness, e.g. $k_T = k_N/2$. Sherif and Kossa conducted experiments to develop a more robust relationship between k_T and k_N [87], as

$$k_T = \pi \frac{1-\nu}{2(2-\nu)} k_N \tag{2.28}$$

where ν is the Poisson's ratio of the material making up the contacting bodies. A two-mass system connected by a penalty and Jenkins element in shown in Figure 2.25, along with their respective force-displacement relationships.

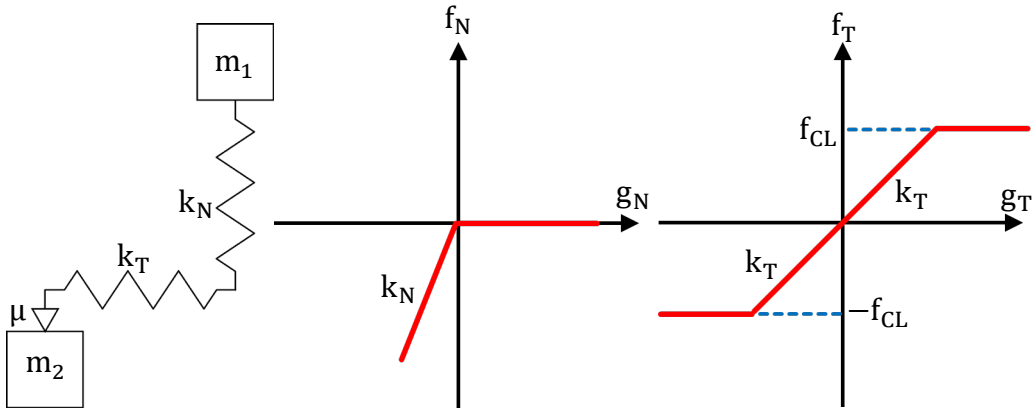

Figure 2.25. *Left:* Two-mass system connected by a penalty spring and Jenkins element. *Middle:* Penalty spring force-displacement relationship. *Right:* Jenkins element force-displacement relationship.

The penalty-Jenkins system shown in Figure 2.25 is limited to two-dimensional contact, where the friction forces act in only one direction. Real mechanical joints, of course, act in three dimensions, with two coupled tangential components. Yang and Menq [88] extended the 2D penalty-Jenkins system to include a second frictional component (see Figure 2.26). The Yang-Menq model introduces the slider displacement vector (**w**) as a new state variable. As such, every node pair within an interface has eight degrees of freedom (DOF) associated with it: three translational DOF for node (1) three translational DOF for node (2), and two translational DOF for the slider (one for each tangential direction). The vector of slider displacements is given by

$$\mathbf{w}(t) = \begin{Bmatrix} w_{T1}(t) \\ w_{T2}(t) \end{Bmatrix} \tag{2.29}$$

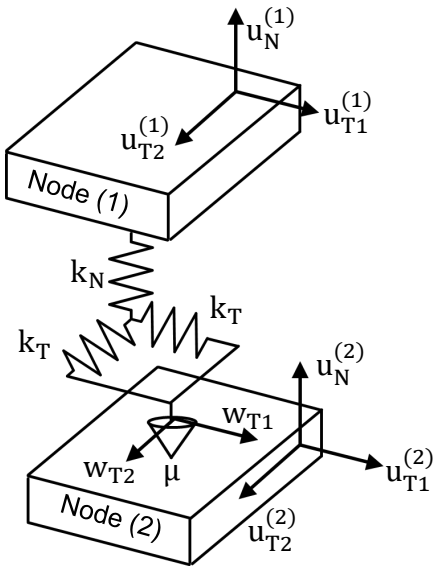

Figure 2.26. 3D contact model of Yang and Menq [88].

and the tangential stiffness is now a tangential stiffness matrix $\mathbf{K}_T$, stated as

$$\mathbf{K}_T = \begin{bmatrix} k_{T1} & 0 \\ 0 & k_{T2} \end{bmatrix} \tag{2.30}$$

For a homogeneous, isotropic material, $k_{T1} = k_{T2} = k_T$.

In this model, the normal contact force is still computed according to Equation (2.25), but the tangential force is updated to reflect the coupling between the two tangential directions. Zucca and Firrone [89] developed an intuitive computational procedure for state determination of a given contact pair that simultaneously updates the tangential forces and slider displacements. Thus far, the Zucca-Firrone approach has only been applied to 2D Yang-Menq models. Chapter 6 of this dissertation presents a novel extension of the Zucca-Firrone approach to a 3D Yang-Menq model with coupled frictional components.

This dissertation will focus on the former class of contact models, which considers node-to-node contact explicitly using penalty springs and Jenkins elements. The following section

details existing methods for reducing the number of DOF in such models using a technique called projection-based model order reduction.

2.6. Projection-Based Reduced Order Models

Node-to-node and surface-to-surface contact elements, such as the Yang-Menq model (see Figure 2.26), relate relative interface displacements to proportional interface forces for a single node pair. In a large finite element model with multiple joints, thousands to tens of thousands of such elements are necessary to accurately predict the interface mechanics. In many cases, direct use of a full-order finite element model may be computationally intractable, with hundreds of thousands to millions of DOF. Consequently, research dating back to the middle of the 20th century has strived to develop reduced-order models (ROMs) that reduce the number of DOF to a manageable level.

Projection-based model order reduction is one of the most ubiquitous techniques for reducing the number of DOF in a dynamic system. The key principle of these methods is Galerkin projection [90], which projects a large solution space onto a smaller subspace with suitable accuracy. Linear modal analysis is perhaps the most common type of Galerkin projection in structural dynamics analysis. Consider a dynamic system with mass matrix $\mathbf{M}$ and stiffness matrix $\mathbf{K}$. For a system with n DOF, each of these matrices is n × n. A truncated set of r < n eigenmodes can be computed via

$$\left(\mathbf{K} - \omega_j^2 \mathbf{M}\right)\boldsymbol{\phi}_j = \mathbf{0} \quad j = 1, 2, \dots, r \tag{2.31}$$

where ω_j^2 is the jth eigenfrequency and $\boldsymbol{\phi}_j$ is its associated eigenmode. Assemble the r eigenmodes as columns of the eigenmatrix as

$$\boldsymbol{\Phi} = [\boldsymbol{\phi}_1 \quad \boldsymbol{\phi}_2 \quad \cdots \quad \boldsymbol{\phi}_r] \tag{2.32}$$

The original displacement vector $\mathbf{u}(t)$ is projected onto a modal subspace $\mathbf{q}$ through pre-multiplication by $\boldsymbol{\Phi}$:

$$\mathbf{u}(t) = \boldsymbol{\Phi}\mathbf{q}(t) \tag{2.33}$$

The reduced-order mass and stiffness matrices, are computed via

$$\bar{\mathbf{M}} = \boldsymbol{\Phi}^T\mathbf{M}\boldsymbol{\Phi} \tag{2.34a}$$

$$\bar{\mathbf{K}} = \boldsymbol{\Phi}^T\mathbf{K}\boldsymbol{\Phi} \tag{2.34b}$$

This newly created ROM has r DOF. Typically, r is chosen to be much smaller than n, such that the new model captures the essential dynamic characteristics at a greatly reduced computational cost.

Another projection-based ROM technique is static condensation, sometimes referred to as Guyan reduction [91]. Consider a partitioning of the system described by $\mathbf{M}$ and $\mathbf{K}$ into primary DOF (p) and secondary DOF (s), as

$$\mathbf{M} = \begin{bmatrix} \mathbf{M}_{pp} & \mathbf{M}_{ps} \\ \mathbf{M}_{sp} & \mathbf{M}_{ss} \end{bmatrix} \tag{2.35a}$$

$$\mathbf{K} = \begin{bmatrix} \mathbf{K}_{pp} & \mathbf{K}_{ps} \\ \mathbf{K}_{sp} & \mathbf{K}_{ss} \end{bmatrix} \tag{2.35b}$$

Static equilibrium of this system is described by

$$\mathbf{K}\mathbf{u} = \mathbf{f} \tag{2.36}$$

where $\mathbf{u}$ is the displacement vector and $\mathbf{f}$ is an arbitrary loading vector. In partitioned form, this is stated as

$$\begin{bmatrix} \mathbf{K}_{pp} & \mathbf{K}_{ps} \\ \mathbf{K}_{sp} & \mathbf{K}_{ss} \end{bmatrix} \begin{Bmatrix} \mathbf{u}_p \\ \mathbf{u}_s \end{Bmatrix} = \begin{Bmatrix} \mathbf{f}_p \\ \mathbf{f}_s \end{Bmatrix} \tag{2.37}$$

Suppose that loading at the secondary DOF is unimportant or negligible, that is, $\mathbf{f_s} = \mathbf{0}$. The bottom row of Equation (2.37) becomes

$$\mathbf{K}_{sp}\mathbf{u}_p + \mathbf{K}_{ss}\mathbf{u}_s = \mathbf{0} \tag{2.38}$$

Solving for $\mathbf{u_s}$ yields

$$\mathbf{u_s} = -\mathbf{K}_{ss}^{-1}\mathbf{K}_{sp}\mathbf{u}_p \tag{2.39}$$

The term $-\mathbf{K}_{ss}^{-1}\mathbf{K}_{sp}$ is often referred to as a constraint mode matrix, abbreviated $\mathbf{\Psi}$. Displacements can be projected onto a subspace of only the primary DOF, as

$$\begin{Bmatrix}\mathbf{u}_p(\mathrm{t}) \\ \mathbf{u_s}(\mathrm{t})\end{Bmatrix} = \begin{bmatrix}\mathbf{I} \\ \mathbf{\Psi}\end{bmatrix}\mathbf{u}_p(\mathrm{t}) \tag{2.40}$$

where $\mathbf{I}$ is an identity matrix. In compact form,

$$\mathbf{u}(\mathrm{t}) = \mathbf{T}\mathbf{q}(\mathrm{t}) \tag{2.41}$$

where $\mathbf{u}(\mathrm{t}) = [\mathbf{u}_p(\mathrm{t}) \quad \mathbf{u}_s(\mathrm{t})]^{\mathrm{T}}$, $\mathbf{q}(\mathrm{t}) = \mathbf{u}_p(\mathrm{t})$, and $\mathbf{T} = [\mathbf{I} \quad \mathbf{\Psi}]^{\mathrm{T}}$. The reduced system matrices are

$$\bar{\mathbf{M}} = \mathbf{T}^{\mathrm{T}}\mathbf{M}\mathbf{T} \tag{2.42a}$$

$$\bar{\mathbf{K}} = \mathbf{T}^{\mathrm{T}}\mathbf{K}\mathbf{T} \tag{2.42b}$$

The original model had $\mathrm{n} = \mathrm{n_p} + \mathrm{n_s}$ DOF, and the ROM has only $\mathrm{n_p}$ DOF. Static condensation has been extended to so-called dynamic condensation [92–94], which includes the mass matrix. These methods invariably require some form of frequency-dependence, however, and have not gained as much traction as traditional static condensation.

Equations (2.41) and (2.42) reveal a generalized form of projection-based ROMs. For example, the modal ROM in Equations (2.33) and (2.34) can be stated in such a form by setting $\mathbf{T} = \mathbf{\Phi}$. Other ROMs employ different types and combinations of static modes (e.g. $\mathbf{\Psi}$) and dynamic modes (e.g. $\mathbf{\Phi}$).

Component mode synthesis (CMS) is a vital part of many ROMs of systems with multiple substructures. CMS methods first divide a structure into multiple substructures that are joined by connections that may be linear or nonlinear. Next, a truncated set of component modes are computed, which reduce the interior (i.e. non-interface) DOF, while leaving the interface DOF intact. The level of truncation in the component modes provides the actual model order reduction. Finally, the reduced-order components are assembled into a "superelement" coupled by one or more contact interfaces. Hurty [95] proposed the first CMS method in 1960, which used fixed-interface (FI) eigenmodes, rigid body modes, and static constraint modes [91]. Eight years later, Craig and Bampton [96] refined Hurty's original method by showing that the rigid body modes were unnecessary, and the famous Hurty/Craig-Bampton (HCB) method was born.

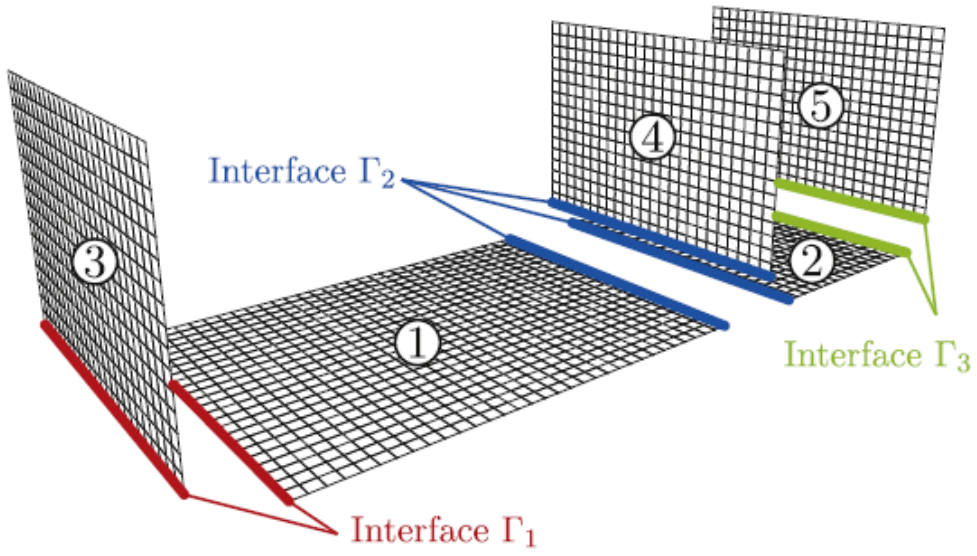

Figure 2.27. W-bracket system divided into five substructures with three interfaces [97].

The HCB transformation for the k^{th} substructure is

$$\mathbf{T}_k = \begin{bmatrix} \boldsymbol{\Phi}_k^{\mathrm{FI}} & \boldsymbol{\Psi}_k \\ \mathbf{0} & \mathbf{I} \end{bmatrix} \tag{2.48}$$

where $\boldsymbol{\Phi}_k^{\mathrm{FI}}$ are the FI modes and $\boldsymbol{\Psi}_k$ are static constraint modes. $\mathbf{T}_k$ transforms the full order component displacements $\mathbf{u}_k(\mathrm{t}) = [\mathbf{u}_{i,k}(\mathrm{t}) \quad \mathbf{u}_{b,k}(\mathrm{t})]^{\mathrm{T}}$ to HCB displacements $\bar{\mathbf{u}}_k(\mathrm{t}) = [\mathbf{q}_{i,k}(\mathrm{t}) \quad \mathbf{u}_{b,k}(\mathrm{t})]^{\mathrm{T}}$. The interior DOF are now generalized modal coordinates ($\mathbf{q}_{i,k}$), while the boundary DOF remain physical ($\mathbf{u}_{b,k}$). Full derivation of the HCB superelement is shown in Chapter 6 of this dissertation. Krattiger et al. [97] also provides a detailed derivation for a W-bracket system with five substructures and three interfaces (see Figure 2.27).

MacNeal [98], Rubin [99], and Craig and Chang [100] modified the HCB method by using attachment modes instead of FI modes, but the HCB method remains the preeminent CMS technique for its simple construction and ease of use.

Even on modern computing systems, a CMS-derived ROM may still be too large to run dynamic analyses, particularly in the time domain. An HCB-reduced model, though highly reduced on the interior partition, may still be bogged down by tens of thousands or millions of interface DOF. For node-to-node contact representations in particular, the number of DOF in the b set tends to be very high, in order to accurately capture the frictional effects within a joint. In this case, the interface DOF can be reduced through a secondary transformation. Craig and Chang developed one of the first method of DOF reduction in linear interfaces [101], but it was not widely adopted. System-level characteristic constraint (SCC) modes were developed by Castanier et al. [102] by computing eigenmodes on the $b - b$ partition of an HCB model, i.e.

$$\left[\bar{\mathbf{K}}_{bb} - \left(\bar{\omega}_j^{\mathrm{SCC}}\right)^2 \bar{\mathbf{M}}_{bb}\right] \bar{\boldsymbol{\Phi}}_j^{\mathrm{SCC}} = \mathbf{0} \quad j = 1, 2, \ldots, \mathrm{n}_{\mathrm{SCC}} \tag{2.49}$$

where $\bar{\omega}_j^{\mathrm{SCC}}$ is the j$^{\mathrm{th}}$ SCC frequency and $\bar{\boldsymbol{\Phi}}_j^{\mathrm{SCC}}$ is the corresponding SCC mode. These modes are referred to as "system-level" because they are computed on the $b - b$ partition of the entire HCB

superelement. The number of retained SCC modes (n_{SCC}) is less than the original number of boundary DOF (n_b), which provides the desired reduction of interface DOF. The SCC modes are concatenated into the SCC eigenmatrix as

$$\bar{\boldsymbol{\Phi}}^{\mathrm{SCC}} = \left[\bar{\boldsymbol{\phi}}_1^{\mathrm{SCC}} \quad \bar{\boldsymbol{\phi}}_2^{\mathrm{SCC}} \quad \cdots \quad \bar{\boldsymbol{\phi}}_{n_{\mathrm{SCC}}}^{\mathrm{SCC}}\right] \tag{2.50}$$

Thus, the SCC transformation is

$$\bar{\mathbf{u}}(t) = \bar{\mathbf{T}}\bar{\bar{\mathbf{u}}}(t) \tag{2.51a}$$

$$\begin{Bmatrix}\mathbf{q}_i(t)\\ \mathbf{u}_b(t)\end{Bmatrix} = \begin{bmatrix}\mathbf{I} & \mathbf{0}\\ \mathbf{0} & \bar{\boldsymbol{\Phi}}^{\mathrm{SCC}}\end{bmatrix}\begin{Bmatrix}\mathbf{q}_i(t)\\ \mathbf{q}_b(t)\end{Bmatrix} \tag{2.51b}$$

Many other interface reduction (IR) techniques have been developed, such as local-level characteristic constraint (LCC) modes [103,104], which compute interface eigenmodes using the uncoupled component matrices (i.e. using $\mathbf{M}_{bb,k}$ and $\mathbf{K}_{bb,k}$). Hybrid characteristic constraint (HCC) modes have also been proposed, which use a combination of SCC and LCC modes [97,105]. A whole-joint style technique referred to as the virtual node (VN) method has also been proposed [106], which reduces all interface DOF to three translations and three rotations. IR methods inherently rely on their parent CMS technique, so most are based on the HCB transformation due to its prevalence in research and industry.

Until recently, IR methods were limited to rigidly-connected linear interfaces. The computational savings for linear interfaces is extraordinary – thousands of interface degrees of freedom can be reduced to a handful with negligible loss of fidelity [97]. If applied to nonlinear structures, linear IR models tend to require many interface modes, to the point where almost no computational savings are achieved [107]. The need for ROMs of structures with nonlinear interfaces (e.g. systems with intermittent contact) drove the development of nonlinear interface reduction (NLIR) techniques. The aim of NLIR is to develop sophisticated mode shapes that can approximate essential interface dynamics at a significantly reduced computational cost, relative to

analogous linear IR methods. Early efforts in NLIR applied linear IR methodologies to nonlinear problems [94,108,109]. Gaul and Becker [76] used SCC modes and a free-interface reduction approach to estimate structural damping in a beam-damper assembly. Kuether et al. [110] used LCC modes to approximate system-level displacements of two blocks colliding with frictionless contact. Gram-Schmidt interface (GSI) [111] modes have been proposed as an improved SCC method that accommodates active and loaded DOF in the boundary partition.

NLIR techniques requiring more labor-intensive basis computation procedures have developed, such as adaptive microslip projection (AMP) modes [112,113] and Jacobian projection [114]. Modal derivatives (MDs), which compute the derivative of mode shapes with respect to modal coordinates [115,116], have also been proposed as a NLIR tool [117,118]. Regardless of their specific methodology, almost all NLIR techniques require some use of the full-order finite element model, which can DOF numbering in the millions. Furthermore, these methods are usually restricted to the frequency domain, and few have explored the use of interface-reduced models for transient dynamic simulations with arbitrary loading. Chapter 6 of this dissertation lays the theoretical groundwork for response history analysis of HCB superelements with bolted joints and nonlinear interface reduction. Chapter 7 introduces a family of novel interface reduction techniques that address gaps in the existing body of knowledge by (1) requiring only the HCB superelement for interface basis computation, (2) having direct applicability to problems in the time domain, and (3) exhibiting good accuracy in local interface response metrics.

References

1. Bertero VV, Collins RG. Investigation of the failures of the Olive View stairtowers during the San Fernando earthquake and their implications on seismic design. *Earthquake Engineering Research Center* 1973.

2. Rosenbluth E. The Mexican Earthquake: A Firsthand Report. *Civil Engineering - ASCE* 1986; **56**(1): 38–40.

3. Rosenbluth E, Meli R. The 1985 Mexico City Earthquake. *Concrete International* 1986; **8**(5).

4. Priestly MJN, Calvi GM, Seible F. *Seismic design and retrofit of bridges*. New York, USA: Wiley; 1996.

5. Kasai K, Maison BF. Building pounding damage during the 1989 Loma Prieta earthquake. *Engineering Structures* 1997; **19**(3): 195–207. DOI: 10.1016/S0141-0296(96)00082-X.

6. (EERI) EERI. Northridge Earthquake Reconaissance Report. *Earthquake Engineering Research Institute* 1995.

7. Nagarajaiah S, Sun X, Angeles TL, Fire C, Building B isolated FCC. Base-Isolated FCC Building: Impact Response in Northridge Earthquake. *Journal of Structural Engineering* 2001; **127**(September): 1063–1075. DOI: 10.1061/(ASCE)0733-9445(2001)127:9(1063).

8. (EERI) EERI. The Hyogo-Ken Nanbu Earthquake Reconaissance Report. *Earthquake Engineering Research Institute* 1995.

9. Otsuka H, Unjoh S, Terayama T, Hoshikuma J, Kosa K. Damage to highway bridges by the 1995 Hyogoken Nanbu earthquake and the retrofit of highway bridges in Japan. *Proceedings of the 3rd US-Japan Workshop on the Seismic Retrofit of Bridges*, 1996.

10. (EERI) EERI. 1999 Chi-Chi, Taiwan Earthquake Reconaissance Report. *Earthquake Engineering Research Institute* 2001.

11. Gillies AG, Anderson DL, Mitchell D, Tinawi R, Saatcioglu M, Gardner NJ, Ghoborah A. The August 17, 1999, Kocaeli (Turkey) earthquake - Lifelines and preparedness. *Canadian Journal of Civil Engineering* 2001; **28**(6): 881–890. DOI: 10.1139/cjce-28-6-881.

12. Vasiliadis L, Elenas A. Performance of school buildings during the Athens earthquake of September 7 1999. *12th European Conference on Earthquake Engineering*, 2002.

13. Cole GL, Dhakal RP, Carr AJ, Bull DK. Case studies of observed pounding damage during the 2010 Darfield earthquake. *Proceedings of the Ninth Pacific Conference on Earthquake Engineering Building an Earthquake-Resilient Society* 2011(173): No.173.

14. Kumar MP, Kumar JDC. Seismic Pounding of the Adjacent Buildings with Different Heights. *International Journal of Engineering Research and Science & Technology* 2015; **4**(4): 350–362.

15. Goldsmith W. *Impact: The Theory and Behaviour of Colliding Solids*. London, UK: Edward Arnold; 1960.

16. Goland M, Wickersham PD, Dengler MA. Propagation of elastic impact in beams in bending. *Journal of Applied Mechanics* 1955; **22**: 1–7.

17. Van Mier JGM, Pruijssers AF, Reinhardt HW, Monnier T. Load-time response of colliding concrete bodies. *Journal of Structural Engineering* 1991; **117**: 354–374.

18. Jankowski R. Experimental study on earthquake-induced pounding between structural elements made of different building materials. *Earthquake Engineering and Structural Dynamics* 2010. DOI: 10.1002/eqe.941.

19. Maison BF, Kasai K. Analysis for type of structural pounding. *Journal of Structural Engineering* 1990; **116**: 957–977.

20. Maison BF, Kasai K. Dynamics of pounding when two buildings collide. *Earthquake Engineering & Structural Dynamics* 1992; **21**: 771–786.

21. Filiatrault A, Wagner P, Cherry S. Analytical prediction of experimental building pounding. *Earthquake Engineering & Structural Dynamics* 1995; **24**: 1131–1154.

22. Zanardo G, Hao H, Modena C. Seismic response of multi-span simply supported bridges to a spatially varying earthquake ground motion. *Earthquake Engineering & Structural Dynamics* 2002; **31**: 1325–1345.

23. Kim SH, Shinozuka M. Effects of seismically induced pounding at expansion joints of concrete bridges. *Journal of Engineering Mechanics* 2003; **129**: 1225–1234.

24. Karayannis CG, Favvata MJ. Earthquake-induced interaction between adjacent reinforced concrete structures with non-equal heights. *Earthquake Engineering & Structural Dynamics* 2005; **34**: 1–20.

25. Wolf JP, Skrikerud PE. Mutual pounding odf adjacent structures during earthquakes. *Nuclear Engineering and Design* 1980; **57**: 253–275.

26. Anagnostopoulos SA. Pounding of buildings in series during earthquakes. *1Earthquake Engineering & Structural Dynamics* 1988; **16**: 443–456.

27. Anagnostopoulos SA. Building pounding re-examined: how serious a problem is it? *Eleventh World Conference on Earthquake Engineering*, Acapulco, Mexico: 1996.

28. Goyal S, Pinson EN, Sinden FW. Simulation of dynamics of interacting rigid bodies including friction I: General problem and contact model. *Engineering with Computers* 1994. DOI: 10.1007/BF01198742.

29. Goyal S, Pinson EN, Sinden FW. Simulation of dynamics of interacting rigid bodies including friction II: Software system design and implementation. *Engineering with Computers* 1994. DOI: 10.1007/BF01198743.

30. Brogliato B. Nonsmooth mechanics: Models, dynamics and control, Third edition. *Communications and Control Engineering*, 2016. DOI: 10.1007/978-3-319-28664-8.

31. Jankowski R. Non-linear viscoelastic modelling of earthquake-induced structural pounding. *Earthquake Engineering and Structural Dynamics* 2005; **34**(6): 595–611. DOI: 10.1002/eqe.434.

32. Jankowski R. Analytical expression between the impact damping ratio and the coefficient of restitution in the non-linear viscoelastic model of structural pounding. *Earthquake Engineering and Structural Dynamics* 2006; **35**(4): 517–524. DOI: 10.1002/eqe.537.

33. Jankowski R. Theoretical and experimental assessment of parameters for the non-linear viscoelastic model of structural pounding. *Journal of Theoretical and Applied Mechanics (Poland)* 2007.

34. Lankarani HM, Nikravesh PE. A Contact Force Model with Hysteresis Damping for Impact Analysis of Multibody Systems. *Journal of Mechanical Design* 1990; **112**(3): 369–376. DOI: 10.1115/1.2912617.

35. Muthukumar S, DesRoches R. A Hertz contact model with non-linear damping for pounding simulation. *Earthquake Engineering and Structural Dynamics* 2006; **35**(7): 811–828. DOI: 10.1002/eqe.557.

36. Ye K, Li L, Zhu H. A note on the Hertz contact model with nonlinear damping for pounding simulation. *Earthquake Engineering and Structural Dynamics* 2009; **38**: 1135–1142. DOI: 10.1002/eqe.

37. Hertz H. On the contact of elastic solids. *Reine Angew Mathematik* 1881; **92**: 156–171.

38. Hertz H. *Collected Works*. Leipzig, Germany: 1895.

39. Muthukumar S. A Contact Element Approach with Hysteresis Damping for the Analysis and Design of Pounding in Bridges. 2003. DOI: 10.16309/j.cnki.issn.1007-1776.2003.03.004.

40. Sarebanha A, Mosqueda G, Kim MK, Kim JH. Seismic response of base isolated nuclear power plants considering impact to moat walls. *Nuclear Engineering and Design* 2018; **328**(December 2017): 58–72. DOI: 10.1016/j.nucengdes.2017.12.021.

41. Papadrakakis M, Apostolopoulou C, Zacharopoulos A, Bitzarakis S. Three-dimensional simulation of structural pounding during earthquakes. *Engineering Mechanics* 1996; **122**: 423–431.

42. Leibovich E, Rutenberg A, Yankelevsky DZ. On eccentric seismic pounding of symmetric buildings. *Earthquake Engineering & Structural Dynamics* 1996; **25**: 219–233.

43. Jankowski R. Non-linear FEM analysis of earthquake-induced pounding between the main building and the stairway tower of the Olive View Hospital. *Engineering Structures* 2009; **31**(8): 1851–1864. DOI: 10.1016/j.engstruct.2009.03.024.

44. Bi K, Hao H, Chouw N. 3D FEM analysis of pounding response of bridge structures at a canyon site to spatially varying ground motions. *Advances in Structural Engineering* 2013; **16**(4): 619–640. DOI: 10.1260/1369-4332.16.4.619.

45. Jameel M, Saiful Islam ABM, Hussain RR, Hasan SD, Khaleel M. Non-linear FEM analysis of seismic induced pounding between neighbouring Multi-storey Structures. *Latin American Journal of Solids and Structures* 2013. DOI: 10.1590/S1679-78252013000500004.

46. Christopoulos C, Filiatrault A. Principles of Passive Supplemental Damping and Seismic Isolation. *IUSS Press* 2006.

47. Sueoka T, Torii S, Tsuneki Y. The Application of Response Control Design Using Middle-Story Isolation System to High-Rise Building. *13th World Conference on Earthquake Engineering*, Vancouver, B.C., Canada: 2004.

48. Loh CH, Weng JH, Chen CH, Lu KC. System identification of mid-story isolation building using both ambient and earthquake response data. *Structural Control and Health Monitoring* 2013. DOI: 10.1002/stc.479.

49. Makris N. Seismic isolation: Early history. *Earthquake Engineering and Structural Dynamics* 2019; **48**(2): 269–283. DOI: 10.1002/eqe.3124.

50. Touaillon J. Improvement in buildings. U.S. Patent No. 99. 973, 1870.

51. Bechtold J. Earthquake-proof buildings. U.S. Patent No. 845. 046, 1907.

52. Kelly JM. Aseismic base isolation. *Shock and Vibration Digest* 1985; **17**(7): 3–14.

53. Kelly JM. Aseismic base isolation: review and bibliography. *Soil Dynamics and Earthquake Engineering1* 1986; **5**(3): 202–216.

54. Calantarients JA. Improvements in and connected with building and other works and appurtenances to resist the action of earthquakes and the like. *Stanford University* 1909(paper no. 325371).

55. Buckle IG, Mayes RL. Seismic isolation: history, application and performance - a world view. *1Earthquake Spectra* 990; **6**(2): 161–201.

56. Walker B. Mr. Wright's Wonderful Hotel. *Earthquake*, Alexandria, VA, USA: Time-Life Books; 1982.

57. Sarebanha A. Experimental and Numerical Simulation of Seismically Isolated Critical Facilities under Extreme Seismic Loading. University of California, San Diego, 2018.

58. Feng D, Miyama T, Masuda K, Liu W, Zhou F, Zheng B, Li, Z. A Detailed Experimental Study on Chinese Lead Rubber Bearing. *12th World Conference on Earthquake Engineering (12WCEE)*, 2000.

59. Weber F, Distl J, Braun C. Isolation Performance Assessment of Adaptive Behaviour of Triple Friction Pendulum. *Journal of Civil Engineering Research* 2017; **7**(1): 17–33. DOI: 10.5923/j.jce.20170701.03.

60. Masroor A, Mosqueda G. Seismic response of base isolated buildings considering pounding to moat walls. *Technical Report MCEER-13-0003* 2013.

61. Gavin HP, Wilkinson G. Preliminary observations of the effects of the 2010 darfield earthquake on the base-isolated christchurch women's hospital. *Bulletin of the New Zealand Society for Earthquake Engineering* 2010; **43**(4): 360–367. DOI: 10.5459/bnzsee.43.4.360-367.

62. Gavin HP, Nigbor RL. Performance of the base-isolated Christchurch women's hospital in the Sep. 4 2010 Dar field earthquake and the Feb.22 2011 Christchurch earthquake. *20th Analysis and Computation Specialty Conference - Proceedings of the Conference* 2012(4): 554–563. DOI: 10.1061/9780784412374.049.

63. Tsai HC. Dynamic analysis of base-isolated shear beams bumping against stops. *Earthquake Engineering and Structural Dynamics* 1997; **26**(5): 515–528. DOI: 10.1002/(SICI)1096-9845(199705)26:5<515::AID-EQE654>3.0.CO;2-C.

64. Malhotra PK. Dynamics of seismic impacts in base-isolated buildings. *Earthquake Engineering & Structural Dynamics* 1997; **26**(8): 797–813. DOI: 10.1002/(sici)1096-9845(199708)26:8<797::aid-eqe677>3.3.co;2-y.

65. Komodromos P, Polycarpou PC, Papaloizou L, Phocas MC. Response of seismically isolated buildings considering poundings. *Earthquake Engineering and Structural Dynamics* 2007. DOI: 10.1002/eqe.692.

66. Masroor A, Mosqueda G. Experimental simulation of base-isolated buildings pounding against moat wall and effects on superstructure response. *Earthquake Engineering and Structural Dynamics* 2012; **41**: 2093–2109. DOI: 10.1002/eqe.2177.

67. Sasaki T, Sato E, Fukuyama K, Kajiwara K. Enhancement of Base-Isolation Based on E-Defense Full- Scale Shake Table Experiments : Dynamic Response of Base- Isolated Building Under Impact Due To Pounding 2017; **4082**(Abstract ID).

68. Kitayama S, Constantinou MC. Collapse performance of seismically isolated buildings designed by the procedures of ASCE/SEI 7. *Engineering Structures* 2018; **164**(March): 243–258. DOI: 10.1016/j.engstruct.2018.03.008.

69. Rao JS. *Turbomachine blade vibration*. New Age International; 1991.

70. Fregly BJ, Zajac FE, Dairaghi CA. Bicycle Drive System Dynamics: Theory and Experimental Validation. *Journal of Biomechanical Engineering* 2000; **122**(4): 446–452.

71. Gaul L, Nitsche R. The role of friction in mechanical joints. *Applied Mechanics Reviews* 2002; **54**(2): 93–106.

72. Wriggers P. *Computational Contact Mechanics*. 2006.

73. Brach RM, Brach MR. A Review of Impact Models for Vehicle Collision. *SAE International* 1987; **96**(1): 175–190.

74. Ambrósio JAC. Contact and impact models for vehicle crashworthiness simulation. *International Journal of Crashworthiness* 2010; **8**(1): 73–86.

75. Padmanahban K, Murty A. Damping in structural joints subjected to tangential laods. *Proceedings of the Institution of Mechanical Engineers, Part C: Journal of Mechanical Engineering Science* 1991; **205**(2): 121–129.

76. Gaul L, Becker J. Damping prediction of structures with bolted joints. *Shock and Vibration* 2010; **17**(4–5): 359–371. DOI: 10.3233/SAV-2010-0532.

77. Singh A, Scapolan M, Saito Y, Allen MS, Roettgen D, Pacini B, Kuether RJ. Experimental characterization of a new benchmark structure for prediction of damping nonlinearity. *Nonlinear Dynamics, Volume 1* 2019: 57–78.

78. Segalman DJ. Modelling joint friction in structural dynamics. *Structural Control and Health Monitoring* 2006; **13**(1): 430–453. DOI: 10.1002/stc.119.

79. Hallquist J. *LS-DYNA® theory manual*. 2006.

80. Simulia. Abaqus 6.11 Theory Manual. *Providence, RI, USA: DS SIMULIA Corp* 2017.

81. Smallwood DO, Gregory D, Coleman RG. A three-parameter constitutive model for a joint which echibits a power law relationship. *Proceedings of the 72nd Shock and Vibration Symposium*, Destin, FL, USA: 2001.

82. Gaul L, Lenz J. Nonlinear dynamics of structures assembled by bolted joints. *Acta Mechanica* 1997; **125**(1–4): 169–181.

83. Iwan WD. Distributed-element model for hysteresis and its steady-state dynamic response. *ASME Journal of Applied Mechanics* 1966; **33**(4): 893–900.

84. Iwan WD. On a class of models for yielding behavior of continuous and composite systems. *ASME Journal of Applied Mechanics1* 1967; **34**(3): 612–617.

85. Segalman DJ. A Four-Parameter Iwan Model for Lap-Type Joints. *Journal of Applied Mechanics* 2005; **72**: 752–760. DOI: 10.1115/1.1989354.

86. Berger EJ. Friction modeling for dynamic system simulations. *Applied Mechanics Reviews2* 2AD; **55**(6): 535–577.

87. Sherif HA, Kossa SS. Relationship between normal and tangential contact stiffness of nominally flat surfaces. *Wear* 1991; **151**: 49–62. DOI: 10.1016/0043-1648(91)90345-U.

88. Yang BD, Menq CH. Characterization of 3D contact Kinematics and Prediction of Resonant Response of Structures Having 3D Frictional Constraint. *Journal of Sound and Vibration* 1998; **217**(5): 909–925. DOI: 10.1006/jsvi.1998.1802.

89. Zucca S, Firrone CM. Nonlinear dynamics of mechanical systems with friction contacts: Coupled static and dynamic Multi-Harmonic Balance Method and multiple solutions. *Journal of Sound and Vibration* 2014; **333**: 916–926. DOI: 10.1016/j.jsv.2013.09.032.

90. Galerkin BG. Rods and plates. Series occurring in various questions concerning the elastic equilibrium of rods and plates. *Engineering and Technologists Bulletin* 1915; **19**: 897–908.

91. Guyan RJ. Reduction of Stiffness and Mass Matrices. *1AIAA Journal* 1965; **3**(2): 380.

92. Leung AYT. An accurate method of dynamic condensation in structural analysis. *International Journal for Numerical Methods in Engineering* 1978; **12**(11): 1705–1715.

93. Paz A. Dynamic condensation. *AIAA Journal* 1984; **22**(5): 724–727.

94. Qu ZQ. Model reduction for dynamical systems with local nonlinearities. *AIAA Journal* 2002; **40**(2): 327–333. DOI: 10.2514/2.1649.

95. Hurty W. Vibrations of Structural Systems by Component Mode Synthesis. *Transactions of the American Society of Civil Engineers* 1960.

96. Craig RR, Bampton MCC. Coupling of substructures for dynamic analyses. *AIAA Journal* 1968. DOI: 10.2514/3.4741.

97. Krattiger D, Wu L, Zacharczuk M, Buck M, Kuether RJ, Allen MS, Tiso P, Brake MW. Interface reduction for Hurty/Craig-Bampton substructured models: Review and improvements. *Mechanical Systems and Signal Processing* 2019; **114**: 579–603. DOI: 10.1016/j.ymssp.2018.05.031.

98. MacNeal RH. A hyrbid method of component mode synthesis. *Computers & Structures* 1971; **1**: 581–601.

99. Rubin S. Improved component-mode representation for structural dynamic analysis. *AIAA Journal* 1975; **13**(8): 995–1006. DOI: 10.2514/3.60497.

100. Craig RR, Chang CJ. On the use of attachment modes in substructure coupling for dynamic analysis 1977: 89–99. DOI: 10.2514/6.1977-405.

101. Craig RR, Chang CJ. *Substructure Coupling for Dynamic Analysis and Testing*. 1977.

102. Castanier MP, Tan YC, Pierre C. Characteristic Constraint Modes for Component Mode Synthesis. *AIAA Journal* 2001; **39**(6): 1182–1187.

103. Hong SK, Epureanu BI, Castanier MP. Next-generation parametric reduced-order models. *Mechanical Systems and Signal Processing* 2013; **37**(1–2): 403–421. DOI: 10.1016/j.ymssp.2012.12.012.

104. Kuether RJ. Modal substructuring of geometrically nonlinear finite element models with interface reduction. *AIAA Journal* 2017; **55**(5): 1695–1706.

105. Aoyama Y, Yagawa G. Component mode synthesis for large-scale structural analysis. *Computers and Structures* 2001; **79**(6): 605–615.

106. Lindberg E, Hörlin NE, Göransson P. Component mode synthesis using undeformed interface coupling modes to connect soft and stiff substructures. *Shock and Vibration* 2013; **20**: 157–170.

107. Hughes PJ, Scott W, Wu W, Kuether RJ, Allen MS, Tiso P. Interface reduction on hurty/craig-bampton substructures with frictionless contact. *Conference Proceedings of the Society for Experimental Mechanics Series* 2019; **1**: 1–16. DOI: 10.1007/978-3-319-74280-9_1.

108. Friswell MI, Penny JET, Garvey SD. Using linear model reduction to investigate the dynamics of structures with local non-linearities. *Mechanical Systems and Signal Processing* 1995; **9**(3): 317–328. DOI: 10.1006/mssp.1995.0026.

109. Segalman DJ. Model reduction of systems with localized nonlinearities. *Journal of Computational and Nonlinear Dynamics* 2007; **2**(3): 249–266. DOI: 10.1115/1.2727495.

110. Kuether RJ, Coffin PB, Brink AR. On Hurty/Craig-Bampton Substructuring with Interface Reduction on Contacting Surfaces. *Proceedings of the ASME 2017 International Design Engineering Technical Conferences and Computes and Information in Engineering Conference (IDETC/CIE 2017)*, Cleveland, Ohio, USA: 2017.

111. Battiato G, Firrone CM, Berruti TM, Epureanu BI. Reduction and coupling of substructures via Gram–Schmidt Interface modes. *Computer Methods in Applied Mechanics and Engineering* 2018; **336**: 187–212. DOI: 10.1016/j.cma.2018.03.001.

112. Mitra M, Zucca S, Epureanu BI. Adaptive Microslip Projection for Reduction of Frictional and Contact Nonlinearities in Shrouded Blisks. *Journal of Computational and Nonlinear Dynamics* 2016; **11**(4): 1–15. DOI: 10.1115/1.4033003.

113. Mitra M, Epureanu BI. Dynamic Modeling and Projection-Based Reduction Methods for Bladed Disks with Nonlinear Frictional and Intermittent Contact Interfaces. *Applied Mechanics Reviews* 2019; **71**(5). DOI: 10.1115/1.4043083.

114. Gastaldi C, Zucca S, Epureanu BI. Jacobian projection reduced-order models for dynamic systems with contact nonlinearities. *Mechanical Systems and Signal Processing* 2018; **100**: 550–569. DOI: 10.1016/j.ymssp.2017.07.049.

115. Idelsohn SR, Cardona A. A reduction method for nonlinear structural dynamic analysis. *Computer Methods in Applied Mechanics and Engineering* 1985. DOI: 10.1016/0045-7825(85)90125-2.

116. Idelsohn SR, Cardona A. A load-dependent basis for reduced nonlinear structural dynamics. *Computers and Structures* 1985. DOI: 10.1016/0045-7949(85)90069-0.

117. Witteveen W, Pichler F. Efficient model order reduction for the dynamics of nonlinear multilayer sheet structures with trial vector derivatives. *Shock and Vibration* 2014; **2014**: 147–155. DOI: 10.1155/2014/913136.

118. Pichler F, Witteveen W, Fischer P. Reduced-order modeling of preloaded bolted structures in multibody systems by the use of trial vector derivatives. *Journal of Computational and Nonlinear Dynamics* 2017. DOI: 10.1115/1.4036989.

Chapter 3 Evaluation of Uniaxial Contact Models for Moat Wall Pounding Simulation

3.1. Introduction

Base isolation is a proven seismic protection strategy that partially decouples the superstructure from the ground through an interfacial layer of flexible isolators [1]. The isolators elongate the fundamental vibration period, decreasing structural accelerations at the cost of increased displacements at the isolation plane. Excessive isolator deformation can usually be avoided by providing supplemental damping devices [2–4], but under extreme ground motion, the base mat displacement may exceed the provided gap distance and impact the moat wall [5,6].

Moat wall pounding can induce very large accelerations and drift demands, diminishing the effectiveness of the isolation system [7–11]. Figure 3.1 shows prototypical deformation patterns for three types of buildings: a traditional fixed-based building, a base-isolated building with no impact, and a base-isolated building with impact. In general, a base-isolated building will behave like a rigid body if there is no impact. If impact occurs, however, the structure temporarily

loses the isolation benefits and will undergo deformations akin to a fixed-based building. Recent studies [9,12–14] indicate that if the moat wall clearance is not sufficiently large, or if the isolation system is not adequately restrained, the probability of collapse of a base isolated building exceeds the limitations targeted by current design standards.

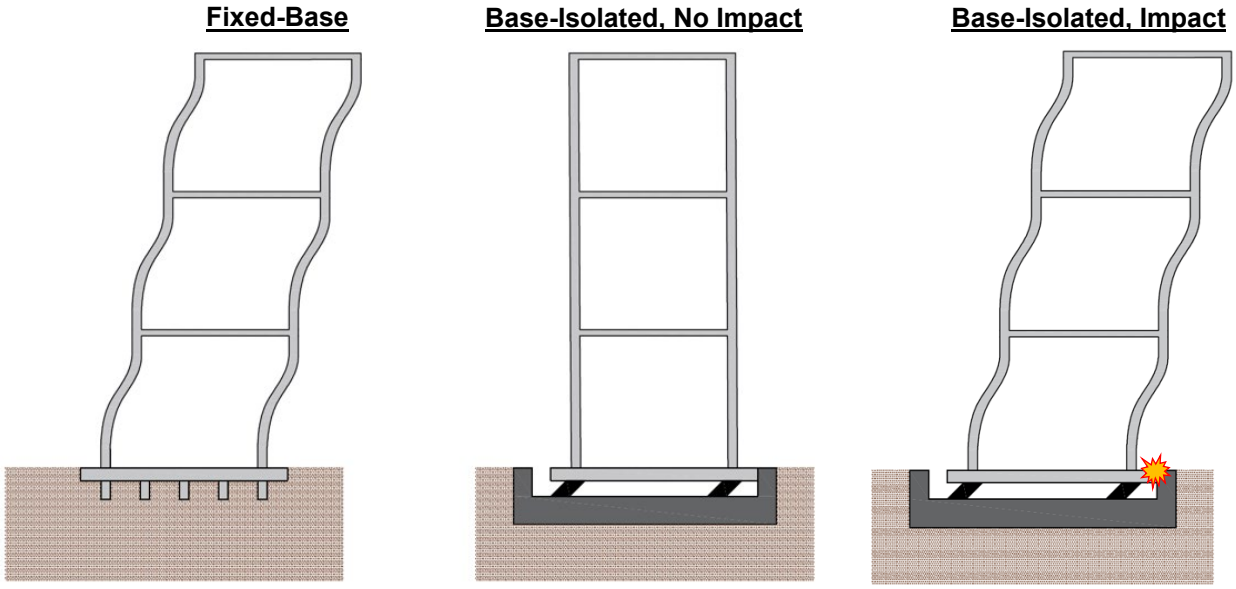

Figure 3.1. Typical seismic deformation patterns for a fixed-base building (left), base-isolated building with no impact (middle), and base-isolaed building with impact (right).

Studies of pounding in seismically isolated buildings and bridges very often employ so-called macro models to represent the contact interface [5,8,15–18]. That is, contact between the base mat and moat wall is defined using one or more uniaxial springs, which may have nonlinear features and/or viscous damping associated with it. As a result, analysts working on seismic pounding problems can choose from a wide range of contact models [19–27]. Indeed, Banerjee et al. [28] provides an in-depth review and comparison of many state-of-the-art contact models.

With many options available, several researchers [15,17,19,22] have assessed how the choice of contact model affects the response of structures subjected to seismically-induced pounding. The analysis in these studies is limited to single degree of freedom examples, or only consider a linear elastic superstructure. This study extends the work of previous researchers, to account for nonlinearity in both the superstructure and moat wall. Specifically, this work compares the performance of five different contact elements when implemented in an experimentally-calibrated OpenSees [29,30] model. This model was calibrated to experimental data by Masroor and Mosqueda [7,8] for moat wall pounding in a quarter-scale base-isolated moment frame. This research extends previous work by the authors [31], which focused on local-level response metrics for a single ground motion. Experimental data and existing numerical models [32,33] were obtained from DesignSafe DataDepot [34] repositories.

It is important to note that this study is limited to unidirectional pounding, where the superstructure base collides with the moat wall at a perfectly perpendicular angle. Pant and Wijeyewickrema [35] showed that only considering pounding in one direction can lead to unconservative conclusions, and Mavronicola et al [36] showed that non-perpendicular impact angles tend to induce larger impact forces. However, the previous experimentation and model calibration [7,8] only considered unidirectional pounding, thus this research is also limited to single component ground motions and perpendicular impacts.

The first section of this work outlines five uniaxial contact models that are commonly used by researchers and practitioners. A common set of parameters for each model are derived based on fundamental physical properties of the contacting bodies. Next, two different studies will examine the performance of each contact model when implemented in the calibrated OpenSees

model: (1) detailed comparison of time histories and hysteresis loops, and (2) statistical analysis of peak response over a suite of 28 ground motions. Finally, results and implications are discussed.

3.2. Uniaxial Contact Models

Normal contact models represent a family of material constitutive laws that govern the unidirectional contact force generated when two flexible bodies collide with one another. The models relate the contact force (f_c) to the material-level indentation (δ) through a relationship of the form

$$f_c(t) = f(\delta(t)) \tag{3.1}$$

where t is time and $f(\delta(t))$ is some function of the indentation. Some of these models may also consider rate effects, i.e.

$$f_c(t) = f\left(\delta(t), \dot{\delta}(t)\right) \tag{3.2}$$

where $\dot{\delta}$ is the first derivative of the material indentation with respect to time, hereafter referred to as the indentation velocity. In this work, the contact force, and corresponding indentation, are considered positive in compression.

This section summarizes the five normal contact models that will be compared in this study, ranging from the very simple to the more complex. Specifically, this study will examine the linear elastic, linear viscoelastic (Kelvin-Voigt) [19–21], Jankowski [22–24], Hertzdamp [25–27], and Muthukumar [37] contact models. Every model has a different set of parameters with various physical meanings. As such, the parameters will be derived based on a consistent set of fundamental system properties, namely: the Poisson's ratios (ν_1, ν_2), Young's moduli (E_1, E_2), volumes (V_1, V_2), and masses (m_1, m_2) of each colliding body. Furthermore, the coefficient of

restitution (e) and the maximum expected indentation (δ_{me}) will be employed in the parameter derivations.

In the context of moat wall pounding, the colliding bodies are the moat wall (subscript 1) and superstructure base level (subscript 2). This allows for a safe comparison between models with very different input parameters. The maximum expected indentation (δ_{me}) is a heuristic parameter that is difficult to measure. It is usually set to some arbitrarily small number (e.g. $\delta_{me} < 0.1$ cm). All five of the models considered here use the Hertz stiffness (k_h), given by

$$k_h = \frac{4}{3\left[\left(\frac{1-\nu_1^2}{E_1}\right)+\left(\frac{1-\nu_2^2}{E_2}\right)\right]\sqrt{\left(\frac{4\pi}{V_1}\right)^{1/3}+\left(\frac{4\pi}{V_2}\right)^{1/3}}} \tag{3.3}$$

This expression was derived by Goldsmith [38], who considered an impact between two colliding spheres with material properties (ν_1, ν_2) and (E_1, E_2), and volumes (V_1, V_2).

The linear viscoelastic [19–21] and Jankowski [22–24] models both employ the effective mass of the colliding bodies (m_{eff}), a useful quantity from classical stereomechanics that can be derived by applying conservation of energy and momentum for an inelastic impact between bodies with masses (m_1, m_2) [38]:

$$m_{eff} = \frac{m_1 m_2}{m_1 + m_2} \tag{3.4}$$

3.2.1. Linear Elastic Model

The simplest normal contact model represents the contact force with a linear elastic spring:

$$f_c(t) = k_{eff}\delta(t) \tag{3.5}$$

where the only parameter is k_{eff}, the effective stiffness, equal to

$$k_{eff} = k_h\sqrt{\delta_{me}} \tag{3.6}$$

3.2.2. Linear Viscoelastic (Kelvin-Voigt) Model

Adding viscous damping to the linear elastic contact model gives rise to the linear viscoelastic model, sometimes referred to as the Kelvin-Voigt contact model [19–21]. This model predicts the contact force via

$$f_c(t) = k_{eff}\delta(t) + c_{eff}\dot{\delta}(t) \tag{3.7}$$

The viscoelastic formulation depends on the indentation velocity ($\dot{\delta}$), and has a new parameter c_{eff}, the effective damping coefficient, given by

$$c_{eff} = 2\xi_{KV}\sqrt{m_{eff}k_{eff}} \tag{3.8}$$

where ξ_{KV} is the Kelvin-Voigt damping ratio, related to the coefficient of restitution (e) through the implicit equation developed by Brogliato [21]:

$$\ln\left(\frac{1}{e}\right) = \frac{2\xi_{KV}}{\sqrt{1-\xi_{KV}^2}}\arctan\left(\frac{\sqrt{1-\xi_{KV}^2}}{\xi_{KV}}\right) \tag{3.9}$$

3.2.3. Jankowski Model

The Jankowski model of contact [22–24] can be viewed as a nonlinear extension of the Kelvin-Voigt contact model. Specifically, the Jankowski model modifies the damping coefficient to be a function of the indentation, such that the contact force is zero when the indentation is zero. Furthermore, the Jankowski model only applies damping during the approach phase of contact, when the indentation velocity is positive. This model has the constitutive law

$$f_c(t) = \begin{cases} k_h\delta(t)^{\frac{3}{2}} + c_J(t)\dot{\delta}(t) & , \quad \dot{\delta}(t) > 0 \quad (approach) \\ k_h\delta(t)^{\frac{3}{2}} & , \quad \dot{\delta}(t) \leq 0 \quad (restitution) \end{cases} \tag{3.10}$$

where c_J is the deformation-dependent Jankowski damping coefficient, equal to

$$c_J(t) = 2\xi_J\sqrt{m_{eff}k_h\sqrt{\delta(t)}} \tag{3.11}$$

The Jankowski damping ratio ξ_J can be written as an explicit function of the coefficient of restitution (e), as

$$\xi_J = \frac{9\sqrt{5}}{2}\cdot\frac{1-e^2}{e(e(9\pi-16)+16)} \tag{3.12}$$

3.2.4. Hertzdamp Model

The Hertzian law of contact [38] with added damping is often abbreviated as the Hertzdamp model [25–27]. This model has a force-indentation relationship governed by

$$f_c(t) = k_h\delta(t)^{\frac{3}{2}} + c_h(t)\dot{\delta}(t) \tag{3.13}$$

where c_h is the Hertz damping coefficient, given by

$$c_h(t) = \xi_h\frac{k_h}{\dot{\delta}_0}\delta(t)^{\frac{3}{2}} \tag{3.14}$$

This expression depends on the pre-impact indentation velocity ($\dot{\delta}_0$), as well as the Hertz damping ratio (ξ_h). The pre-impact indentation velocity is simply the indentation velocity just before the colliding bodies come into contact, and the Hertz damping ratio is related to the coefficient of restitution (e) via

$$\xi_h = \frac{8}{5}\cdot\frac{1-e}{e} \tag{3.15}$$

3.2.5. Muthukumar Model

The Muthukumar model [37] is based on a bilinear approximation of the Hertzdamp model, summarized by the following hysteretic rules.

$$f_c(t)=\begin{cases} k_1\delta(t) & , \ \dot{\delta}(t)>0 \ \text{and} \ \delta(t)\leq\delta_y & (\textit{approach 1}) \\ k_1\delta_y+k_2\left[\delta(t)-\delta_y\right] & , \ \dot{\delta}(t)>0 \ \text{and} \ \delta(t)>\delta_y & (\textit{approach 2}) \\ f_m-k_1[\delta_m-\delta(t)] & , \ \dot{\delta}(t)\leq 0 \ \text{and} \ \delta_m-\delta_y<\delta(t)\leq\delta_m & (\textit{restitution 1}) \\ f_m-k_1\left(\delta_m-\delta_y\right)-k_2\left[\delta_m-\delta_y-\delta(t)\right] & , \ \dot{\delta}(t)\leq 0 \ \text{and} \ \delta(t)<\delta_m-\delta_y & (\textit{restitution 2}) \end{cases} \tag{3.16}$$

There are several new parameters in the Muthukumar model. The yield indentation (δ_y) is given as a fraction of the maximum expected indentation, i.e.

$$\delta_y = a\delta_{me} \tag{3.17}$$

where a is the yield indentation ratio, which must be a positive value less than $1-\frac{2}{5}(1-e^2)$. This parameter should be set to an arbitrarily small value (e.g. a = 0.1), such that energy dissipation is still present in impacts with small indentations [37]. The initial stiffness (k_1) and the secondary stiffness (k_2) are derived based on the assumption that, if the maximum indentation is equal to δ_{me}, the Muthukumar model will yield the same energy dissipation as that of the Hertzdamp model. The result of this assumption is

$$k_1 = \left(1+\frac{2}{5}\cdot\frac{1-e^2}{a}\right)k_h\sqrt{\delta_{me}} \tag{3.18a}$$

$$k_2 = \left(1-\frac{2}{5}\cdot\frac{1-e^2}{1-a}\right)k_h\sqrt{\delta_{me}} \tag{3.18b}$$

The quantities f_m and δ_m are not actual parameters, and simply represent the actual maximum force and indentation, respectively, that the Muthukumar model computes for a particular impact event. One drawback of the Muthukumar contact model is that, in general, $\delta_m \neq \delta_{me}$. That is, the

actual maximum indentation (δ_m) is not necessarily equal to the expected maximum indentation (δ_{me}), which must be input to the model as a parameter.

3.2.6. Summary of Uniaxial Contact Models

Table 1 summarizes the five contact models considered in this work, along with their corresponding input parameters and how they are computed from the fundamental system properties. Figure 3.2 shows the individual force-indentation curves for each model.

Table 3.1. Summary of normal contact models.

Model Name	Constitutive Law	Input Parameters
Linear Elastic	$f_c(t) = k_{eff}\delta(t)$	$k_{eff} = k_h\sqrt{\delta_{me}}$
Linear Viscoelastic	$f_c(t) = k_{eff}\delta(t) + c_{eff}\dot{\delta}(t)$	$k_{eff} = k_h\sqrt{\delta_{me}}$ $c_{eff} = 2\xi_{KV}\sqrt{m_{eff}k_{eff}}$ $\ln\left(\frac{1}{e}\right) = \frac{2\xi_{KV}}{\sqrt{1-\xi_{KV}^2}}\arctan\left(\frac{\sqrt{1-\xi_{KV}^2}}{\xi_{KV}}\right)$
Jankowski	$f_c(t) = \begin{cases} k_h\delta(t)^{\frac{3}{2}} + c_J(t)\dot{\delta}(t) & , \ \dot{\delta}(t) > 0 \\ k_h\delta(t)^{\frac{3}{2}} & , \ \dot{\delta}(t) \le 0 \end{cases}$	k_h $c_J = 2\xi_J\sqrt{m_{eff}k_h\sqrt{\delta}}$ $\xi_J = \frac{9\sqrt{5}}{2}\cdot\frac{1-e^2}{e(e(9\pi-16)+16)}$
Hertzdamp	$f_c(t) = k_h\delta(t)^{\frac{3}{2}} + c_h(t)\dot{\delta}(t)$	k_h $c_h = \xi_h\frac{k_h}{\dot{\delta}_0}\delta^{3/2}$ $\xi_h = \frac{8}{5}\cdot\frac{1-e}{e}$
Muthukumar	$f_c(t) = \begin{cases} k_1\delta(t) & , \ \dot{\delta}(t)>0 & \delta(t)\le\delta_y \\ k_1\delta_y + k_2[\delta(t)-\delta_y] & , \ \dot{\delta}(t)>0 & \delta(t)>\delta_y \\ f_m - k_1[\delta_m-\delta(t)] & , \ \dot{\delta}(t)\le 0 & \delta_m-\delta_y<\delta(t)\le\delta_m \\ f_m - k_1(\delta_m-\delta_y) - k_2[\delta_m-\delta_y-\delta(t)] & , \ \dot{\delta}(t)\le 0 & \delta(t)<\delta_m-\delta_y \end{cases}$	$k_1 = \left(1+\frac{2}{5}\cdot\frac{1-e^2}{a}\right)k_{eff}$ $k_2 = \left(1-\frac{2}{5}\cdot\frac{1-e^2}{1-a}\right)k_{eff}$ $\delta_y = a\delta_{me}$ $0 < a < \frac{2}{5}(1-e^2)$

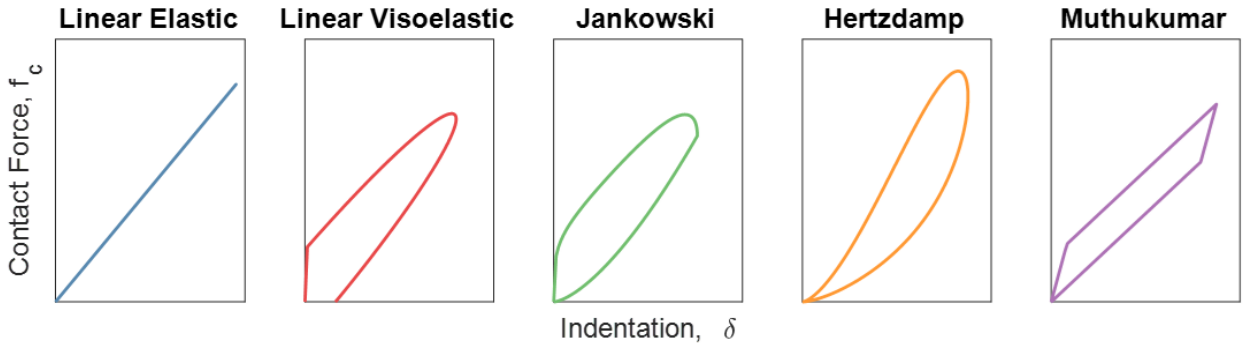

Figure 3.2. Contact force-indentation ($f_c - \delta$) curves for five different uniaxial contact models.

3.3. Contact Model Comparison

The five aforementioned contact models are compared using nonlinear time history analysis of a complete base isolated building and moat wall. The structural model has been calibrated to the experimentation described in [7], both in terms of the local impact response (i.e. impact forces, moat wall displacements), and global response of the superstructure (i.e. floor accelerations, interstory drifts). This model employs the Masroor impact element [8], which was shown to adequately capture the dynamic characteristics of the moat wall specimens [10]. The Masroor impact element, shown in Figure 3.1, is characterized by a local contact spring, modeled using Muthukumar's approach [37], and a single degree-of-freedom (SDOF) system to represent the global vibrational behavior of the moat wall.

In Figure 3.3, the right side of the impact element is fixed and the left side is free. The contact spring, which assumes one of the five contact laws shown in Table 1 and Figure 3.2, represents the local material indentation that precedes observable vibration. The SDOF system represents the joint vibration behavior of the connected system formed by the moat wall and superstructure base.

The simulations are conducted using OpenSees version 3.1.0 [29,30], which has the linear elastic and Muthukumar elements available for use as contact elements through the uniaxial material commands *ElasticPPGap* and *ImpactMaterial*, respectively. For this study, three new uniaxial materials were added to the OpenSees library: *ViscoelasticGap*, *JankowskiImpact*, and *Hertzdamp*.

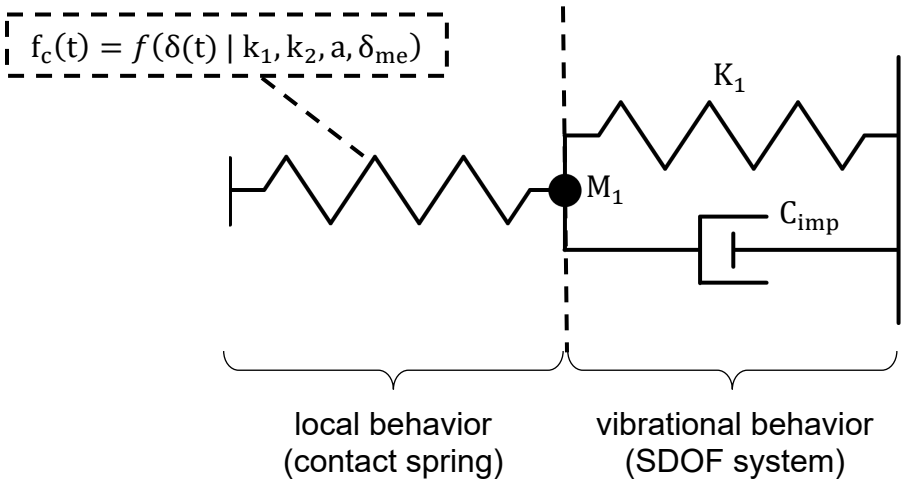

Figure 3.3. Masroor impact element.

All five contact models considered here share a common set of parameters (k_{eff}, m_{eff}, δ_{me}, and e). Furthermore, the vibrational part of the Masroor impact element has three parameters of its own: the 1st modal stiffness (K_1), 1st modal mass (M_1), and the impact damping ratio (C_{imp}). Modal quantities of the moat wall (K_1 and M_1) are calculated from the closed-form solution to problem of free vibration of a continuous beam with lateral soil springs. The impact damping ratio (C_{imp}) is determined experimentally.

All values for the contact and vibrational components of the Masroor impact element are summarized in Table 2. This study considers two types of moat walls (15-cm-thick concrete box

with soil backfill, and a wedge-shaped steel wall), so there are two parameter sets listed. For both concrete and steel moat walls, the maximum expected indentation (δ_{me}) is set to 0.025 in = 0.064 cm, and the yield indentation ratio (a) is set to 0.1, per the recommendations in [37]. The coefficient of restitution (e) is 0.7 for both walls, a nominal value for civil engineering materials subject to low-velocity impacts [39]. For both concrete and steel moat walls, the second colliding body is a concrete block [7,10] with Poisson's ratio $\nu_2 = 0.20$, Young's modulus $E_2 = 28{,}000$ MPa, and volume $V_2 = 68{,}800$ cm^3. The mass of the second colliding body (m_{eff}) is taken as the total mass of the superstructure's bottom floor: 840 kg.

Table 3.2. Common parameters used in the Masroor impact element.

Type	Parameter	Symbol	Moat Wall Type		Units
			Concrete	Steel	
Fundamental Properties	Poisson's ratio	ν_1	0.20	0.30	-
	Young's modulus	E_1	28,000	200,000	MPa
	Volume	V_1	170,000	70,000	cm^3
	Mass	m_1	130	180	kg
Contact Spring	Hertz stiffness	k_h	7,400	12,000	kN/cm$^{3/2}$
	Effective mass	m_{eff}	130	180	kg
	Maximum expected indentation	δ_{me}	0.064	0.064	cm
	Coefficient of restitution	e	0.70	0.70	-
	Yield indentation ratio	a	0.10	0.10	-
Vibration Spring	1st modal stiffness	K_1	4.2	180	kN/cm
	1st modal weight	$M_1 \cdot g$	130	180	kg
	Impact damping ratio	ξ_{imp}	200	40	%
	Impact damping coefficient	C_{imp}	580,000	890,000	kg/sec

The OpenSees model of the superstructure and isolation system are explained in detail in [10], and summarized here for completeness. Inelastic deformation is considered using concentrated plastic hinges that follow the modified Ibarra-Krawinkler deterioration model [40,41] (*Bilin* material command). Furthermore, the flexibility of the moment connections is modeled

using panel zones, according to Gupta [42]. The friction pendulum isolation system is modeled using the *SingleFPBearing* element command. The fundamental period of the scaled, base-isolated structure is approximately 1.8 sec based on pendulum motion with a sliding radius of 81 cm. A diagram of the calibrated OpenSees model is shown in Figure 3.4.

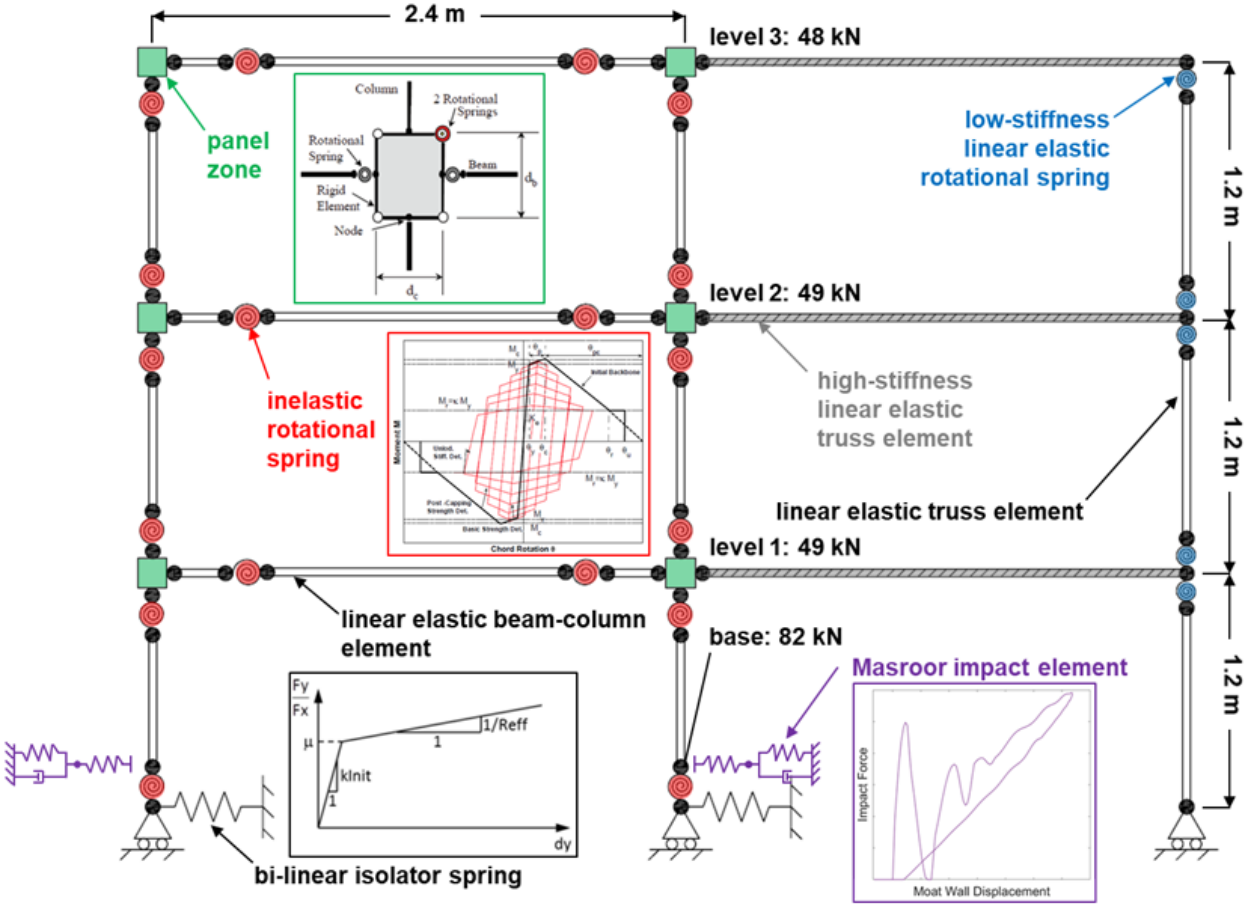

Figure 3.4. Schematic of the calibrated OpenSees model [after 8,10,40–42].

3.3.1. Detailed Analysis for a Single Ground Motion

The ground motion used during the shake table experiments was the N-S component of the 1992 Erzincan, Turkey earthquake, scaled to a peak ground acceleration (PGA) of 0.91 g. This same ground motion is used here to examine the impact models in detail. The experimental

specimen was constructed at quarter-scale, with the actual input ground motion used in the experimental program having a 20-second duration as shown in Figure 3.5. The input ground motions used for the analysis that follow correspond to the measured acceleration from the experiments being simulated.

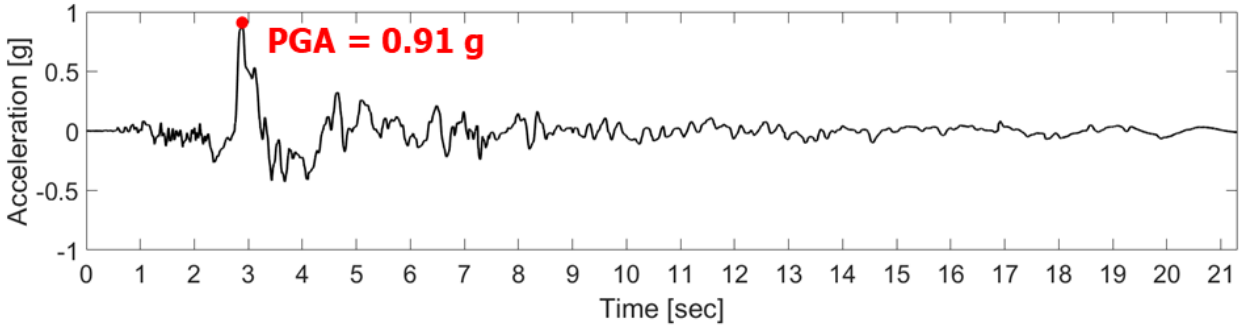

Figure 3.5. Impact-inducing ground motion (Erzincan 1992, N-S).

This acceleration record was input to the calibrated OpenSees model as a base excitation loading pattern, considering two different moat wall types (concrete, steel) and five different contact models for the impact element. The gap distance is set to 10.2 cm to coincide with the experimental setup. These results of the nonlinear dynamic time history analyses are summarized in Figures 3.6 – 3.11.

Figure 3.6 shows the impact force time histories for the concrete and steel moat walls with the time scale based on the data acquisition time. For both wall types, there are noticeable differences between models in the early part of the contact duration (before 5.75 sec in the concrete wall and before 4.69 sec in the steel wall). During this period, the contact spring dominates the impact force levels and the vibrational spring is not yet active. In particular, the linear elastic model shows higher-amplitude oscillations relative to the other contact models. This is because the linear

elastic model is the only contact model that has no type of associated damping (neither viscous nor hysteretic). Still, all models have very similar predictions for the peak impact force. After a certain time, the contact spring is fully compressed, and the vibrational spring dominates the response – this is noted with the black dot in Figure 3.6.

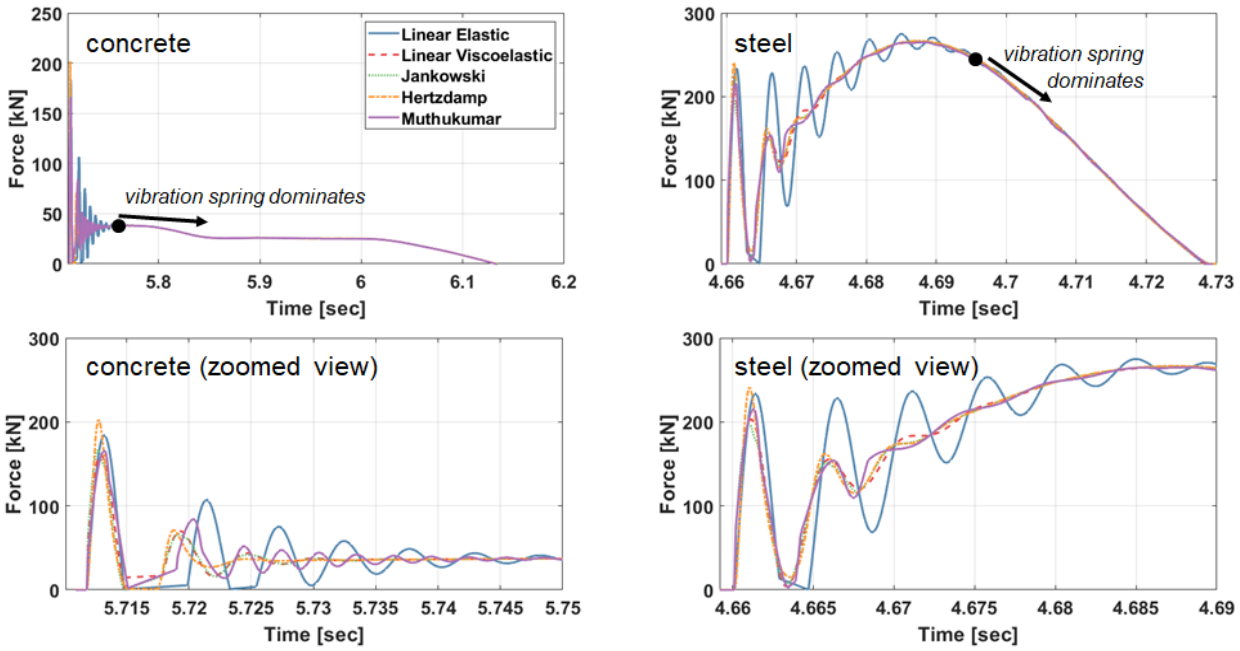

Figure 3.6. Impact force time histories.

Figure 3.7 highlights the most obvious difference between the contact models – the local hysteresis of the contact spring. This figure shows the same basic shapes shown in Figure 3.2, but now the high-frequency impact is causing hysteretic oscillations within the contact spring. As before, all models show a similar prediction of the peak impact force, even if the hysteresis loops are significantly different.

Contrary to the local hysteresis curves, the global force-displacement curves in Figure 3.8 show less significant differences between the contact models. This is because, at the global

displacement level, the impact force is governed by the vibration spring, which is much more flexible than the contact spring. To help understand this, consider a static form of the Masroor impact element as two linear springs in series, as shown in Figure 3.9.

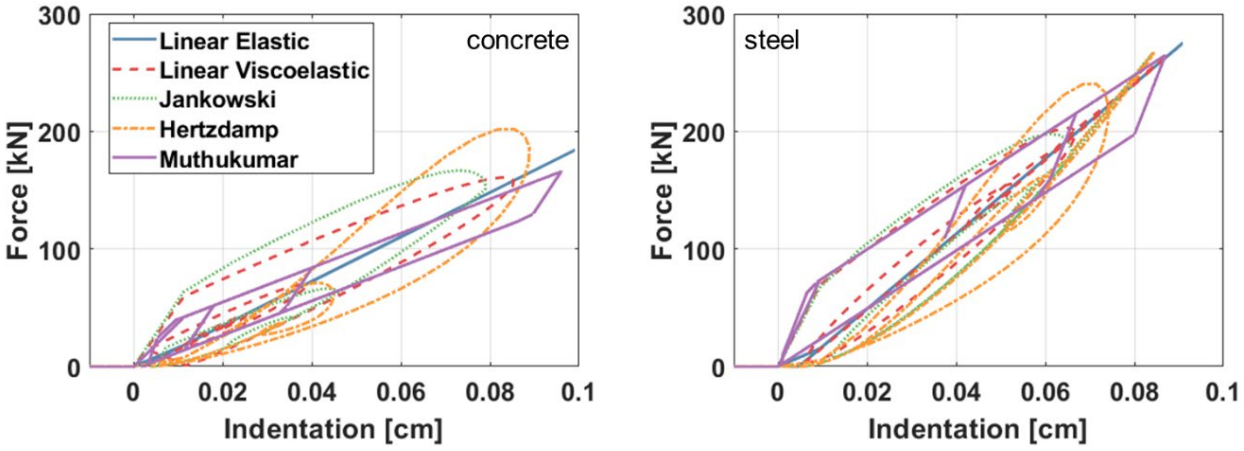

Figure 3.7. Hysteresis of local contact springs.

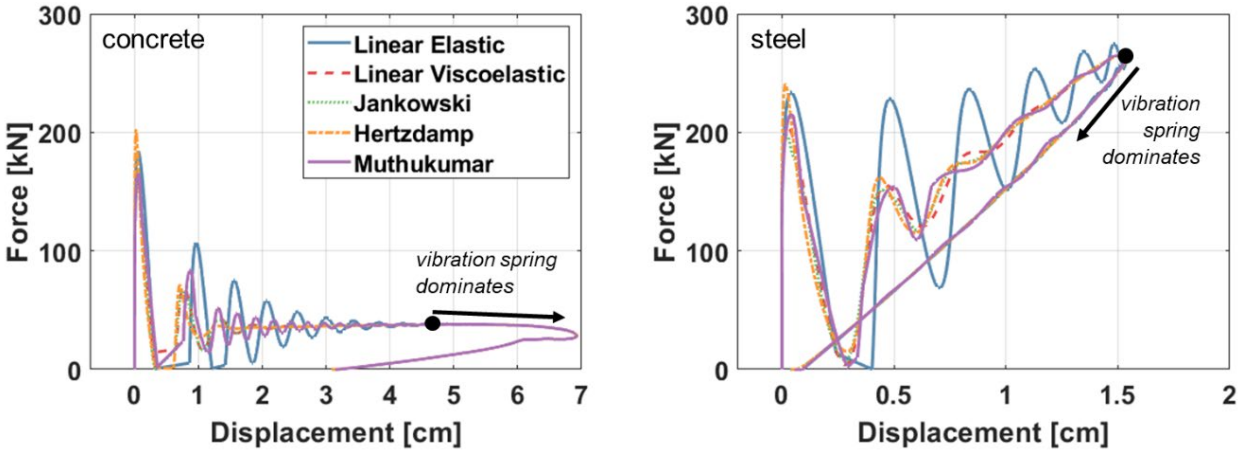

Figure 3.8. Hysteresis of vibrational spring.

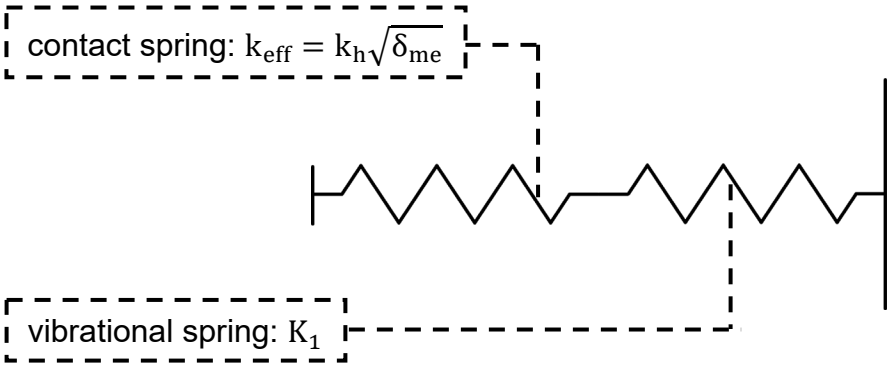

Figure 3.9. The Masroor impact element interpreted as two linear springs in series.

The stiffness of the static system in Figure 3.9 (K_{sys}) is equal to

$$K_{sys} = \frac{k_{eff}K_1}{k_{eff} + K_1} \tag{3.19}$$

For the concrete and steel moat walls, k_{eff} = 1,900 kN/cm and 3,100 kN/cm, respectively. Thus, for both moat wall types, it is true that $k_{eff} \gg K_1$, so Equation (3.19) can be rewritten as

$$K_{sys} = \frac{k_{eff}K_1}{k_{eff} + K_1} \approx \frac{k_{eff}K_1}{k_{eff}} = K_1 \tag{3.20}$$

As such, the overall response of the moat wall system represented by the Masroor impact element should be largely controlled by the vibrational spring. This is consistent with the observations shown in Figure 3.8, where the global force-displacement curve of the moat wall is largely unaffected by the choice of contact spring. Similar to the impact force time history, the differences between models is most significant in the early phase of impact, where the contact spring is not yet fully engaged. Following this, the contact spring is fully compressed, and the vibrational spring dominates, denoted with a black dot as before.

The discussion so far has been limited to the response of the moat wall at the contact interface, where the choice of contact model is most likely to have an effect. In the following figures, the discussion moves to the response of the base-isolated superstructure, namely, floor

accelerations and interstory drifts. Floor accelerations are an important metric for the general seismic behavior of the structure, and may be of critical importance for the design of nonstructural components. Interstory drift is also considered here because it is a common indicator of structural damage and likelihood of collapse. Figures 3.10 and 3.11 examine how the choice of contact model affects these global response metrics.

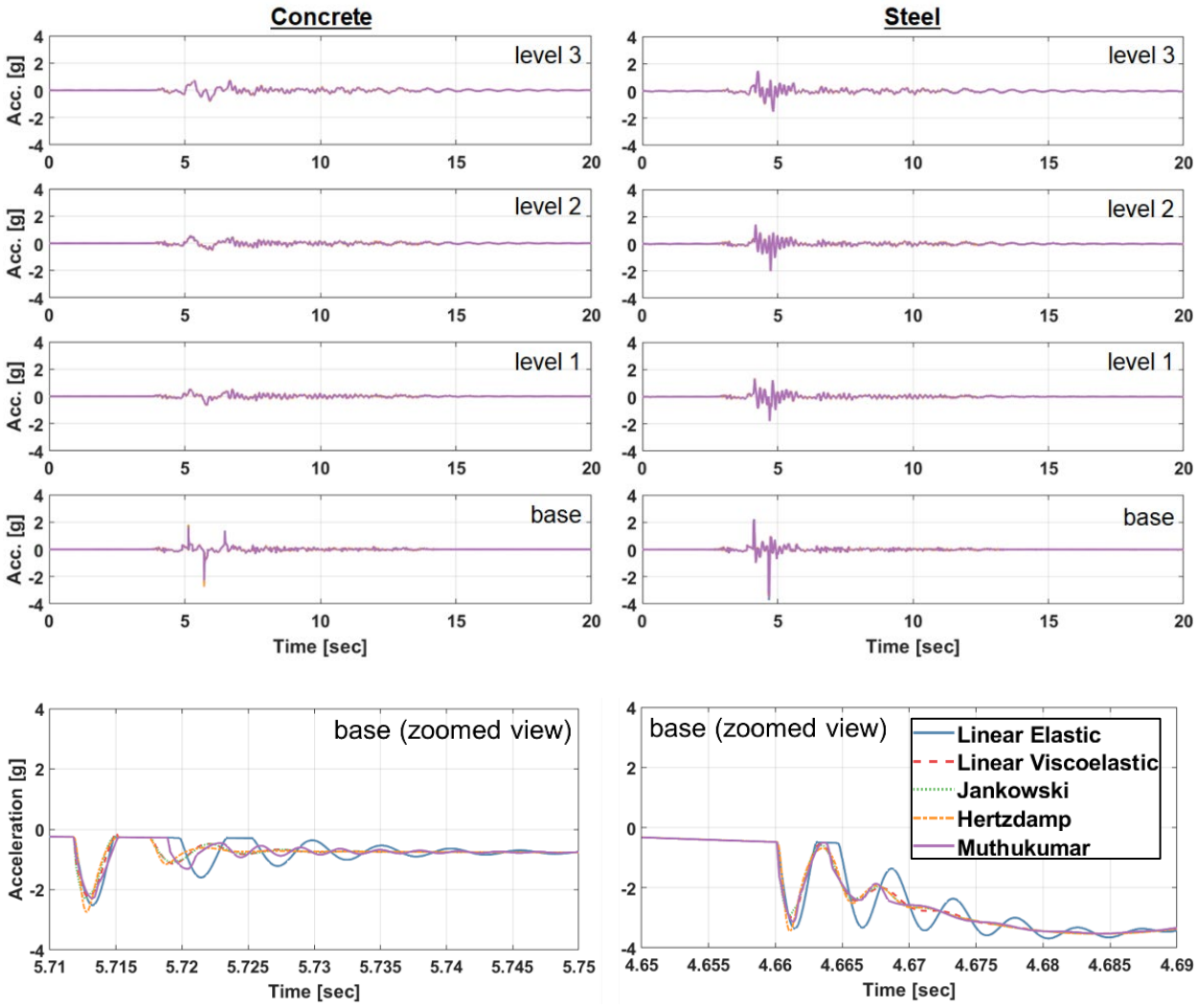

Figure 3.10. Floor acceleration time histories.

Figure 3.10 shows that accelerations in the upper floors (i.e. above the isolation plane) are not affected by the choice of contact model. The base accelerations shown in the zoomed view have a similar trend as the impact force time histories: the contact models induce different fluctuations in the acceleration, but the overall envelope is the same, and the peak acceleration values are approximately the same for all contact models.

The impact force time history shown in Figure 3.6 can be viewed as a short-duration pulse applied to the base of the superstructure. This pulse has localized differences depending on the contact model chosen, but the overall force envelope is the same. Specifically, the impulse (area under the force-time curve) is very similar for all model choices. As demonstrated by Chopra [43], the impulse of a short-duration pulse load is the governing factor for structural response, independent of the actual shape of the force-time curve. Consequently, the interstory drifts shown in Figure 3.11 are completely insensitive to the choice of contact model.

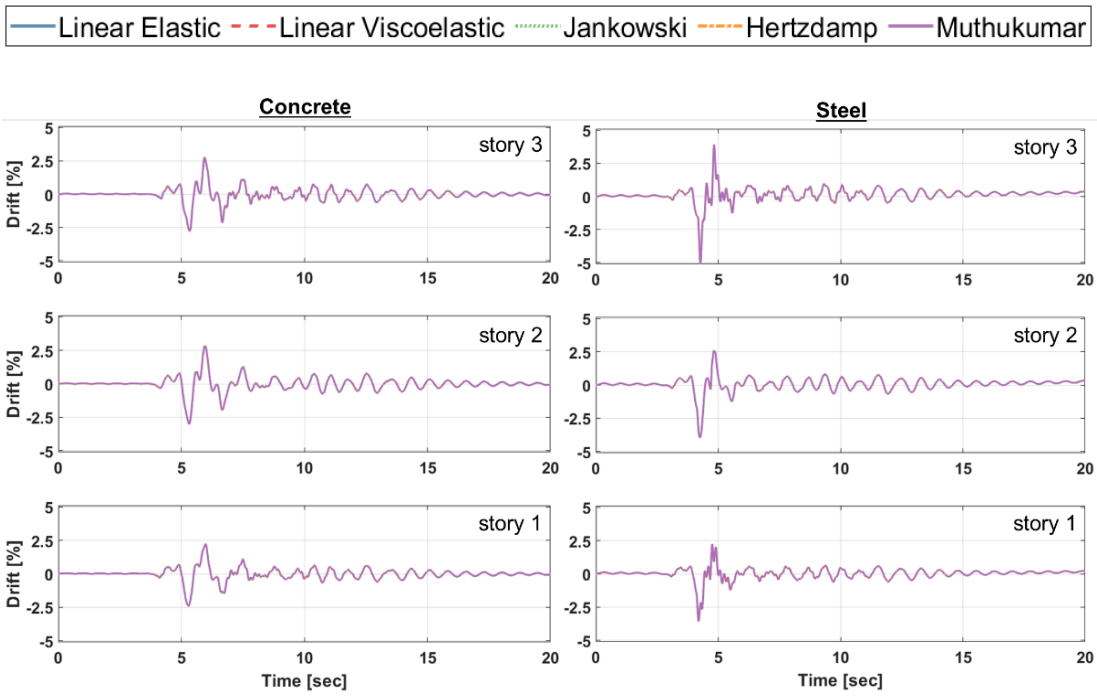

Figure 3.11. Interstory drift time histories.

3.3.2. Parametric Study Using 28 Ground Motions

This subsection extends the previous parametric study to include 28 ground motions. Specifically, the ATC-63/FEMA P695 [44] near-field ground motions (pulse subset) are used because these are the most likely to induce impact. The previous earthquake considered (1992 Erzincan N-S) is among the records in this set. For consistency with the previous simulations based on the experimental program, the ground motion time scales are unchanged. Time scaling of the motions resulted in very limited cases of impact. The acceleration and displacement response spectra for the motions used in this numerical study are shown in Figure 3.12.

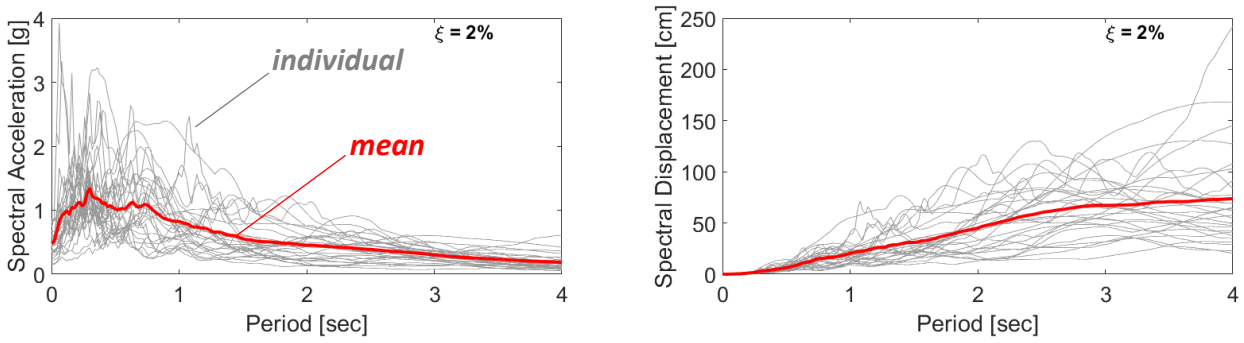

Figure 3.12. Acceleration and displacement response spectra for ATC-63 near-field ground motion set (pulse subset).

In addition to expanding the ground motion set, the parametric study also considers different gap distances (8, 10, 13, 15, and 18 cm). Consequently, a total of 1,400 nonlinear dynamic time history analyses are performed. This allows a more rigorous statistical study on how the choice of contact model affects the structural response. This study examines the building response in terms of the peak values of impact force, wall displacement, base acceleration, upper story acceleration, and interstory drift.

Some of the ground motions are very intense, so to ensure the fidelity of the calibrated OpenSees model, the peak values are obtained before drifts exceeds 5% in any story. This is a practical drift limit for intermediate moment frames [45], and values over this threshold are likely outside the valid range of applicability for the calibrated OpenSees model. Average peak responses over the entire ground motion set are also limited to more significant cases of impact, where the impact velocity is greater than 10 cm/sec and the peak impact force is greater than 5 kN. This prevents weaker, low-velocity collisions from skewing the mean responses towards low-damage impact events. The impact velocity is computed as the relative velocity between the base mat and the moat wall just before the moment of impact.

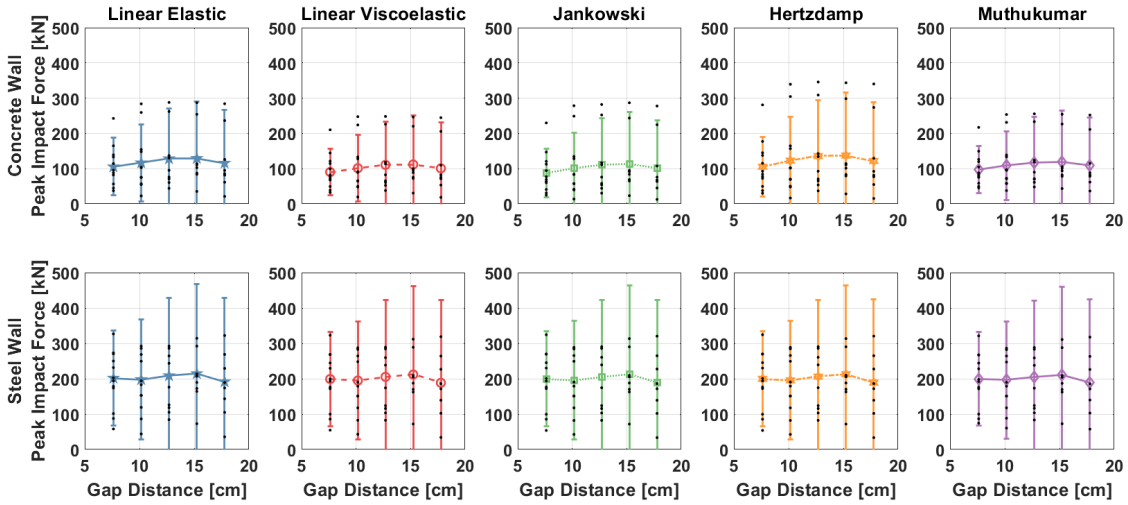

Figure 3.13. Peak impact forces for ATC-63 near field motion set (pulse subset).

In Figures 3.13 – 3.17, each black dot represents the peak response value of a particular contact model, gap distance, and ground motion. The colored shapes mark the mean of the peak responses across the entire ground motion suite, and the error bars denote one standard deviation. Figures 3.13 – 3.17 show a large variation in the peak responses across the set of 28 ground

motions. In particular, the coefficient of variation (standard deviation divided by mean) is visibly larger than one for every response metric. Despite the record-to-record discrepancies, the differences between contact models is minimal, as shown by the mean response summary in Figures 3.18 and 3.19.

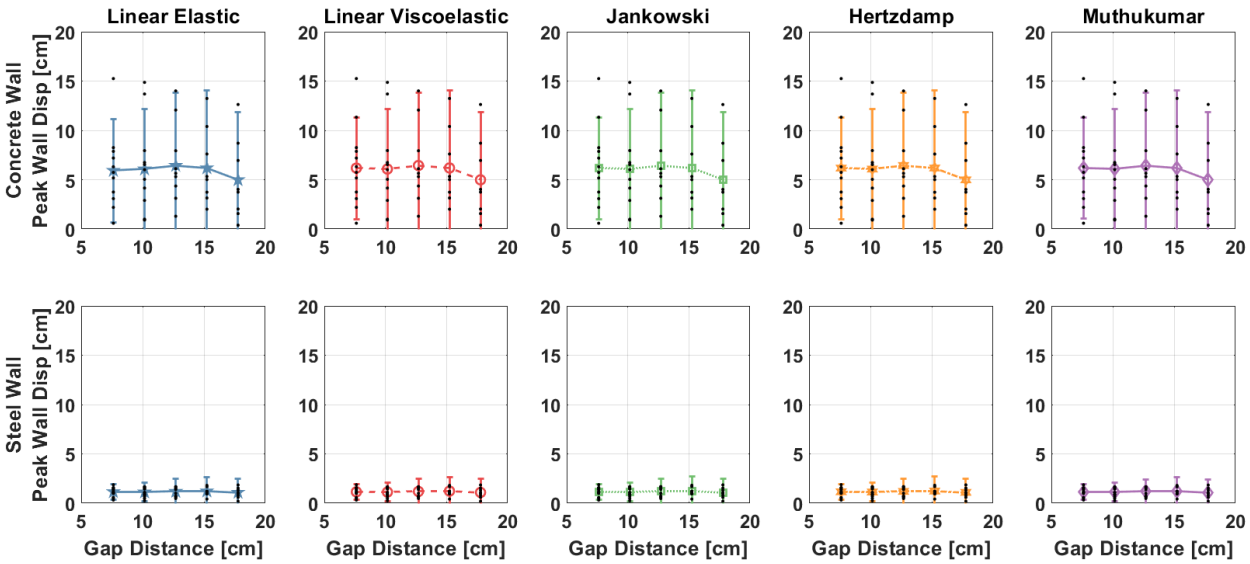

Figure 3.14. Peak wall displacements for ATC-63 near field motion set (pulse subset).

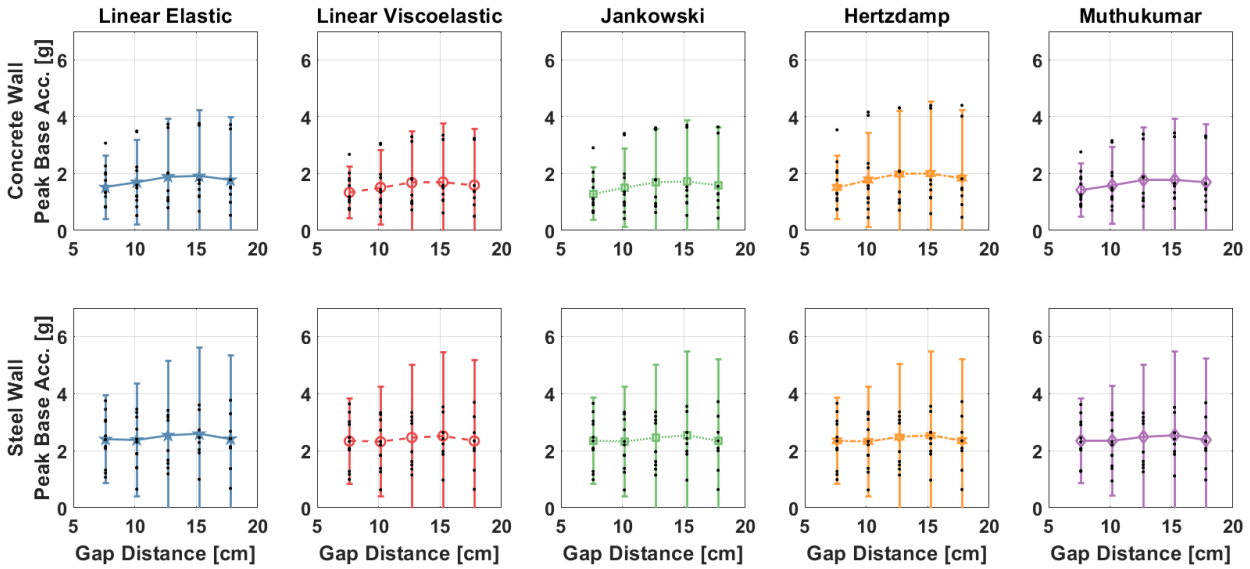

Figure 3.15. Peak base accelerations for ATC-63 near field motion set (pulse subset).

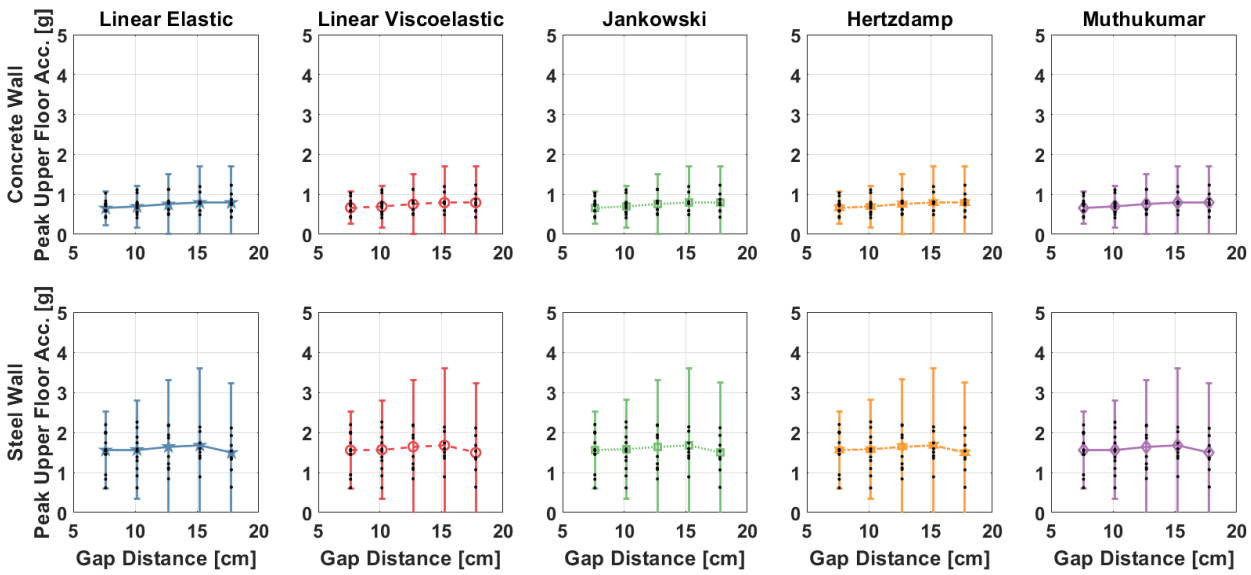

Figure 3.16. Peak upper floor accelerations for ATC-63 near field motion set (pulse subset).

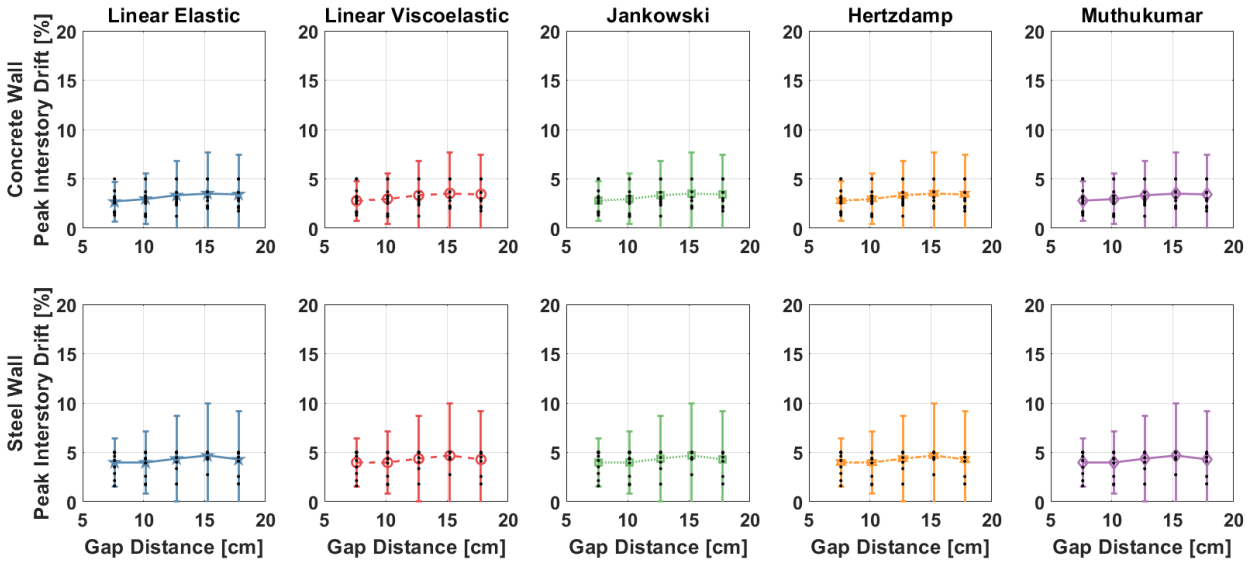

Figure 3.17. Peak interstory drifts for ATC-63 near field motion set (pulse subset).

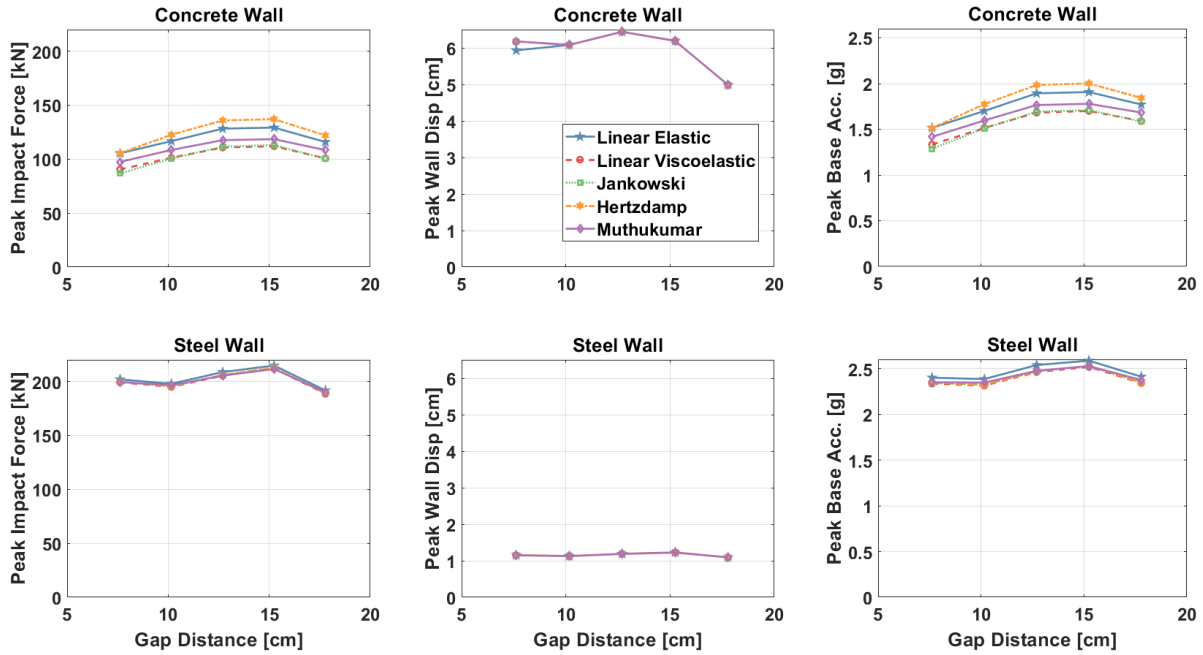

Figure 3.18. Summary of local response averages for ATC-63 near field motion set (pulse subset).

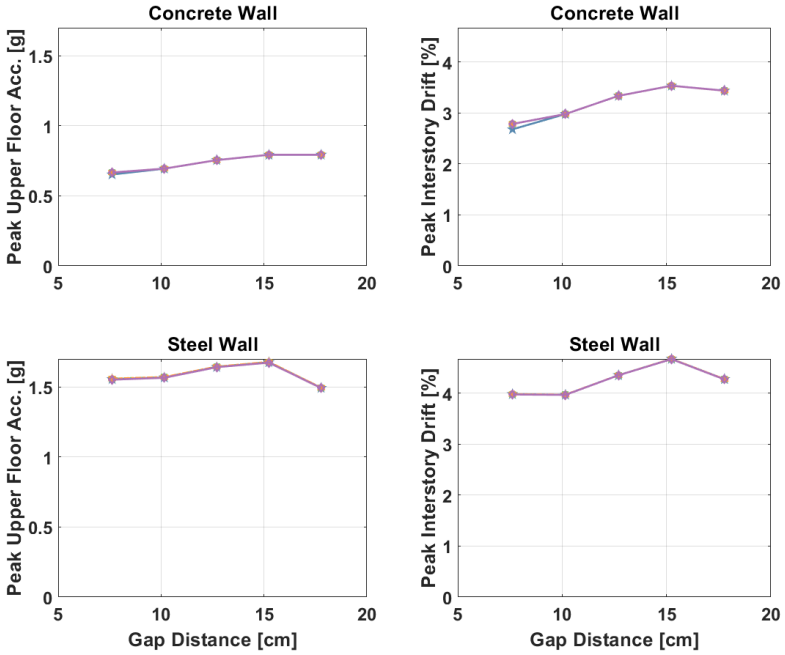

Figure 3.19. Summary of global response averages for ATC-63 near field motion set (pulse subset).

Figure 3.18 shows that, while the record-to-record variation in the peak responses is significant, the choice in contact model has little effect on this disparity. There is a difference of approximately +/- 11% in the peak impact force and peak base accelerations for the concrete moat wall, but every other response metric is not sensitive to the choice of contact model. The steel moat wall, on the other hand, shows almost no variation between contact models. This is likely due to the higher K_1 value (175 kN/cm, compared to 4.2 kN/cm for the concrete wall), which increases the degree to which the Masroor impact element is controlled by the vibrational behavior component (see Figure 3.9 and corresponding discussions). Moreover, the choice of contact model apparently only matters if the analyst is concerned with the details of the contact interface. Otherwise, any of the five contact models shown here will provide similar results.

Figures 3.20 and 3.21 show the impact force vs. impact velocity relationship for concrete and steel moat walls, respectively. The relationship between peak impact force and corresponding impact velocity is important for the future development of a velocity-based impact design [46]. In these figures, the contact models are abbreviated as: E = linear elastic, V = linear viscoelastic, J = Jankowski, H = Hertzdamp, and M = Muthukumar. Furthermore, the number placed after the abbreviation signals a particular gap distance. For example, “H13” corresponds to the Hertzdamp contact model with a 13 cm gap distance.

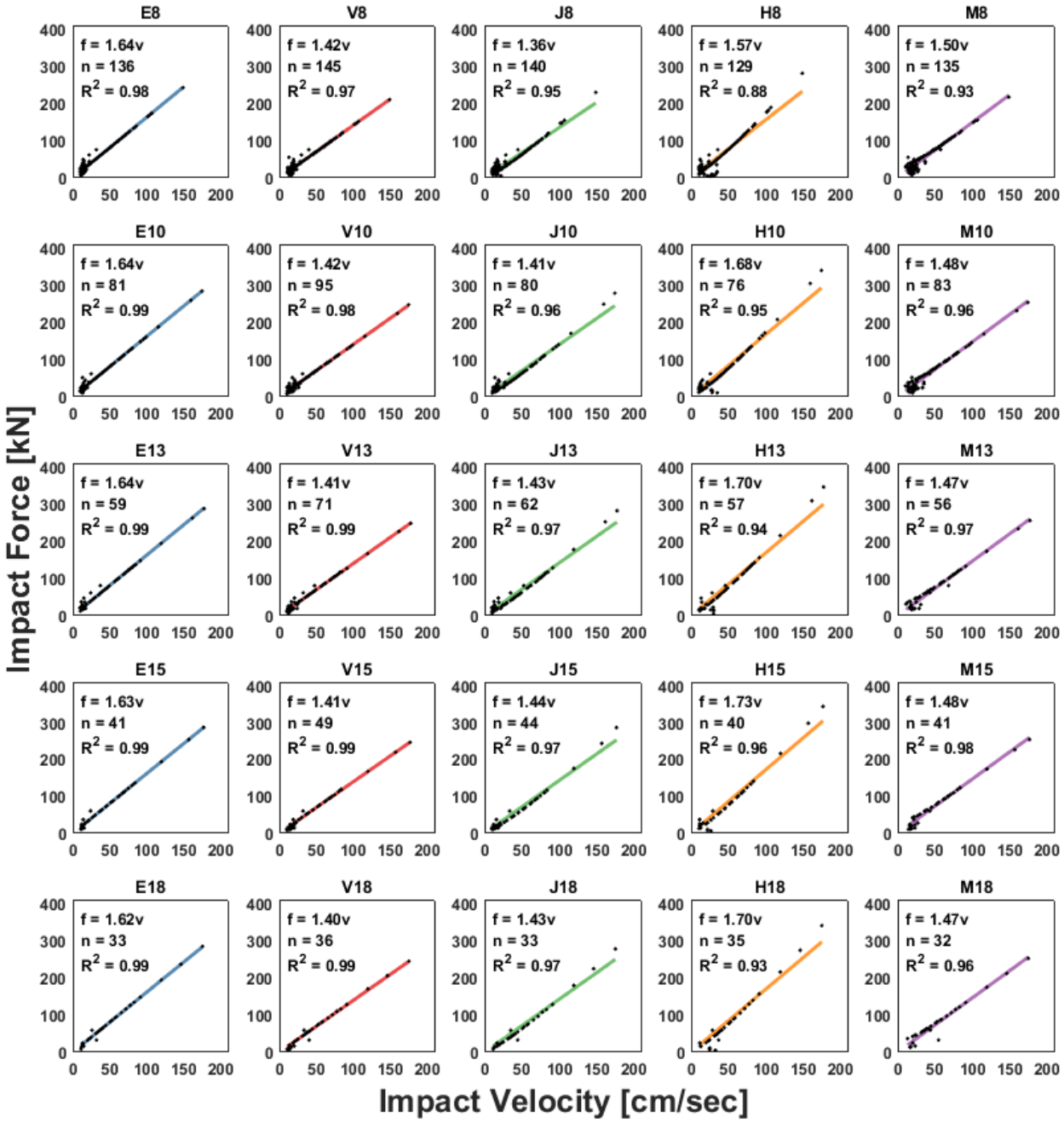

Figure 3.20. Impact force vs. impact velocity for ATC-63 near field motion set (pulse subset), concrete moat walls.

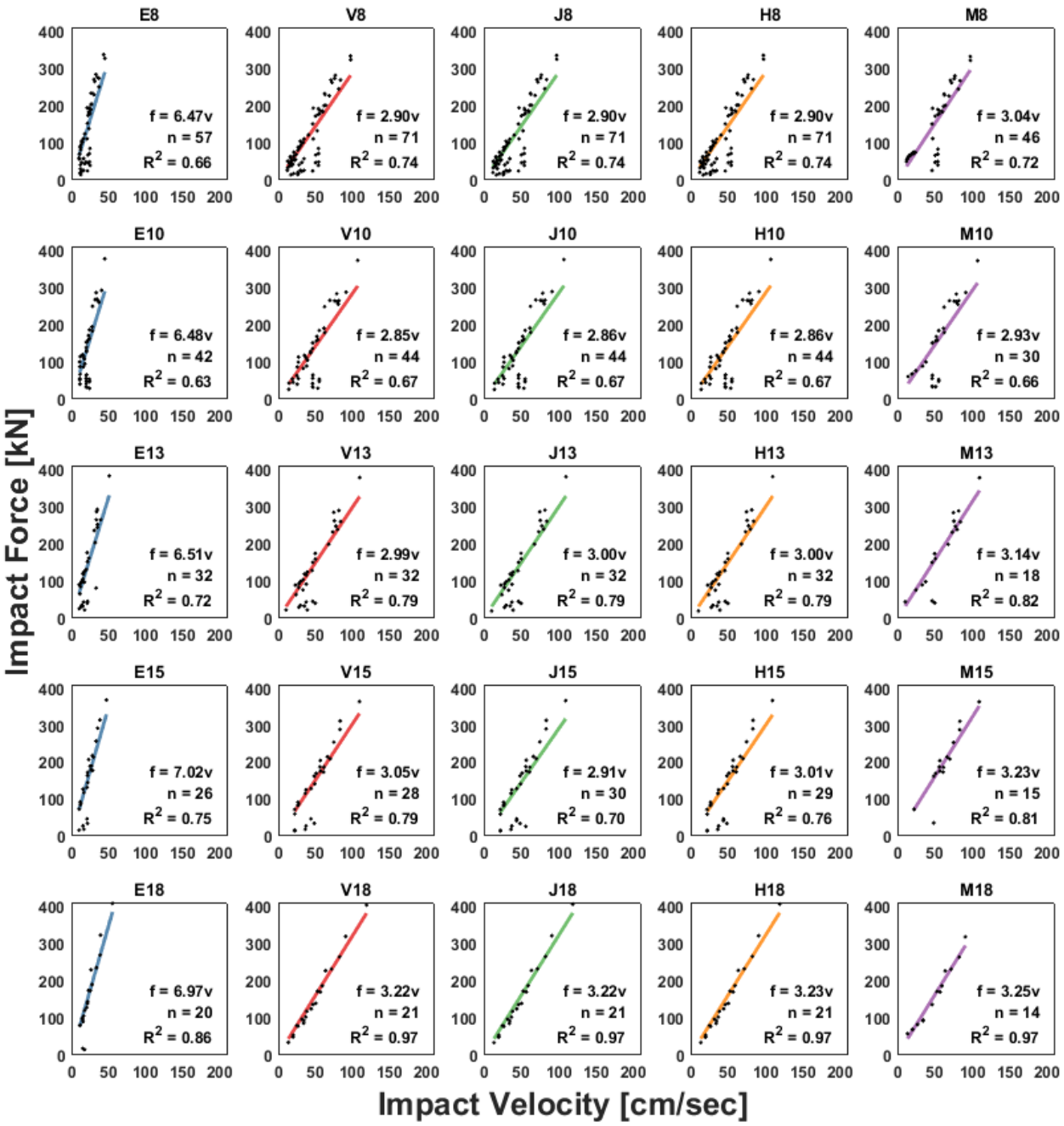

Figure 3.21. Impact force vs. impact velocity for ATC-63 near field motion set (pulse subset), steel moat walls.

The equation $f = \lambda v$ is the best-fit linear relationship between the impact force (f) and the impact velocity (v), where λ is the slope of the line, with units of kN-sec/in. The fitted line minimizes the sum of the square errors between itself (colored line) and the numerical data (black dots). Also, n refers to the number of impacts, and R^2 is the coefficient of determination for the best fit line. Cases with n > 28 imply that, for that combination of contact model and gap distance, there were multiple impacts for one or more of the ground motions.

Figure 3.20 illustrates a very strong linear relationship between impact force and impact velocity, across all gap distances and contact models. Indeed, the coefficient of determination is very high for the concrete moat walls ($0.88 \leq R^2 \leq 0.99$). This range is much wider for the steel walls shown in Figure 3.21, with $0.63 \leq R^2 \leq 0.97$. In particular, the steel moat wall with the linear elastic contact model has the lowest R^2values, indicating a relatively higher amount of variance than cannot be explained with a straight line. Furthermore, the slope of the best-fit line (λ) is also the highest for these cases ($2.85 \leq \lambda \leq 7.02$). The linear elastic model has no damping associated with it (neither viscous nor hysteretic), which can explain the higher forces occurring at lower impact velocities (larger λ values), as well as the overall uncertainty (smaller R^2values).

As expected, larger gap distances are associated with a lower number of impacts (n). Interestingly, the choice of contact model also has some effect on the number of impacts: for an 8 cm gap distance, $32 \leq n \leq 145$ for the concrete moat walls, and $14 \leq n \leq 71$ for the steel walls. This suggests that, for small gap distances, the choice in contact model may induce different numbers of rebound impacts, where the exit velocity of the base mat after one impact is high enough to induce another impact at the opposite wall.

3.4. Conclusions

This research provides an in-depth review of several state-of-the-art uniaxial contact models, namely: linear elastic, linear viscoelastic (or Kelvin-Voigt), Jankowski, Hertzdamp, and Muthukumar. Each model has its own set of advantages and disadvantages, depending on the needs of the analyst. This study compares how each model influences the response of a base-isolated building subjected to seismically-induced moat wall pounding. Unlike previous studies before it, this work uses a nonlinear finite element model that has been calibrated to experimental moat wall pounding tests. Each model was implemented into OpenSees, as the initial contact portion of the Masroor impact element.

The first analysis done in this work examined the detailed response of the moat wall and superstructure under one specific ground motion. This revealed that the choice in contact model can cause small variations at the local level of contact forces, wall displacements, and base floor accelerations. In particular, the linear elastic contact model exhibited high-frequency oscillations in the pounding force not seen in the other models. Still, the envelope of contact forces, wall displacements, and base accelerations followed the same general trajectory. Acceleration in the upper floors, as well as interstory drifts, were shown to be almost completely insensitive to the choice of contact model.

The second analysis shown here consisted of a larger parametric study across 28 near-fault ground motion records, and five different gap distances between the base mat and moat wall. In this study, the peak response values were recorded for each ground motion, gap distance, wall type, and contact model, for a total of 1,400 analysis cases. Results indicate that, for the concrete moat wall cases, peak values of impact force and base acceleration are somewhat sensitive to the choice in contact model. The stiffer steel moat wall exhibited a response more dominated by the

vibrational spring, with little to no variation in the peak response envelope. In both the steel and concrete moat wall cases, the peak wall displacements, upper floor accelerations, and interstory drifts were not affected by the contact model.

Finally, the peak impact force was shown to have a very strong linear relationship with the impact velocity, particularly for the concrete moat wall cases. This is promising for the potential development of a velocity-based pounding design, where a spectral prediction of impact velocity can be related to the design pounding force.

Overall, this study shows that, in most cases, the analyst's choice in contact model has little to no effect on the peak response quantities for pounding in base-isolated buildings. By that reasoning, the simplest model – a linear elastic spring – may be enough to estimate moat wall pounding forces. Still, the linear elastic model did show oscillatory behavior not seen in the other models. This can potentially cause numerical instabilities, in which case the linear viscoelastic model should suffice. If it is available, the authors would recommend using the Jankowski or Hertzdamp contact models, as these require relatively straightforward material inputs, and do not require a priori estimation of maximum wall indentation.

Chapter 3 is, in part, a reprint of the material as in appears in "Evaluation of Uniaxial Contact Models for Moat Wall Pounding Simulation," Hughes, P. J., Mosqueda, G. *Earthquake Engineering and Structural Dynamics* (2020). The dissertation author was the primary investigator and author of this paper.

References

1. Christopoulos C, Filiatrault A. Principles of Passive Supplemental Damping and Seismic Isolation. *IUSS Press* 2006.

2. Hall JF, Ryan KL. Isolated Buildings and the 1997 UBC Near-Source Factors. *Earthquake Spectra* 2000. DOI: 10.1193/1.1586118.

3. Providakis CP. Effect of supplemental damping on LRB and FPS seismic isolators under near-fault ground motions. *Soil Dynamics and Earthquake Engineering* 2009. DOI: 10.1016/j.soildyn.2008.01.012.

4. Wolff ED, Ipek C, Constantinou MC, Tapan M. Effect of viscous damping devices on the response of seismically isolated structures. *Earthquake Engineering and Structural Dynamics* 2015. DOI: 10.1002/eqe.2464.

5. Nagarajaiah S, Sun X, Angeles TL, Fire C, Building B isolated FCC. Base-Isolated FCC Building: Impact Response in Northridge Earthquake. *Journal of Structural Engineering* 2001; **127**(September): 1063–1075. DOI: 10.1061/(ASCE)0733-9445(2001)127:9(1063).

6. Gavin HP, Nigbor RL. Performance of the base-isolated Christchurch women's hospital in the Sep. 4 2010 Darfield earthquake and the Feb. 22 2011 Christchurch earthquake. *20th Analysis and Computation Specialty Conference - Proceedings of the Conference* 2012(4): 554–563. DOI: 10.1061/9780784412374.049.

7. Masroor A, Mosqueda G. Experimental simulation of base-isolated buildings pounding against moat wall and effects on superstructure response. *Earthquake Engineering and Structural Dynamics* 2012. DOI: 10.1002/eqe.2177.

8. Masroor A, Mosqueda G. Impact model for simulation of base isolated buildings impacting flexible moat walls. *Earthquake Engineering and Structural Dynamics* 2013. DOI: 10.1002/eqe.2210.

9. Masroor A, Mosqueda G. Assessing the Collapse Probability of Base-Isolated Buildings Considering Pounding to Moat Walls Using the FEMA P695 Methodology. *Earthquake Spectra* 2015; **31**(4): 2069–2086. DOI: 10.1193/092113EQS256M.

10. Masroor A, Mosqueda G. Seismic Response of Base Isolated Buildings Considering Pounding to Moat Walls. *Technical Report MCEER-13-0003* 2013.

11. Sasaki T, Sato E, Fukuyama K, Kajiwara K. Enhancement of Base-Isolation Based on E-Defense Full- Scale Shake Table Experiments : Dynamic Response of Base- Isolated Building Under Impact Due To Pounding, 2017.

12. Kitayama S, Constantinou MC. Collapse performance of seismically isolated buildings designed by the procedures of ASCE/SEI 7. *Engineering Structures* 2018; **164**(March): 243–258. DOI: 10.1016/j.engstruct.2018.03.008.

13. Kazantzi AK, Vamvatsikos D. Prescriptive approaches in performance-based design? A case-study on base isolation. *13th International Conference on Applications of Statistics and Probability in Civil Engineering, ICASP 2019* 2019: 1–8.

14. Shao B, Mahin SA. A probabilistic design method to achieve targeted levels of reliability for seismically isolated structures. *Earthquake Spectra* 2020: 1–26. DOI: 10.1177/8755293019891728.

15. Tsai H chuan C. Dynamic Analysis of Base-Isolated Shear Beams Bumping Against Stops. *Earthquake Engineering and Structural Dynamics* 1997; **26**: 515–528. DOI: 10.1002/(SICI)1096-9845(199705)26:5<515::AID-EQE654>3.0.CO;2-C.

16. Malhotra PK. Dynamics of seismic impacts in base-isolated buildings. *Earthquake Engineering & Structural Dynamics* 1997; **26**(8): 797–813. DOI: 10.1002/(SICI)1096-9845(199708)26:8<797::AID-EQE677>3.3.CO;2-Y.

17. Komodromos P, Polycarpou PC, Papaloizou L, Phocas MC. Response of seismically isolated buildings considering poundings. *Earthquake Engineering and Structural Dynamics* 2007. DOI: 10.1002/eqe.692.

18. Sarebanha A, Mosqueda G, Kim MK, Kim JH. Seismic response of base isolated nuclear power plants considering impact to moat walls. *Nuclear Engineering and Design* 2018; **328**(December 2017): 58–72. DOI: 10.1016/j.nucengdes.2017.12.021.

19. Goyal S, Pinson EN, Sinden FW. Simulation of dynamics of interacting rigid bodies including friction I: General problem and contact model. *Engineering with Computers* 1994. DOI: 10.1007/BF01198742.

20. Goyal S, Pinson EN, Sinden FW. Simulation of dynamics of interacting rigid bodies including friction II: Software system design and implementation. *Engineering with Computers* 1994. DOI: 10.1007/BF01198743.

21. Brogliato B. Nonsmooth mechanics: Models, dynamics and control, Third edition. *Communications and Control Engineering*, 2016. DOI: 10.1007/978-3-319-28664-8.

22. Jankowski R. Non-linear viscoelastic modelling of earthquake-induced structural pounding. *Earthquake Engineering and Structural Dynamics* 2005; **34**(6): 595–611. DOI: 10.1002/eqe.434.

23. Jankowski R. Analytical expression between the impact damping ratio and the coefficient of restitution in the non-linear viscoelastic model of structural pounding. *Earthquake Engineering and Structural Dynamics* 2006; **35**(4): 517–524. DOI: 10.1002/eqe.537.

24. Jankowski R. Theoretical and experimental assessment of parameters for the non-linear viscoelastic model of structural pounding. *Journal of Theoretical and Applied Mechanics (Poland)* 2007.

25. Lankarani HM, Nikravesh PE. A Contact Force Model with Hysteresis Damping for Impact Analysis of Multibody Systems. *Journal of Mechanical Design* 1990; **112**: 369–376. DOI: 10.1115/1.2912617.

26. Muthukumar S, DesRoches R. A Hertz contact model with non-linear damping for pounding simulation. *Earthquake Engineering and Structural Dynamics* 2006; **35**: 811–828. DOI: 10.1002/eqe.557.

27. Ye K, Li L, Zhu H. A note on the Hertz contact model with nonlinear damping for pounding simulation. *Earthquake Engineering and Structural Dynamics* 2009; **38**: 1135–1142. DOI: 10.1002/eqe.

28. Banerjee A, Chanda A, Das R. Historical Origin and Recent Development on Normal Directional Impact Models for Rigid Body Contact Simulation: A Critical Review. *Archives of Computational Methods in Engineering* 2017; **24**(2): 397–422. DOI: 10.1007/s11831-016-9164-5.

29. McKenna F, Fenves GL, Scott MH. Open system for earthquake engineering simulation. University of California, Berkeley, 2000.

30. Mazzoni S, McKenna F, Scott MH, Fenves GL. Open System for Earthquake Engineering Simulation (OpenSEES) User Command-Language Manual. *Pacific Earthquake Engineering Research Center* 2006.

31. Hughes PJ, Mosqueda G. Comparison of Contact Models for Moat Wall Pounding in a Base-Isolated Moment Frame. *17th World Conference on Earthquake Engineering*, Sendai, JP: 2020.

32. Masroor A, Mosqueda G, Diehl J. Limit State Behavior of Base Isolated Structures: Base Isoalted Isolated Frame with Impact on Concrete Moat Wall 2010. DOI: 10.4231/D3804XJ8B.

33. Masroor A, Mosqueda G, Diehl J. Limit State Behavior of Base Isolated Structures: Base Isolated Moment Frame with Impact on Steel Moat Wall 2010. DOI: 10.4231/D34746R33.

34. Rathje EM, Dawson C, Padgett JE, Pinelli JP, Stanzione D, Adair A, Arduino P, Brandenberg SJ, Cockerill T, Dey C, Esteva M. DesignSafe: New Cyberinfrastructure for Natural Hazards Engineering. *Natural Hazards Review* 2017; **18**(3): 1–7. DOI: 10.1061/(ASCE)NH.1527-6996.0000246.

35. Pant DR, Wijeyewickrema AC. Performance of base-isoalted reinforced concrete buildings under bidirectional seismic excitation considering pounding with retaining walls including friction effects. *Earthquake Engineering and Structural Dynamics* 2014; **43**: 1521–1541.

36. Mavronicola EA, Polycarpou PC, Komodromos P. Effect of ground motion directionality on the seismic response of base isolated buildings pounding against adjacent buildings. *Earthquake Engineering & Structural Dynamics* 2020; **207**(110202): 1–12.

37. Muthukumar S. A Contact Element Approach with Hysteresis Damping for the Analysis and Design of Pounding in Bridges. 2003. DOI: 10.16309/j.cnki.issn.1007-1776.2003.03.004.

38. Goldsmith W. Chapter IV. Contact Phenomena Produced by the Impact of Elastic Bodies. *Impact: The Theory and Physical Behavior of Colliding Solids*, London: E. Arnold; 1960.

39. Jankowski R. Experimental study on earthquake-induced pounding between structural elements made of different building materials. *Earthquake Engineering and Structural Dynamics* 2010. DOI: 10.1002/eqe.941.

40. Ibarra LF, Krawinkler H. Global Collapse of Frame Structures under Seismic Excitations. *The John A Blume Earthquake Engineering Center Reprot No 152* 2005.

41. Lignos DG, Krawinkler H. Deterioration modeling of steel components in support of collapse prediction of steel moment frames under earthquake loading. *Journal of Structural Engineering* 2011. DOI: 10.1061/(ASCE)ST.1943-541X.0000376.

42. Gupta A, Krawinkler H. Seismic Demands for Performance Evaluation of Steel Moment Resisting Frame Structures. *John A Blume Earthquake Engineering Center Technical Report No 132* 1999.

43. Chopra AK. 4. Response to Arbitrary, Step, and Pulse Excitations. *Dynamics of Structures: Theory and Applications to Earthquke Engineering*. 4th ed., 2012.

44. ATC, FEMA P695. Quantification of building seismic performance factors. *Fema P695* 2009(June): 421.

45. Federal Emergency Management Agency. *FEMA 356: Prestandard and Commentary for the Seismic Rehabilitation of Buildings*. 2000.

46. Sarebanha A, Mosqueda G, Kim MK, Kim JH. Modeling of moat wall compliance during impact in seismically isolated nuclear power plants. *24th Conference on Structural Mechanics in Reactor Technology*, Busan, Korea: 2017.

Chapter 4 Moat Wall Pounding Force Prediction Using a High-Fidelity Finite Element Model

4.1. Introduction

Chapter 3 showed how different impact "macro" models can capture the behavior of base-isolated buildings subjected to moat wall pounding. These models are useful for large parametric studies, or when computational resources are scarce, but invariably overlook potentially important details of the impact event. Transient contact area changes, spatial variation of contact forces, and higher-mode vibrations are largely unachievable with the macro model approach. Localized damage features, such as crack patterns and strain concentrations, are also missed by simple contact elements. High-fidelity models of moat wall pounding, which often employ the finite element method (FEM) [1], can reveal these and other important characteristics of the impact

response. Moreover, in the absence of experimental data, detailed FEM analysis may be the best alternative for verification and benchmarking.

Formidable computational costs associated with using large finite element models has made the relevant literature scarce – and literature specifically focusing on moat wall pounding scarcer still. Jankowski [2] and Jameel et al. [3] were early pioneers in nonlinear finite element analysis of seismic pounding in general, but limited their studies to building-to-building impact. Hughes et al. [4] examined moat wall pounding using detailed FEM simulations, and showed that replacing rigid inter-component connections with more realistic bolted connections can change the peak impact force by up to a factor of three. Cheng et al. [5] used both simple contact models and detailed finite elements to analyze the seismic response of a base-isolated liquid storage structure. Their results indicate that the macro element approach was sufficient for the most part, but noticeably deviated from the FEM solution after a period of time.

Chapters 4 and 5 of this dissertation add to the limited body of knowledge regarding high-fidelity FEM analysis of moat wall pounding. Each chapter will consider a different base-isolated structure, with different analysis methods. This chapter will focus on numerical prediction of the moat wall pounding force time history for a single, unidirectional ground motion. Only the contact duration is simulated in this approach, with a preliminary phase to ramp up displacements and velocities to their pre-impact values. Chapter 5 analyzes a full-scale building subjected to three-dimensional ground excitation, and focuses on replication of the superstructure response (i.e. floor accelerations, interstory drifts). In this case, an entire earthquake record is simulated on a complete base-isolated building model with moat walls. In both cases, results of the numerical simulations are compared with experimental data, a unique feature of this work.

The following sections of this chapter outline a high-fidelity FEM analysis of a moat wall pounding experiment conducted at the University at Buffalo. Section 4.2 describes the key characteristics of the quarter-scale building specimen and moat walls. Section 4.3 defines the detailed FEM model generated using LS-DYNA. Section 4.4 explains the various analyses performed on the model, and Section 4.5 summarizes the key results. Section 4.6 explains why some of the measured pounding forces may not be reliable, and Section 4.7 provides concluding remarks.

4.2. Description of the Experiments

Numerical studies in this chapter are modeled after experimental testing conducted at the University at Buffalo [6]. The building specimen in these experiments was a quarter-scale, single-bay, three-story, base isolated moment frame. The bay is 2.4 m wide, and each story is 1.2 m tall. A pinned gravity frame supports concrete blocks on each floor, which provide realistic building masses. The bottom floor weighs 8400 kg, and the upper floors weigh 4800 kg. The lateral force resisting system is a unidirectional intermediate moment frame, with S section columns and beams. Both columns were constructed from S5×10 sections, and S4×9.5, S4×7.7, and S3×7.5 sections were used for the second floor, third floor, and roof beams, respectively. Pre-shaking system identification determined that the first three translational modal frequencies are 1.5 Hz, 5.5 Hz, and 11 Hz, respectively. The corresponding damping ratios are 5.6%, 2.2%, and 3.8%. Figure 4.1 shows a schematic and photograph of the specimens tested at the University at Buffalo. Note that this is the same structure that was modeled using in Chapter 3 using uniaxial contact models for the moat walls (see Figure 3.4).

Two different moat walls were tested in the experiments: a reinforced concrete box filled with sandbags, and a wedge-shaped steel wall intended to represent a quasi-rigid impact surface. This study is limited to analysis of the steel moat wall, to avoid the uncertainties associated with soil modeling. Both sides of the superstructure's base plate were outfitted with reinforced concrete impact blocks, which act as realistic contact surfaces. Impact forces are measured using a special load cell installed between the impact block and two support angles (i.e. L-sections), as shown in Figure 4.1. As such, the measured impact force is not the true impact force between the moat wall and base mat, but the compressive force between the impact block and support angles. If the connections between the base plate, impact block, load cell, and support angles are perfectly rigid, then there should be no difference between these two forces. If there is any slop in the connections, however, the forces will be different. This will be examined later in this chapter.

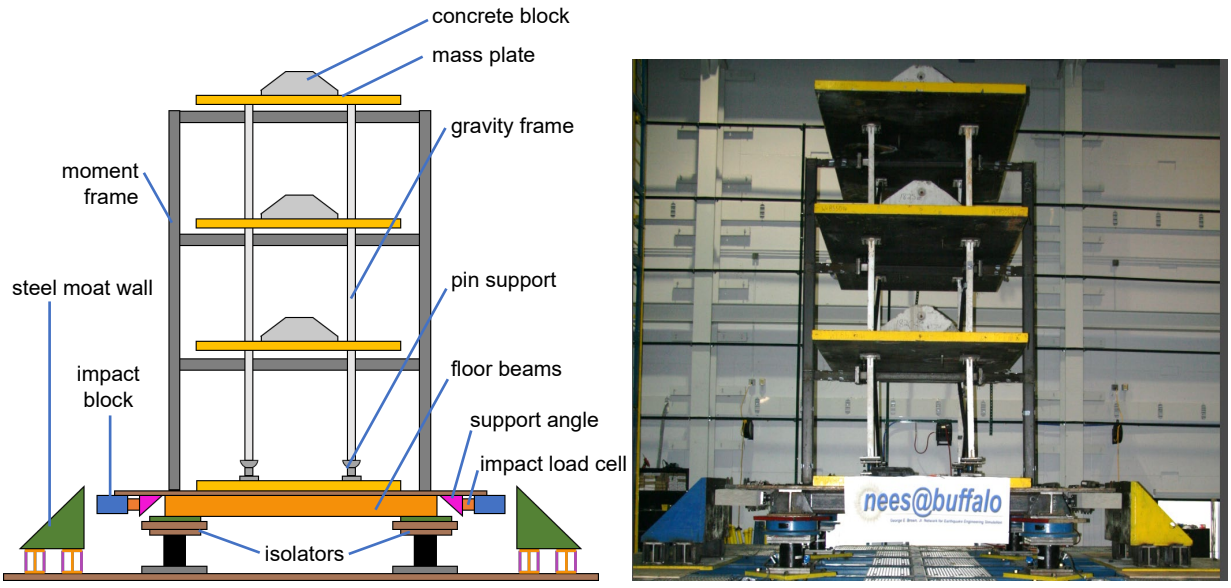

Figure 4.1. Schematic (left) and photograph (right) of the building and steel moat wall specimens at the University at Buffalo [6].

Four identical single friction pendulum isolators were installed underneath the moment frame. The isolators have a sliding radius of 81 cm and maximum displacement capacity of 20 cm. Figure 4.2 shows some experimental hysteresis curves for the four isolators (NW, NE, SW, SE), when subjected to an impact-inducing ground motion. In this case, the initial gap distance was approximately 10 cm. Impact occurs when the base mat displaces beyond this value, which can be seen from the high-frequency force oscillations in Figure 4.2. A schematic of the isolators is shown in Figure 4.3.

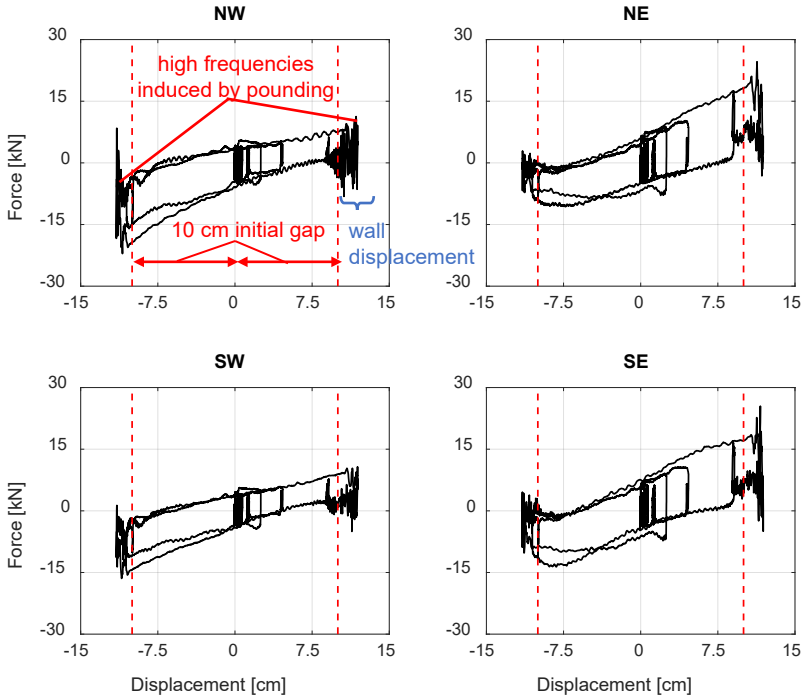

Figure 4.2. Isolator hysteresis for an impact-inducing ground motion. Impact occurs when the base displacement exceeds the 10 cm initial gap, provoking high-frequency forces and deformation in the moat wall.

As stated in Section 3.3.1, the only ground motion that actually triggered moat wall impact in the Buffalo experiments was the N-S component of the 1992 Erzincan earthquake (see Figure

4.4 below). This ground motion record was scaled to a peak ground acceleration (PGA) of 0.91 g, and has a 20-second duration. The first impact event occurred at approximately 4.10 sec, with a second rebound impact at 4.68 sec. This research analyzes the second impact, which, according to the impact load cells, generated a larger peak pounding force. The measured impact force time history is shown in Figure 4.5.

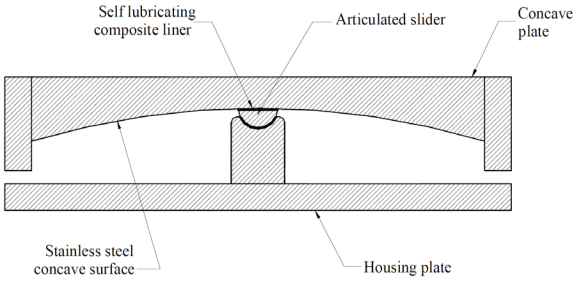

Figure 4.3. Schematic of a single friction pendulum isolator [7].

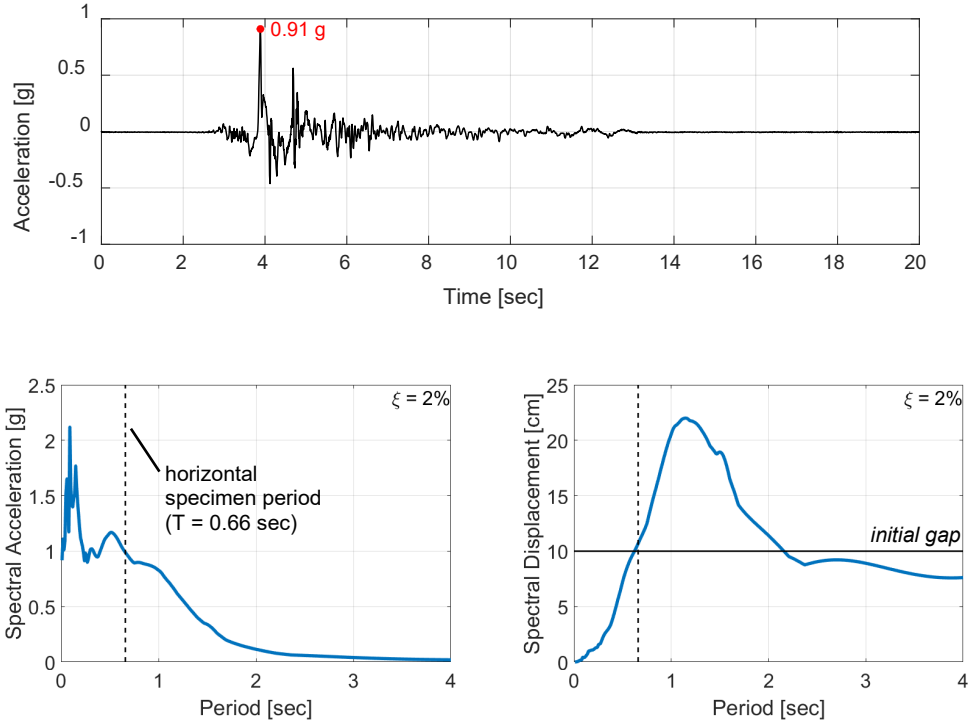

Figure 4.4. Time history (top) and spectra (bottom) of the 1992 Erzincan N-S record.

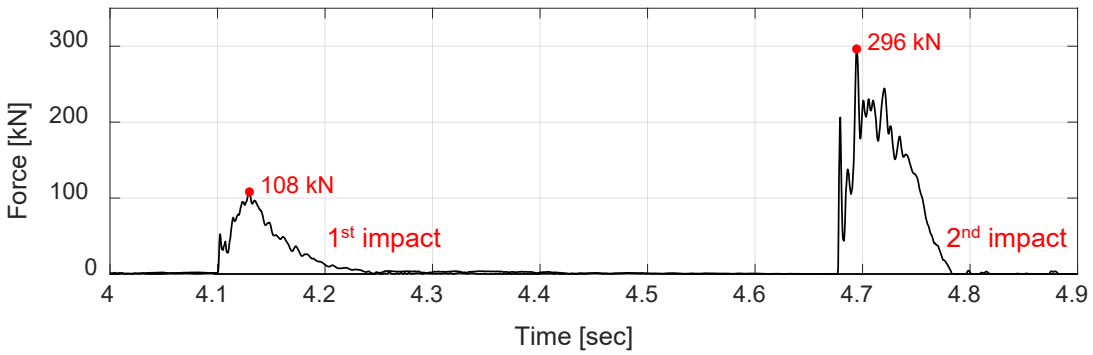

Figure 4.5. Experimentally measured impact forces. Numerical studies shown here focus on the second impact event.

4.3. Description of the Finite Element Model

Figure 4.6 shows the LS-DYNA finite element model used to simulate moat wall impact, which is comprised of

- one 366 cm × 274 cm × 4 cm steel base plate
- one base frame, made of two 274 cm-long W8×58 sections, two 237 cm-long W8×58 sections, and several ½″ (1.27 cm) stiffener plates
- one 122 cm × 37 cm × 15 cm concrete impact block
- two L8×8×½ support angles with ½″ (1.27 cm) stiffener plates
- two 11 cm-diameter load cells
- one 152 cm × 36 cm × 36 cm triangular moat wall made from 1″ (2.54 cm) steel plates
- one support pedestal, made of four 30 cm-long W8×58 sections with ½″ (1.27 cm) stiffener plates

All parts are made of solid hexahedral elements, with a uniform mesh size of ½″ (1.27 cm). Component parts are connected by steel bolts, modeled as beam elements, with rigid "spider" connections at their ends to simulate the clamping effect. Steel reinforcement in the concrete block

is explicitly modeled using beam elements. Coupling between the concrete and rebar is achieved using the **CONSTRAINED_BEAM_IN_SOLID* keyword. Figures 4.7 and 4.8 show the details of the base frame beams, moat wall assembly, and impact block.

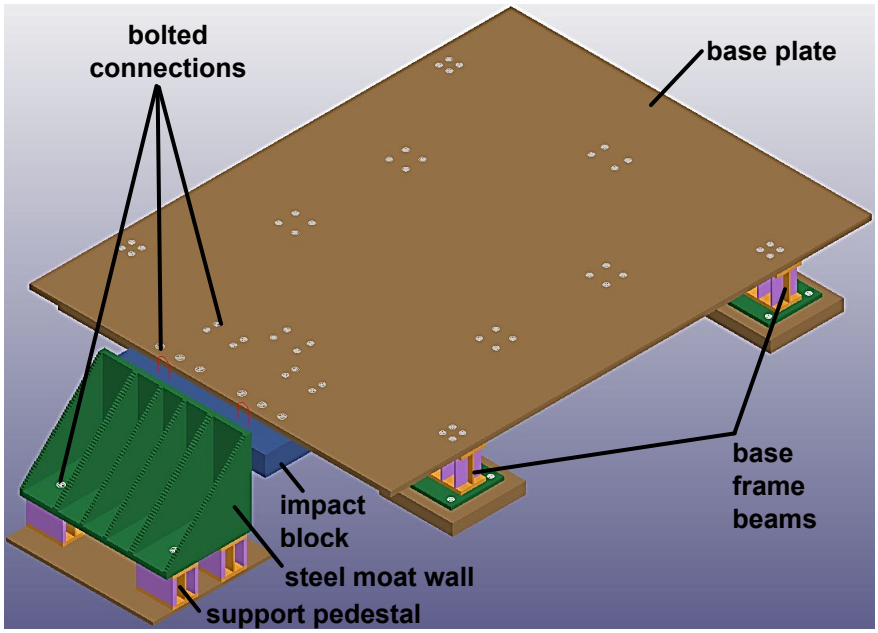

Figure 4.6. LS-DYNA moat wall impact model.

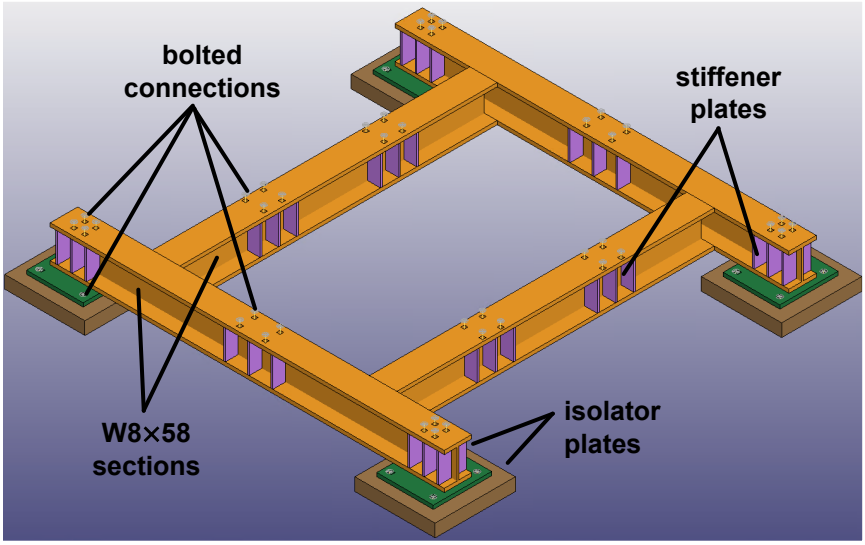

Figure 4.7. Base frame beam details.

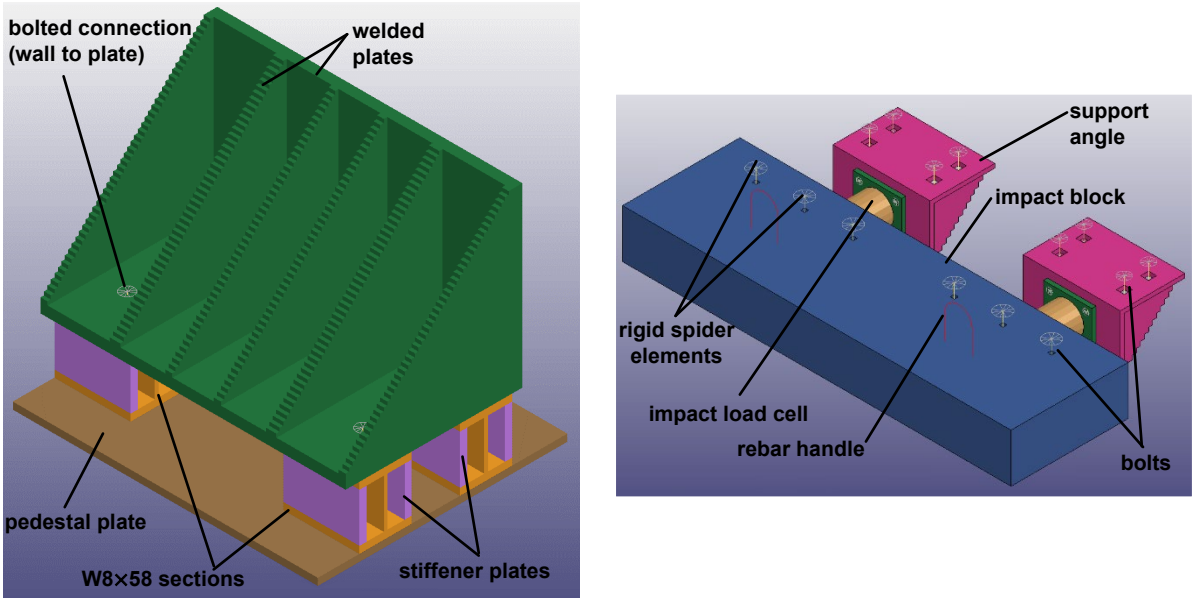

Figure 4.8. Model details for moat wall assembly (left) and impact block (right).

The concrete block uses the **MAT_PSEUDO_TENSOR* material model in mode 2 [8], which generates a standard concrete constitutive law when the only known quantity is the compressive strength. In this case, the compressive strength is assumed to be 34 MPa. Steel elements employ a viscoplastic formulation of **MAT_PLASTIC_KINEMATIC*, with a Young's modulus of 200 GPa and Poisson's ratio of 0.30. All steel components, save for the bolts, are assumed to be low-grade A36 quality, with a 248 MPa yield stress and secondary modulus of 4 GPa (2% of the initial modulus). Bolt elements are assumed to be A490 steel, with a yield stress of 1000 MPa. All other material properties for the A490 bolt elements are identical to the A36 elements. In either case, the hardening parameter **BETA* is set to zero (i.e. no hardening). Concrete and steel stress-strain curves were generated by dynamically applying cyclic displacements to a unit cube solid element. Results are shown in Figure 4.9.

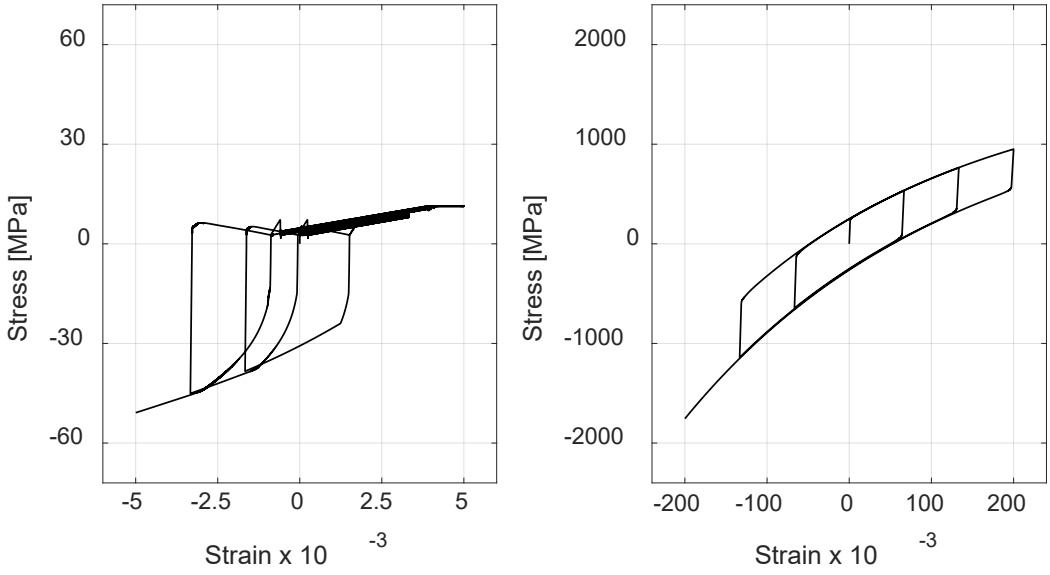

Figure 4.9 Stress-strain relationship for concrete (left) and steel (right) in the LS-DYNA model. Concrete parts use **MAT_PSEUDO_TENSOR* (mode 2). Steel parts use **MAT_PLASTIC_KINEMATIC* with no hardening and viscoplastic effects activated.

Frictional surface-to-surface contact is considered at all possible contact interfaces through the **CONTACT_AUTOMATIC_NODES_TO_SURFACE* keyword, with the **SOFT* flag set to one. Steel-to-steel contacts assumed a friction coefficient of 0.50, and steel-to-concrete contacts assume 0.65.

Finally, it is important to note that the LS-DYNA moat wall pounding model does not include the upper floors. This simulation is highly localized, and response comparison will focus solely on the impact force time histories. Moreover, the inertial force contribution from the upper floors is negligible compared to that of the base level, especially during impact. Figure 4.10, which shows the experimental inertial forces of the base mat and combined upper floors, confirms as much.

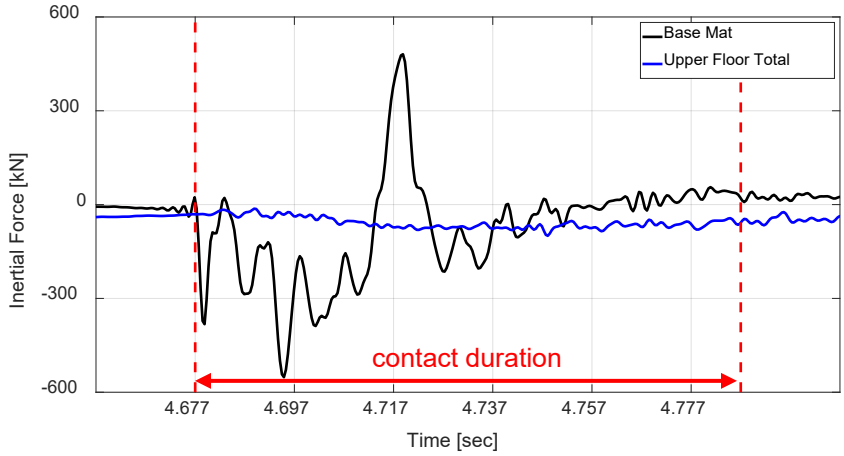

Figure 4.10. Inertial force time histories during impact.

4.4. Analysis Procedures

Simulation of moat wall pounding in the LS-DYNA model is limited to the contact duration, and dived into two phases. The first phase applies multiple preloads, as will be explained in Section 4.4.1. Following this, the impact analysis phase is carried out in one of two ways: applying relative velocities to the base mat assembly and moat wall assembly (Section 4.4.2), or prescribing displacements of the base mat and moat wall throughout the entire contact duration (Section 4.4.3). In either case, the simulation is limited to the 0.1052 sec contact duration, plus 0.05 sec of dynamic preload time.

4.4.1. Explicit Dynamic Preload Analysis

As shown in Figures 4.6 – 4.9, the LS-DYNA pounding model contains numerous bolted joints. Realistic analysis of this system, then, must preload the bolts in some way. LS-DYNA provides numerous bolt preloading options, including static implicit analysis, dynamic relaxation

(explicit or implicit), and the option that will be used here: transient explicit analysis with mass-proportional damping [9]. In this alternative, the preload is achieved during a dynamic simulation, before other dynamic loads are applied (e.g. earthquake motion, initial velocities, etc.). The preload is ramped up to its final value, and mass-proportional damping is applied temporarily to reduce undesired transient oscillations.

In this study, the preload is applied by decreasing the temperature of the bolt elements. The bolts will shrink according to the coefficient of thermal expansion, thus applying a preload. The **MAT_ADD_THERMAL_EXPANSION* keyword adds thermal effects to the bolts, **DEFINE_CURVE* determines how temperature change varies with time, and **LOAD_THERMAL_VARIABLE_BEAM_SET* applies the thermal load. In general, this is an iterative process to determine the temperature change ΔT that induces the desired level of preload stress (σ_0). ΔT can be estimated using the following formula:

$$\Delta T = -\frac{\sigma_0}{E\alpha} \tag{4.1}$$

where E is the Young's modulus of the bolts (200 GPa) and α is the coefficient of thermal expansion (6E-6/°F). Equation (4.1) will exactly predict the required temperature decrease for a single-bolt system with no part connectivity, but iterations on ΔT are required for realistic systems with multiple components and fasteners. Temperatures are selected such that the axial stresses coincide with the minimum bolt pretension levels specified in Table J3.1 of the AISC Steel Construction Manual [10]. For the wall bolts, the required temperature was approximately -500°F. All other bolts assumed ΔT = -100°F.

Mass-proportional damping is applied once the preload is at its final value. This quickly eliminates transient oscillations caused by the preload, such that other dynamic loads can be applied on a system that is practically at rest. Additionally, setting the damping coefficient to a

near-critical value further reduces the time required to damp out the unwanted vibrations. In short, the damping coefficient input to the **DAMPING_PART_MASS_SET* keyword should be equal to $2\xi\omega_1$, where ξ is a damping ratio set close to unity (set to 0.99 in the moat wall impact model), and ω_1 is the first natural circular frequency of the part or subassembly of interest. Figure 4.11 shows how the explicit dynamic preloading is accomplished.

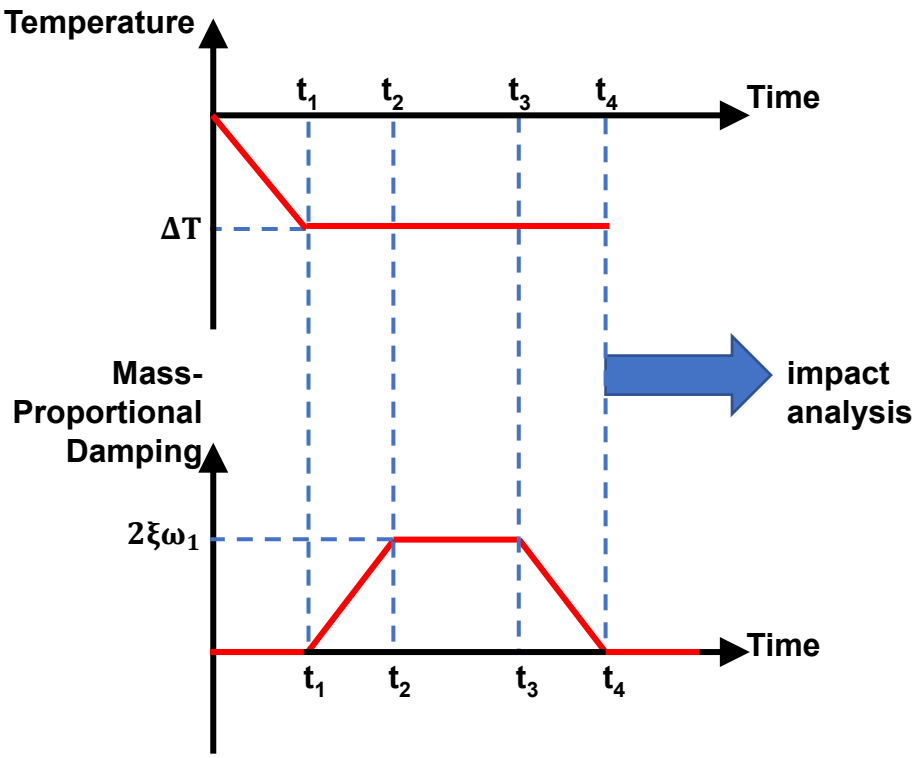

Figure 4.11. Explicit dynamic bolt preload via temperature decrease (top) and temporary mass-proportional damping (bottom).

The time variables t_1, t_2, t_3, and t_4 are defined by the user. They should be large enough that the system is effectively at rest when $t = t_4$, but small enough to allow for a fast and efficient preload step. In this study, t_1 = 0.010 sec, t_2 = 0.011 sec, t_3 = 0.049 sec, and t_4 = 0.050 sec. The following sections explains two different approaches for the subsequent impact analysis, which occurs once the preload is established (i.e. at t = 0.050 sec).

4.4.2. Impact Analysis Using Initial Velocities

Once the preload stage is complete, impact between the moat wall and base mat is accomplished in one of two ways. This section highlights the first such method, based on application of initial velocities (using the **INITIAL_VELOCITY_GENERATION* keyword). In this approach, pre-impact velocities of the base mat and moat wall assemblies are applied to their numerical counterparts in LS-DYNA. The moat wall is set very close to the impact block (i.e. 1 cm away), such that contact initiates immediately after initial velocities are applied. Displacement signals from string potentiometers, originally sampled at 2500 Hz, are filtered using a 50 Hz low-pass filter. The filtered displacements are then differentiated with respect to time to generate the velocity curves shown in Figure 4.12 below. The original displacement signals are measured from an off-table reference point. That is, displacements are measured in an absolute coordinate system that does not move with the ground.

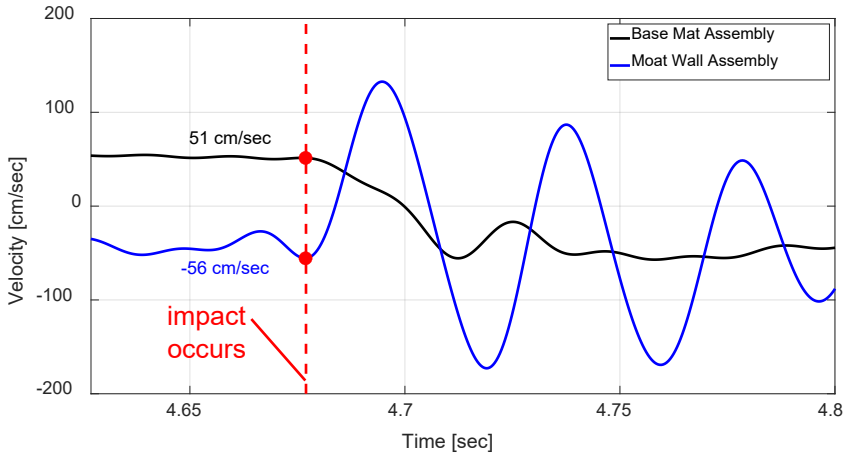

Figure 4.12. Velocity time histories of the base mat and shake table. "Initial" velocities of 51 cm/sec and -56 cm/sec are applied to the base mat and moat wall assemblies, respectively, after the 0.05 sec preload step.

4.4.3. Impact Analysis Using Prescribed Displacements

The second and final impact analysis approach prescribes absolute displacements throughout the preload phase and contact duration. During the preload phase, displacements of the base mat and moat wall assemblies are steadily increased to initiate contact with the correct velocities at t = 0.05 sec. A cubic ramping function is used to smoothly vary the displacements, and in turn, the velocities, during preloading. Following this, the measured displacements are imposed for the remainder of the simulation (i.e. for the 0.1052 sec contact duration). The moat wall and impact block are initially separated by a distance equal to their relative displacements at the end of the preload phase, as shown in Figure 4.13. This approach employs the **BOUNDARY_PRESCRIBED_MOTION_SET* keyword to apply motions to each assembly, and **DEFINE_CURVE* to set the displacement vs. time function.

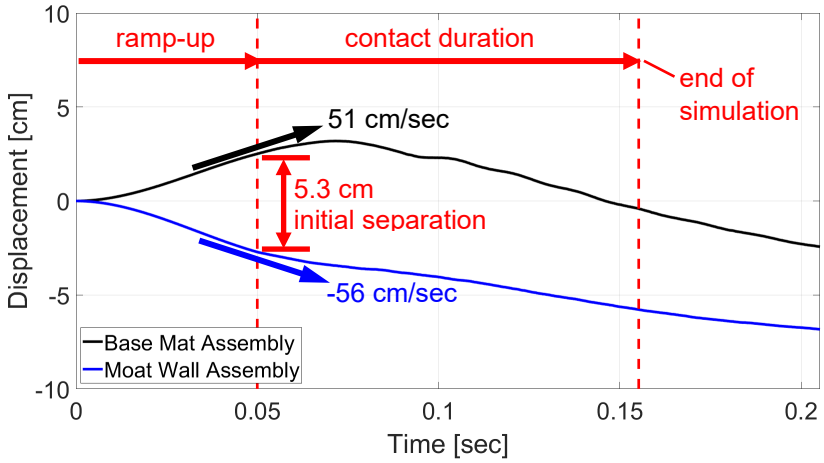

Figure 4.13. Base mat and pedestal displacements are ramped up to their pre-impact values over 0 sec ≤ t ≤ 0.05 sec , and then the experimental values are applied over the contact duration (0.05 sec < t ≤ 0.155 sec).

4.5. Results

Impact forces from the LS-DYNA model are extracted from the normal-direction contact force that the load cell elements exert on the impact block. This is consistent with the experimentally-measured impact force, which was obtained from cylindrical load cells attached between the support angles and impact block (see Figures 4.1 and 4.8). Figure 4.14 shows the impact force time histories from the experiment and both FEM approaches. At first glance, both of the numerical approaches greatly differ from one another, and differ from the experiment to an even greater degree. The measured contact duration was approximately 0.11 sec. FEM results , on the other hand, show vastly different contact durations: 0.0059 sec for the initial velocity approach and 0.035 sec for prescribed displacement approach. Furthermore, predicted impact forces were 550 kN and 574 kN, while the measured peak impact force was only 296 kN.

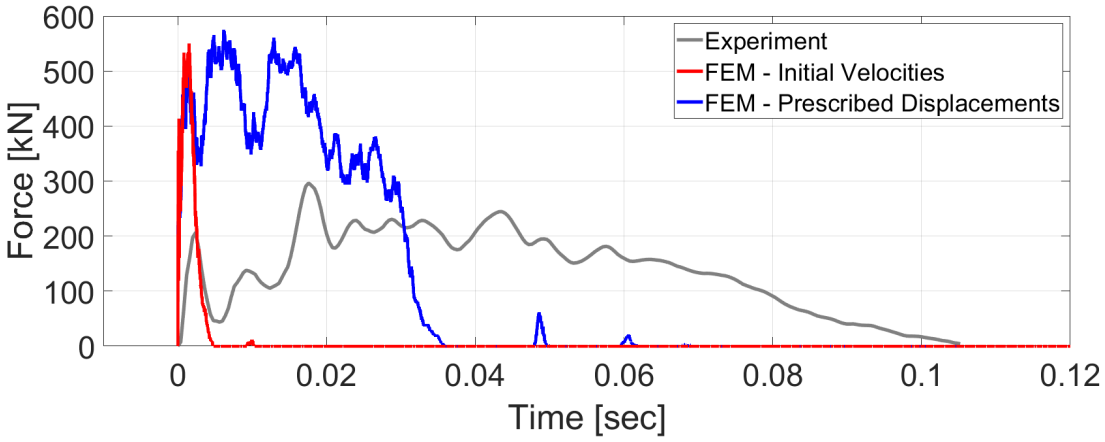

Figure 4.14. Impact force time histories.

Significant differences between the experimental and numerical impact forces expose the flaws in the current modeling approach. The initial velocity approach, for example, does not

impose any lateral forces on either the base mat or moat wall pedestal during the contact duration. As a result, the bodies come out of contact with one another quite rapidly, after only 0.0059 sec. Imposing the measured displacements, then, should alleviate this issue. As Figure 4.15 shows, though, this is only partially true. Prescribing the exact displacements does elongate the contact duration, but only to roughly a third of what was measured (0.035 sec predicted vs. 0.11 sec measured). The moat wall displacements are imposed at the base of the support pedestal, so it is likely that errors in this approach arise from poor representation of the moat wall features. Numerous contact nonlinearities are present in the steel moat wall – at the interfaces between the pedestal plate, support beams, stiffener plates, and the wall itself – which are more difficult to accurately represent in a finite element modeling environment. In this case, the local intricacies of the bolted connections and contact interfaces are clearly important features in capturing the impact response.

Still, some interesting observations can be made from the FEM results. First, generate a normalized force by dividing each ordinate value from Figure 4.15 by its maximum value. That is, constrain the force signals to vary between 0 and 1. Furthermore, divide the abscissae by the respective contact durations, such that the normalized time also varies between 0 and 1. Figure 4.15 shows the results of this normalization, which reveal that, despite the myriad errors present in the FEM results, the numerical models do capture the essential physical behavior, albeit on different scales. Indeed, all normalized forces exhibit an initial spike at a normalized time of roughly 0.1. Following this, both the experimental and FEM results oscillate near the peak impact force, and steadily decrease as the bodies come out of contact. The second FEM model, which prescribed measured displacements, even displays the same basic shape as the experimental

results. Quantitative errors notwithstanding, then, the FEM models shown here could be useful for future qualitative assessment of moat wall pounding behavior.

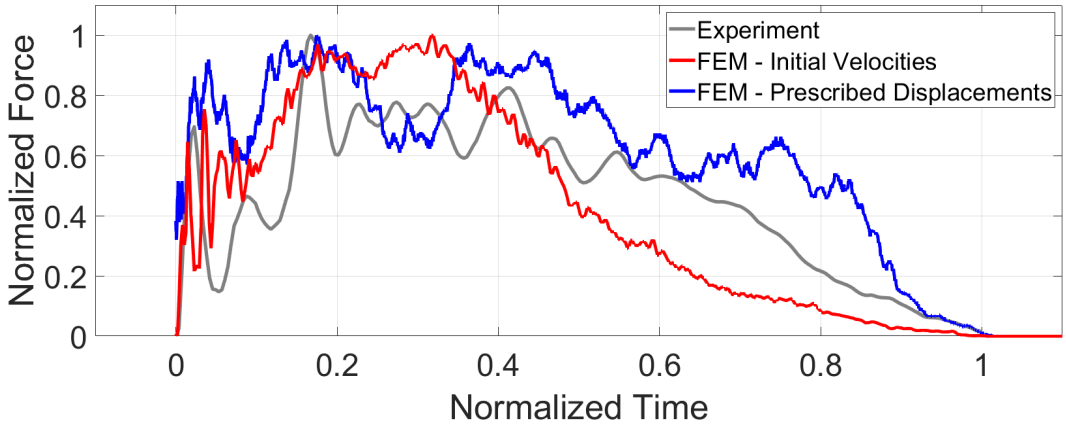

Figure 4.15. Normalized impact force time histories. Forces are divided by the respective maximum forces, and time is divided by the respective contact durations.

As has been mentioned throughout this chapter, the experimental impact force is truly a measure of the compressive force in the cylindrical load cells, and not the force exerted by the moat walls onto the impact block. The latter force was not measured during testing, but the difference between the two forces can still be examined using the finite element models. Figure 4.16 compares the time history of normal-direction forces at the load cells (left) and at the block-wall interface (right). Again, it is important to mention that the FEM results are different from the experiment in terms of peak force and contact duration, but the models can still show the relative difference between the load cell forces and the block-wall forces. In particular, the numerical models show that the peak block-wall interface force is 1,130 kN for the initial velocity approach, and 1,240 kN for the imposed displacement approach. Recalling from the previous discussion that the models respectively predicted load cell forces of 550 kN and 574 kN, the block-wall interface

forces are greater than the load cell forces by a factor of two. The difference between these forces can be attributed to frictional effects at the various connections around the impact load cells. This adds further weight to the claim that contact and friction at mechanical joints plays an important role in the moat wall pounding response of this particular system.

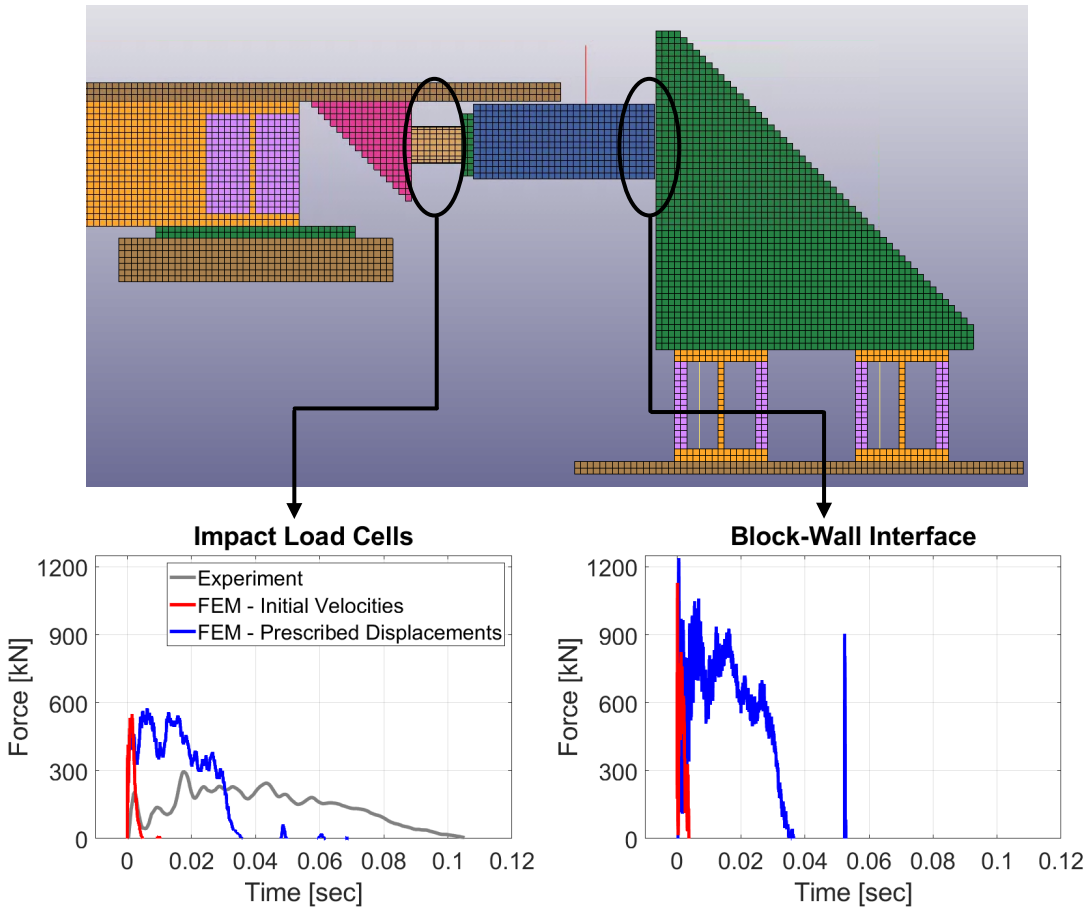

Figure 4.16. Contact forces are significantly different at the impact load cells (left) and block-wall interface (right).

4.6. A Note on the Measured Pounding Forces

During a pounding event, the isolators, superstructure, and moat wall form a coupled system that must satisfy dynamic equilibrium. The sum of the inertial forces at the base (f_b^I), second floor (f_2^I), third floor (f_3^I), and roof (f_r^I) form the total inertial force (f^I) as

$$f^I(t) = f_b^I(t) + f_2^I(t) + f_3^I(t) + f_r^I(t) \tag{4.2}$$

where t refers to time. Similarly, the lateral force of each isolator (f_i^R; i = 1, 2, 3, 4) contributes to the total restoring force f^R:

$$f^R(t) = f_1^R(t) + f_2^R(t) + f_3^R(t) + f_4^R(t) \tag{4.3}$$

While the base mat and moat wall are in contact, the pounding force (f^P) is equal to the difference between f^I and f^R, and equal to zero at all other times.

$$f^P(t) = \begin{cases} f^I(t) - f^R(t) & during\ impact \\ 0 & all\ other\ times \end{cases} \tag{4.4}$$

This concept is shown in Figure 4.17.

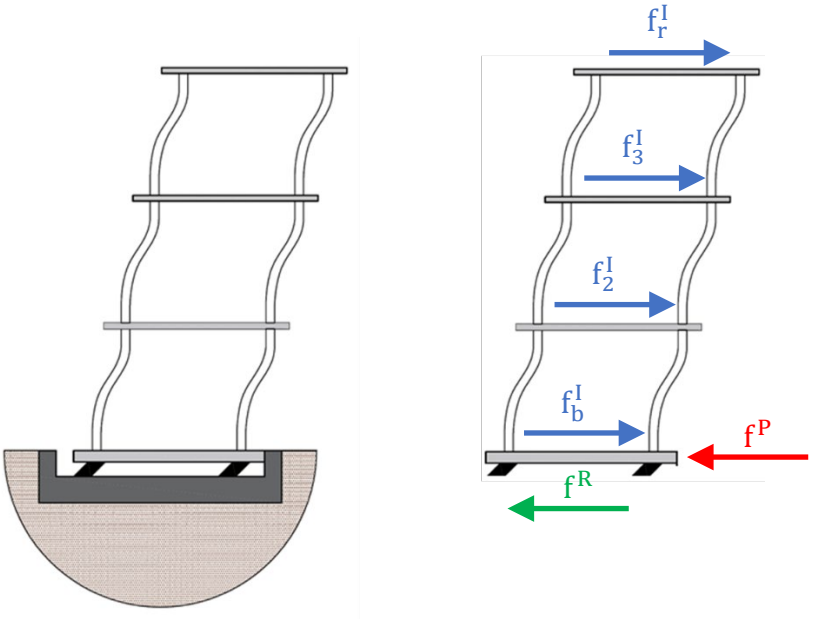

Figure 4.17. Dynamic equilibrium of a base-isolated building during moat wall pounding.

An indirect estimate of the pounding force can be obtained by applying dynamic equilibrium to the base-isolated moment frame specimen. Inertial forces are computed by scaling the floor accelerometer signals by the corresponding mass, and the isolator restoring forces were measured directly. Subtracting the restoring force from the total inertial force results in the pounding force, as shown in Equation (4.4). Figure 4.18 compares the estimated pounding force with the load cell measurement. Peak pounding forces vary significantly, with the dynamic equilibrium estimate exceeding the load cell measurement by a factor of two to three. Furthermore, the computed pounding force becomes negative at certain times, implying that the moat wall is applying a tensile force to the superstructure. As shown in Figure 4.16, it is possible that the true impact force is greater than the compressive force in the load cell, but tensile pounding forces are not physically possible. As such, it is likely that the accelerometer measurements, particularly at the base, are in error. High-frequency waves propagate throughout the structure during impact, which may be detected by the accelerometers and further excite the instrument itself. These localized accelerations are mostly internal, however, and do not contribute to the macro-scale acceleration of the floor, nor to the overall inertial force.

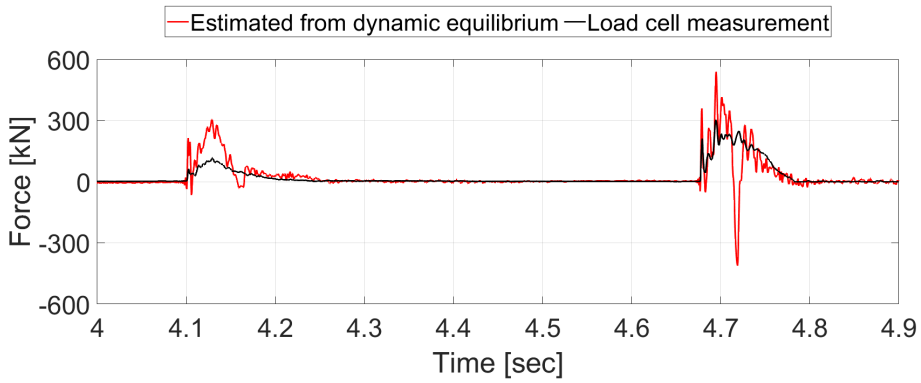

Figure 4.18. Moat wall pounding forces estimated by the dynamic equilibrium approach and measured by the impact load cells.

4.7. Conclusions

This chapter developed a high-fidelity finite element model of moat wall pounding, and tested its effectiveness against measured experimental data. Impact force time histories were investigated using two different numerical approaches: (1) application of pre-impact relative velocities, and (2) direction prescription of time-varying displacements throughout the contact duration. Both approaches yielded significantly different impact force time histories from the experimental benchmark. The initial velocity approach failed because it does not apply dynamic action to the colliding bodies during contact. The imposed displacement approach failed due to poor representation of the complex system of bolted connections that make up the moat wall and support pedestal.

Nevertheless, the detailed models shown here do reveal some interesting characteristics of the moat wall pounding event. The overall shape and trajectory of impact forces is consistent with the experimental measurements, implying that the models are capturing the underlying physics during impact, even if it is occurring on a different time scale. Consequently, the high-fidelity models shown here may be (cautiously) used for further qualitative estimation of moat wall pounding behavior. Furthermore, both finite element models indicate that the compressive force at the load cells is likely very different from the interfacial force between the impact block and moat wall. The degree to which these forces are different remains to be seen, but inter-component contact forces clearly plays an important role in the response of the steel moat wall shown here.

This research also demonstrated that the measured pounding forces may not be reliable. Computation of the pounding force via dynamic equilibrium exceeded the load cell measurements by a factor of two to three. Moreover, the dynamic equilibrium estimate is negative at certain times,

indicating a physically impossible tensile force. Therefore, it can be concluded that one or more of the accelerometers made erroneous measurements.

Future work on high-fidelity moat wall pounding models should take into consideration the lessons gleaned from this research. Namely, reducing the simulation time to focus solely on the contact duration is likely to give inaccurate results. A full earthquake acceleration time history analysis, with accurate modeling of isolation devices, may be the best path forward. Future research should also investigate a more robust methodology for estimating the moat wall pounding force. As evidenced in Section 4.6, the accelerometer and/or load cell measurements are not reliable during impact, which may require post-hoc correction using spectral approaches.

References

1. Hughes TJR. *The Finite Element Method: Linear Static and Dynamic Finite Element Analysis*. Courier Corporation; 2012. DOI: 10.1111/j.1467-8667.1989.tb00025.x.

2. Jankowski R. Non-linear FEM analysis of earthquake-induced pounding between the main building and the stairway tower of the Olive View Hospital. *Engineering Structures* 2009; **31**(8): 1851–1864. DOI: 10.1016/j.engstruct.2009.03.024.

3. Jameel M, Saiful Islam ABM, Hussain RR, Hasan SD, Khaleel M. Non-linear FEM analysis of seismic induced pounding between neighbouring Multi-storey Structures. *Latin American Journal of Solids and Structures* 2013. DOI: 10.1590/S1679-78252013000500004.

4. Hughes PJ, Sarebanha A, Mosqueda G. Finite Element Analysis of Moat Wall Pounding in Base-Isolated Buildings. *11th U.S. National Conference on Earthquake Engineering*, Los Angeles, CA, USA: 2018.

5. Cheng X, Jing W, Qi L, Gong L. Pounding Dynamic Responses and Mitigation Measures of Sliding Base-isolated Concrete Rectangular Liquid Storage Structuress. *KSCE Journal of Civil Engineering* 2019; **23**(7): 3146–3161. DOI: 10.1007/s12205-019-0082-6.

6. Masroor A, Mosqueda G. Experimental simulation of base-isolated buildings pounding against moat wall and effects on superstructure response. *Earthquake Engineering and Structural Dynamics* 2012; **41**: 2093–2109. DOI: 10.1002/eqe.2177.

7. Mosqueda G, Whittaker AS, Fenves GL, Mahin SA. Experimental and Analytical Studies of the Friction Pendulum System for the Seismic Protection of Simple Bridges. *UCB/EERC 2004-01* 2004.

8. Livermore Software Technology Corporation. *LS-DYNA Keyword User's Manual, Volume II: Material Models*. 2017.

9. Livermore Software Technology Corporation. Preloads in LS-DYNA 2011. https://ftp.lstc.com/anonymous/outgoing/jday/bolt_preload3.pdf.

10. Steel Construction Manual. *Steel Construction Manual*. 2005. DOI: 10.1016/B978-075065546-0/50014-1.

Chapter 5 Finite Element Analysis of a Full-Scale Base-Isolated Building Subjected to Three-Dimensional Ground Motion and Moat Wall Pounding

5.1. Introduction

Chapter 4 focused on predicting the local pounding response (i.e. impact force) using a high-fidelity finite element model. Results from those simulations were limited to the contact duration, and varied significantly from the experimental measurements. This chapter continues that work, but focuses on global response prediction (i.e. floor accelerations, interstory drifts) of a full-scale base-isolated building subjected to pounding induced three-dimensional (3D) ground shaking. As before, the numerical studies parallel a building model that was tested in an earthquake simulation facility. Section 5.2 describes the experimental specimen and Section 5.3

details the corresponding finite element model, constructed in ABAQUS [1]. Section 5.4 summarizes the numerical findings and conclusions are given in Section 5.5.

5.2. Description of the Experiments

In August of 2013, a full-scale base-isolated building structure was subjected to three-dimensional ground motion at the Hyogo Earthquake Engineering Research Center (AKA "E-Defense") in Kobe, Japan [2]. One goal of these experiments was to evaluate the seismic response of a realistic building structure when subjected to moat wall pounding. The four-story reinforced concrete (RC) building specimen, shown in Figure 5.1, was constructed at full-scale and contained numerous nonstructural components, such as a functioning garage door, internal lighting fixtures, and freestanding furniture. In fact, each floor was outfitted to imitate real-life spaces. The first floor functioned as a storage room, with a garage door and shutters. The second floor was a computational laboratory equipped with server racks and living spaces. The third floor contained medical and control equipment, and the fourth floor contained school furniture and a faux-museum. Figure 5.1 also shows the global coordinate directions (X, Y and Z) that will be referred to in this chapter, as well as a north indicator (N). The total weight of the base-isolated building was 676.6 metric tons, and its fundamental vibration period was determined to be 1.4 sec.

Base isolation of the building specimen was achieved using two different types of bearing devices: rubber bearings in the SW and NE corners, and a combination rubber-slider bearing in the NW and SE corners. The rubber bearings were essentially linear elastic, with manufacturer-listed stiffnesses of 8 kN/cm in the horizontal directions and 19,600 kN/cm in the vertical directions. The NW and SE corners each implemented an elastic slider bearing, consisting of a rubber bearing attached to the top of a low-friction slider bearing. For the slider bearings, the

manufacturer listed horizontal stiffnesses of 15.7 kN/cm, vertical stiffnesses of 22,700 kN/cm, and friction coefficients that varied between 0.014 and 0.018.

Figure 5.1. Base-isolated building specimen with moat walls.

In addition to the isolation bearings, three different configurations of base-level damping devices were considered during experimentation. Configuration #1 used two steel U-shaped dampers, Configuration #2 added a single steel damper and four oil dampers, and Configuration #3 used four oil dampers and no steel dampers. All base configurations are shown in Figure 5.2,

with photographs of the isolation and damping devices. This study focuses on Configuration #3, with two types of isolators (rubber and slider) and one type of damper (oil).

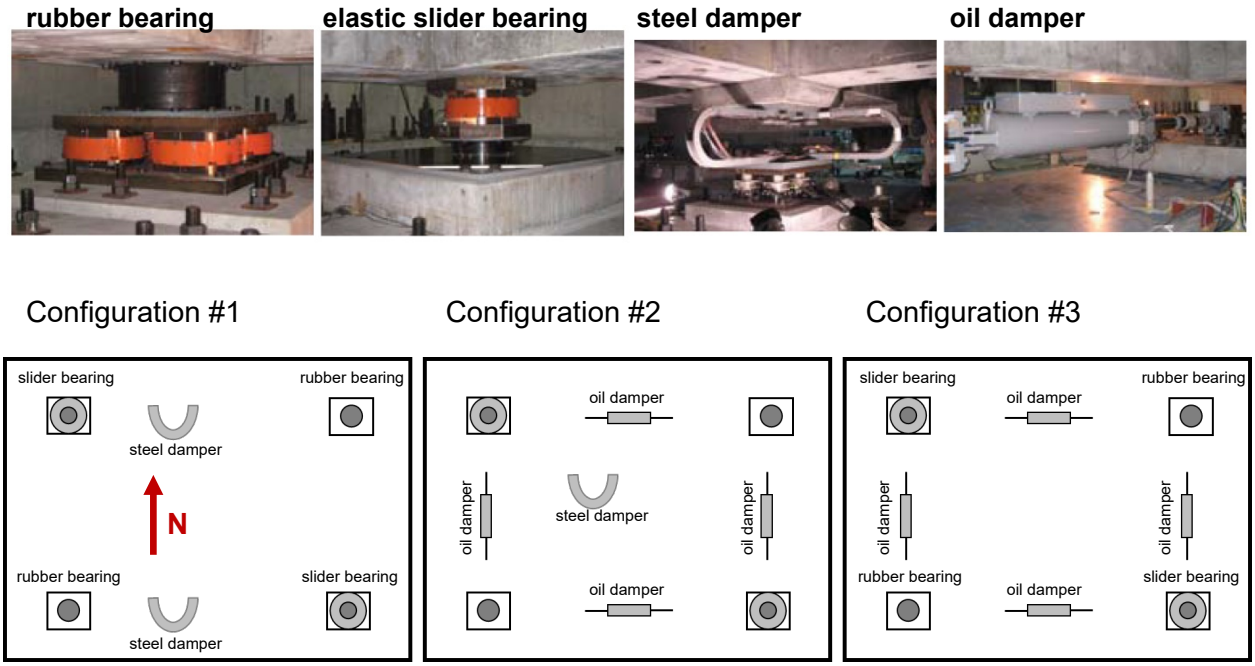

Figure 5.2. Isolation and damping device configurations.

The building specimen is surrounded on all sides by RC moat walls. Two 40 cm-thick moat walls, dubbed "BW40", are installed on east and west sides of the building. Likewise, two 20 cm-thick "BW20" moat walls are installed on the north and south sides of the building. Each moat wall is reinforced with different sizes of rebar, varying from D10 to D19. Both walls are 2.3 m high, and are installed 40 cm away from the base mat of the superstructure. Figure 5.3 shows detailed design drawings for the BW40 and BW20 moat walls.

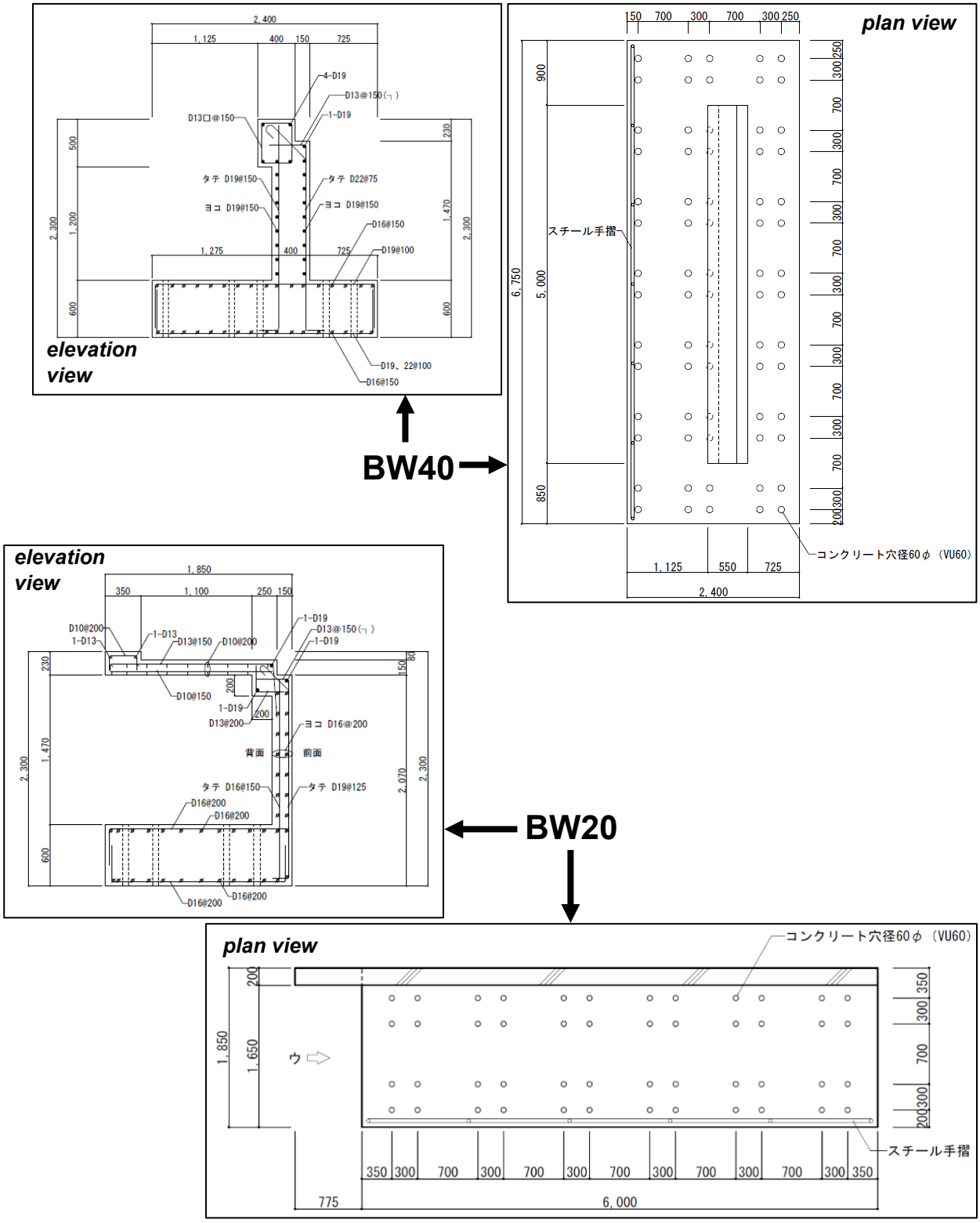

Figure 5.3. Design drawings for the BW40 and BW20 moat walls. Dimensions are in mm.

Numerous impact-inducing ground motions were applied to base isolated building and moat walls. This study will focus on one such motion: the 1995 JR Takatori record, scaled to 90% of its original amplitude. The X, Y, and Z components of this record's acceleration time history, as well as the acceleration and displacement response spectra, are shown in Figure 5.4.

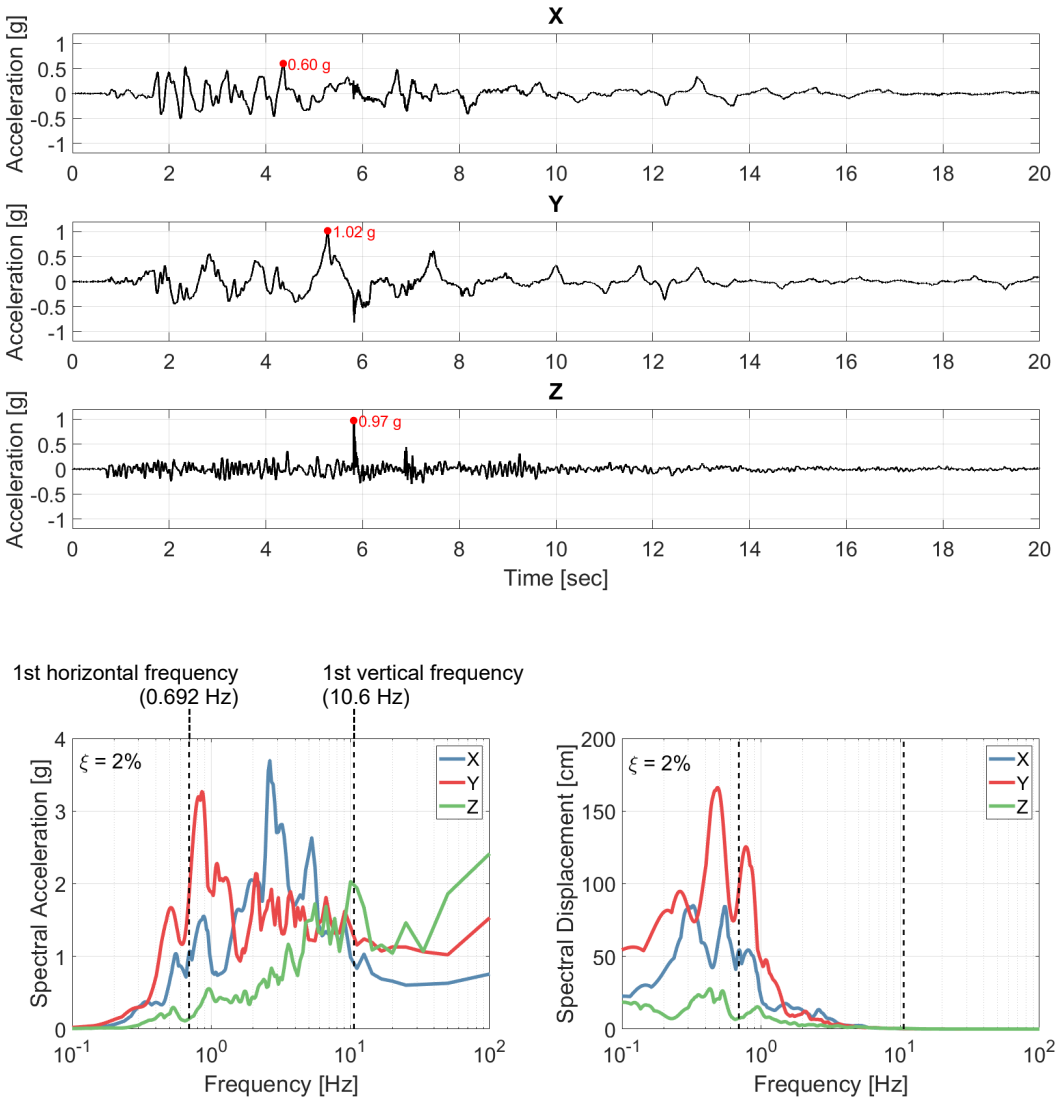

Figure 5.4. Time histories (top) and spectra (bottom) for three components of the JR Takatori (90%) earthquake record.

5.3. Description of the Finite Element Model

A three-dimensional, high-fidelity finite element model of the E-Defense specimen was constructed in ABAQUS [1]. Displayed in Figure 5.5, most of this model is comprised of solid hexahedral elements, with shell elements used to model the slabs and beam elements used to model the embedded rebar. The superstructure model is made of linear elastic elements, and was previously calibrated to modal data [3]. The superstructure was not visibly damaged after moat wall pounding [2], so the linear elastic model is adequate for this analysis. A ring of solid elements was tied to the perimeter of the base mat shell elements, for easier contact definition between the base mat and moat walls. Experimental data indicated that impact occurred in the Y direction when the base displacement was 37.9 cm (west impact) and 39.6 cm (east impact), so the numerical gap distances are set as such. No impacts occurred in the X direction, so those gap distances are left at a nominal 40 cm.

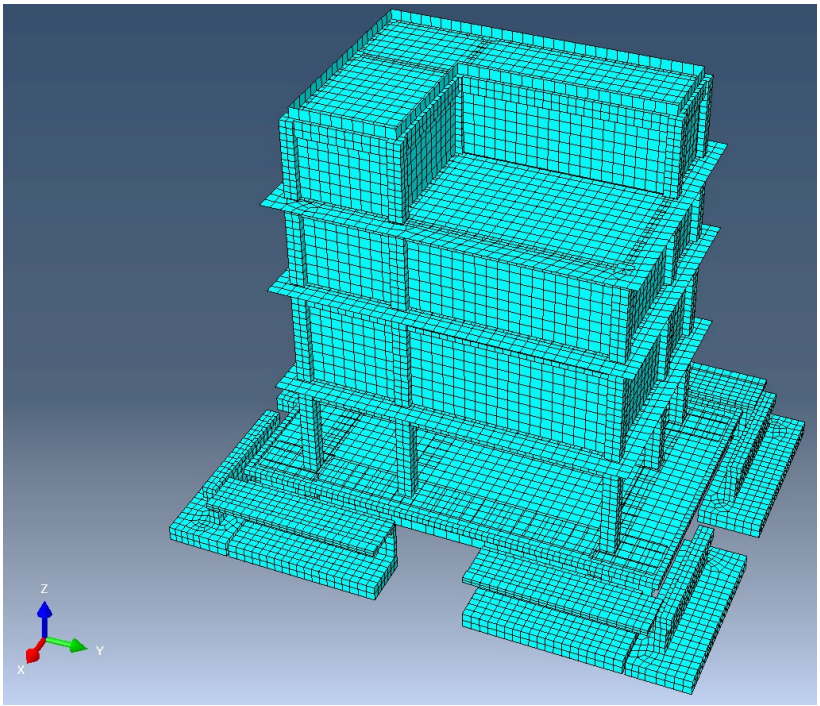

Figure 5.5. ABAQUS moat wall impact model.

The moat walls, however, consider significant material nonlinearities. In this study, the concrete damaged plasticity (CDP) model [4] is used for confined and unconfined concrete, with compression and tension backbone curves following the Mander model [5]. The assumed compressive strength is 50 MPa, which is consistent with experimental cylinder tests. Using the Mander model, then, the tensile strength is 3.10 MPa, and the Young's modulus is 26.7 GPa. The reinforcing steel assumes a bilinear material law, with a Young's modulus of 200 GPa, yield strength of 414 MPa, and secondary modulus of 4 GPa (2% of initial). Stress-strain relationships for the moat walls' concrete and steel are shown in Figures 5.6 and 5.7, respectively.

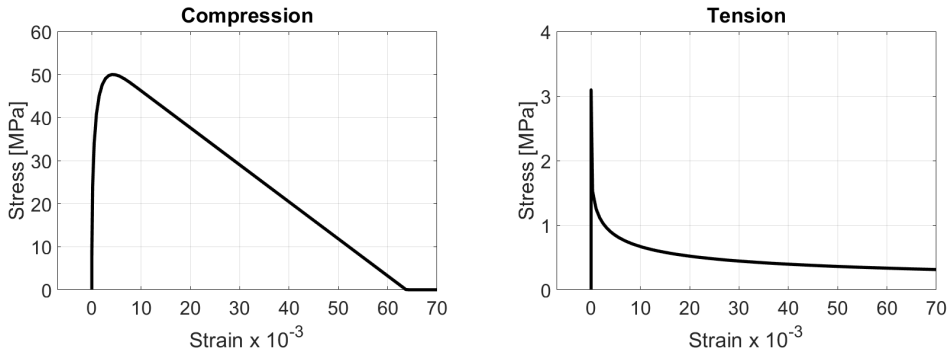

Figure 5.6. Stress-strain curves of the moat wall concrete material in compression (left) and tension (right).

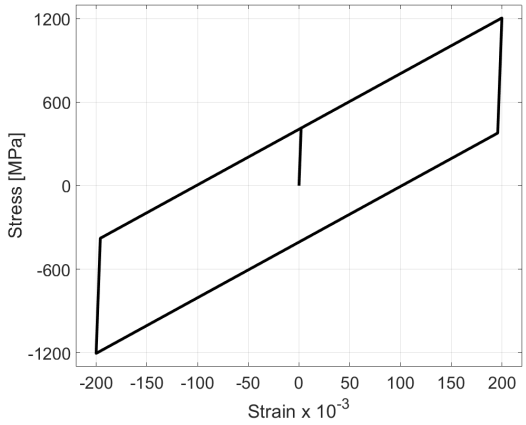

Figure 5.7. Stress-strain hysteresis of the moat wall rebar material.

All isolation and damping hardware at the base of the superstructure are modeled using connector elements within ABAQUS [4]. Connectors allow the user to define the desired characteristics (elasticity, plasticity, damping, friction, etc.) in a zero-length element attached to a moving ground. Rubber bearings are modeled as linear elastic, with uncoupled stiffnesses in the X, Y, and Z directions. The elastic slider bearings employ a penalty friction model with a coupled X-Y force potential. The force potential (P) is given by

$$P = \sqrt{f_X^2 + f_Y^2} \tag{5.1}$$

where f_X and f_Y are the X and Y components of the friction force, respectively. Essentially, Equation (5.1) describes a circular yield function, where the system is sticking if $P < \mu|f_Z|$ (inside the circle), and slipping if $P = \mu|f_Z|$ (on the circle). In this expression, μ is the friction coefficient and f_Z is the normal contact force in the Z direction. The friction forces are limited by $\mu|f_Z|$, so a state of $P > \mu|f_Z|$ is not permitted. Oil dampers are modeled as linear viscous. Connector parameters in this study coincide with the values determined from a prior study on the E-Defense specimen [6]. Oil dampers were not considered in that study, so their parameters (i.e. the damping coefficients) are determined by fitting a line through the experimentally-measured force-velocity data of each damping device. Tables 5.1 and 5.2 summarizes the parameters of isolation devices and oil dampers, respectively.

The ABAQUS model is first subjected to a gradually-applied gravity load. During this phase, the ground nodes and moat wall base nodes are fixed in all directions. Following the gravity load, the fixed conditions are released, and three components of ground motion are applied over 20 seconds. The ABAQUS model contains no inherent damping.

Table 5.1. Isolator properties.

Device Name	Location	Stiffness [kN/m]			Friction Coefficient
		X	Y	Z	
Rubber Bearing	SW	830	787	1,196,000	N/A
	NE	714	746	1,196,000	
Elastic Slider Bearing	NW	1,570	1,570	2,270,000	0.02
	SE	1,570	1,570	2,270,000	0.02

Table 5.2. Damper properties.

Device Name	Location	Direction	Damping Coefficient [kN/(m/sec)]
Oil Damper	W	X	255
	E	X	250
	S	Y	255
	N	Y	257

5.4. Results

Performance of the ABAQUS moat wall impact model is assessed in multiple ways. The accuracy of the isolator and damper elements is determined first, as these will have the greatest effect on the overall behavior of the model. Next, the floor accelerations and displacements are compared against corresponding measurements from the experiment. Finally, moat wall accelerations and displacements are examined as local response metrics.

Figures 5.8 and 5.9 show the force-displacement hysteresis of the rubber bearings and elastic slider bearings, respectively. The rubber bearing models match the experimental values particularly well, owing to their simple, linear elastic behavior. The elastic slider bearings have much more complicated hysteresis loops, resulting from the three-dimensional force coupling embedded in the friction model. High-frequency force oscillations, associated with variations in the normal contact pressure, are present in the ABAQUS model, but they differ from those in the

experiment. These differences can be attributed to the slider bearing connector model, which assumes a constant coefficient of friction and an identical sticking stiffness in X and Y. In reality, the coefficient of friction will vary with the sliding velocity and normal contact pressure, and the sticking stiffness may be different in each horizontal direction, or change as a function of the deformation history [6]. Figure 5.10 shows the force-velocity relationship of the oil dampers, as determined from the experiment and finite element model. Still, the FEM predictions of peak force and peak displacement are similar to the corresponding experimental values.

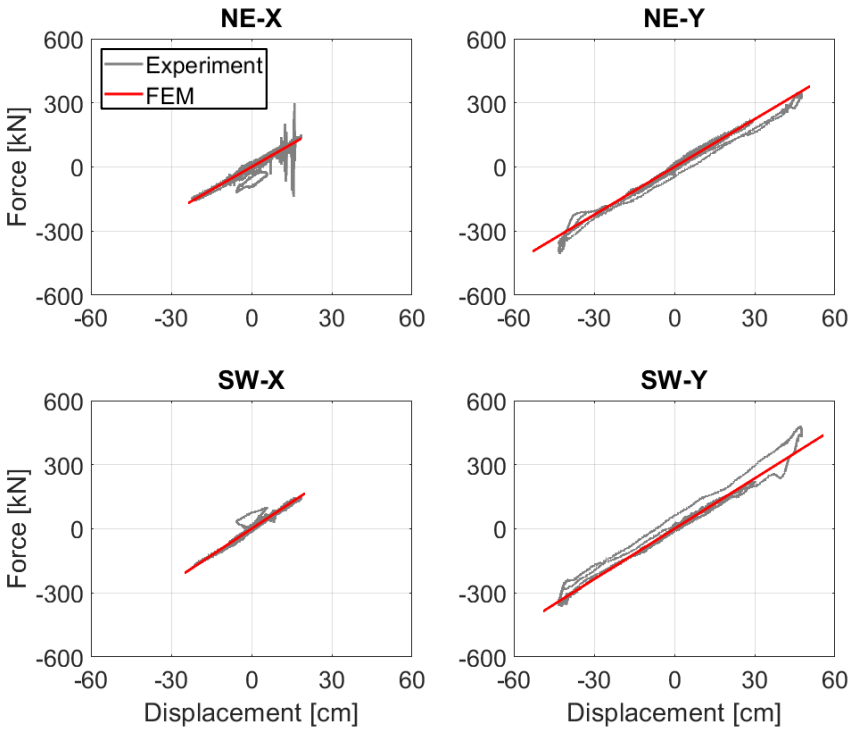

Figure 5.8. Rubber bearing hysteresis.

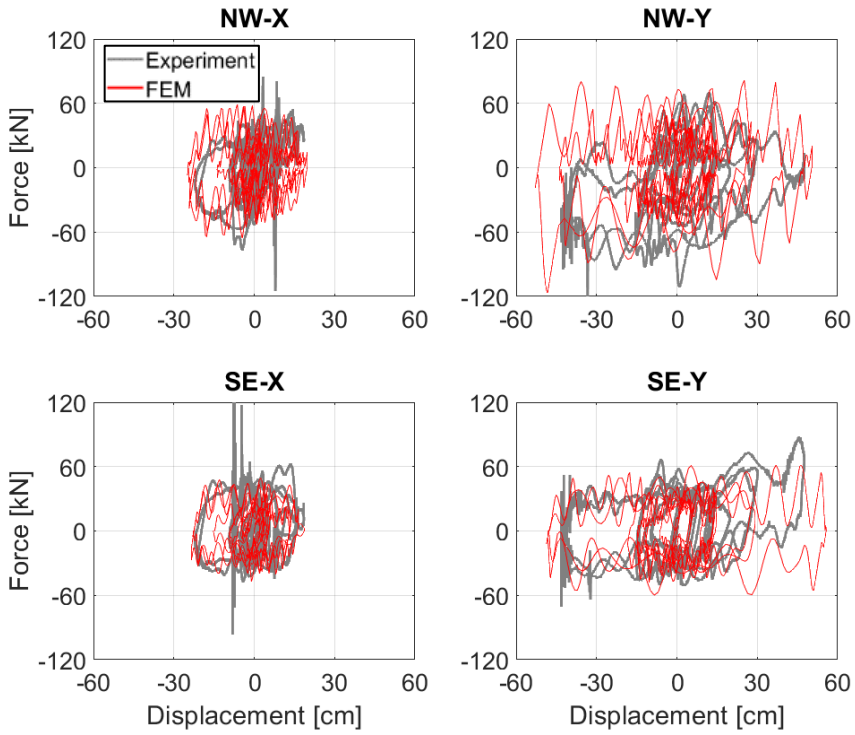

Figure 5.9. Slider bearing hysteresis.

Figures 5.10 and 5.11 show, respectively, the force-displacement and force-velocity relationship of the oil dampers. The experimental data indicate that the oil dampers have a small degree of nonlinearity. That is, the relationship between damping force and velocity is not exactly linear. Furthermore, the damping forces do not descend on the same velocity branch on which they ascended due to friction and other nonlinearities in their behavior that are not modeled here. Nevertheless, the FEM predictions correlate well with the measured response, so the linear viscous representation of the oil dampers is considered sufficient in this case.

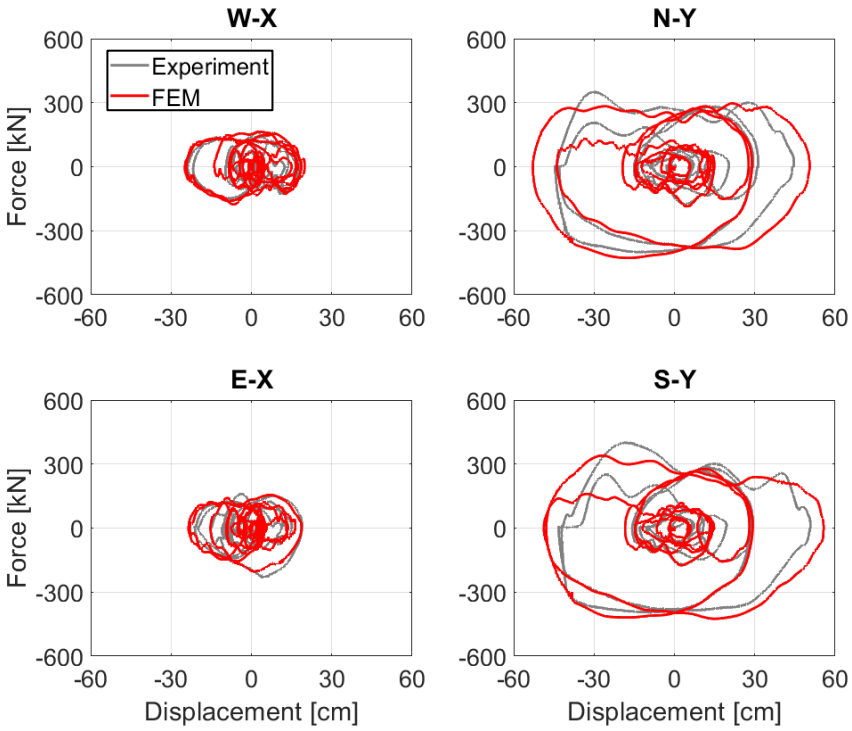

Figure 5.10. Oil damper hysteresis.

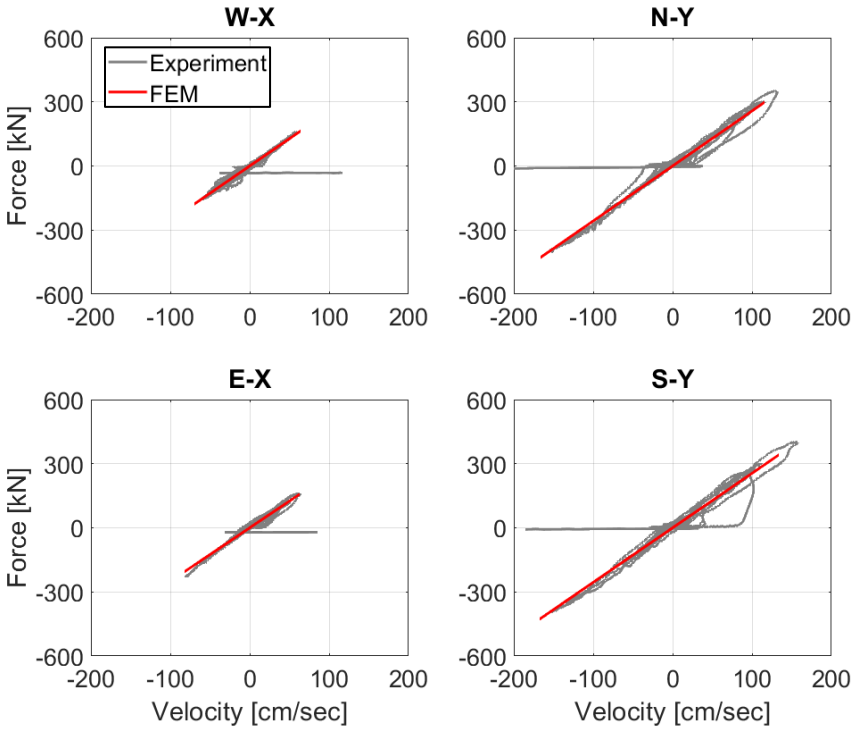

Figure 5.11. Force-velocity behavior of the oil dampers.

Figure 5.12 shows the floor acceleration time histories in both horizontal directions (i.e. X and Y). Both the experimental data and the ABAQUS model indicate that three impacts happen in the Y direction, at approximately 5.75 sec, 6.79 sec, and 8.02 sec. The first impact occurred at the west walls, followed by successive rebound impacts to the east and west walls. Furthermore, although no impacts occurred in the X direction (experiment or FEM), the X-direction accelerations do show a sudden increase in magnitude when the first impact occurs. This is due to geometric asymmetry in the building model, which induces torsional vibrations. Besides correctly predicting the number of impacts, the ABAQUS model correlates well with the experimental data. In general, the FEM predictions overestimate the peak accelerations during impact, but otherwise correctly determine when and where the impacts occur.

Figure 5.13 plots the horizontal displacement time histories for all floors of the building model. In the experiment and finite element model, displacements are computed relative to the moving ground. FEM displacements are reported from a node at the SW corner of each floor, to coincide with available measurements. Predicted displacements in the X and Y directions are in generally good agreement with the experiment, but visible departures from the measured response are visible, particularly during impact. Displacement errors near the time of impact can be attributed to the approximate representation of the moat walls and modeling of the contact interface. The predicted base displacement in the Y direction, for example, is greater than the corresponding measured displacement. In this case, the moat walls are too compliant, and allow greater displacements than what was measured. These errors carry through to the interstory drift time histories, shown in Figure 5.14. Interstory drifts predicted by ABAQUS correlate well with the experimental measurements, but underestimate the peak values that occur during impact.

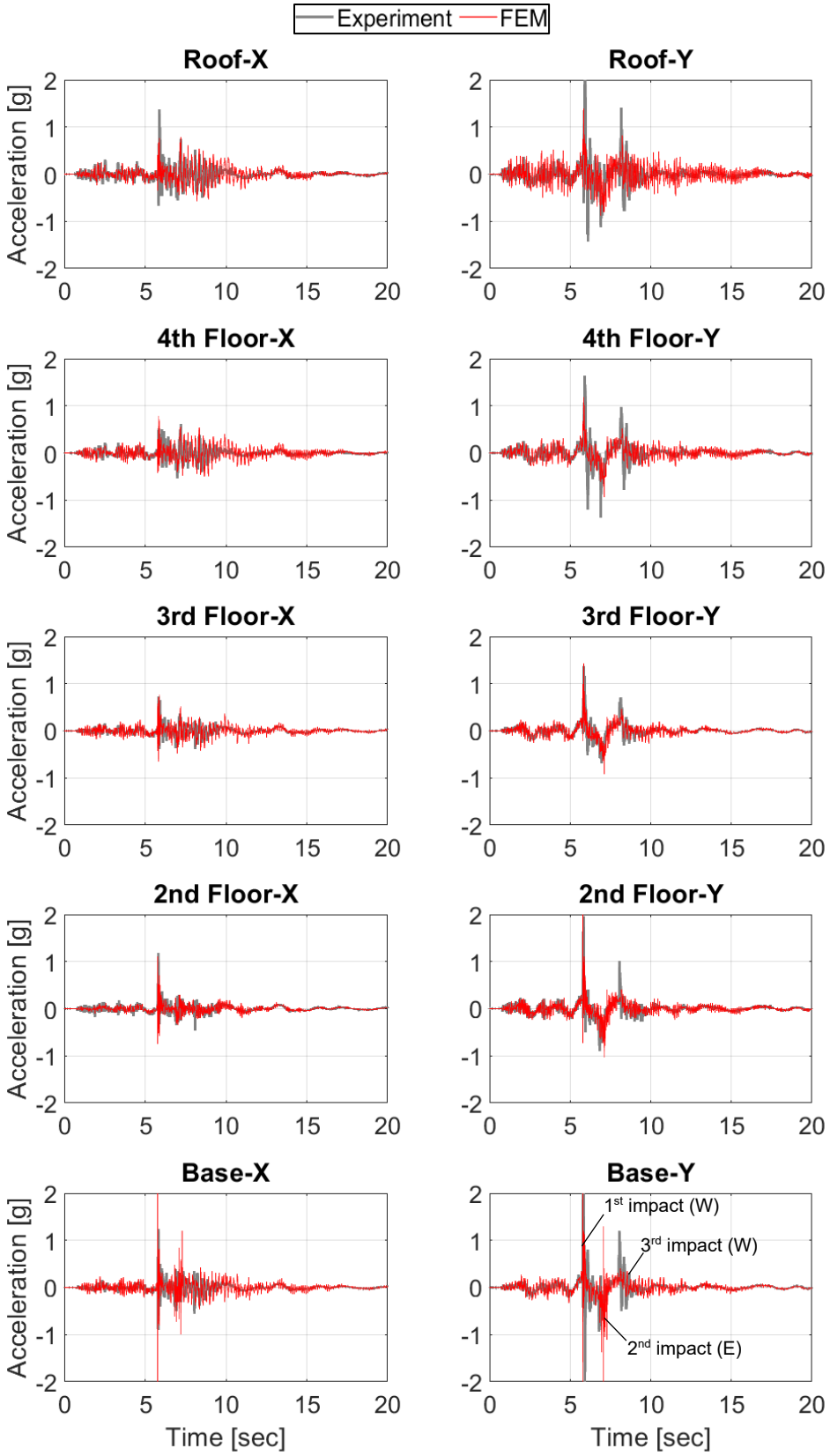

Figure 5.12. Horizontal floor acceleration time histories.

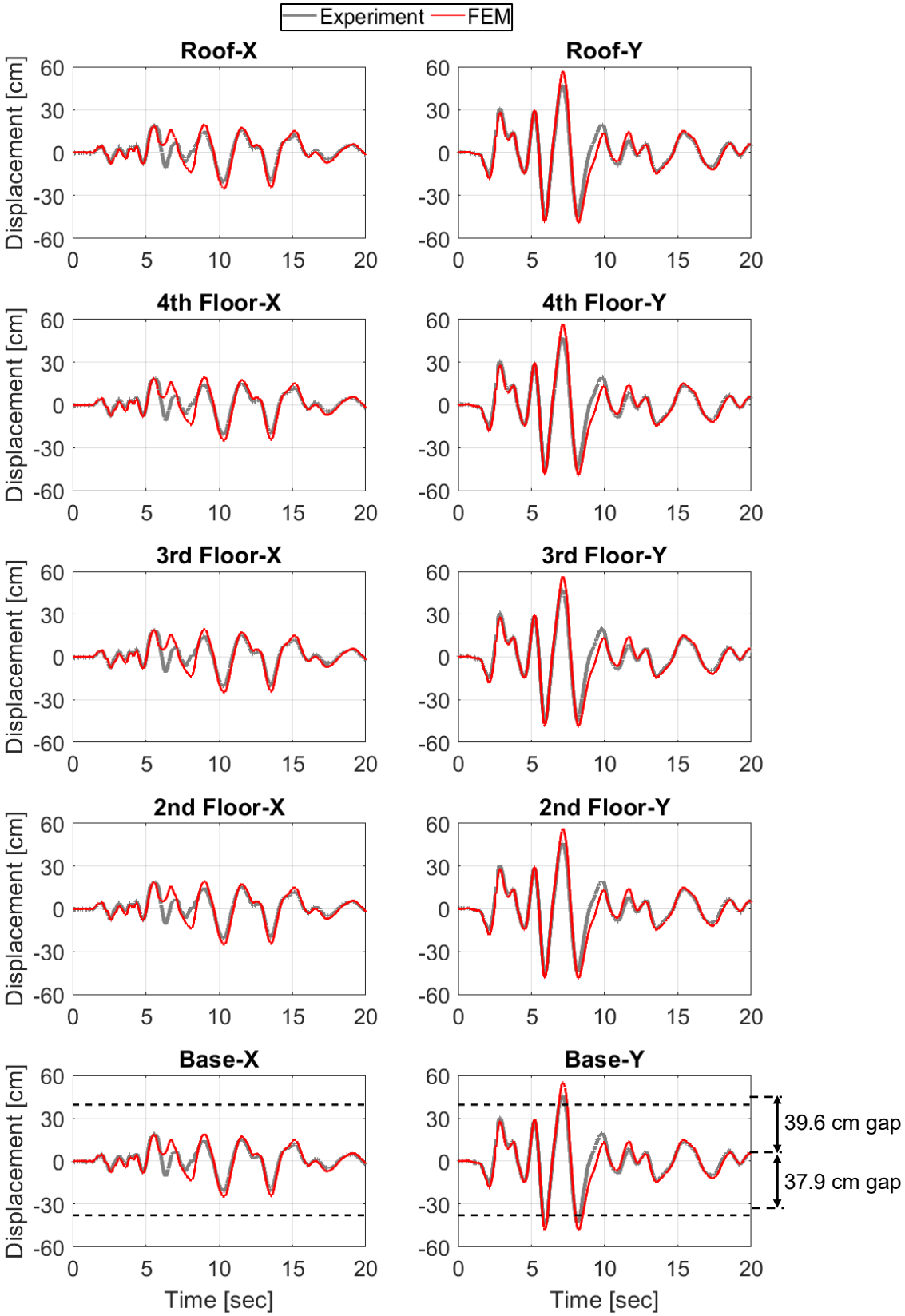

Figure 5.13. Horizontal floor displacement time histories.

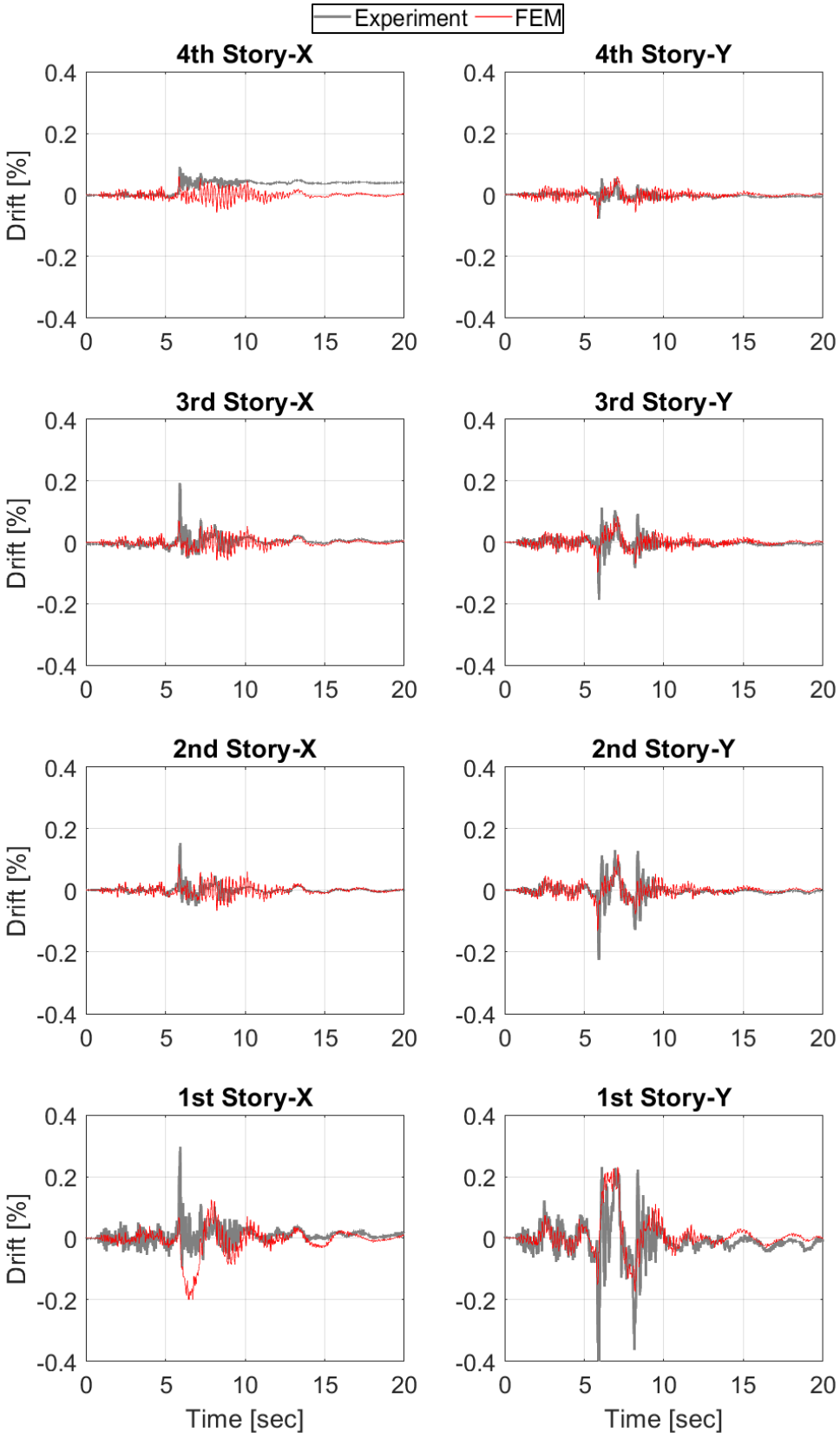

Figure 5.14. Interstory drift time histories.

The experimental measurements show a residual drift in the X direction of the 4th story (see the top-left of Figure 5.14). There was no evident yielding or damage in the building, however, so this is likely a minor instrumentation error. In both the experimental measurements and FEM predictions, computation of interstory drifts are sensitive to the location at which displacements are reported. As previously stated, displacements in this study are reported from a single location at the SW corner of each floor. Different interstory drifts should be expected if displacements are computed at a different location, or if displacements are averaged across multiple locations.

Figure 5.15 plots acceleration time histories of the four BW40 moat walls, which experienced impact in the Y direction during seismic shaking. As previously stated, the base mat accelerations indicate three impact events, at around 5.75 sec, 6.79 sec, and 8.02 sec. Moat wall accelerations confirm as much, but also enhance the understanding of exactly how the impacts occurred. The first impact occurred at the western walls, and, as evidenced by the experimental measurements and FEM predictions, the base mat collided with the NW and SW walls at almost the same exact time. That is, the collision occurred with minimal twisting about the Z axis. Following this, the base mat rebounded and collided with the eastern walls, again, at practically the same time. The third and final impact, however, was clearly influenced by torsional vibrations. The SW accelerometer signal shows a sudden jump in acceleration at 8.02 sec, but the increase is not as pronounced in the NW sensor, implying that the final collision trajectory was skewed towards the SW wall. In the ABAQUS simulation, the base mat did not contact the NW wall at all, and the NW wall experienced no acceleration jump at 8.02 sec. This suggests that the ABAQUS model underwent more significant rotations about the Z axis than the experimental model.

Accelerometer signals for the NW wall and, to a lesser extent, the SE wall, display a non-physical offset that occurs after impact. In the NW wall, the accelerometer signal offsets by

approximately 1 g following the first impact. The SE wall offset by a smaller amount – roughly 0.3g – after the 2nd impact. Besides these instances of accelerometer offset, the ABAQUS model accurately predicts the moat wall accelerations.

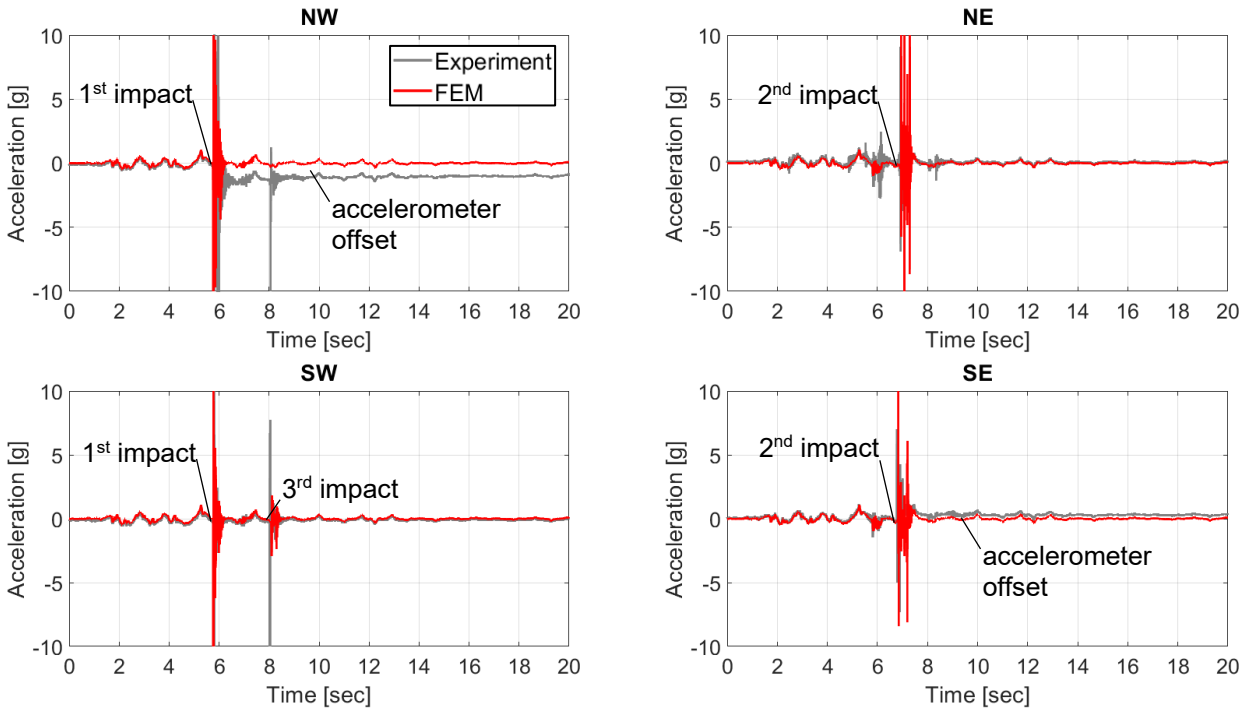

Figure 5.15. Moat wall acceleration time histories (Y direction).

Figure 5.16 shows the moat wall displacement time histories, which confirms earlier discussions and observations. The simulated moat walls are more flexible than in the experiment, and overestimate displacements by as much as 11 cm, roughly 400% of the corresponding experimental measurement. The moat walls were modeled based on nominal material properties and the observed experimental failure mode of the wall was not captured by the model, as shown in Figure 5.17. Given the accuracy of the floor acceleration and displacement responses, however, this implies that the superstructure response is insensitive to the moat wall deformation. During the third and final impact, measured displacements in the NW wall are smaller than those in the

SW wall, indicating once again that the impact direction was skewed towards the SW wall. The simulated NW wall does not deform after the first impact, indicating, as before, that the third impact in the ABAQUS model only affected the SW wall.

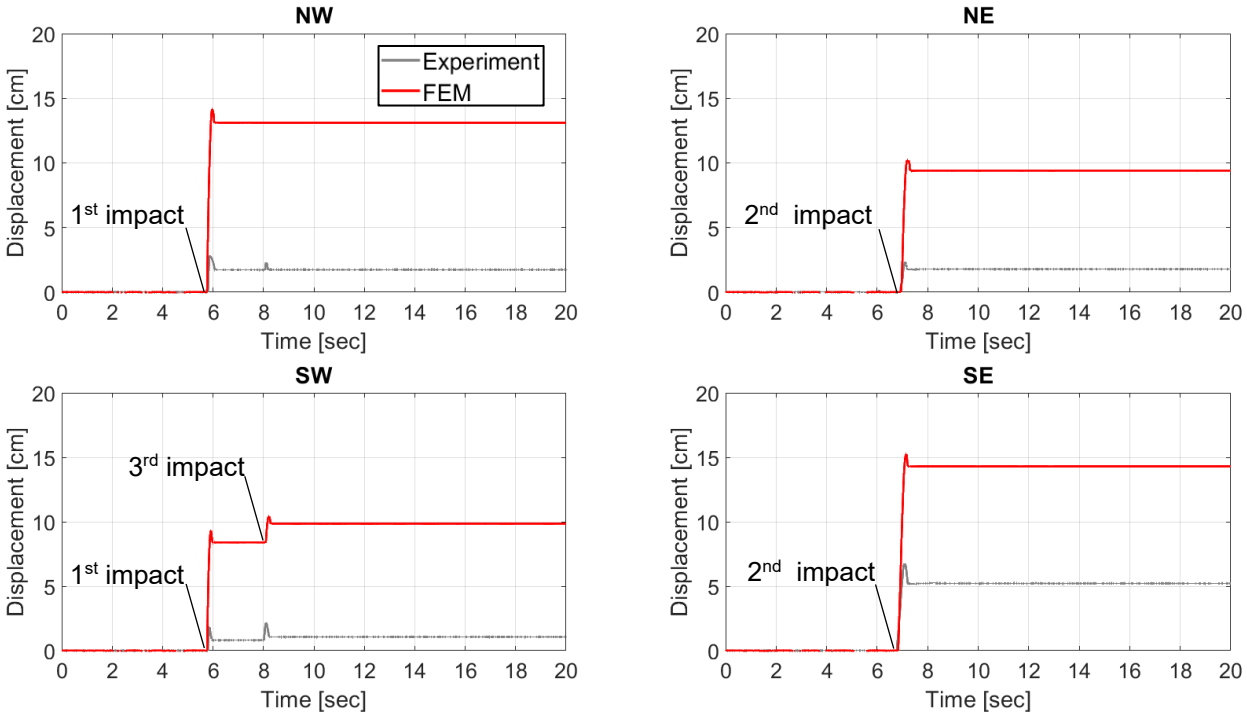

Figure 5.16. Moat wall displacement time histories (Y direction).

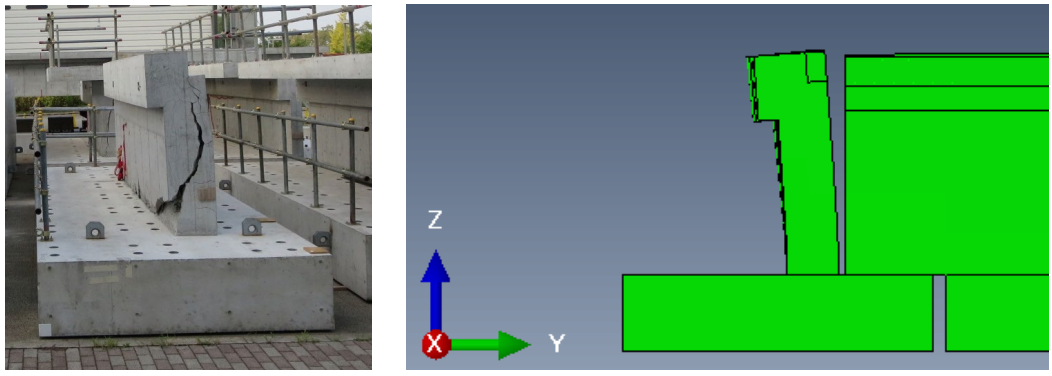

Figure 5.17. During the experiment, the moat walls failed in shear (left). The ABAQUS model (right) exhibited flexural failure, with inelastic hinging at the base (deformations shown at 1:1 scale).

5.5. Conclusions

First and foremost, this chapter shows that it is possible to predict the structural response of a base-isolated building subjected to seismically-induced moat wall pounding. The numerical studies shown here are promising for the future of advanced dynamic modeling of civil structures. Similar to the results of chapter 4, capturing the detailed local response of the impact remains a challenge.

Chapters 4 and 5 chiefly differ in the scale of their respective simulations. Chapter 4 attempted to predict moat wall pounding forces by recreating dynamic conditions just before impact, and then simulating the response only over the contact duration. Chapter 5, on the other hand, analyzed a complete dynamic system over an entire earthquake record. The result: quantitatively accurate results were achieved in chapter 5, but not in chapter 4. Clearly, history-dependent interactions between the superstructure, moat wall, and isolation layer, over the duration of an entire earthquake, are critical for accurate moat wall pounding simulation.

These studies also show that the overall global seismic performance of the structure may not be sensitive to the behavior and modeling of the moat walls. Moat wall accelerations, which strongly correlate with impact forces, exhibited peak values between 5- 10 g in the experiment and in the numerical model. Still, the superstructure deformation was relatively insensitive to these high-magnitude dynamic loads. Still, the impacts did induce relatively high floor accelerations (e.g. 1-2 g). Moat wall pounding forces may not damage the superstructure, then, but can still be hazardous to acceleration-sensitive nonstructural components. Furthermore, the ABAQUS model overestimated moat wall displacements by 100-400%, but still accurately predicted floor accelerations and displacements. Further studies are needed to explore modeling options for the moat wall and impact interface that may better simulate the experimental results.

References

1. Hibbit HD, Karlsson BI, Sorensen EP. ABAQUS user manual, version 6.14. *Simulia* 2014. DOI: 10.1577/T09-122.1.

2. Sasaki T, Sato E, Fukuyama K, Kajiwara K. Enhancement of Base-Isolation Based on E-Defense Full- Scale Shake Table Experiments : Dynamic Response of Base- Isolated Building Under Impact Due To Pounding 2017; **4082**(Abstract ID).

3. Tianhao Y, Johnson EA, Brewick PT, Christenson RE. Modeling and model updating of a full-scale experimental base-isolated building. *Structural Control and Health Monitoring (Under Review)* 2020.

4. Simulia. Abaqus 6.11 Theory Manual. *Providence, RI, USA: DS SIMULIA Corp* 2017.

5. Mander JB, Priestly MJN, Park R. Theoretical stress-strain model for confined concrete. *Journal of Structural Engineering* 1988; **114**(8): 1804–1826.

6. Brewick PT, Johnson EA, Sato E, Sasaki T. Modeling the Dynamic Behavior of Isolation Devices in a Non-homogeneous Base-Isolation Layer 2021; **146**(11): 1–42. DOI: 10.1061/(ASCE)EM.1943-7889.0001774.

Chapter 6 Theoretical Background of Nonlinear Hurty/Craig-Bampton Superelements with Interface Reduction

6.1. Introduction

Modern numerical models of contacting structures demand accurate resolution of interface dynamics, which strongly affect the system-level stiffness and damping. The high-resolution finite element meshes necessary to resolve inter-component contact tend to be computationally expensive, particularly when the analyst is interested in response time histories. The Hurty/Craig-Bampton (HCB) transformation [1–3] is a widely-used method of component mode synthesis (CMS), which reduces the interior portion of a finite element model while retaining all interface degrees of freedom (DOF). For large-scale finite element models, the number of interface DOF may still be large – on the order of thousands of DOF, depending on the problem. In an effort to

further reduce the size of models with many (potentially nonlinear) interface DOF, researchers have devised so-called nonlinear interface reduction (NLIR) methods [4–10].

Recent NLIR efforts include adaptive microslip projection (AMP) [7], which computes mode shapes from specially-chosen linear systems that exist in between fully stuck and fully slipping contact states. The Jacobian projection technique applies specific contact boundary conditions, and then computes a reduction basis by differentiating the contact forces with respect to nodal displacements [9]. So-called trial vector derivatives were employed by Pichler et al. [10] to reduce the nonlinear interface DOF of a friction bar and piston rod bearing cap. Many of these approaches suffer from one or more of the following drawbacks: (1) limited to frequency domain analysis, (2) strictly require the full-order finite element model for interface basis generation, or (3) ignore detailed kinematics at the interfaces. In many cases, the time-domain response of the system may be a primary concern. Additionally, the full-order model may be too large for practical computation of interface basis vectors, or it may contain proprietary information that cannot be transferred between agencies.

Chapter 7 of this dissertation derives novel interface reduction techniques that overcome the limitations of previous studies. This chapter lays the theoretical groundwork for those interface reduction methods. First, Section 6.2 derives the HCB transformation and discusses how the HCB superelement is formed. Section 6.3 outlines a generic mathematical formulation for projection-based interface reduction. Section 6.4 details a new three-dimensional element used to model the contacting surfaces. Section 6.5 shows how a HCB superelement is preloaded using explicit dynamics. Finally, Section 6.6 unifies the chapter and shows how to conduct a nonlinear dynamic time history simulation for a coupled HCB superelement with interface reduction.

6.2. Hurty/Craig-Bampton Transformation

Consider a structure made of multiple linear elastic components, with all nonlinearities concentrated at discrete contact interfaces. Finite element discretization of the k^{th} substructure yields the following semi-discrete equation.

$$\mathbf{M}_k\ddot{\mathbf{u}}_k(\mathrm{t}) + \mathbf{K}_k\mathbf{u}_k(\mathrm{t}) + \mathbf{f}_k^{\mathrm{c}}(\mathbf{u}_k(\mathrm{t})) = \mathbf{f}_k^{\mathrm{ext}}(\mathrm{t}) \tag{6.1}$$

Equation (6.1) is semi-discrete because it has been discretized in space using the finite element method, but still depends on a continuous time variable t. $\mathbf{M}_k$ and $\mathbf{K}_k$ are the mass and stiffness matrices of the k^{th} substructure, respectively. The time-dependent displacement vector is denoted by $\mathbf{u}_k(\mathrm{t})$, and each overdot represents a differentiation with respect to time. Displacement-dependent contact forces are represented by $\mathbf{f}_k^{\mathrm{c}}\big(\mathbf{u}_k(\mathrm{t})\big)$, and $\mathbf{f}_k^{\mathrm{ext}}(\mathrm{t})$ is the external force vector. Equation (6.1) can be partitioned into $n_{i,k}$ interior DOF (i) and $n_{b,k}$ boundary DOF (b) as

$$\begin{bmatrix}\mathbf{M}_{ii,k} & \mathbf{M}_{ib,k}\\ \mathbf{M}_{bi,k} & \mathbf{M}_{bb,k}\end{bmatrix}\begin{Bmatrix}\ddot{\mathbf{u}}_{i,k}(\mathrm{t})\\ \ddot{\mathbf{u}}_{b,k}(\mathrm{t})\end{Bmatrix} + \begin{bmatrix}\mathbf{K}_{ii,k} & \mathbf{K}_{ib,k}\\ \mathbf{K}_{bi,k} & \mathbf{K}_{bb,k}\end{bmatrix}\begin{Bmatrix}\mathbf{u}_{i,k}(\mathrm{t})\\ \mathbf{u}_{b,k}(\mathrm{t})\end{Bmatrix} + \begin{Bmatrix}\mathbf{0}\\ \mathbf{f}_{b,k}^{\mathrm{c}}\big(\mathbf{u}_{b,k}(t)\big)\end{Bmatrix} = \begin{Bmatrix}\mathbf{f}_{i,k}^{\mathrm{ext}}(\mathrm{t})\\ \mathbf{f}_{b,k}^{\mathrm{ext}}(\mathrm{t})\end{Bmatrix} \tag{6.2}$$

Note that the contact forces only act on the boundary DOF.

The Hurty/Craig-Bampton (HCB) transformation [1–3] employs fixed-interface (FI) eigenmodes and static constraint modes. The FI modes for substructure k are computed from

$$\left[\mathbf{K}_{ii,k} - \left(\omega_{j,k}^{\mathrm{FI}}\right)^2\mathbf{M}_{ii,k}\right]\boldsymbol{\phi}_{j,k}^{\mathrm{FI}} = \mathbf{0} \quad , \quad j = 1, 2, \dots, n_{FI,k} \tag{6.3}$$

where $\omega_{j,k}^{\mathrm{FI}}$ is the j^{th} FI frequency, $\boldsymbol{\phi}_{j,k}^{\mathrm{FI}}$ is the corresponding FI mode shape vector, and $n_{FI,k}$ is the number of FI modes retained for the k^{th} substructure. In general, the FI mode set is significantly truncated for each substructure, i.e. $n_{FI,k} \ll n_{i,k}$. Each FI mode is assembled into the FI matrix as

$$\boldsymbol{\Phi}_k^{\mathrm{FI}} = \begin{bmatrix}\boldsymbol{\phi}_{1,k}^{\mathrm{FI}} & \boldsymbol{\phi}_{2,k}^{\mathrm{FI}} & \cdots & \boldsymbol{\phi}_{n_{FI},k}^{\mathrm{FI}}\end{bmatrix} \tag{6.4}$$

Next, the constraint modes of substructure k are given by

$$\boldsymbol{\Psi}_k = -\mathbf{K}_{ii,k}^{-1}\mathbf{K}_{ib,k} \tag{6.5}$$

Finally, the k^{th} HCB transformation matrix is

$$\mathbf{T}_k = \begin{bmatrix} \boldsymbol{\Phi}_k^{\mathrm{FI}} & \boldsymbol{\Psi}_k \\ \mathbf{0} & \mathbf{I} \end{bmatrix} \tag{6.6}$$

This matrix maps the full-order coordinates $\mathbf{u}_k(\mathrm{t})$ to HCB coordinates $\bar{\mathbf{u}}_k(\mathrm{t})$ as

$$\mathbf{u}_k(\mathrm{t}) = \mathbf{T}_k\bar{\mathbf{u}}_k(\mathrm{t}) \tag{6.7a}$$

$$\begin{Bmatrix} \mathbf{u}_{i,k}(\mathrm{t}) \\ \mathbf{u}_{b,k}(\mathrm{t}) \end{Bmatrix} = \begin{bmatrix} \boldsymbol{\Phi}_k^{\mathrm{FI}} & \boldsymbol{\Psi}_k \\ \mathbf{0} & \mathbf{I} \end{bmatrix} \begin{Bmatrix} \mathbf{q}_{i,k}(\mathrm{t}) \\ \mathbf{u}_{b,k}(\mathrm{t}) \end{Bmatrix} \tag{6.7b}$$

where $\mathbf{q}_{i,k}(t)$ is the vector of FI modal coordinates for substructure k. The corresponding HCB system matrices and force vectors are

$$\bar{\mathbf{M}}_k = \mathbf{T}_k{}^{\mathrm{T}}\mathbf{M}_k\mathbf{T}_k = \begin{bmatrix} \mathbf{I} & \bar{\mathbf{M}}_{ib,k} \\ \bar{\mathbf{M}}_{bi,k} & \bar{\mathbf{M}}_{bb,k} \end{bmatrix} \quad , \quad \bar{\mathbf{K}}_k = \mathbf{T}_k{}^{\mathrm{T}}\mathbf{K}_k\mathbf{T}_k = \begin{bmatrix} \left(\boldsymbol{\Omega}_k^{\mathrm{FI}}\right)^2 & \mathbf{0} \\ \mathbf{0} & \bar{\mathbf{K}}_{bb,k} \end{bmatrix} \tag{6.8a}$$

$$\bar{\mathbf{f}}_k^{\mathrm{c}}(\bar{\mathbf{u}}_k(\mathrm{t})) = \mathbf{T}_k^{\mathrm{T}}\mathbf{f}_k^{\mathrm{c}}(\mathbf{u}_k(\mathrm{t})) = \begin{Bmatrix} \mathbf{0} \\ \mathbf{f}_{b,k}^{\mathrm{c}}\left(\mathbf{u}_{b,k}(\mathrm{t})\right) \end{Bmatrix} \quad , \quad \bar{\mathbf{f}}_k^{\mathrm{ext}}(t) = \mathbf{T}_k^{\mathrm{T}}\mathbf{f}_k^{\mathrm{ext}}(\mathrm{t}) = \begin{Bmatrix} \mathbf{p}_{i,k}^{\mathrm{ext}}(\mathrm{t}) \\ \mathbf{f}_{b,k}^{\mathrm{ext}}(\mathrm{t}) \end{Bmatrix} \tag{6.8b}$$

where $\mathbf{p}_{i,k}^{\mathrm{ext}}(\mathrm{t})$ is the vector of modal external forces applied to the interior DOF partition, and an overbar denotes a quantity in HCB coordinates. $\boldsymbol{\Omega}_k^{\mathrm{FI}}$ is the diagonal matrix of FI eigenfrequencies for substructure k, i.e.

$$\boldsymbol{\Omega}_k^{\mathrm{FI}} = \begin{bmatrix} \omega_{1,k}^{\mathrm{FI}} & & & \\ & \omega_{2,k}^{\mathrm{FI}} & & \\ & & \ddots & \\ & & & \omega_{n_{FI},k}^{\mathrm{FI}} \end{bmatrix} \tag{6.9}$$

Note that, in Equation (6.8a), the $i-i$ partition of the HCB component mass matrix is equal to the $n_{FI,k} \times n_{FI,k}$ identity matrix. This is because the FI modes contained in $\boldsymbol{\Phi}_k^{\mathrm{FI}}$ are mass-normalized

during construction. Considering the orthogonality of the FI modes with respect to $\mathbf{M}_{ii,k}$ and $\mathbf{K}_{ii,k}$, it is true that, for j = 1, 2, …, $n_{FI,k}$ and l = 1, 2, …, $n_{FI,k}$,

$$\left(\boldsymbol{\phi}_{j,k}^{\mathrm{FI}}\right)^{\mathrm{T}}\mathbf{M}_{ii,k}\boldsymbol{\phi}_{l,k}^{\mathrm{FI}} = 1 \tag{6.10a}$$

$$\left(\boldsymbol{\phi}_{j,k}^{\mathrm{FI}}\right)^{\mathrm{T}}\mathbf{K}_{ii,k}\boldsymbol{\phi}_{j,k}^{\mathrm{FI}} = \left(\omega_{j,k}^{\mathrm{FI}}\right)^{2} \tag{6.10b}$$

when $j = l$, and

$$\left(\boldsymbol{\phi}_{j,k}^{\mathrm{FI}}\right)^{\mathrm{T}}\mathbf{M}_{ii,k}\boldsymbol{\phi}_{l,k}^{\mathrm{FI}} = \left(\boldsymbol{\phi}_{j,k}^{\mathrm{FI}}\right)^{\mathrm{T}}\mathbf{K}_{ii,k}\boldsymbol{\phi}_{l,k}^{\mathrm{FI}} = 0 \tag{6.11}$$

when $j \neq l$. The $i - b$ partition of $\overline{\mathbf{K}}_k$ is equal to a zero matrix because

$$\begin{aligned}
\overline{\mathbf{K}}_{ib,k} &= \left(\boldsymbol{\Phi}_{k}^{\mathrm{FI}}\right)^{\mathrm{T}}\left(\mathbf{K}_{ib,k} + \mathbf{K}_{ii,k}\boldsymbol{\Psi}_{k}\right) \\
&= \left(\boldsymbol{\Phi}_{k}^{\mathrm{FI}}\right)^{\mathrm{T}}\left[\mathbf{K}_{ib,k} + \mathbf{K}_{ii,k}\left(-\mathbf{K}_{ii,k}^{-1}\mathbf{K}_{ib,k}\right)\right] \\
&= \left(\boldsymbol{\Phi}_{k}^{\mathrm{FI}}\right)^{\mathrm{T}}\left(\mathbf{K}_{ib,k} - \mathbf{K}_{ii,k}\mathbf{K}_{ii,k}^{-1}\mathbf{K}_{ib,k}\right) \\
&= \left(\boldsymbol{\Phi}_{k}^{\mathrm{FI}}\right)^{\mathrm{T}}\left(\mathbf{K}_{ib,k} - \mathbf{K}_{ib,k}\right) \\
&= \mathbf{0}
\end{aligned} \tag{6.12}$$

By symmetry, the $b - i$ partition of $\overline{\mathbf{K}}_k$ is also a zero matrix, i.e.

$$\overline{\mathbf{K}}_{bi,k} = \left(\overline{\mathbf{K}}_{ib,k}\right)^{\mathrm{T}} = \mathbf{0} \tag{6.13}$$

The HCB procedure can be repeated at every substructure for k = 1, 2, …, n_{SS}, where n_{SS} is the number of substructures. All reduced substructure system matrices and force vectors are then assembled using an appropriate mapping matrix $\mathbf{L}_k$, i.e.

$$\overline{\mathbf{M}} = \sum_{k=1}^{\mathrm{n_{ss}}}\mathbf{L}_k^{\mathrm{T}}\overline{\mathbf{M}}_k\mathbf{L}_k = \begin{bmatrix}\mathbf{I} & \overline{\mathbf{M}}_{ib} \\ \overline{\mathbf{M}}_{bi} & \overline{\mathbf{M}}_{bb}\end{bmatrix} \quad , \quad \overline{\mathbf{K}} = \sum_{k=1}^{\mathrm{n_{ss}}}\mathbf{L}_k^{\mathrm{T}}\overline{\mathbf{K}}_k\mathbf{L}_k = \begin{bmatrix}(\boldsymbol{\Omega}^{\mathrm{FI}})^2 & \mathbf{0} \\ \mathbf{0} & \overline{\mathbf{K}}_{bb}\end{bmatrix} \tag{6.14a}$$

$$\bar{\mathbf{f}}^{\mathrm{c}}(\bar{\mathbf{u}}(\mathrm{t})) = \sum_{k=1}^{\mathrm{n_{ss}}} \mathbf{L}_k^{\mathrm{T}} \bar{\mathbf{f}}_k^{\mathrm{c}}(\bar{\mathbf{u}}_k(\mathrm{t})) = \begin{Bmatrix} \mathbf{0} \\ \mathbf{f}_b^{\mathrm{c}}(\mathbf{u}_b(\mathrm{t})) \end{Bmatrix} \quad , \quad \bar{\mathbf{f}}^{\mathrm{ext}}(\mathrm{t}) = \sum_{k=1}^{\mathrm{n_{ss}}} \mathbf{L}_k^{\mathrm{T}} \bar{\mathbf{f}}_k^{\mathrm{ext}}(\mathrm{t}) = \begin{Bmatrix} \mathbf{p}_i^{\mathrm{ext}}(\mathrm{t}) \\ \mathbf{f}_b^{\mathrm{ext}}(\mathrm{t}) \end{Bmatrix} \quad (6.14b)$$

where $\bar{\mathbf{u}}(\mathrm{t})$ is the displacement vector for the coupled HCB superelement, partitioned as

$$\bar{\mathbf{u}}(\mathrm{t}) = \begin{Bmatrix} \mathbf{q}_i(\mathrm{t}) \\ \mathbf{u}_b(\mathrm{t}) \end{Bmatrix} \quad (6.15)$$

This new displacement vector contains all FI modal DOF within $\mathbf{q}_i(t)$ and all boundary DOF within $\mathbf{u}_b(t)$. $\boldsymbol{\Omega}^{\mathrm{FI}}$ is a diagonal matrix that contains the FI eigenvalues of all substructures:

$$\boldsymbol{\Omega}^{\mathrm{FI}} = \begin{bmatrix} \boldsymbol{\Omega}_1^{\mathrm{FI}} & & & \\ & \boldsymbol{\Omega}_2^{\mathrm{FI}} & & \\ & & \ddots & \\ & & & \boldsymbol{\Omega}_{n_{ss}}^{\mathrm{FI}} \end{bmatrix} \quad (6.16)$$

At this stage, the number of DOF in the system has been greatly reduced, but only within the interior partition. All interface DOF are physically intact. In many cases, the size of the model may still be too large, with thousands or tens of thousands of interface DOF slowing down the simulations. The following section will introduce the concept of interface reduction, which applies a secondary reduction on the HCB model in order to decrease the overall model size.

6.3. Conceptual Interface Reduction and Corresponding Equations of Motion

The interface reduction methods shown here operate on a pre-compiled HCB superelement, which has modal DOF on the interior and physical DOF at the component boundaries, given by $\mathbf{q}_i(\mathrm{t})$ and $\mathbf{u}_b(\mathrm{t})$, respectively. In essence, interface reduction schemes seek a small modal basis on which the interface DOF are projected, to provide the desired model order reduction. Schematically, this is stated as

$$\begin{Bmatrix}\mathbf{q}_i(\mathrm{t})\\ \mathbf{u}_b(\mathrm{t})\end{Bmatrix} \xrightarrow{interface\ reduction} \begin{Bmatrix}\mathbf{q}_i(\mathrm{t})\\ \mathbf{q}_b(\mathrm{t})\end{Bmatrix} \tag{6.17}$$

On the righthand side of this expression, the interface DOF are now represented by some modal coordinate vector $\mathbf{q}_b(\mathrm{t})$. The size of $\mathbf{q}_b(\mathrm{t})$ will depend on how many interface modes are retained in the reduction basis. This is similar to the initial HCB transformation, but now the interior DOF are unchanged and the boundary DOF are reduced to a smaller modal subspace.

Ultimately, Equation (6.17) will take the form

$$\bar{\mathbf{u}}(\mathrm{t}) = \bar{\mathbf{T}}\bar{\bar{\mathbf{u}}}(\mathrm{t}) \tag{6.18}$$

As before, a single overbar denotes a quantity in HCB coordinates, and a double overbar denotes a quantity in interface-reduced (IR) coordinates. Therefore, $\bar{\mathbf{T}}$ is comprised of mode shapes computed in the parent HCB system. The exact contents of $\bar{\mathbf{T}}$ depend on the method in question, and its formulation is the key challenge of interface reduction.

A few numerical treatments must be applied to $\bar{\mathbf{T}}$ to ensure a well-conditioned IR model. First, each column of $\bar{\mathbf{T}}$ is divided by its Euclidean norm, such that $\bar{\mathbf{T}}$ becomes a matrix of unit vectors. Normalization ensures that the relative magnitudes of the columns of $\bar{\mathbf{T}}$ do not influence their modal participation factors. Following this, the normalized $\bar{\mathbf{T}}$ is replaced by its left singular vectors, as determined by the singular value decomposition (SVD). This guarantees that the columns of $\bar{\mathbf{T}}$ are linearly independent, which in turn guarantees a numerically stable IR model. The process of normalization and SVD in sequence is sometimes referred to as deflation.

Equation (6.18) takes the same form as Equation (6.7a): a kinematic quantity in the parent domain ($\mathbf{u}_k$ or $\bar{\mathbf{u}}$) can be recovered by pre-multiplying the corresponding quantity in the child domain ($\bar{\mathbf{u}}_k$ or $\bar{\bar{\mathbf{u}}}$) by a matrix that relates the two coordinate systems ($\mathbf{T}$ or $\bar{\mathbf{T}}$). Indeed, the analogy extends further, and the IR system matrices and force vectors are computed in the same way as Equation (6.8)

$$\bar{\bar{\mathbf{M}}} = \bar{\mathbf{T}}^{\mathrm{T}}\bar{\mathbf{M}}\bar{\mathbf{T}} \quad , \quad \bar{\bar{\mathbf{K}}} = \bar{\mathbf{T}}^{\mathrm{T}}\bar{\mathbf{K}}\bar{\mathbf{T}} \tag{6.19a}$$

$$\bar{\bar{\mathbf{f}}}^{\mathrm{c}}(\bar{\mathbf{T}}\bar{\bar{\mathbf{u}}}(\mathrm{t})) = \bar{\mathbf{T}}^{\mathrm{T}}\bar{\mathbf{f}}^{\mathrm{c}}(\bar{\mathbf{u}}(\mathrm{t})) \quad , \quad \bar{\bar{\mathbf{f}}}^{\mathrm{ext}}(\mathrm{t}) = \bar{\mathbf{T}}^{\mathrm{T}}\bar{\mathbf{f}}^{\mathrm{ext}}(\mathrm{t}) \tag{6.19b}$$

In general, $\bar{\bar{\mathbf{M}}}$ and $\bar{\bar{\mathbf{K}}}$ are full matrices. The lack of sparsity can reduce the effectiveness of IR models during time integration, particularly for explicit time-marching schemes that rely on some bandedness or diagonality in the system matrices. This issue is alleviated by applying a tertiary eigenvalue transformation to the IR system described by Equation (6.19). First, let n_{IR} be the number of DOF in the IR model. All n_{IR} eigenmodes of the IR system are computed as

$$\left(\bar{\bar{\mathbf{K}}} - \bar{\bar{\omega}}_j^2\bar{\bar{\mathbf{M}}}\right)\bar{\bar{\boldsymbol{\phi}}}_j = \mathbf{0} \quad , \quad j = 1, 2, \ldots, n_{IR} \tag{6.20}$$

where $\bar{\bar{\omega}}_j$ is the j^{th} IR eigenfrequency and $\bar{\bar{\boldsymbol{\phi}}}_j$ is its corresponding eigenmode. The IR eigenanalyses is computationally feasible because n_{IR} is generally a small number. All IR eigenmodes are assembled into an eigenmatrix as

$$\bar{\bar{\boldsymbol{\Phi}}} = \left[\bar{\bar{\boldsymbol{\phi}}}_1 \quad \bar{\bar{\boldsymbol{\phi}}}_2 \quad \cdots \quad \bar{\bar{\boldsymbol{\phi}}}_{n_{IR}}\right] \tag{6.21}$$

Each column of $\bar{\bar{\boldsymbol{\Phi}}}$ is normalized by the IR mass matrix $\bar{\bar{\mathbf{M}}}$. The IR transformation matrix ($\bar{\mathbf{T}}$) can be redefined as

$$\breve{\mathbf{T}} = \bar{\mathbf{T}}\bar{\bar{\boldsymbol{\Phi}}} \tag{6.22}$$

which maps HCB coordinates $\bar{\mathbf{u}}(\mathrm{t})$ to a new vector of IR coordinates $\breve{\bar{\mathbf{u}}}(\mathrm{t})$ via

$$\bar{\mathbf{u}}(\mathrm{t}) = \breve{\mathbf{T}}\breve{\bar{\mathbf{u}}}(\mathrm{t}) \tag{6.23}$$

The modal displacements contained in $\breve{\bar{\mathbf{u}}}(\mathrm{t})$ have the same accuracy as $\bar{\bar{\mathbf{u}}}(\mathrm{t})$ because all eigenmodes are retained in $\bar{\bar{\boldsymbol{\Phi}}}$. A new IR model, with sparse system matrices, is formed by $\breve{\mathbf{T}}$ as

$$\breve{\bar{\mathbf{M}}} = \breve{\mathbf{T}}^{\mathrm{T}}\bar{\mathbf{M}}\breve{\mathbf{T}} = \mathbf{I} \quad , \quad \breve{\bar{\mathbf{K}}} = \breve{\mathbf{T}}^{\mathrm{T}}\bar{\mathbf{K}}\breve{\mathbf{T}} = \bar{\bar{\boldsymbol{\Omega}}}^2 \tag{6.24a}$$

$$\breve{\bar{\mathbf{f}}}^{\mathrm{c}}\left(\breve{\mathbf{T}}\breve{\bar{\mathbf{u}}}(\mathrm{t})\right) = \breve{\mathbf{T}}^{\mathrm{T}}\bar{\mathbf{f}}^{\mathrm{c}}(\bar{\mathbf{u}}(\mathrm{t})) \quad , \quad \breve{\bar{\mathbf{f}}}^{\mathrm{ext}}(\mathrm{t}) = \breve{\mathbf{T}}^{\mathrm{T}}\bar{\mathbf{f}}^{\mathrm{ext}}(\mathrm{t}) \tag{6.24b}$$

Due to the mass-normalization of the IR eigenmodes, $\breve{\breve{\mathbf{M}}}$ is equal to the $n_{IR} \times n_{IR}$ identity matrix and $\breve{\breve{\mathbf{K}}}$ is equal to the square of $\bar{\bar{\mathbf{\Omega}}}$, a diagonal matrix of IR eigenfrequencies:

$$\bar{\bar{\mathbf{\Omega}}} = \begin{bmatrix} \bar{\bar{\omega}}_1 & & & \\ & \bar{\bar{\omega}}_2 & & \\ & & \ddots & \\ & & & \bar{\bar{\omega}}_{n_{IR}} \end{bmatrix} \tag{6.25}$$

The equations of motion in the IR system are

$$\breve{\breve{\ddot{\mathbf{u}}}}(t) + \bar{\bar{\mathbf{\Omega}}}^2 \breve{\breve{\mathbf{u}}}(t) + \breve{\breve{\mathbf{f}}}^{c}\left(\bar{\bar{\mathbf{T}}}\bar{\bar{\mathbf{u}}}(t)\right) = \breve{\breve{\mathbf{f}}}^{ext}(t) \tag{6.26}$$

Five different displacement coordinates have been presented thus far, corresponding to full-order finite element components ($\mathbf{u}_k$), the HCB components ($\bar{\mathbf{u}}_k$), the HCB superelement ($\bar{\mathbf{u}}$), the full-matrix IR model ($\bar{\bar{\mathbf{u}}}$), and the sparse-matrix IR model ($\breve{\breve{\mathbf{u}}}$). A schematic flow of the different coordinate systems is shown in Equation (6.27). Of these, only two are needed dynamic simulation: (1) the HCB superelement coordinates ($\bar{\mathbf{u}}$), which contain the physical interface displacements ($\mathbf{u}_b$) necessary for contact force computation; and (2) the sparse IR coordinates, which must satisfy Equation (6.26) at every timestep. A detailed look at how these two coordinate systems interact during a dynamic simulation is explained in Section 6.5.

$$\begin{Bmatrix} \mathbf{u}_k(t) \\ full-order \\ component \end{Bmatrix} \xrightarrow{\mathbf{T}_k} \begin{Bmatrix} \bar{\mathbf{u}}_k(t) \\ HCB \\ component \end{Bmatrix} \xrightarrow{\mathbf{L}_k} \underbrace{\begin{Bmatrix} \bar{\mathbf{u}}(t) \\ HCB \\ superelement \end{Bmatrix}}_{\substack{used\ for \\ contact\ force \\ computation}} \xrightarrow{\bar{\bar{\mathbf{T}}}} \begin{Bmatrix} \bar{\bar{\mathbf{u}}}(t) \\ full \\ IR \end{Bmatrix} \xrightarrow{\bar{\bar{\mathbf{\Phi}}}} \underbrace{\begin{Bmatrix} \breve{\breve{\mathbf{u}}}(t) \\ sparse \\ IR \end{Bmatrix}}_{\substack{used\ for \\ time-marching \\ algorithms}} \tag{6.27}$$

6.4. Three-Dimensional Time Domain Contact Elements

In this research work, interface forces are represented using node-to-node contact elements, with a scalar normal force $f_{N,j}(t)$ and 2×1 tangential contact force vector $\mathbf{f}_{T,j}(t)$. Every contact

element applies forces of equal magnitude and opposite direction on each side of the j^{th} node pair. The derivations shown here assume an interface with two contacting bodies. Contacting interfaces on the first and second bodies are denoted with superscript (1) and (2), respectively. Furthermore, it is assumed that the displacements are small enough that linear geometry holds, and nodal contact pairs do not change during dynamic loading.

The normal-direction gap for node pair j is computed as

$$g_{N,j}(t) = \left[x_{N,j}^{(1)} + u_{N,j}^{(1)}(t)\right] - \left[x_{N,j}^{(2)} + u_{N,j}^{(2)}(t)\right] \tag{6.28}$$

where $x_{N,j}^{(1)}$ and $x_{N,j}^{(2)}$ are the initial normal coordinates of node pair j for the first and second contacting bodies, respectively. Similarly, $u_{N,j}^{(1)}(t)$ and $u_{N,j}^{(2)}(t)$ are the normal displacements of bodies 1 and 2, respectively, at node pair j. Essentially, $g_{N,j}(t)$ represents the normal-direction overlap between the two contacting bodies at the j^{th} node pair, which is penalized [11] by a proportional contact force $f_{N,j}(t)$, as

$$f_{N,j}(t) = \begin{cases} k_N g_{N,j}(t) & , \quad g_{N,j}(t) < 0 \quad (contacting) \\ 0 & , \quad g_{N,j}(t) \geq 0 \quad (gapping) \end{cases} \tag{6.29}$$

where k_N is the normal contact stiffness, sometimes referred to as the penalty stiffness. This quantity is usually determined using an iterative procedure that minimizes nodal overlap (i.e. g_N), but ensures a numerically stable solution.

Tangential (i.e. frictional) contact is considered through the Yang-Menq model [12], shown schematically in Figure 6.1. This model includes a slider displacement vector $\mathbf{w}_j(t)$, stated in terms of its components as

$$\mathbf{w}_j(t) = \begin{Bmatrix} w_{T1,j}(t) \\ w_{T2,j}(t) \end{Bmatrix} \tag{6.30}$$

where subscripts T1 and T2 indicate the first and second tangential directions, respectively. Sticking behavior is governed by the tangential contact stiffness k_T, and slipping behavior is governed by the Coulomb slider with friction coefficient μ.

Zucca and Firrone developed a user-friendly version of the 2D Yang-Menq model that can be easily adapted to time-marching schemes [13]. Their adaptation assumed that, for a given advance in time for the time integration scheme, the joint is stuck. After computing the sticking force, the assumption is "tested" against a known slipping force. If the sticking force is greater than the cutoff force, then the initial assumption was wrong, and the node is actually slipping. Finally, the friction force is updated to reflect the slip state. Despite this more intuitive implementation, Zucca and Firrone limited their study to unidirectional friction. This study proposes an extension of the Zucca-Firrone methodology from 2D contact (one friction component) to 3D contact (two coupled friction components), henceforth referred to as the 3D time domain contact model, abbreviated TD3.

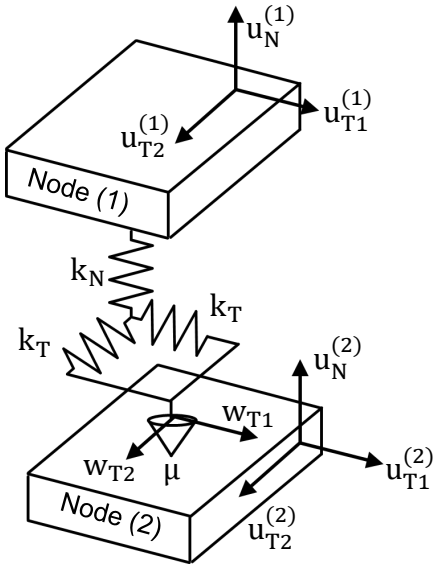

Figure 6.1. 3D contact model of Yang and Menq [12].

Firstly, the tangential gap vector is computed as

$$\mathbf{g}_{\mathrm{T},j}(\mathrm{t}) = \begin{Bmatrix} \mathrm{g}_{\mathrm{T1},j}(\mathrm{t}) \\ \mathrm{g}_{\mathrm{T2},j}(\mathrm{t}) \end{Bmatrix} = \begin{Bmatrix} \left[\mathrm{x}^{(1)}_{\mathrm{T1},j} + \mathrm{u}^{(1)}_{\mathrm{T1},j}(\mathrm{t})\right] - \left[\mathrm{x}^{(2)}_{\mathrm{T1},j} + \mathrm{u}^{(2)}_{\mathrm{T1},j}(\mathrm{t})\right] \\ \left[\mathrm{x}^{(1)}_{\mathrm{T2},j} + \mathrm{u}^{(1)}_{\mathrm{T2},j}(\mathrm{t})\right] - \left[\mathrm{x}^{(2)}_{\mathrm{T2},j} + \mathrm{u}^{(2)}_{\mathrm{T2},j}(\mathrm{t})\right] \end{Bmatrix} \tag{6.31}$$

As before, x refers to initial coordinates and u refers to displacements relative to the initial coordinates. Friction force computation in the TD3 model initially assumes that, at the current solution time t, the node pair is in a stuck state, i.e. $\mathbf{w}(\mathrm{t}) = \mathbf{w}(\mathrm{t} - \Delta\mathrm{t})$. Following this, the sticking force is computed as

$$\mathbf{f}_j^{\mathrm{stick}}(\mathrm{t}) = \mathbf{K}_{\mathrm{T}}\left[\mathbf{g}_{\mathrm{T},j}(\mathrm{t}) - \mathbf{w}_j(\mathrm{t})\right] \tag{6.32}$$

where $\mathbf{K}_{\mathrm{T}}$ is tangential contact stiffness matrix. For a homogeneous, isotropic material, $\mathbf{K}_{\mathrm{T}}$ is given by

$$\mathbf{K}_{\mathrm{T}} = \begin{bmatrix} \mathrm{k}_{\mathrm{T}} & 0 \\ 0 & \mathrm{k}_{\mathrm{T}} \end{bmatrix} \tag{6.33}$$

where k_{T} is the nodal tangential contact stiffness. In this work, k_{T} is computed using the relationship developed by Sherif and Kossa [14]

$$\mathrm{k}_{\mathrm{T}} = \pi \frac{1-\nu}{2(2-\nu)} \mathrm{k}_{\mathrm{N}} \tag{6.34}$$

where ν is the Poisson's ratio of contacting bodies.

The TD3 model considers friction as a coupled entity, so the "test" for sticking is based on the vector magnitude of the sticking force, rather than the scalar magnitude. That is, the node is sticking if $\left\|\mathbf{f}_j^{\mathrm{stick}}(\mathrm{t})\right\| \leq \mathrm{f}_j^{\mathrm{CL}}(\mathrm{t})$, and slipping if $\left\|\mathbf{f}_j^{\mathrm{stick}}(\mathrm{t})\right\| > \mathrm{f}_j^{\mathrm{CL}}(\mathrm{t})$, where $\mathrm{f}^{\mathrm{CL}}(\mathrm{t})$ is the Coulomb limit force, given by

$$\mathrm{f}_j^{\mathrm{CL}}(\mathrm{t}) = \mu\left|\mathrm{f}_{\mathrm{N},j}(\mathrm{t})\right| \tag{6.35}$$

The slipping force is a vector in the direction of the assumed sticking force, with a magnitude equal to the Coulomb limit, i.e.

$$\mathbf{f}_j^{\text{slip}}(\mathrm{t}) = \frac{\mathbf{f}_j^{\text{stick}}(\mathrm{t})}{\left\|\mathbf{f}_j^{\text{stick}}(\mathrm{t})\right\|} \mathrm{f}_j^{\mathrm{CL}}(\mathrm{t}) \tag{6.36}$$

Equation (6.36) reveals that the friction force coupling is achieved through the computation of $\left\|\mathbf{f}_j^{\text{stick}}(\mathrm{t})\right\|$, which involves both tangential components. Tangential contact force computation in the TD3 model is summarized as

$$\mathbf{f}_{\mathrm{T},j}(\mathrm{t}) = \begin{cases} \mathbf{f}_j^{\text{stick}}(\mathrm{t}) & , \quad \mathrm{g}_{\mathrm{N}}(\mathrm{t}) < 0 \quad \& \quad \left\|\mathbf{f}_j^{\text{stick}}(\mathrm{t})\right\| \le \mathrm{f}_j^{\mathrm{CL}}(\mathrm{t}) & (sticking) \\ \mathbf{f}_j^{\text{slip}}(\mathrm{t}) & , \quad \mathrm{g}_{\mathrm{N}}(\mathrm{t}) < 0 \quad \& \quad \left\|\mathbf{f}_j^{\text{stick}}(\mathrm{t})\right\| > \mathrm{f}_j^{\mathrm{CL}}(\mathrm{t}) & (slipping) \\ \mathbf{0} & , \quad \mathrm{g}_{\mathrm{N}}(\mathrm{t}) \ge 0 & (gapping) \end{cases} \tag{6.37}$$

Once the force vector is obtained, the slider displacements are updated via

$$\mathbf{w}_j(\mathrm{t}) = \begin{cases} \mathbf{w}_j(\mathrm{t}-\Delta\mathrm{t}) & , \quad \mathrm{g}_{\mathrm{N},j}(\mathrm{t}) < 0 \quad \& \quad \left\|\mathbf{f}_j^{\text{stick}}(\mathrm{t})\right\| \le \mathrm{f}_j^{\mathrm{CL}}(\mathrm{t}) & (sticking) \\ \mathbf{g}_{\mathrm{T},j}(\mathrm{t}) - \mathbf{K}_{\mathrm{T}}^{-1}\mathbf{f}^{\text{slip}}(\mathrm{t}) & , \quad \mathrm{g}_{\mathrm{N},j}(\mathrm{t}) < 0 \quad \& \quad \left\|\mathbf{f}_j^{\text{stick}}(\mathrm{t})\right\| > \mathrm{f}_j^{\mathrm{CL}}(\mathrm{t}) & (slipping) \\ \mathbf{g}_{\mathrm{T},j}(\mathrm{t}) & , \quad \mathrm{g}_{\mathrm{N},j}(\mathrm{t}) \ge 0 & (gapping) \end{cases} \tag{6.38}$$

The TD3 model considers intermittent contact and stick-slip transitions on a node-by-node basis. Each node has a unique state of sticking, slipping, or gapping for a given timestep, but a TD3 joint will generally have all three states represented during dynamic loading. Aggregation of individual node slippage will cause joint macroslip. Algorithm 6.1 provides a lightweight MATLAB function that will compute the TD3 contact forces.

```
function [fN, fT, w] = TD3 (gN, gT, w, mu, kN, KT)

% inputs
      % gN  = current normal gap
      % gT  = current tangential gap vector
      % w   = previous slider displacement vector
      % mu  = friction coefficient
      % kN  = normal contact stiffness
      % KT  = tangential contact stiffness matrix
% outputs
      % fN  = normal contact force
      % fT  = friction force vector
      % w   = current slider displacement vector

if gN < 0
      fN  = kN * gN       ; % normal contact force
      fCL = abs(mu * fN)  ; % Coulomb limit force
      fT  = KT * (gT - w) ; % sticking force
      if norm(fT) >= fCL
            fT = fT/norm(fT) * fCL ; % slipping: friction force vector
            w  = gT - K\fT         ; % slipping: slider displacement vector
      end
else
      fN = 0     ; % gapping: normal contact force
      fT = [0;0] ; % gapping: friction force vector
      w  = gT    ; % gapping: slider displacement vector
end

end % function TD3
```

Algorithm 6.1. MATLAB function for the 3D time domain (TD3) contact model.

Figure 6.2 shows a typical friction force orbital of the TD3 model with a constant axial load and varying axial load. The solid black line represents the variation of the two friction force components f_{T1} and f_{T2}. The dashed red line is the initial Coulomb sliding limit, which appears as a circle with radius equal to $f^{CL}(0)$. When the axial load is constant, the Coulomb limit is also constant, so the friction forces exist only within the red circle. The node pair is sticking when inside the Coulomb circle, and slipping when on the circle. When the axial load varies, the Coulomb limit varies with it, so the friction forces are not bound by the red circle, but by a circle that changes radius at every timestep. This behavior is sometimes referred to as a friction cone, or slip cone .

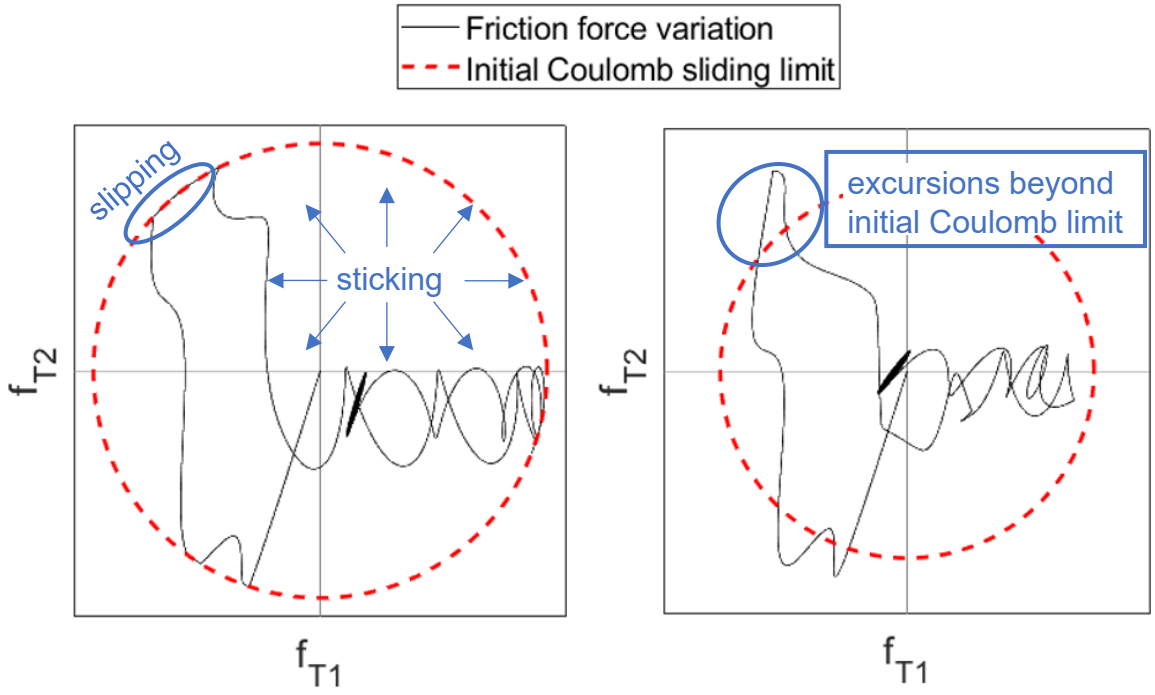

Figure 6.2. Friction force oribtal for the TD3 model with constant axial load (left) and varying axial load (right).

6.5. Explicit Dynamic Preloading of a Structure with Bolted Joints

The interface reduction methods shown in this research apply to HCB superelements with preloaded bolted joints. As such, the interface reduction basis must, in some way, account for the deformations induced by bolt preload. Furthermore, the methods shown rely completely on mode shapes computed in the HCB system, so the preload displaced shape must be computed in HCB coordinates. The static equation of preload in HCB coordinates is

$$\bar{\mathbf{K}}\bar{\mathbf{u}}^{\mathrm{PL}} + \bar{\mathbf{f}}^{\mathrm{c}}(\bar{\mathbf{u}}^{\mathrm{PL}}) = \bar{\mathbf{f}}^{\mathrm{PL}} \tag{6.39}$$

where $\bar{\mathbf{u}}^{\mathrm{PL}}$ is the preload displacement vector in HCB coordinates, and $\bar{\mathbf{f}}^{\mathrm{PL}}$ is the HCB preload force.

Traditionally, Equation (6.39) is solved via implicit static analysis with some nonlinear solution algorithm, such as Newton-Raphson. If the contact nonlinearity is severe, however, the solution algorithms can suffer from convergence issues. In such a case, it may be more computationally prudent to analyze the system as an explicit dynamics problem, i.e.

$$\bar{\mathbf{M}}\ddot{\bar{\mathbf{u}}}(t) + \bar{\mathbf{C}}(t)\dot{\bar{\mathbf{u}}}(t) + \bar{\mathbf{K}}\bar{\mathbf{u}}(t) + \bar{\mathbf{f}}^{c}(\bar{\mathbf{u}}(t)) = \bar{\mathbf{f}}^{\mathrm{ext}}(t) \tag{6.40}$$

where $\bar{\mathbf{f}}^{\mathrm{ext}}(t)$ is the time-varying preload force, given by

$$\bar{\mathbf{f}}^{\mathrm{ext}}(t) = \bar{\mathbf{f}}^{\mathrm{PL}} \cdot \eta_f(t) \tag{6.41}$$

The force scale factor $s_f(t)$ is

$$\eta_f(t) = \begin{cases} \dfrac{t}{t_1} & , \quad t < t_1 \\ 1 & , \quad t \geq t_1 \end{cases} \tag{6.42}$$

Thus, the preload force ramps up to $\bar{\mathbf{f}}^{\mathrm{PL}}$ from $t = 0$ to $t = t_1$, and remains constant after $t = t_1$. $\bar{\mathbf{C}}(t)$ is a time-varying, mass-proportional damping matrix computed via

$$\bar{\mathbf{C}}(t) = \alpha \cdot \bar{\mathbf{M}} \cdot \eta_C(t) \tag{6.43}$$

The proportionality constant α is related to the first HCB frequency (ω_1) and the damping ratio (ξ): which should be close to 1

$$\alpha = 2\xi\omega_1 \tag{6.44}$$

The damping ratio should be close to unity (i.e. critically damped), to ensure transient oscillations are damped out at the end of the dynamic simulation (e.g. $0.9 \leq \xi \leq 0.99$). The damping scale factor $\eta_C(t)$ is

$$\eta_C(t) = \begin{cases} 0 & , \quad t \le t_1 \\ \dfrac{t - t_1}{t_2 - t_1} & , \quad t_1 < t < t_2 \\ 1 & , \quad t_2 \le t \le t_3 \\ 1 - \dfrac{t - t_3}{t_4 - t_3} & , \quad t_3 < t < t_4 \\ 0 & , \quad t \ge t_4 \end{cases} \tag{6.45}$$

The damping matrix is $\mathbf{0}$ when $t \le t_1$, varies linearly between $\mathbf{0}$ and $\alpha\bar{\mathbf{M}}$ when $t_1 < t < t_2$, constantly equals $\alpha\bar{\mathbf{M}}$ when $t_2 \le t \le t_3$, varies linearly between $\alpha\bar{\mathbf{M}}$ and $\mathbf{0}$ when $t_3 < t < t_4$, and remains at $\mathbf{0}$ for $t \ge t_4$. A plot of the damping and force scale factors is shown in Figure 6.3.

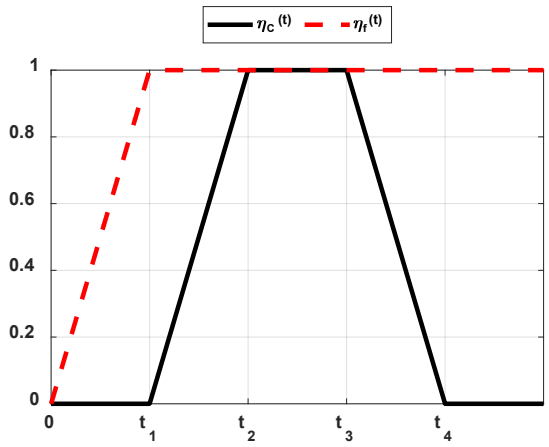

Figure 6.3. Scaling factors for damping (η_C) and force (η_f) for an explicit dynamic preload simulation.

The time variables t_1, t_2, t_3, and t_4 must be defined by the user. Ideally, they should be large enough such that the structure is essentially at rest when $t = t_4$. In this formulation, similar to the one shown in Section 4.4.1, the desired preload deformation is equal to the displacement vector at the end of the explicit dynamic simulation, i.e.

$$\bar{\mathbf{u}}^{PL} = \bar{\mathbf{u}}(t_4) \tag{6.46}$$

6.6. Putting It All Together: Time Integration of a Preloaded Bolted Structure with Nonlinear Interface Reduction

At this stage, the Hurty/Craig-Bampton (HCB) transformation has been derived (Section 6.2), with secondary and tertiary transformations that yielded an interface-reduced (IR) model with sparse system matrices (Section 6.3). Intercomponent contact in these systems is modeled using node-to-node TD3 elements, outlined in Section 6.4. Section 6.5 showed how the HCB model will be preloaded before interface reduction is carried out. This section will bring these pieces together in a concise computational framework.

First, consider the equations of motion in a coupled HCB superelement, subjected to a constant preload $\bar{\mathbf{f}}^{\mathrm{PL}}$ and arbitrary dynamic loading $\bar{\mathbf{f}}^{\mathrm{ext}}(\mathrm{t})$:

$$\bar{\mathbf{M}}\ddot{\bar{\mathbf{u}}}(\mathrm{t}) + \bar{\mathbf{C}}\dot{\bar{\mathbf{u}}}(\mathrm{t}) + \bar{\mathbf{K}}\bar{\mathbf{u}}(\mathrm{t}) + \bar{\mathbf{f}}^{\mathrm{c}}\big(\bar{\mathbf{u}}(\mathrm{t})\big) = \bar{\mathbf{f}}^{\mathrm{PL}} + \bar{\mathbf{f}}^{\mathrm{ext}}(\mathrm{t}) \tag{6.47}$$

$\bar{\mathbf{C}}$ is an arbitrary damping matrix (e.g. proportional damping, Rayleigh damping, modal damping, etc.). HCB displacements ($\bar{\mathbf{u}}$) can be written in terms of the preload displacement ($\bar{\mathbf{u}}^{\mathrm{PL}}$) and the IR displacement ($\breve{\bar{\mathbf{u}}}$), as

$$\bar{\mathbf{u}}(\mathrm{t}) = \bar{\mathbf{u}}^{\mathrm{PL}} + \bar{\mathbf{T}}\breve{\bar{\mathbf{u}}}(\mathrm{t}) \tag{6.48}$$

Equation (6.48) computes the IR displacements ($\breve{\bar{\mathbf{u}}}$) relative to a preloaded configuration $\bar{\mathbf{u}}^{\mathrm{PL}}$, whereas Equation (6.23) directly maps $\breve{\bar{\mathbf{u}}}(\mathrm{t})$ to $\bar{\mathbf{u}}(\mathrm{t})$, without consideration for the preloaded state. The advantage of this formulation is that the IR system starts from zero initial conditions, with no need to transform $\bar{\mathbf{u}}^{\mathrm{PL}}$ to IR coordinates. Differentiating Equation (6.48) with respect to time yields

$$\dot{\bar{\mathbf{u}}}(\mathrm{t}) = \bar{\mathbf{T}}\dot{\breve{\bar{\mathbf{u}}}}(\mathrm{t}) \tag{6.49a}$$

$$\ddot{\bar{\mathbf{u}}}(\mathrm{t}) = \bar{\mathbf{T}}\ddot{\breve{\bar{\mathbf{u}}}}(\mathrm{t}) \tag{6.49b}$$

where $\dot{\breve{\mathbf{u}}}(t)$ and $\ddot{\breve{\mathbf{u}}}(t)$ are the IR velocity and acceleration vectors, respectively. Substituting Equations (6.48) and (6.49) into Equation (6.47) yields

$$\bar{\mathbf{M}}\underbrace{\breve{\mathbf{T}}\ddot{\breve{\mathbf{u}}}(t)}_{\ddot{\mathbf{u}}(t)} + \bar{\mathbf{C}}\underbrace{\breve{\mathbf{T}}\dot{\breve{\mathbf{u}}}(t)}_{\dot{\mathbf{u}}(t)} + \bar{\mathbf{K}}\underbrace{\left[\bar{\mathbf{u}}^{PL} + \breve{\mathbf{T}}\breve{\mathbf{u}}(t)\right]}_{\bar{\mathbf{u}}(t)} + \bar{\mathbf{f}}^{c}\left(\underbrace{\bar{\mathbf{u}}^{PL} + \breve{\mathbf{T}}\breve{\mathbf{u}}(t)}_{\bar{\mathbf{u}}(t)}\right) = \bar{\mathbf{f}}^{PL} + \bar{\mathbf{f}}^{ext}(t) \tag{6.50}$$

Assuming that the $\bar{\mathbf{u}}^{PL}$ obtained from explicit dynamics also satisfies Equation (6.39), the preload force ($\bar{\mathbf{f}}^{PL}$) is substituted into Equation (6.50) as

$$\bar{\mathbf{M}}\breve{\mathbf{T}}\ddot{\breve{\mathbf{u}}}(t) + \bar{\mathbf{C}}\breve{\mathbf{T}}\dot{\breve{\mathbf{u}}}(t) + \bar{\mathbf{K}}\left[\bar{\mathbf{u}}^{PL} + \breve{\mathbf{T}}\breve{\mathbf{u}}(t)\right] + \bar{\mathbf{f}}^{c}\left(\bar{\mathbf{u}}^{PL} + \breve{\mathbf{T}}\breve{\mathbf{u}}(t)\right) = \underbrace{\left[\bar{\mathbf{K}}\bar{\mathbf{u}}^{PL} + \bar{\mathbf{f}}^{c}(\bar{\mathbf{u}}^{PL})\right]}_{\bar{\mathbf{f}}^{PL}} + \bar{\mathbf{f}}^{ext}(t) \tag{6.51}$$

which can be simplified to

$$\bar{\mathbf{M}}\breve{\mathbf{T}}\ddot{\breve{\mathbf{u}}}(t) + \bar{\mathbf{C}}\breve{\mathbf{T}}\dot{\breve{\mathbf{u}}}(t) + \bar{\mathbf{K}}\breve{\mathbf{T}}\breve{\mathbf{u}}(t) + \bar{\mathbf{f}}^{c}\left(\bar{\mathbf{u}}^{PL} + \breve{\mathbf{T}}\breve{\mathbf{u}}(t)\right) - \bar{\mathbf{f}}^{c}(\bar{\mathbf{u}}^{PL}) = \bar{\mathbf{f}}^{ext}(t) \tag{6.52}$$

Pre-multiply by $\breve{\mathbf{T}}^{T}$ to impose orthogonality between the residual error and the reduction basis:

$$\breve{\mathbf{T}}^{T}\bar{\mathbf{M}}\breve{\mathbf{T}}\ddot{\breve{\mathbf{u}}}(t) + \breve{\mathbf{T}}^{T}\bar{\mathbf{C}}\breve{\mathbf{T}}\dot{\breve{\mathbf{u}}}(t) + \breve{\mathbf{T}}^{T}\bar{\mathbf{K}}\breve{\mathbf{T}}\breve{\mathbf{u}}(t) + \breve{\mathbf{T}}^{T}\left[\bar{\mathbf{f}}^{c}\left(\bar{\mathbf{u}}^{PL} + \breve{\mathbf{T}}\breve{\mathbf{u}}(t)\right) - \bar{\mathbf{f}}^{c}(\bar{\mathbf{u}}^{PL})\right] = \breve{\mathbf{T}}^{T}\bar{\mathbf{f}}^{ext}(t) \tag{6.53}$$

Finally, recall from Equation (6.24) that $\breve{\bar{\mathbf{M}}} = \breve{\mathbf{T}}^{T}\bar{\mathbf{M}}\breve{\mathbf{T}} = \mathbf{I}$, $\breve{\bar{\mathbf{K}}} = \breve{\mathbf{T}}^{T}\bar{\mathbf{K}}\breve{\mathbf{T}} = \breve{\bar{\mathbf{\Omega}}}^{2}$, and $\breve{\bar{\mathbf{f}}}^{ext}(t) = \breve{\mathbf{T}}^{T}\bar{\mathbf{f}}^{ext}(t)$. Also let $\breve{\bar{\mathbf{C}}} = \breve{\mathbf{T}}^{T}\bar{\mathbf{C}}\breve{\mathbf{T}}$, such that

$$\ddot{\breve{\mathbf{u}}}(t) + \breve{\bar{\mathbf{C}}}\dot{\breve{\mathbf{u}}}(t) + \breve{\bar{\mathbf{\Omega}}}^{2}\breve{\mathbf{u}}(t) + \breve{\mathbf{T}}^{T}\left[\bar{\mathbf{f}}^{c}\left(\bar{\mathbf{u}}^{PL} + \breve{\mathbf{T}}\breve{\mathbf{u}}(t)\right) - \bar{\mathbf{f}}^{c}(\bar{\mathbf{u}}^{PL})\right] = \breve{\bar{\mathbf{f}}}^{ext}(t) \tag{6.54}$$

Considering that $\breve{\bar{\mathbf{C}}}$, $\breve{\bar{\mathbf{\Omega}}}^{2}$, $\breve{\mathbf{T}}$, $\bar{\mathbf{u}}^{PL}$, and $\breve{\bar{\mathbf{f}}}^{ext}(t)$ are all known quantities, Equation (6.54) is a nonlinear second-order ordinary differential equation with respect to $\breve{\mathbf{u}}(t)$. The only remaining step is to discretize in time and apply a integration scheme to compute the solution over a specified period $0 \leq t \leq t_f$.

This research employs the Chung-Lee time integration scheme [15], an explicit 2nd-order accurate method akin to the central difference method. Let t_n be a multiple of the timestep length

Δt, i.e. $t_n = n\Delta t$. Also let the IR displacement, velocity, acceleration, and external force at time t_n be given by $\mathbf{d}_n$, $\mathbf{v}_n$, $\mathbf{a}_n$, and $\mathbf{f}_n^{\text{ext}}$, respectively, i.e.

$$\breve{\tilde{\mathbf{u}}}(t_n) = \mathbf{d}_n \tag{6.55a}$$

$$\dot{\breve{\tilde{\mathbf{u}}}}(t_n) = \mathbf{v}_n \tag{6.55b}$$

$$\ddot{\breve{\tilde{\mathbf{u}}}}(t_n) = \mathbf{a}_n \tag{6.55c}$$

$$\breve{\tilde{\mathbf{f}}}^{\text{ext}}(t_n) = \mathbf{f}_n^{\text{ext}} \tag{6.55d}$$

First, compute the contact force in HCB coordinates at time t_n:

$$\bar{\mathbf{f}}_n^{\text{c}} = \bar{\mathbf{f}}^{\text{c}}\left(\bar{\mathbf{u}}^{\text{PL}} + \breve{\mathbf{T}}\mathbf{d}_n\right) \tag{6.56}$$

Next, compute the IR contact force by subtracting the preload-induced contact force and transforming to IR coordinates:

$$\breve{\tilde{\mathbf{f}}}_n^{\text{c}} = \breve{\mathbf{T}}^{\text{T}}\left[\bar{\mathbf{f}}_n^{\text{c}} - \bar{\mathbf{f}}^{\text{c}}(\bar{\mathbf{u}}^{\text{PL}})\right] \tag{6.57}$$

The Chung-Lee algorithm can now proceed in IR coordinates. The nonlinear restoring force at time t_n is

$$\mathbf{N}_n = \breve{\tilde{\mathbf{C}}}\mathbf{v}_n + \breve{\bar{\boldsymbol{\Omega}}}^2\mathbf{d}_n + \breve{\tilde{\mathbf{f}}}_n^{\text{c}} \tag{6.58}$$

Following this, update the acceleration at time t_{n+1} as

$$\mathbf{a}_{n+1} = \breve{\tilde{\mathbf{M}}}^{-1}(\mathbf{f}_n^{\text{ext}} - \mathbf{N}_n) \tag{6.59}$$

$\breve{\tilde{\mathbf{M}}} = \mathbf{I}$, so no matrix inversion is necessary, and Equation (6.59) can be rewritten as

$$\mathbf{a}_{n+1} = \mathbf{f}_n^{\text{ext}} - \mathbf{N}_n \tag{6.60}$$

Finally, update the displacement and velocity via

$$\mathbf{d}_{n+1} = \mathbf{d}_n + \Delta t\mathbf{v}_n + \left(\frac{1}{2} - \beta\right)\Delta t^2\mathbf{a}_n + \beta\Delta t^2\mathbf{a}_{n+1} \tag{6.61a}$$

$$\mathbf{v}_{n+1} = \mathbf{v}_n - \frac{\Delta t}{2}\mathbf{a}_n + \frac{3\Delta t}{2}\mathbf{a}_{n+1} \tag{6.61b}$$

where β is the sole parameter of the Chung-Lee scheme. Numerical stability of the Chung-Lee algorithm requires that $1 \leq \beta \leq \frac{28}{27}$, with maximum numerical dissipation at $\beta = \frac{28}{27}$ and no numerical dissipation at $\beta = 1$. The critical timestep length (Δt_{cr}) is

$$\Delta t_{cr} = \frac{2}{\bar{\bar{\omega}}_{max}\sqrt{4\beta - 3}} \tag{6.62}$$

where $\bar{\bar{\omega}}_{max}$ is the maximum natural circular frequency of the IR system. Setting $\beta = 1$ yields

$$\Delta t_{cr} = \frac{2}{\bar{\bar{\omega}}_{max}} \tag{6.63}$$

revealing that the $\beta = 1$ variant of the Chung-Lee algorithm is spectrally identical to the central difference method. Figure 6.4 shows a flow chart that neatly summarizes the time integration procedures for a preloaded bolted structure with nonlinear interface reduction.

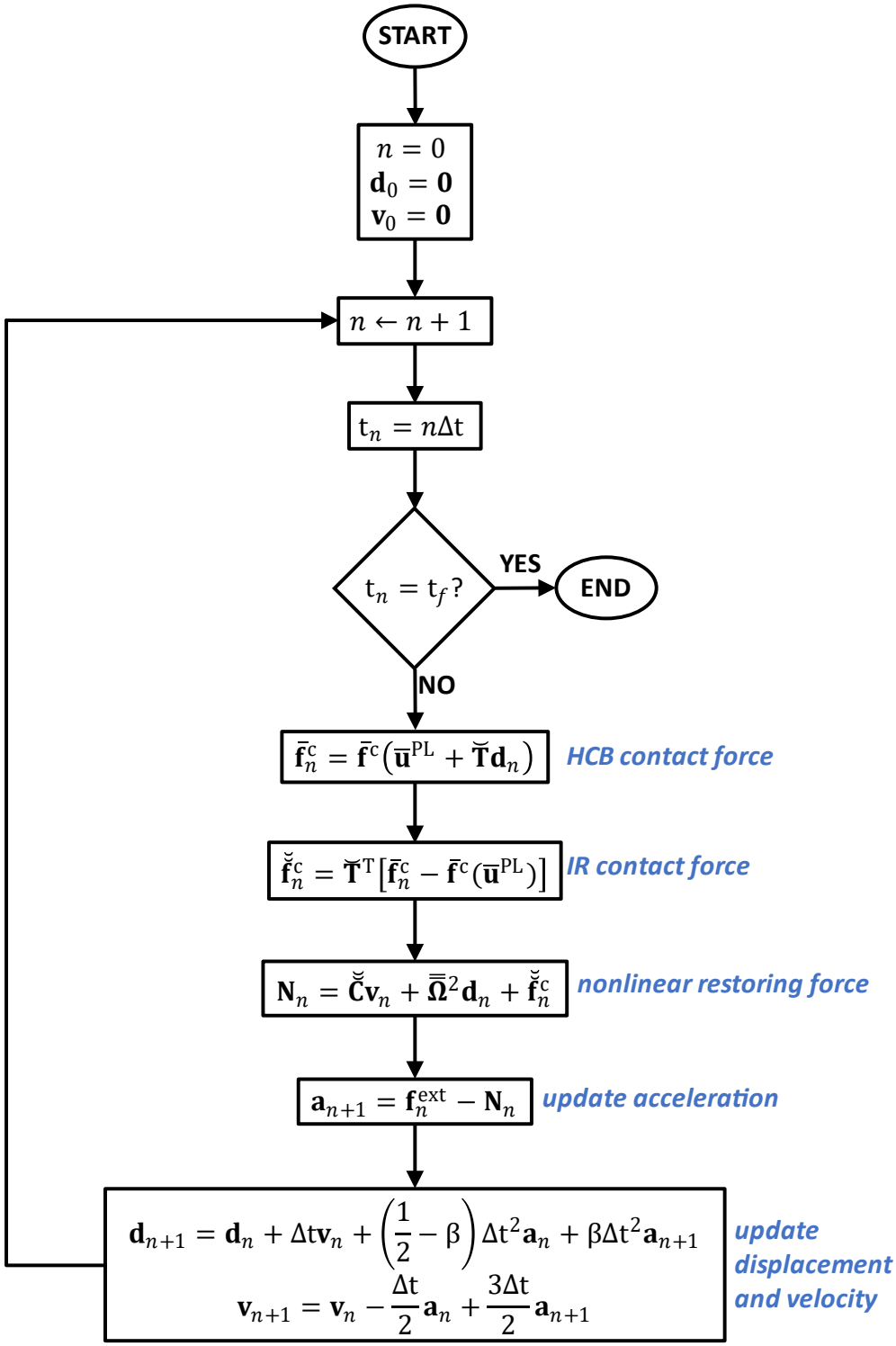

Figure 6.4. Time integration for a preloaded bolted structure with nonlinear interface reduction.

References

1. Hurty W. Vibrations of Structural Systems by Component Mode Synthesis. *Transactions of the American Society of Civil Engineers* 1960.

2. Hurty WC. Dynamic analysis of structural systems using component modes. *AIAA Journal* 1965. DOI: 10.2514/3.2947.

3. Craig RR, Bampton MCC. Coupling of substructures for dynamic analyses. *AIAA Journal* 1968. DOI: 10.2514/3.4741.

4. Segalman DJ. Model reduction of systems with localized nonlinearities. *Journal of Computational and Nonlinear Dynamics* 2007; **2**(3): 249–266. DOI: 10.1115/1.2727495.

5. Hong SK, Epureanu BI, Castanier MP. Next-generation parametric reduced-order models. *Mechanical Systems and Signal Processing* 2013; **37**(1–2): 403–421. DOI: 10.1016/j.ymssp.2012.12.012.

6. Zucca S, Epureanu BI. Bi-linear reduced-order models of structures with friction intermittent contacts. *Nonlinear Dynamics* 2014. DOI: 10.1007/s11071-014-1363-8.

7. Mitra M, Zucca S, Epureanu BI. Adaptive Microslip Projection for Reduction of Frictional and Contact Nonlinearities in Shrouded Blisks. *Journal of Computational and Nonlinear Dynamics* 2016; **11**(4): 1–15. DOI: 10.1115/1.4033003.

8. Kuether RJ, Coffin PB, Brink AR. On Hurty/Craig-Bampton Substructuring with Interface Reduction on Contacting Surfaces. *Proceedings of the ASME 2017 International Design Engineering Technical Conferences and Computes and Information in Engineering Conference (IDETC/CIE 2017)*, Cleveland, Ohio, USA: 2017.

9. Gastaldi C, Zucca S, Epureanu BI. Jacobian projection reduced-order models for dynamic systems with contact nonlinearities. *Mechanical Systems and Signal Processing* 2018; **100**: 550–569. DOI: 10.1016/j.ymssp.2017.07.049.

10. Pichler F, Witteveen W, Fischer P. Reduced-order modeling of preloaded bolted structures in multibody systems by the use of trial vector derivatives. *Journal of Computational and Nonlinear Dynamics* 2017. DOI: 10.1115/1.4036989.

11. Wriggers P. *Computational Contact Mechanics*. 2006.

12. Yang BD, Menq CH. Characterization of 3D contact Kinematics and Prediction of Resonant Response of Structures Having 3D Frictional Constraint. *Journal of Sound and Vibration* 1998; **217**(5): 909–925. DOI: 10.1006/jsvi.1998.1802.

13. Zucca S, Firrone CM. Nonlinear dynamics of mechanical systems with friction contacts: Coupled static and dynamic Multi-Harmonic Balance Method and multiple solutions. *Journal of Sound and Vibration* 2014; **333**: 916–926. DOI: 10.1016/j.jsv.2013.09.032.

14. Sherif HA, Kossa SS. Relationship between normal and tangential contact stiffness of nominally flat surfaces. *Wear* 1991; **151**: 49–62. DOI: 10.1016/0043-1648(91)90345-U.

15. Chung J, Lee JM. A New Family of Explicit Time Integration Methods for Linear and Non-Linear Structural Dynamics. *IOP Conference Series: Materials Science and Engineering* 1994; **37**: 3961–3976. DOI: 10.1088/1757-899X/10/1/012145.

Chapter 7 Interface Reduction Methods for Hurty/Craig-Bampton Superelements with Preloaded Bolted Joints

7.1. Introduction

Chapter 6 described how a Hurty/Craig-Bampton (HCB) [1–3] superelement is formed, and how the nonlinear interface degrees of freedom (DOF) can be reduced by subsequent coordinates transformations. It did not, however, explain how the interface reduction bases are formed. This chapter details a family of methods to develop the interface reduction matrix $\overline{\mathbf{T}}$, and compares the relative performance of each method. Section 7.2 describes the formation of the initial reduction basis using system-level characteristic constraint (SCC) modes [4–6] or joint-interface (JI) modes [7]. A variant of the SCC method using Gram-Schmidt interface (GSI) modes [8] is also shown. Section 7.3 explains how the initial basis can be augmented using approximate residual interface (ARI) modes and interface modal derivatives (IMDs). Section 7.4 describes a

prototype beam assembly used to demonstrate the relative effectiveness of each interface reduction method. Section 7.5 summarizes the accuracy and efficiency of each method, and Section 7.6 provides concluding remarks.

7.2. Interface Reduction Bases

Three different interface reduction bases are shown in this section: system-level characteristic constraint (SCC) modes [4–6], Gram-Schmidt interface (GSI) modes, and joint interface (JI) modes [7].

7.2.1. System-Level Characteristic Constraint (SCC) Modes

In structures with bolted joints, it is beneficial to retain certain boundary DOF in the physical domain. This allows nodal loads, such as preloads, to be directly applied in the IR system. As such, consider a partitioning of the HCB mass and stiffness matrices into n_{FI} interior (i) DOF, n_r interface (r), and n_a active DOF (a).

$$\bar{\mathbf{M}} = \begin{bmatrix} \mathbf{I} & \bar{\mathbf{M}}_{ir} & \bar{\mathbf{M}}_{ia} \\ \bar{\mathbf{M}}_{ri} & \bar{\mathbf{M}}_{rr} & \bar{\mathbf{M}}_{ra} \\ \bar{\mathbf{M}}_{ai} & \bar{\mathbf{M}}_{ar} & \bar{\mathbf{M}}_{aa} \end{bmatrix} \tag{7.1a}$$

$$\bar{\mathbf{K}} = \begin{bmatrix} (\boldsymbol{\Omega}^{\mathrm{FI}})^2 & \mathbf{0} & \mathbf{0} \\ \mathbf{0} & \bar{\mathbf{K}}_{rr} & \bar{\mathbf{K}}_{ra} \\ \mathbf{0} & \bar{\mathbf{K}}_{ar} & \bar{\mathbf{K}}_{aa} \end{bmatrix} \tag{7.1b}$$

The interior partitioning is unchanged, but now the boundary partition (b) has been split into interface (r) and active (a) DOF. Interface reduction should only affect the interface DOF, so the system-level characteristic constraint (SCC) modes [4–6] will be computed on the $r - r$ partition. Furthermore, the modes will be computed using a constrained stiffness matrix ($\bar{\mathbf{K}}^{\mathbf{c}}$), which

accounts for contributions from the contact elements when linearized about the preload equilibrium*:

$$\bar{\mathbf{K}}^{\mathrm{c}} = \bar{\mathbf{K}}(\bar{\mathbf{u}}^{\mathrm{PL}}) = \bar{\mathbf{K}} + \left.\frac{\partial \bar{\mathbf{f}}^{\mathrm{c}}(\bar{\mathbf{u}})}{\partial \bar{\mathbf{u}}}\right|_{\bar{\mathbf{u}}=\bar{\mathbf{u}}^{\mathrm{PL}}} = \begin{bmatrix} (\boldsymbol{\Omega}^{\mathrm{FI}})^2 & \mathbf{0} & \mathbf{0} \\ \mathbf{0} & \bar{\mathbf{K}}^{\mathrm{c}}_{rr} & \bar{\mathbf{K}}_{ra} \\ \mathbf{0} & \bar{\mathbf{K}}_{ar} & \bar{\mathbf{K}}_{aa} \end{bmatrix} \tag{7.2}$$

Note that $\bar{\mathbf{K}}^{\mathrm{c}}$ is only different from $\bar{\mathbf{K}}$ on the $r-r$ partition, which contains all interface DOF. The SCC modes are computed according to

$$\left[\bar{\mathbf{K}}^{\mathrm{c}}_{rr} - \bar{\omega}_j^2 \bar{\mathbf{M}}_{rr}\right]\bar{\boldsymbol{\phi}}_j = \mathbf{0} \quad ; \quad j = 1, 2, \ldots, n_{SCC} \tag{7.3}$$

where $\bar{\omega}_j$ is the j^{th} SCC frequency, $\bar{\boldsymbol{\phi}}_j$ is its corresponding SCC mode, and n_{SCC} is the number of retained SCC modes. Keeping n_{SCC} much smaller than the original number of interface DOF (n_r) provides the desired model order reduction. The SCC modes are assembled into an eigenmatrix ($\bar{\boldsymbol{\Phi}}$) as

$$\bar{\boldsymbol{\Phi}} = \begin{bmatrix} \bar{\boldsymbol{\phi}}_1 & \bar{\boldsymbol{\phi}}_2 & \cdots & \bar{\boldsymbol{\phi}}_{n_{SCC}} \end{bmatrix} \tag{7.4}$$

Computation of eigenmodes according to Equation (7.3) assumes no deformation on the active DOF partition. This is alleviated by adding interface constraint (IC) modes, computed in a similar fashion to the HCB constraint modes from Equation (6.5):

$$\bar{\boldsymbol{\Psi}} = -(\bar{\mathbf{K}}^{\mathrm{c}}_{rr})^{-1}\bar{\mathbf{K}}_{ra} \tag{7.5}$$

Finally, the SCC transformation matrix is assembled as

$$\bar{\mathbf{T}} = \begin{bmatrix} \mathbf{I} & \mathbf{0} & \mathbf{0} \\ \mathbf{0} & \bar{\boldsymbol{\Phi}} & \bar{\boldsymbol{\Psi}} \\ \mathbf{0} & \mathbf{0} & \mathbf{I} \end{bmatrix} \tag{7.6}$$

which has $(n_{FI} + n_r + n_a)$ rows and $(n_{FI} + n_{SCC} + n_a)$ columns. Reduction of the interface DOF is achieved by choosing n_{SCC} to be much smaller than n_r. Comparison between Equation (6.6) and

* Derivation of $\frac{\partial \bar{\mathbf{f}}^{\mathrm{c}}(\bar{\mathbf{u}})}{\partial \bar{\mathbf{u}}}$ for a TD3 contact element is shown in Appendix A1.

Equation (7.6) shows that the SCC transformation shown here is, in fact, a secondary HCB transformation on the interface DOF. A MATLAB [9] function to compute an SCC transformation matrix is shown in Algorithm 7.1.

```
function T = SCC(M, Kc, i, r, a, nSCC)

% inputs
      % M    = sorted HCB mass matrix
      % Kc   = sorted HCB stiffness matrix w/ contact contributions
      % i    = indices of fixed-interface DOF
      % r    = indices of interface DOF
      % a    = indices of active DOF
      % nSCC = number of SCC modes to retain
% outputs
      % T   = SCC transformation matrix

%% SCC basis
nFI      = length(i)                                ; % number of FI modes
nr       = length(r)                                ; % number of r DOF
na       = length(a)                                ; % number of a DOF
[Phi, ~] = eigs(Kc(r,r), M(r,r), nSCC, 'sm')        ; % eigenmodes
Phi      = Phi * diag(sqrt(diag(Phi'*M*Phi).^-1))   ; % mass-normalize
Psi      = -Kc(r,r)\Kc(r,a)                         ; % constraint modes
T        = [                                  …
             eye(nFI), zeros(nFI,nSCC+na) ; …
             zeros(nr,nFI), Phi, Psi      ; …
             zeros(na,nFI+nSCC), eye(na)    …
]                                           ; % SCC transformation matrix

%% deflation
T        = T * diag(sqrt(diag(T'*T).^-1)) ; % convert to unit vectors
[T,~,~]  = svd(T, 'econ')                 ; % replace with singular vectors


end % function SCC
```

Algorithm 7.1. Interface reduction with SCC modes.

7.2.2. Gram-Schmidt Interface (GSI) Modes

A modification to the traditional SCC approach was suggest by Battiatio et al. [8], which first computes all eigenmodes on the entire boundary partition, i.e.

$$\left[\overline{\mathbf{K}}_{bb}^{\mathrm{c}} - \overline{\omega}_j^2 \overline{\mathbf{M}}_{bb}\right]\overline{\boldsymbol{\phi}}_j = \mathbf{0} \quad , \quad j = 1, 2, \ldots, n_b \tag{7.7}$$

In Equation (7.7), $\overline{\omega}_j$ is the j^{th} boundary eigenfrequency and $\overline{\boldsymbol{\phi}}_j$ is the j^{th} boundary eigenmode. The partitioned mass matrix ($\overline{\mathbf{M}}_{bb}$) and stiffness matrix ($\overline{\mathbf{K}}_{bb}^{\mathrm{c}}$) are

$$\overline{\mathbf{M}}_{bb} = \begin{bmatrix} \overline{\mathbf{M}}_{rr} & \overline{\mathbf{M}}_{ra} \\ \overline{\mathbf{M}}_{ar} & \overline{\mathbf{M}}_{aa} \end{bmatrix} \tag{7.8}$$

$$\overline{\mathbf{K}}^{\mathrm{c}} = \begin{bmatrix} \overline{\mathbf{K}}_{rr}^{\mathrm{c}} & \overline{\mathbf{K}}_{ra} \\ \overline{\mathbf{K}}_{ar} & \overline{\mathbf{K}}_{aa} \end{bmatrix} \tag{7.9}$$

and n_b is the total number of boundary DOF, i.e. $n_b = n_r + n_a$. The boundary eigenvectors are assembled as

$$\overline{\boldsymbol{\Phi}} = \begin{bmatrix} \overline{\boldsymbol{\phi}}_1 & \overline{\boldsymbol{\phi}}_2 & \cdots & \overline{\boldsymbol{\phi}}_{n_b} \end{bmatrix} = \begin{bmatrix} \overline{\boldsymbol{\Phi}}_{rr} & \overline{\boldsymbol{\Phi}}_{ra} \\ \overline{\boldsymbol{\Phi}}_{ar} & \overline{\boldsymbol{\Phi}}_{aa} \end{bmatrix} \tag{7.10}$$

Extract the $r - r$ partition of $\overline{\boldsymbol{\Phi}}$, perform Gram-Schmidt orthogonalization, and retain the first n_{GSI} columns to obtain the Gram-Schmidt Interface (GSI) modes:

$$\overline{\boldsymbol{\Phi}}_{rr} \xrightarrow[\text{truncation}]{\substack{Gram-Schmidt \\ + \\ truncation}} \hat{\overline{\boldsymbol{\Phi}}} \tag{7.11}$$

The GSI transformation matrix is assembled similarly to Equation (7.6), but no IC modes are required:

$$\overline{\mathbf{T}} = \begin{bmatrix} \mathbf{I} & \mathbf{0} & \mathbf{0} \\ \mathbf{0} & \hat{\overline{\boldsymbol{\Phi}}} & \mathbf{0} \\ \mathbf{0} & \mathbf{0} & \mathbf{I} \end{bmatrix} \tag{7.12}$$

which has $(n_{FI} + n_r + n_a)$ rows and $(n_{FI} + n_{GSI} + n_a)$ columns. Selecting n_{GSI} to be much smaller than n_r provides the desired model order reduction. Algorithm 7.2 contains a MATLAB function that can be used to compute a GSI basis.

```
function T = GSI(M, Kc, i, r, a, nGSI)

% inputs
      % M    = sorted HCB mass matrix
      % Kc   = sorted HCB stiffness matrix w/ contact contributions
      % i    = indices of fixed-interface DOF
      % r    = indices of interface DOF
      % a    = indices of active DOF
      % nGSI = number of GSI modes to retain
% outputs
      % T   = GSI transformation matrix
% required subroutines
      % GramSchmidt(): returns a matrix orthogonalized by the Gram-Schmidt
      %                procedure

%% GSI basis
b        = [r(:);a(:)]                        ; % boundary DOF indices
nr       = length(r)                          ; % number of r DOF
nFI      = length(i)                          ; % number of FI modes
na       = length(a)                          ; % number of a DOF
[Phi, ~] = eigs(Kc(b,b), M(b,b), nGSI, 'sm') ; % eigenmodes
Phi      = GramSchmidt(Phi(1:nr,1:nr))        ; % GSI modes
T        = blkdiag(eye(nFI),Phi,eye(na))      ; % transformation matrix

%% deflation
T        = T * diag(sqrt(diag(T'*T).^-1)) ; % convert to unit vectors
[T,~,~]  = svd(T, 'econ')                 ; % replace with singular vectors



end % function GSI
```

Algorithm 7.2. Interface reduction with GSI modes.

7.2.3. Joint Interface (JI) Modes

Joint Interface (JI) modes are based on quasi-static enforcement of Newton's third law at the interfaces of a structure. That is, JI modes pre-constrain the system such that all contact forces on one side of an interface are equal and opposite to the forces on the other side. As such, it is necessary to split the interface DOF into those from the first body (r_1) and those from the second body (r_2):

$$\bar{\mathbf{M}} = \begin{bmatrix} \mathbf{I} & \bar{\mathbf{M}}_{ir_1} & \bar{\mathbf{M}}_{ir_2} & \bar{\mathbf{M}}_{ia} \\ \bar{\mathbf{M}}_{r_1 i} & \bar{\mathbf{M}}_{r_1 r_1} & \bar{\mathbf{M}}_{r_1 r_2} & \bar{\mathbf{M}}_{r_1 a} \\ \bar{\mathbf{M}}_{r_2 i} & \bar{\mathbf{M}}_{r_2 r_1} & \bar{\mathbf{M}}_{r_2 r_2} & \bar{\mathbf{M}}_{r_2 a} \\ \bar{\mathbf{M}}_{ai} & \bar{\mathbf{M}}_{ar_1} & \bar{\mathbf{M}}_{ar_2} & \bar{\mathbf{M}}_{aa} \end{bmatrix} \tag{7.13a}$$

$$\bar{\mathbf{K}} = \begin{bmatrix} (\boldsymbol{\Omega}^{\mathrm{FI}})^2 & \mathbf{0} & \mathbf{0} & \mathbf{0} \\ \mathbf{0} & \bar{\mathbf{K}}_{r_1 r_1} & \bar{\mathbf{K}}_{r_1 r_2} & \bar{\mathbf{K}}_{r_1 a} \\ \mathbf{0} & \bar{\mathbf{K}}_{r_2 r_1} & \bar{\mathbf{K}}_{r_2 r_2} & \bar{\mathbf{K}}_{r_2 a} \\ \mathbf{0} & \bar{\mathbf{K}}_{ar_1} & \bar{\mathbf{K}}_{ar_2} & \bar{\mathbf{K}}_{aa} \end{bmatrix} \tag{7.13b}$$

The r_1 partition has n_{r1} DOF and the r_2 partition has n_{r2} DOF. Thus, $n_r = n_{r1} + n_{r2}$ and $n_{r1} = n_{r2} = \frac{n_r}{2}$. Consider an arbitrary static loading of the HCB system in partitioned coordinates:

$$\underbrace{\begin{bmatrix} (\boldsymbol{\Omega}^{\mathrm{FI}})^2 & \mathbf{0} & \mathbf{0} & \mathbf{0} \\ \mathbf{0} & \bar{\mathbf{K}}_{r_1 r_1} & \bar{\mathbf{K}}_{r_1 r_2} & \bar{\mathbf{K}}_{r_1 a} \\ \mathbf{0} & \bar{\mathbf{K}}_{r_2 r_1} & \bar{\mathbf{K}}_{r_2 r_2} & \bar{\mathbf{K}}_{r_2 a} \\ \mathbf{0} & \bar{\mathbf{K}}_{ar_1} & \bar{\mathbf{K}}_{ar_2} & \bar{\mathbf{K}}_{aa} \end{bmatrix}}_{\bar{\mathbf{K}}} \underbrace{\begin{Bmatrix} \mathbf{q}_i \\ \mathbf{u}_{r_1} \\ \mathbf{u}_{r_2} \\ \mathbf{u}_a \end{Bmatrix}}_{\bar{\mathbf{u}}} + \underbrace{\begin{Bmatrix} \mathbf{0} \\ \mathbf{f}^{\mathrm{c}}_{r_1}(\mathbf{u}_r) \\ \mathbf{f}^{\mathrm{c}}_{r_2}(\mathbf{u}_r) \\ \mathbf{0} \end{Bmatrix}}_{\bar{\mathbf{f}}^{\mathrm{c}}(\bar{\mathbf{u}})} = \underbrace{\begin{Bmatrix} \mathbf{0} \\ \mathbf{0} \\ \mathbf{0} \\ \mathbf{f}_a \end{Bmatrix}}_{\bar{\mathbf{f}}} \tag{7.14}$$

Note that the contact forces $\bar{\mathbf{f}}^{\mathrm{c}}(\bar{\mathbf{u}})$ only apply on the interface DOF and the static force $\bar{\mathbf{f}}$ only applies to the active DOF. Application of Newton's third law at the interface implies

$$\mathbf{f}^{\mathrm{c}}_{r_2}(\mathbf{u}_r) = -\mathbf{f}^{\mathrm{c}}_{r_1}(\mathbf{u}_r) \tag{7.15}$$

Substituting the second and third rows of Equation (7.14) into Equation (7.15) yields

$$-\left(\bar{\mathbf{K}}_{r_2 r_1}\mathbf{u}_{r_1} + \bar{\mathbf{K}}_{r_2 r_2}\mathbf{u}_{r_2} + \bar{\mathbf{K}}_{r_2 a}\mathbf{u}_a\right) = \bar{\mathbf{K}}_{r_1 r_1}\mathbf{u}_{r_1} + \bar{\mathbf{K}}_{r_1 r_2}\mathbf{u}_{r_2} + \bar{\mathbf{K}}_{r_1 a}\mathbf{u}_a \tag{7.16}$$

Grouping by terms gives

$$\left(\bar{\mathbf{K}}_{r_1 r_1} + \bar{\mathbf{K}}_{r_2 r_1}\right)\mathbf{u}_{r_1} + \left(\bar{\mathbf{K}}_{r_1 r_2} + \bar{\mathbf{K}}_{r_2 r_2}\right)\mathbf{u}_{r_2} + \left(\bar{\mathbf{K}}_{r_1 a} + \bar{\mathbf{K}}_{r_2 a}\right)\mathbf{u}_a = \mathbf{0} \tag{7.17}$$

Solve for $\mathbf{u}_{r_1}$ to obtain

$$\mathbf{u}_{r_1} = -\left(\bar{\mathbf{K}}_{r_1 r_1} + \bar{\mathbf{K}}_{r_2 r_1}\right)^{-1}\left[\left(\bar{\mathbf{K}}_{r_1 r_2} + \bar{\mathbf{K}}_{r_2 r_2}\right)\mathbf{u}_{r_2} + \left(\bar{\mathbf{K}}_{r_1 a} + \bar{\mathbf{K}}_{r_2 a}\right)\mathbf{u}_a\right] \tag{7.18}$$

Written another way,

$$\mathbf{u}_{r_1} = \bar{\mathbf{G}}\mathbf{u}_{r_2} + \bar{\mathbf{H}}\mathbf{u}_a \tag{7.19}$$

where

$$\bar{\mathbf{G}} = -\left(\bar{\mathbf{K}}_{r_1 r_1} + \bar{\mathbf{K}}_{r_2 r_1}\right)^{-1}\left(\bar{\mathbf{K}}_{r_1 r_2} + \bar{\mathbf{K}}_{r_2 r_2}\right) \tag{7.20a}$$

$$\bar{\mathbf{H}} = -\left(\bar{\mathbf{K}}_{r_1 r_1} + \bar{\mathbf{K}}_{r_2 r_1}\right)^{-1}\left(\bar{\mathbf{K}}_{r_1 a} + \bar{\mathbf{K}}_{r_2 a}\right) \tag{7.20b}$$

Equation (7.19) forms the following transformation

$$\bar{\mathbf{u}} = \bar{\mathbf{L}}\hat{\mathbf{u}} \tag{7.21a}$$

$$\begin{Bmatrix} \mathbf{q}_i \\ \mathbf{u}_{r_1} \\ \mathbf{u}_{r_2} \\ \mathbf{u}_a \end{Bmatrix} = \begin{bmatrix} \mathbf{I} & \mathbf{0} & \mathbf{0} \\ \mathbf{0} & \bar{\mathbf{G}} & \bar{\mathbf{H}} \\ \mathbf{0} & \mathbf{I} & \mathbf{0} \\ \mathbf{0} & \mathbf{0} & \mathbf{I} \end{bmatrix} \begin{Bmatrix} \mathbf{q}_i \\ \mathbf{u}_{r_2} \\ \mathbf{u}_a \end{Bmatrix} \tag{7.21b}$$

where $\hat{\mathbf{u}}$ is a vector of displacements with statically-reduced interface coordinates, and $\bar{\mathbf{L}}$ is a locking matrix that maps $\hat{\mathbf{u}}$ back to the original HCB coordinates ($\bar{\mathbf{u}}$). Equation (7.21) constitutes a change of coordinates where $\mathbf{u}_{r_1}$ is written in terms of $\mathbf{u}_{r_2}$; it can be equivalently formulated by determining $\mathbf{u}_{r_2}$ in terms of $\mathbf{u}_{r_1}$ from Equation (7.17).

Next, compute the reduced mass and stiffness matrices using the locking matrix $\bar{\mathbf{L}}$:

$$\hat{\mathbf{M}} = \bar{\mathbf{L}}^{\mathrm{T}}\bar{\mathbf{M}}\bar{\mathbf{L}} = \begin{bmatrix} \mathbf{I} & \hat{\mathbf{M}}_{ir_2} & \hat{\mathbf{M}}_{ia} \\ \hat{\mathbf{M}}_{r_2 i} & \hat{\mathbf{M}}_{r_2 r_2} & \hat{\mathbf{M}}_{r_2 a} \\ \hat{\mathbf{M}}_{ai} & \hat{\mathbf{M}}_{ar_2} & \hat{\mathbf{M}}_{aa} \end{bmatrix} \tag{7.22a}$$

$$\hat{\mathbf{K}}^{\mathrm{c}} = \bar{\mathbf{L}}^{\mathrm{T}}\bar{\mathbf{K}}^{\mathrm{c}}\bar{\mathbf{L}} = \begin{bmatrix} (\boldsymbol{\Omega}^{\mathrm{FI}})^2 & \mathbf{0} & \mathbf{0} \\ \mathbf{0} & \hat{\mathbf{K}}^{\mathrm{c}}_{r_2 r_2} & \hat{\mathbf{K}}_{r_2 a} \\ \mathbf{0} & \hat{\mathbf{K}}_{ar_2} & \hat{\mathbf{K}}_{aa} \end{bmatrix} \tag{7.22b}$$

Interface eigenmodes are computed in the reduced system via

$$\left(\hat{\mathbf{K}}^{\mathrm{c}}_{r_2 r_2} - \hat{\omega}_j^2 \hat{\mathbf{M}}_{r_2 r_2}\right)\hat{\boldsymbol{\phi}}_j = \mathbf{0} \;;\; j = 1,2,\dots,n_{JI} \tag{7.23}$$

where $\hat{\omega}_j$ is the j^{th} reduced interface eigenfrequency, $\hat{\boldsymbol{\phi}}_j$ is the corresponding eigenmode, and n_{JI} is the number of retained modes. The reduction of DOF is afforded by the fact that $n_{JI} \ll \frac{n_r}{2}$. The reduced interface eigenmodes are assembled into an eigenmatrix ($\hat{\boldsymbol{\Phi}}$) as

$$\widehat{\boldsymbol{\Phi}} = \begin{bmatrix} \widehat{\boldsymbol{\phi}}_1 & \widehat{\boldsymbol{\phi}}_2 & \cdots & \widehat{\boldsymbol{\phi}}_{n_{JI}} \end{bmatrix} \tag{7.24}$$

Following this, compute reduced IC modes via

$$\widehat{\boldsymbol{\Psi}} = -\left(\widehat{\mathbf{K}}^{\mathrm{c}}_{r_2 r_2}\right)^{-1} \widehat{\mathbf{K}}_{r_2 a} \tag{7.25}$$

$\widehat{\boldsymbol{\Phi}}$ and $\widehat{\boldsymbol{\Psi}}$ form the reduced transformation matrix $\widehat{\mathbf{T}}$ as

$$\widehat{\mathbf{T}} = \begin{bmatrix} \mathbf{I} & \mathbf{0} & \mathbf{0} \\ \mathbf{0} & \widehat{\boldsymbol{\Phi}} & \widehat{\boldsymbol{\Psi}} \\ \mathbf{0} & \mathbf{0} & \mathbf{I} \end{bmatrix} \tag{7.26}$$

Finally, pre-multiply by $\bar{\mathbf{L}}$ to transform $\widehat{\mathbf{T}}$ to unreduced HCB coordinates, as

$$\overline{\mathbf{T}} = \bar{\mathbf{L}}\widehat{\mathbf{T}} = \begin{bmatrix} \mathbf{I} & \mathbf{0} & \mathbf{0} \\ \mathbf{0} & \overline{\boldsymbol{\Phi}} & \overline{\boldsymbol{\Psi}} \\ \mathbf{0} & \mathbf{0} & \mathbf{I} \end{bmatrix} \tag{7.27}$$

which has $(n_{FI} + n_r + n_a)$ rows and $(n_{FI} + n_{JI} + n_a)$ columns. Model order reduction is achieved by choosing n_{JI} to be much smaller than n_r. The JI eigenmodes are given by

$$\overline{\boldsymbol{\Phi}} = \begin{bmatrix} \overline{\mathbf{G}}\widehat{\boldsymbol{\Phi}} \\ \widehat{\boldsymbol{\Phi}} \end{bmatrix} \tag{7.28}$$

and the JI constraint modes are

$$\overline{\boldsymbol{\Psi}} = \begin{bmatrix} \overline{\mathbf{G}} + \overline{\mathbf{H}}\widehat{\boldsymbol{\Psi}} \\ \widehat{\boldsymbol{\Psi}} \end{bmatrix} \tag{7.29}$$

Similar to the SCC approach, the JI transformation in Equation (7.27) can be interpreted as a secondary HCB transformation on the interface DOF. A MATLAB function to compute a JI basis is shown in Algorithm 7.3. It is possible to combine JI modes with a GSI modification, but it is not shown in this study for the sake of brevity.

```
function T = JI(M, K, Kc, i, r1, r2, a, nJI)

% inputs
       % M    = sorted HCB mass matrix
       % K    = sorted linear HCB stiffness matrix
       % Kc   = sorted HCB stiffness matrix w/ contact contributions
       % i    = indices of fixed-interface DOF
       % r1   = indices of interface DOF (side 1)
       % r2   = indices of interface DOF (side 2)
       % a    = indices of active DOF
       % nGSI = number of GSI modes to retain
% outputs
       % T    = JI transformation matrix

%% JI basis
nFI      = length(i)                                    ; % number of FI modes
nr       = length(r1) + length(r2)                      ; % number of r DOF
na       = length(a)                                    ; % number of a DOF
G        = -(K(r1,r1)+K(r2,r1))\(K(r1,r2)+ K(r2,r2))    ; % 1st locking matrix
H        = -(K(r1,r1)+K(r2,r1))\(K(r1,a)+ K(r2,a))      ; % 2nd locking matrix
L        = blkdiag(eye(nFI), [G, H; eye(nr/2+na)])      ; % locking matrix
M        = L' * M * L                                   ; % JI mass matrix
Kc       = L' * Kc * L                                  ; % JI stiffness matrix
r        = [(nFI+1):(nFI+nr/2)]'                        ; % update r DOF indices
a        = [(nFI+1):(nFI+nr/2+na)]'                     ; % update a DOF indices
[Phi,~]  = eigs(Kc(r,r), M(r,r), nJI, 'sm')             ; % eigenmodes
Psi      = -Kc(r,r)\Kc(r,p)                             ; % constraint modes
Phi      = [G*Phi; Phi]                                 ; % unlock eigenmodes
Psi      = [(G*Psi+H); Psi]                             ; % unlock constraint modes
T        = [                                              …
             eye(nFI), zeros(nFI,nJI+na)                ; …
             zeros(nr,nFI), Phi, Psi                    ; …
             zeros(na,nFI+nJI), eye(na)                   …
]                                                       ; % JI transformation matrix

%% deflation
T             = T * diag(sqrt(diag(T'*T).^-1))  ; % convert to unit vectors
[T,~,~]       = svd(T, 'econ')                  ; % replace with singular vectors


end % function JI
```

Algorithm 7.3. Interface reduction with JI modes.

7.3. Interface Basis Enrichment

In nonlinear interface reduction, the modal bases shown in Sections 7.2 may not provide a desirable combination of accuracy and computational savings. In such a case, the original basis can be enriched with more advanced mode shapes to increase the accuracy with a fewer number of modes. This section outlines two new basis enrichment techniques. The first involves a novel

extension of the Enhanced Hurty/Craig-Bampton method [10,11], dubbed approximate residual interface (ARI) modes. The second technique computes interface modal derivatives (IMDs) by differentiating mode shapes with respect to generalized modal coordinates [12–15].

7.3.1. Approximate Residual Interface (ARI) Modes

Every projection-based reduced order model has some truncation error associated with it. In Equation (7.3), only the first n_{SCC} eigenmodes are retained (i.e. the dominant modes), and the remaining $(n_r - n_{SCC})$ modes are discarded (i.e. the residual modes). Approximate residual interface (ARI) modes are based on estimating the dynamic contribution of the residual modes, and then adding them back to the original basis without increasing its size. ARI modes are an extension of the Enhanced Hurty/Craig-Bampton method [10,11]. The derivation for ARI modes with a JI or GSI basis is similar to the one presented for the SCC case, but will not be explicitly derived for brevity.

First, let $\bar{\mathbf{\Phi}}^0$ be the original SCC eigenmatrix from Equation (7.4), and let $\bar{\mathbf{\Psi}}^0$ be the interface constraint modes from Equation (7.5), i.e.

$$\bar{\mathbf{\Phi}}^0 = \begin{bmatrix} \bar{\boldsymbol{\phi}}_1 & \bar{\boldsymbol{\phi}}_2 & \cdots & \bar{\boldsymbol{\phi}}_{n_{SCC}} \end{bmatrix} \tag{7.30a}$$

$$\bar{\mathbf{\Psi}}^0 = -(\bar{\mathbf{K}}_{rr}^{\mathrm{c}})^{-1}\bar{\mathbf{K}}_{ra} \tag{7.30b}$$

Also let $\bar{\mathbf{T}}^0$ be the original SCC transformation matrix, such that

$$\bar{\mathbf{T}}^0 = \begin{bmatrix} \mathbf{I} & \mathbf{0} & \mathbf{0} \\ \mathbf{0} & \bar{\mathbf{\Phi}}^0 & \bar{\mathbf{\Psi}}^0 \\ \mathbf{0} & \mathbf{0} & \mathbf{I} \end{bmatrix} \tag{7.31}$$

The goal of ARI modes is to construct some residual transformation matrix $\bar{\mathbf{T}}^{\mathrm{R}}$ that can be added to $\bar{\mathbf{T}}^0$ to form an improved basis of equal size, i.e.

$$\bar{\mathbf{T}} = \bar{\mathbf{T}}^0 + \bar{\mathbf{T}}^{\mathrm{R}} \tag{7.32}$$

$\bar{\boldsymbol{\Phi}}^0$ is referred to as the dominant interface eigenmatrix because it contains the modes retained in the original transformation. The residual interface eigenmatrix is

$$\bar{\boldsymbol{\Phi}}^{\mathrm{R}} = \begin{bmatrix} \bar{\boldsymbol{\Phi}}_{n_{SCC}+1} & \bar{\boldsymbol{\Phi}}_{n_{SCC}+2} & \cdots & \bar{\boldsymbol{\Phi}}_{n_r} \end{bmatrix} \tag{7.33}$$

and contains all the modes discarded in the original transformation. $\bar{\boldsymbol{\Phi}}^0$ and $\bar{\boldsymbol{\Phi}}^{\mathrm{R}}$ can be combined to form a full-order SCC transformation that includes all interface eigenmodes, as

$$\bar{\mathbf{u}} = \tilde{\mathbf{T}}\tilde{\mathbf{u}} \tag{7.34a}$$

$$\begin{Bmatrix} \mathbf{q}_i \\ \mathbf{u}_r \\ \mathbf{u}_a \end{Bmatrix} = \begin{bmatrix} \mathbf{I} & \mathbf{0} & \mathbf{0} & \mathbf{0} \\ \mathbf{0} & \bar{\boldsymbol{\Phi}}^0 & \bar{\boldsymbol{\Phi}}^{\mathrm{R}} & \bar{\boldsymbol{\Psi}}^0 \\ \mathbf{0} & \mathbf{0} & \mathbf{0} & \mathbf{I} \end{bmatrix} \begin{Bmatrix} \mathbf{q}_i \\ \mathbf{q}_r^0 \\ \mathbf{q}_r^{\mathrm{R}} \\ \mathbf{u}_a \end{Bmatrix} \tag{7.34b}$$

where $\bar{\mathbf{u}} = [\mathbf{q}_i \quad \mathbf{u}_r \quad \mathbf{u}_a]^{\mathrm{T}}$ is the original HCB displacement vector and $\tilde{\mathbf{u}} = [\mathbf{q}_i \quad \mathbf{q}_r^0 \quad \mathbf{q}_r^{\mathrm{R}} \quad \mathbf{u}_a]^{\mathrm{T}}$ is a SCC displacement vector of the same dimension as $\bar{\mathbf{u}}$. $\tilde{\mathbf{T}}$ is a square transformation matrix that maps $\tilde{\mathbf{u}}$ to $\bar{\mathbf{u}}$. This transformation represents a change of coordinates in the r DOF set, with no model order reduction due to the inclusion of all interface eigenmodes. Interior modal coordinates ($\mathbf{q}_i$) and active physical coordinates ($\mathbf{u}_a$) are retained through appropriately-sized identity partitions. The vectors $\mathbf{q}_r^0$ and $\mathbf{q}_r^{\mathrm{R}}$ represent the generalized modal coordinates for the dominant and residual interface modes, respectively.

Application of $\tilde{\mathbf{T}}$ to the HCB mass and stiffness matrices yields

$$\tilde{\mathbf{M}} = \tilde{\mathbf{T}}^{\mathrm{T}}\bar{\mathbf{M}}\tilde{\mathbf{T}} = \begin{bmatrix} \mathbf{I} & \bar{\mathbf{M}}_{ir}\bar{\boldsymbol{\Phi}}^0 & \bar{\mathbf{M}}_{ir}\bar{\boldsymbol{\Phi}}^{\mathrm{R}} & \bar{\mathbf{M}}_{ia}^{\Psi} \\ (\bar{\boldsymbol{\Phi}}^0)^{\mathrm{T}}\bar{\mathbf{M}}_{ri} & \mathbf{I} & \mathbf{0} & (\bar{\boldsymbol{\Phi}}^0)^{\mathrm{T}}\bar{\mathbf{M}}_{ra}^{\Psi} \\ (\bar{\boldsymbol{\Phi}}^{\mathrm{R}})^{\mathrm{T}}\bar{\mathbf{M}}_{ri} & \mathbf{0} & \mathbf{I} & (\bar{\boldsymbol{\Phi}}^{\mathrm{R}})^{\mathrm{T}}\bar{\mathbf{M}}_{ra}^{\Psi} \\ \left(\bar{\mathbf{M}}_{ia}^{\Psi}\right)^{\mathrm{T}} & (\bar{\mathbf{M}}_{ra}^{\Psi})^{\mathrm{T}}\bar{\boldsymbol{\Phi}}^0 & (\bar{\mathbf{M}}_{ra}^{\Psi})^{\mathrm{T}}\bar{\boldsymbol{\Phi}}^{\mathrm{R}} & \bar{\mathbf{M}}_{aa}^{\Psi} + (\bar{\mathbf{M}}_{ra}^{\Psi})^{\mathrm{T}}\bar{\boldsymbol{\Psi}}^0 \end{bmatrix} \tag{7.35a}$$

$$\widetilde{\mathbf{K}}^{\mathrm{c}} = \widetilde{\mathbf{T}}^{\mathrm{T}}\overline{\mathbf{K}}^{\mathrm{c}}\widetilde{\mathbf{T}} = \begin{bmatrix} (\boldsymbol{\Omega}^{\mathrm{FI}})^2 & \mathbf{0} & \mathbf{0} & \mathbf{0} \\ \mathbf{0} & (\overline{\boldsymbol{\Omega}}^{0})^2 & \mathbf{0} & \mathbf{0} \\ \mathbf{0} & \mathbf{0} & (\overline{\boldsymbol{\Omega}}^{\mathrm{R}})^2 & \mathbf{0} \\ \mathbf{0} & \mathbf{0} & \mathbf{0} & \overline{\mathbf{K}}_{aa} \end{bmatrix} \tag{7.35b}$$

where $\overline{\mathbf{M}}_{ia}^{\Psi}$, $\overline{\mathbf{M}}_{ra}^{\Psi}$, and $\overline{\mathbf{M}}_{aa}^{\Psi}$ are constrained interface mass matrices, given by

$$\overline{\mathbf{M}}_{ia}^{\Psi} = \overline{\mathbf{M}}_{ia} + \overline{\mathbf{M}}_{ir}\overline{\boldsymbol{\Psi}}^{0} \tag{7.36a}$$

$$\overline{\mathbf{M}}_{ra}^{\Psi} = \overline{\mathbf{M}}_{ra} + \overline{\mathbf{M}}_{rr}\overline{\boldsymbol{\Psi}}^{0} \tag{7.36b}$$

$$\overline{\mathbf{M}}_{aa}^{\Psi} = \overline{\mathbf{M}}_{aa} + \overline{\mathbf{M}}_{ar}\overline{\boldsymbol{\Psi}}^{0} \tag{7.36c}$$

$\overline{\boldsymbol{\Omega}}^{0}$ and $\overline{\boldsymbol{\Omega}}^{\mathrm{R}}$ are the dominant and residual interface eigenfrequency matrices, stated as

$$\overline{\boldsymbol{\Omega}}^{0} = \begin{bmatrix} \overline{\omega}_1 & & & \\ & \overline{\omega}_2 & & \\ & & \ddots & \\ & & & \overline{\omega}_{n_{SCC}} \end{bmatrix} \tag{7.37a}$$

$$\overline{\boldsymbol{\Omega}}^{\mathrm{R}} = \begin{bmatrix} \overline{\omega}_{n_{SCC}+1} & & & \\ & \overline{\omega}_{n_{SCC}+2} & & \\ & & \ddots & \\ & & & \overline{\omega}_{n_r} \end{bmatrix} \tag{7.37b}$$

Identity partitions appear in Equation (7.35a) due to the mass-normalization of $\overline{\boldsymbol{\Phi}}^{0}$ and $\overline{\boldsymbol{\Phi}}^{\mathrm{R}}$. Several zero matrix partitions that appear in Equations (7.35a) and (7.35b) arise from the orthogonality of the dominant interface modes ($\overline{\boldsymbol{\Phi}}^{0}$) with respect to the residual interface modes ($\overline{\boldsymbol{\Phi}}^{\mathrm{R}}$), stated mathematically as

$$(\overline{\boldsymbol{\Phi}}^{0})^{\mathrm{T}}\mathbf{A}\overline{\boldsymbol{\Phi}}^{\mathrm{R}} = \mathbf{0} \tag{7.38a}$$

$$(\overline{\boldsymbol{\Phi}}^{\mathrm{R}})^{\mathrm{T}}\mathbf{B}\overline{\boldsymbol{\Phi}}^{0} = \mathbf{0} \tag{7.38b}$$

where **A** and **B** are any appropriately-sized matrices. Other zero matrices in (7.35b) arise from the negative inverse stiffness term embedded in $\overline{\boldsymbol{\Psi}}^{0}$. For example, the $r-a$ partition of $\widetilde{\mathbf{K}}^{\mathrm{c}}$ is computed as

$$
\begin{aligned}
\widetilde{\mathbf{K}}^{\mathrm{c}}_{ra} &= \bar{\mathbf{K}}^{\mathrm{c}}_{ra} + \bar{\mathbf{K}}^{\mathrm{c}}_{rr}\bar{\mathbf{\Psi}}^{0} \\
&= \bar{\mathbf{K}}^{\mathrm{c}}_{ra} + \bar{\mathbf{K}}^{\mathrm{c}}_{rr}[-(\bar{\mathbf{K}}^{\mathrm{c}}_{rr})^{-1}\bar{\mathbf{K}}_{ra}] \\
&= \bar{\mathbf{K}}^{\mathrm{c}}_{ra} - \bar{\mathbf{K}}^{\mathrm{c}}_{rr}(\bar{\mathbf{K}}^{\mathrm{c}}_{rr})^{-1}\bar{\mathbf{K}}_{ra} \\
&= \bar{\mathbf{K}}^{\mathrm{c}}_{ra} - \bar{\mathbf{K}}_{ra} \\
&= \mathbf{0}
\end{aligned}
\tag{7.39}
$$

By symmetry, the $a-r$ partition of $\widetilde{\mathbf{K}}^{\mathrm{c}}$ is also a zero matrix, i.e.

$$
\widetilde{\mathbf{K}}^{\mathrm{c}}_{ar} = \left(\widetilde{\mathbf{K}}^{\mathrm{c}}_{ra}\right)^{\mathrm{T}} = \mathbf{0} \tag{7.40}
$$

The equation of free vibration in the system defined by $\widetilde{\mathbf{M}}$ and $\widetilde{\mathbf{K}}^{\mathrm{c}}$ is

$$
\left(\widetilde{\mathbf{K}}^{\mathrm{c}} - \tilde{\omega}^2\widetilde{\mathbf{M}}\right)\tilde{\mathbf{u}} = \mathbf{0} \tag{7.41a}
$$

$$
\begin{bmatrix}
(\mathbf{\Omega}^{\mathrm{FI}})^2 - \tilde{\omega}^2\mathbf{I} & -\tilde{\omega}^2\bar{\mathbf{M}}_{ir}\bar{\mathbf{\Phi}}^{0} & -\tilde{\omega}^2\bar{\mathbf{M}}_{ir}\bar{\mathbf{\Phi}}^{\mathrm{R}} & -\tilde{\omega}^2\bar{\mathbf{M}}^{\Psi}_{ia} \\
-\tilde{\omega}^2(\bar{\mathbf{\Phi}}^{0})^{\mathrm{T}}\bar{\mathbf{M}}_{ri} & (\bar{\mathbf{\Omega}}^{0})^2 - \tilde{\omega}^2\mathbf{I} & \mathbf{0} & -\tilde{\omega}^2(\bar{\mathbf{\Phi}}^{0})^{\mathrm{T}}\bar{\mathbf{M}}^{\Psi}_{ra} \\
-\tilde{\omega}^2(\bar{\mathbf{\Phi}}^{\mathrm{R}})^{\mathrm{T}}\bar{\mathbf{M}}_{ri} & \mathbf{0} & (\bar{\mathbf{\Omega}}^{\mathrm{R}})^2 - \tilde{\omega}^2\mathbf{I} & -\tilde{\omega}^2(\bar{\mathbf{\Phi}}^{\mathrm{R}})^{\mathrm{T}}\bar{\mathbf{M}}^{\Psi}_{ra} \\
-\tilde{\omega}^2\left(\bar{\mathbf{M}}^{\Psi}_{ia}\right)^{\mathrm{T}} & -\tilde{\omega}^2(\bar{\mathbf{M}}^{\Psi}_{ra})^{\mathrm{T}}\bar{\mathbf{\Phi}}^{0} & -\tilde{\omega}^2(\bar{\mathbf{M}}^{\Psi}_{ra})^{\mathrm{T}}\bar{\mathbf{\Phi}}^{\mathrm{R}} & \bar{\mathbf{K}}_{aa} - \tilde{\omega}^2\bar{\mathbf{M}}^{\Psi}_{aa} + (\bar{\mathbf{M}}^{\Psi}_{ra})^{\mathrm{T}}\bar{\mathbf{\Psi}}^{0}
\end{bmatrix}
\begin{Bmatrix}
\mathbf{q}_i \\ \mathbf{q}^{0}_r \\ \mathbf{q}^{\mathrm{R}}_r \\ \mathbf{u}_a
\end{Bmatrix}
=
\begin{Bmatrix}
\mathbf{0} \\ \mathbf{0} \\ \mathbf{0} \\ \mathbf{0}
\end{Bmatrix}
\tag{7.41b}
$$

where $\tilde{\omega}$ is an unknown eigenfrequency. The third line of Equation (7.41b) describes the force equilibrium of the residual interface mode partition, stated as

$$
-\tilde{\omega}^2(\bar{\mathbf{\Phi}}^{\mathrm{R}})^{\mathrm{T}}\bar{\mathbf{M}}_{ri}\mathbf{q}_i + [(\bar{\mathbf{\Omega}}^{\mathrm{R}})^2 - \tilde{\omega}^2\mathbf{I}]\mathbf{q}^{\mathrm{R}}_r - \tilde{\omega}^2(\bar{\mathbf{\Phi}}^{\mathrm{R}})^{\mathrm{T}}\bar{\mathbf{M}}^{\Psi}_{ra}\mathbf{u}_a = \mathbf{0} \tag{7.42}
$$

Solving for $\mathbf{q}^{\mathrm{R}}_r$ yields

$$
\mathbf{q}^{\mathrm{R}}_r = [(\bar{\mathbf{\Omega}}^{\mathrm{R}})^2 - \tilde{\omega}^2\mathbf{I}]^{-1}(\bar{\mathbf{\Phi}}^{\mathrm{R}})^{\mathrm{T}}\tilde{\omega}^2(\bar{\mathbf{M}}_{ri}\mathbf{q}_i + \bar{\mathbf{M}}^{\Psi}_{ra}\mathbf{u}_a) \tag{7.43}
$$

Left-multiply by $\bar{\mathbf{\Phi}}^{\mathrm{R}}$ to obtain

$$
\bar{\mathbf{\Phi}}^{\mathrm{R}}\mathbf{q}^{\mathrm{R}}_r = \bar{\mathbf{\Phi}}^{\mathrm{R}}[(\bar{\mathbf{\Omega}}^{\mathrm{R}})^2 - \tilde{\omega}^2\mathbf{I}]^{-1}(\bar{\mathbf{\Phi}}^{\mathrm{R}})^{\mathrm{T}} \cdot \tilde{\omega}^2(\bar{\mathbf{M}}_{ri}\mathbf{q}_i + \bar{\mathbf{M}}^{\Psi}_{ra}\mathbf{u}_a) \tag{7.44}
$$

Equation (7.44) reveals the residual flexibility matrix $\bar{\mathbf{F}}^{\mathrm{R}}$, equal to

$$
\bar{\mathbf{F}}^{\mathrm{R}} = \bar{\mathbf{\Phi}}^{\mathrm{R}}[(\bar{\mathbf{\Omega}}^{\mathrm{R}})^2 - \tilde{\omega}^2\mathbf{I}]^{-1}(\bar{\mathbf{\Phi}}^{\mathrm{R}})^{\mathrm{T}} \tag{7.45}
$$

$\bar{\mathbf{F}}^{\mathrm{R}}$ is approximated using a Neumann series expansion [16] as

$$
\bar{\mathbf{F}}^{\mathrm{R}} \approx \bar{\mathbf{\Phi}}^{\mathrm{R}}(\bar{\mathbf{\Omega}}^{\mathrm{R}})^{-2}(\bar{\mathbf{\Phi}}^{\mathrm{R}})^{\mathrm{T}} + \tilde{\omega}^2\bar{\mathbf{\Phi}}^{\mathrm{R}}(\bar{\mathbf{\Omega}}^{\mathrm{R}})^{-4}(\bar{\mathbf{\Phi}}^{\mathrm{R}})^{\mathrm{T}} \tag{7.46}
$$

or, in compact form:

$$\bar{\mathbf{F}}^{\mathrm{R}} \approx \bar{\mathbf{F}}^{\mathrm{RS}} + \tilde{\omega}^2 \bar{\mathbf{F}}^{\mathrm{RV}} \tag{7.47}$$

where

$$\bar{\mathbf{F}}^{\mathrm{RS}} = \bar{\boldsymbol{\Phi}}^{\mathrm{R}} (\bar{\boldsymbol{\Omega}}^{\mathrm{R}})^{-2} (\bar{\boldsymbol{\Phi}}^{\mathrm{R}})^{\mathrm{T}} \tag{7.48}$$

is the static residual flexibility matrix, and

$$\bar{\mathbf{F}}^{\mathrm{RV}} = \bar{\boldsymbol{\Phi}}^{\mathrm{R}} (\bar{\boldsymbol{\Omega}}^{\mathrm{R}})^{-4} (\bar{\boldsymbol{\Phi}}^{\mathrm{R}})^{\mathrm{T}} \tag{7.49}$$

is vibratory residual flexibility matrix. $\bar{\mathbf{F}}^{\mathrm{RS}}$ can be written as the difference between the total flexibility matrix and the dominant modal flexibility matrix, i.e.

$$\bar{\mathbf{F}}^{\mathrm{RS}} = \underbrace{(\bar{\mathbf{K}}^{\mathrm{c}}_{rr})^{-1}}_{\substack{total\ interface \\ flexibility\ matrix}} - \underbrace{\bar{\boldsymbol{\Phi}}^{0} (\bar{\boldsymbol{\Omega}}^{0})^{-2} (\bar{\boldsymbol{\Phi}}^{0})^{\mathrm{T}}}_{\substack{flexibility\ matrix \\ from\ dominant \\ interface\ modes}} \tag{7.50}$$

This allows $\bar{\mathbf{F}}^{\mathrm{RS}}$ to be determined without prior computation of $\bar{\boldsymbol{\Omega}}^{\mathrm{R}}$ or $\bar{\boldsymbol{\Phi}}^{\mathrm{R}}$. Substitute Equation (7.47) into Equation (7.44) to obtain

$$\begin{aligned} \bar{\boldsymbol{\Phi}}^{\mathrm{R}} \mathbf{q}_r^{\mathrm{R}} &= (\bar{\mathbf{F}}^{\mathrm{RS}} + \tilde{\omega}^2 \bar{\mathbf{F}}^{\mathrm{RV}}) \cdot \tilde{\omega}^2 (\bar{\mathbf{M}}_{ri} \mathbf{q}_i + \bar{\mathbf{M}}^{\Psi}_{ra} \mathbf{u}_a) \\ &= \tilde{\omega}^2 \bar{\mathbf{F}}^{\mathrm{RS}} (\bar{\mathbf{M}}_{ri} \mathbf{q}_i + \bar{\mathbf{M}}^{\Psi}_{ra} \mathbf{u}_a) + \tilde{\omega}^4 \bar{\mathbf{F}}^{\mathrm{RV}} (\bar{\mathbf{M}}_{ri} \mathbf{q}_i + \bar{\mathbf{M}}^{\Psi}_{ra} \mathbf{u}_a) \end{aligned} \tag{7.51}$$

Discarding terms higher than the order of $\tilde{\omega}^2$ yields

$$\bar{\boldsymbol{\Phi}}^{\mathrm{R}} \mathbf{q}_r^{\mathrm{R}} = \tilde{\omega}^2 \bar{\mathbf{F}}^{\mathrm{RS}} (\bar{\mathbf{M}}_{ri} \mathbf{q}_i + \bar{\mathbf{M}}^{\Psi}_{ra} \mathbf{u}_a) \tag{7.52}$$

Recall that, from the second line of Equation (7.34b),

$$\mathbf{u}_r = \bar{\boldsymbol{\Phi}}^{0} \mathbf{q}_r^{0} + \bar{\boldsymbol{\Phi}}^{\mathrm{R}} \mathbf{q}_r^{\mathrm{R}} + \bar{\boldsymbol{\Psi}}^{0} \mathbf{u}_p \tag{7.53}$$

Substitute Equation (7.52) into Equation (7.53) to obtain

$$\mathbf{u}_r = \bar{\boldsymbol{\Phi}}^{0} \mathbf{q}_r^{0} + \tilde{\omega}^2 \bar{\mathbf{F}}^{\mathrm{RS}} (\bar{\mathbf{M}}_{ri} \mathbf{q}_i + \bar{\mathbf{M}}^{\Psi}_{ra} \mathbf{u}_a) + \bar{\boldsymbol{\Psi}}^{0} \mathbf{u}_a \tag{7.54}$$

or, grouping by individual coordinate vectors,

$$\mathbf{u}_r = \tilde{\omega}^2 \bar{\mathbf{F}}^{\mathrm{RS}} \bar{\mathbf{M}}_{ri} \mathbf{q}_i + \bar{\boldsymbol{\Phi}}^{0} \mathbf{q}_r^{0} + (\bar{\boldsymbol{\Psi}}^{0} + \tilde{\omega}^2 \bar{\mathbf{F}}^{\mathrm{RS}} \bar{\mathbf{M}}^{\Psi}_{ra}) \mathbf{u}_a \tag{7.55}$$

Equation (7.55) reveals the total transformation matrix $\bar{\mathbf{T}}$ as

$$\bar{\mathbf{T}} = \begin{bmatrix} \mathbf{I} & \mathbf{0} & \mathbf{0} \\ \tilde{\omega}^2 \bar{\mathbf{F}}^{\mathrm{RS}} \bar{\mathbf{M}}_{ri} & \bar{\mathbf{\Phi}}^0 & \bar{\mathbf{\Psi}}^0 + \tilde{\omega}^2 \bar{\mathbf{F}}^{\mathrm{RS}} \bar{\mathbf{M}}_{ra}^{\Psi} \\ \mathbf{0} & \mathbf{0} & \mathbf{I} \end{bmatrix} \tag{7.56}$$

For the remainder of the derivations, it is convenient to split $\bar{\mathbf{T}}$ into $\bar{\mathbf{T}}^0$ and $\bar{\mathbf{T}}^{\mathrm{R}}$, according to Equation (7.32). $\bar{\mathbf{T}}^0$ is known from Equation (7.31), and $\bar{\mathbf{T}}^{\mathrm{R}}$ is

$$\bar{\mathbf{T}}^{\mathrm{R}} = \begin{bmatrix} \mathbf{0} & \mathbf{0} & \mathbf{0} \\ \bar{\mathbf{F}}^{\mathrm{RS}} \bar{\mathbf{M}}_{ri} & \mathbf{0} & \bar{\mathbf{F}}^{\mathrm{RS}} \bar{\mathbf{M}}_{ra}^{\Psi} \\ \mathbf{0} & \mathbf{0} & \mathbf{0} \end{bmatrix} \tilde{\omega}^2 \tag{7.57}$$

In its current state, the ARI transformation depends on the unknown frequency $\tilde{\omega}^2$. Using O'Callahan's approach [17], Equation (7.41a) is rewritten as

$$\tilde{\mathbf{K}}^{\mathrm{c}} \tilde{\mathbf{u}} = \tilde{\omega}^2 \tilde{\mathbf{M}} \tilde{\mathbf{u}} \tag{7.58}$$

This can be restated in interface-reduced coordinates as

$$\bar{\bar{\mathbf{K}}}^{\mathrm{c0}} \bar{\bar{\mathbf{u}}} = (\bar{\bar{\omega}}^0)^2 \bar{\bar{\mathbf{M}}}^0 \bar{\bar{\mathbf{u}}} \tag{7.59}$$

where

$$\bar{\bar{\mathbf{M}}}^0 = (\bar{\mathbf{T}}^0)^{\mathrm{T}} \bar{\mathbf{M}} \bar{\mathbf{T}}^0 \approx (\bar{\mathbf{T}}^0)^{\mathrm{T}} \tilde{\mathbf{M}} \bar{\mathbf{T}}^0 \tag{7.60a}$$

$$\bar{\bar{\mathbf{K}}}^{\mathrm{c0}} = (\bar{\mathbf{T}}^0)^{\mathrm{T}} \bar{\mathbf{K}}^{\mathrm{c}} \bar{\mathbf{T}}^0 \approx (\bar{\mathbf{T}}^0)^{\mathrm{T}} \tilde{\mathbf{K}}^{\mathrm{c}} \bar{\mathbf{T}}^0 \tag{7.60b}$$

The approximation made by substituting $\bar{\mathbf{M}}$ and $\bar{\mathbf{K}}^{\mathrm{c}}$with $\tilde{\mathbf{M}}$ and $\tilde{\mathbf{K}}^{\mathrm{c}}$ is purely numerical, because the transformation in Equation (7.35) uses all interface modes. As such, the error introduced by setting $\bar{\mathbf{M}} = \tilde{\mathbf{M}}$ and $\bar{\mathbf{K}}^{\mathrm{c}} = \tilde{\mathbf{K}}^{\mathrm{c}}$ is close to the machine precision threshold. Consequently, $(\bar{\bar{\omega}}^0)^2 \approx \bar{\omega}^2 \approx \tilde{\omega}^2$ for the dominant interface modes. Rearrange Equation (7.59) to obtain

$$\left(\bar{\bar{\mathbf{M}}}^0\right)^{-1} \bar{\bar{\mathbf{K}}}^{\mathrm{c0}} \bar{\bar{\mathbf{u}}} = (\bar{\bar{\omega}}^0)^2 \bar{\bar{\mathbf{u}}} \tag{7.61}$$

or

$$\bar{\bar{\mathbf{R}}}^0 \bar{\bar{\mathbf{u}}} = (\bar{\bar{\omega}}^0)^2 \bar{\bar{\mathbf{u}}} \tag{7.62}$$

where

$$\bar{\bar{\mathbf{R}}}^0 = \left(\bar{\bar{\mathbf{M}}}^0\right)^{-1}\bar{\bar{\mathbf{K}}}^{c0} = \begin{bmatrix} \bar{\bar{\mathbf{R}}}^0_{ii} & \bar{\bar{\mathbf{R}}}^0_{ir} & \bar{\bar{\mathbf{R}}}^0_{ia} \\ \bar{\bar{\mathbf{R}}}^0_{ri} & \bar{\bar{\mathbf{R}}}^0_{rr} & \bar{\bar{\mathbf{R}}}^0_{ra} \\ \bar{\bar{\mathbf{R}}}^0_{ai} & \bar{\bar{\mathbf{R}}}^0_{ar} & \bar{\bar{\mathbf{R}}}^0_{aa} \end{bmatrix} \tag{7.63}$$

Applying Equation (7.62) to Equation (7.57) yields

$$\bar{\mathbf{T}}^R = \begin{bmatrix} \mathbf{0} & \mathbf{0} & \mathbf{0} \\ \bar{\mathbf{F}}^{RS}\bar{\mathbf{M}}_{ri} & \mathbf{0} & \bar{\mathbf{F}}^{RS}\bar{\mathbf{M}}^{\Psi}_{ra} \\ \mathbf{0} & \mathbf{0} & \mathbf{0} \end{bmatrix}\bar{\bar{\mathbf{R}}}^0 \tag{7.64}$$

or, carrying out the matrix multiplications,

$$\bar{\mathbf{T}}^R = \begin{bmatrix} \mathbf{0} & \mathbf{0} & \mathbf{0} \\ \bar{\mathbf{\Gamma}}^R & \bar{\mathbf{\Phi}}^R & \bar{\mathbf{\Psi}}^R \\ \mathbf{0} & \mathbf{0} & \mathbf{0} \end{bmatrix} \tag{7.65}$$

where

$$\bar{\mathbf{\Gamma}}^R = \bar{\mathbf{F}}^{RS}\left(\bar{\mathbf{M}}_{ri}\bar{\bar{\mathbf{R}}}^0_{ii} + \bar{\mathbf{M}}^{\Psi}_{ra}\bar{\bar{\mathbf{R}}}^0_{ai}\right) \tag{7.66a}$$

$$\bar{\mathbf{\Phi}}^R = \bar{\mathbf{F}}^{RS}\left(\bar{\mathbf{M}}_{ri}\bar{\bar{\mathbf{R}}}^0_{ir} + \bar{\mathbf{M}}^{\Psi}_{ra}\bar{\bar{\mathbf{R}}}^0_{ar}\right) \tag{7.66b}$$

$$\bar{\mathbf{\Psi}}^R = \bar{\mathbf{F}}^{RS}\left(\bar{\mathbf{M}}_{ri}\bar{\bar{\mathbf{R}}}^0_{ia} + \bar{\mathbf{M}}^{\Psi}_{ra}\bar{\bar{\mathbf{R}}}^0_{aa}\right) \tag{7.66c}$$

Finally, the ARI transformation matrix is computed using Equation (7.32), yielding

$$\bar{\mathbf{T}} = \begin{bmatrix} \mathbf{I} & \mathbf{0} & \mathbf{0} \\ \bar{\mathbf{\Gamma}}^R & \bar{\mathbf{\Phi}}^0 + \bar{\mathbf{\Phi}}^R & \bar{\mathbf{\Psi}}^0 + \bar{\mathbf{\Psi}}^R \\ \mathbf{0} & \mathbf{0} & \mathbf{I} \end{bmatrix} \tag{7.67}$$

which has $(n_{FI} + n_r + n_a)$ rows and $(n_{FI} + n_{SCC} + n_a)$ columns – the same size as the original SCC transformation matrix. Algorithm 7.4 is a MATLAB function that computes the ARI transformation matrix.

```
function T = ARI(M, Kc, Phi0, Psi0, Omega0, T0, i, r, a, nIR)

% inputs
       % M           =      sorted HCB mass matrix
       % Kc          =      sorted HCB stiffness matrix w/ contact contributions
       % Phi0        =      dominant interface eigenmodes
       % Psi0        =      interface constraint modes
       % Omega0      =      dominant interface eigenfrequency matrix
       % T0          =      initial transformation matrix
       % i           =      indices of fixed-interface DOF
       % r           =      indices of interface DOF
       % a           =      indices of active DOF
       % nIR         =      number of retained modes in the IR model
% outputs
       % T           =      ARI transformation matrix

%% IR basis with ARI enrichment
nFI     = length(i)                                  ; % number of FI modes
nr      = length(r)                                  ; % number of r DOF
na      = length(a)                                  ; % number of a DOF
FRS     = Kc(r,r)\eye(nr) - Phi0*(Omega0^2)\Phi0'    ; % residual flexibility
MPsi    = M(r,a) + M(r,r)*Psi0                       ; % interface mass matrix
M0      = T0' * M * T0                               ; % initial IR mass matrix
Kc0     = T0' * Kc * T0                              ; % initial IR stiffness matrix
R0      = M0\Kc0                                     ; % R0 matrix
rIR     = [(nFI+1):(nFI+nIR)]'                       ; % r DOF indices (IR model)
pIR     = [(nFI+nIR+1):(nFI+nIR+na)]'                ; % a DOF indices (IR model)
GammaR  = FRS * (M(r,i)*R0(i,i) + MPsi*R0(aIR,i))      ; % ARI modes
PhiR    = FRS * (M(r,i)*R0(i,rIR) + MPsi*R0(aIR,rIR)) ; % "   "   "
PsiR    = FRS * (M(r,i)*R0(i,aIR) + MPsi*R0(aIR,aIR)) ; % "   "   "
T       = [                                            …
             eye(nFI), zeros(nFI,nIR+na)               ; …
             GammaR; (Phi0+PhiR); (Psi0+PsiR)          ; …
             zeros(na,nFI+nIR), eye(na)]                 …
]                                                      ; % T enriched by ARI modes

%% deflation
T            = T * diag(sqrt(diag(T'*T).^-1))  ; % convert to unit vectors
[T,~,~]      = svd(T, 'econ')                  ; % replace with singular vectors


end % function ARI
```

Algorithm 7.4. Interface reduction with ARI enrichment.

7.3.2. Interface Modal Derivatives (IMDs)

Another type of basis enrichment can be found in modal derivatives. First proposed by Idelsohn [12,13], modal derivatives are obtained by differentiating static and dynamic mode shapes with respect to generalized modal coordinates. Modal derivatives have recently been adopted for nonlinear interface reduction [18–20], but are computed using the full-order finite

element model. The modal derivatives shown here, on the other hand, are computed from the HCB mass and stiffness matrices alone. They are henceforth referred to as interface modal derivatives (IMDs) because they are determined specifically for interface reduction, using previously-derived interface modes. The following derivations compute IMDs for a SCC basis, with no GSI modification or ARI enrichment. IMDs can be computed using any combination JI modes, GSI modes, and/or ARI modes, but these cases are not shown here for brevity.

To begin, differentiate Equation (7.3) with respect to the k^{th} generalized modal coordinate. That is,

$$\frac{\partial}{\partial \mathrm{q}_k}\left[\left(\bar{\mathbf{K}}_{rr}^{\mathrm{c}} - \bar{\omega}_j^2 \bar{\mathbf{M}}_{rr}\right)\bar{\boldsymbol{\Phi}}_j\right] = \frac{\partial \mathbf{0}}{\partial \mathrm{q}_k} \tag{7.68}$$

where q_k is the k^{th} interface modal coordinate ($k = 1, 2, \ldots, n_{SCC}$). Applying the chain rule of differentiation yields

$$\left(\bar{\mathbf{K}}_{rr}^{\mathrm{c}} - \bar{\omega}_j^2 \bar{\mathbf{M}}_{rr}\right)\frac{\partial \bar{\boldsymbol{\Phi}}_j}{\partial \mathrm{q}_k} + \left(\frac{\partial \bar{\mathbf{K}}_{rr}^{\mathrm{c}}}{\partial \mathrm{q}_k} - \frac{\partial \bar{\omega}_j^2}{\partial \mathrm{q}_k}\bar{\mathbf{M}}_{rr}\right)\bar{\boldsymbol{\Phi}}_j = \mathbf{0} \tag{7.69}$$

where

$$\frac{\partial \bar{\omega}_j^2}{\partial \mathrm{q}_k} = \frac{\partial}{\partial \mathrm{q}_k}\left(\bar{\boldsymbol{\Phi}}_j^{\mathrm{T}} \bar{\mathbf{K}}_{rr}^{\mathrm{c}} \bar{\boldsymbol{\Phi}}_j\right) = \bar{\boldsymbol{\Phi}}_j^{\mathrm{T}} \frac{\partial \bar{\mathbf{K}}_{rr}^{\mathrm{c}}}{\partial \mathrm{q}_k}\bar{\boldsymbol{\Phi}}_j + \bar{\boldsymbol{\Phi}}_j^{\mathrm{T}} \bar{\mathbf{K}}_{rr}^{\mathrm{c}} \frac{\partial \bar{\boldsymbol{\Phi}}_j}{\partial \mathrm{q}_k} + \left(\frac{\partial \bar{\boldsymbol{\Phi}}_j}{\partial \mathrm{q}_k}\right)^{\mathrm{T}} \bar{\mathbf{K}}_{rr}^{\mathrm{c}} \bar{\boldsymbol{\Phi}}_j \tag{7.70}$$

The last two terms in Equation (7.70) vanish due to the orthogonality of dynamic modes with respect to their derivatives, as shown by Mottershead and Friswell [21]. Thus, the derivative of the eigenvalue $\bar{\omega}_j^2$ with respect to modal coordinate q_k is

$$\frac{\partial \bar{\omega}_j^2}{\partial \mathrm{q}_k} = \bar{\boldsymbol{\Phi}}_j^{\mathrm{T}} \frac{\partial \bar{\mathbf{K}}_{rr}^{\mathrm{c}}}{\partial \mathrm{q}_k}\bar{\boldsymbol{\Phi}}_j \tag{7.71}$$

Substituting Equation (7.71) into Equation (7.69) results in

$$\left(\overline{\mathbf{K}}_{rr}^{\mathrm{c}} - \bar{\omega}_j^2 \overline{\mathbf{M}}_{rr}\right) \frac{\partial \overline{\boldsymbol{\Phi}}_j}{\partial \mathrm{q}_k} + \left(\frac{\partial \overline{\mathbf{K}}_{rr}^{\mathrm{c}}}{\partial \mathrm{q}_k} - \overline{\boldsymbol{\Phi}}_j^{\mathrm{T}} \frac{\partial \overline{\mathbf{K}}_{rr}^{\mathrm{c}}}{\partial \mathrm{q}_k} \overline{\boldsymbol{\Phi}}_j \overline{\mathbf{M}}_{rr} \right) \overline{\boldsymbol{\Phi}}_j = \mathbf{0} \tag{7.72}$$

Let $\overline{\boldsymbol{\theta}}_{jk}^{\mathrm{V}} = \frac{\partial \overline{\boldsymbol{\Phi}}_j}{\partial \mathrm{q}_k}$ be the vibratory IMD, equal to

$$\overline{\boldsymbol{\theta}}_{jk}^{\mathrm{V}} = \left(\overline{\mathbf{K}}_{rr}^{\mathrm{c}} - \bar{\omega}_j^2 \overline{\mathbf{M}}_{rr}\right)^{-1} \left(\overline{\boldsymbol{\Phi}}_j^{\mathrm{T}} \frac{\partial \overline{\mathbf{K}}_{rr}^{\mathrm{c}}}{\partial \mathrm{q}_k} \overline{\boldsymbol{\Phi}}_j \overline{\mathbf{M}}_{rr} - \frac{\partial \overline{\mathbf{K}}_{rr}^{\mathrm{c}}}{\partial \mathrm{q}_k} \right) \overline{\boldsymbol{\Phi}}_j \tag{7.73}$$

Witteveen and Pichler showed that the inertial terms of Equation (7.73) can be neglected [22], in order to eliminate the costly computation of $\left(\overline{\mathbf{K}}_{rr}^{\mathrm{c}} - \bar{\omega}_j^2 \overline{\mathbf{M}}_{rr}\right)^{-1}$ for $j = 1, 2, \ldots, n_{SCC}$. Thus,

$$\overline{\boldsymbol{\theta}}_{j,k}^{\mathrm{V}} = \frac{\partial \overline{\boldsymbol{\Phi}}_j}{\partial \mathrm{q}_k} = -(\overline{\mathbf{K}}_{rr}^{\mathrm{c}})^{-1} \frac{\partial \overline{\mathbf{K}}_{rr}^{\mathrm{c}}}{\partial \mathrm{q}_k} \overline{\boldsymbol{\Phi}}_j \tag{7.74}$$

The k^{th} vibratory IMD matrix is

$$\overline{\boldsymbol{\Theta}}_k^{\mathrm{V}} = \begin{bmatrix} \overline{\boldsymbol{\theta}}_{1,k}^{\mathrm{V}} & \overline{\boldsymbol{\theta}}_{2,k}^{\mathrm{V}} & \cdots & \overline{\boldsymbol{\theta}}_{\mathrm{n_{SCC}},k}^{\mathrm{V}} \end{bmatrix} \tag{7.75}$$

or, in compact form,

$$\overline{\boldsymbol{\Theta}}_k^{\mathrm{V}} = \frac{\partial \overline{\boldsymbol{\Phi}}}{\partial \mathrm{q}_k} = -(\overline{\mathbf{K}}_{rr}^{\mathrm{c}})^{-1} \frac{\partial \overline{\mathbf{K}}_{rr}^{\mathrm{c}}}{\partial \mathrm{q}_k} \overline{\boldsymbol{\Phi}} \tag{7.76}$$

In Equation (7.76), $\overline{\boldsymbol{\Phi}}$ is the collection of SCC eigenmodes, and $\frac{\partial \overline{\mathbf{K}}_{rr}^{\mathrm{c}}}{\partial \mathrm{q}_k}$ is the change of the constrained stiffness matrix about the preloaded equilibrium, with respect to the modal amplitude q_k. Thus, the j^{th} column of $\overline{\boldsymbol{\Theta}}_k^{\mathrm{V}}$, stated as $\overline{\boldsymbol{\theta}}_{j,k}^{\mathrm{V}}$, is the static deformation induced by a force equal to $-\frac{\partial \overline{\mathbf{K}}_{rr}^{\mathrm{c}}}{\partial \mathrm{q}_k} \overline{\boldsymbol{\Phi}}_j$.

Equation (7.76) provides a straightforward formula for computing vibratory IMDs, but derivatives of static mode shapes must still be determined. To obtain the static IMDs, first pre-multiply Equation (7.5) by $\overline{\mathbf{K}}_{rr}^{\mathrm{c}}$ to obtain

$$\overline{\mathbf{K}}_{rr}^{\mathrm{c}} \overline{\boldsymbol{\Psi}} = -\overline{\mathbf{K}}_{ra} \tag{7.77}$$

Differentiation with respect to q_k yields

$$\frac{\partial(\bar{\mathbf{K}}_{rr}^{\mathrm{c}}\bar{\boldsymbol{\Psi}})}{\partial \mathrm{q}_k} = -\frac{\partial \bar{\mathbf{K}}_{ra}}{\partial \mathrm{q}_k} \tag{7.78}$$

There are n_a static modes contained in $\bar{\boldsymbol{\Psi}}$, so the index k now varies from 1 to n_a. The right-hand side of Equation (7.78) is zero because only the $r-r$ partition of the stiffness matrix will change under modal perturbation. Apply the chain rule of differentiation to obtain

$$\frac{\partial(\bar{\mathbf{K}}_{rr}^{\mathrm{c}}\bar{\boldsymbol{\Psi}})}{\partial \mathrm{q}_k} = \bar{\mathbf{K}}_{rr}^{\mathrm{c}}\frac{\partial \bar{\boldsymbol{\Psi}}}{\partial \mathrm{q}_k} + \frac{\partial \bar{\mathbf{K}}_{rr}^{\mathrm{c}}}{\partial \mathrm{q}_k}\bar{\boldsymbol{\Psi}} = \mathbf{0} \tag{7.79}$$

Solve for the k^{th} static IMD matrix $\bar{\boldsymbol{\Theta}}^{\mathrm{S}}$ as

$$\bar{\boldsymbol{\Theta}}_k^{\mathrm{S}} = \frac{\partial \bar{\boldsymbol{\Psi}}}{\partial \mathrm{q}_k} = -(\bar{\mathbf{K}}_{rr}^{\mathrm{c}})^{-1}\frac{\partial \bar{\mathbf{K}}_{rr}^{\mathrm{c}}}{\partial \mathrm{q}_k}\bar{\boldsymbol{\Psi}} \tag{7.80}$$

Equations (7.76) and (7.80) have identical forms, implying that the computation of static and vibratory IMD is identical when neglecting inertial terms. As such, a general IMD matrix $\bar{\boldsymbol{\Theta}}_k$ is defined as

$$\bar{\boldsymbol{\Theta}}_k = \frac{\partial \bar{\mathbf{T}}'}{\partial \mathrm{q}_k} = -(\bar{\mathbf{K}}^{\mathrm{c}})^{-1}\frac{\partial \bar{\mathbf{K}}^{\mathrm{c}}}{\partial \mathrm{q}_k}\bar{\mathbf{T}}' \tag{7.81}$$

where $\bar{\mathbf{T}}'$ is a truncated version of $\bar{\mathbf{T}}$ that does not include the columns corresponding to the fixed-interface DOF, i.e.

$$\bar{\mathbf{T}}' = \begin{bmatrix} \mathbf{0} & \mathbf{0} \\ \bar{\boldsymbol{\Phi}} & \bar{\boldsymbol{\Psi}} \\ \mathbf{0} & \mathbf{I} \end{bmatrix} \tag{7.82}$$

The first n_{FI} columns of $\bar{\mathbf{T}}$ are not included in $\bar{\mathbf{T}}'$ because

$$\frac{\partial}{\partial \mathrm{q}_k}\begin{bmatrix} \mathbf{I} \\ \mathbf{0} \\ \mathbf{0} \end{bmatrix} = \begin{bmatrix} \mathbf{0} \\ \mathbf{0} \\ \mathbf{0} \end{bmatrix} \; \forall \; k \tag{7.83}$$

$\bar{\boldsymbol{\Theta}}_k$ is matrix with $(n_{FI} + n_r + n_a)$ rows and $(n_{SCC} + n_a)$ columns. An IMD matrix must be computed for every $k = 1, 2, \ldots, (n_{SCC} + n_a)$, such that

$$\bar{\boldsymbol{\Theta}} = \begin{bmatrix} \bar{\boldsymbol{\Theta}}_1 & \bar{\boldsymbol{\Theta}}_2 & \cdots & \bar{\boldsymbol{\Theta}}_{(n_{SCC}+n_a)} \end{bmatrix} \tag{7.84}$$

$\bar{\boldsymbol{\Theta}}$ has $(n_{FI} + n_r + n_a)$ rows and $(n_{SCC} + n_a)^2$ columns.

IMDs require computation of a stiffness matrix derivative $\frac{\partial \bar{\mathbf{K}}^{\mathrm{c}}}{\partial \mathrm{q}_k}$. In this work, the stiffness matrix derivative is computed numerically using finite difference approximations, as a perturbation about the preloaded state:

$$\left(\frac{\partial \bar{\mathbf{K}}^{\mathrm{c}}}{\partial \mathrm{q}_k}\right)^{+} = \frac{\bar{\mathbf{K}}(\bar{\mathbf{u}}^{\mathrm{PL}} + \mathrm{h}\bar{\mathbf{t}}'_k) - \bar{\mathbf{K}}(\bar{\mathbf{u}}^{\mathrm{PL}})}{\mathrm{h}} \tag{7.85}$$

where h is a user-defined step size and $\bar{\mathbf{t}}'_k$ is the k^{th} column of $\bar{\mathbf{T}}'$ $\left(k = 1, 2, \ldots, (n_{SCC} + n_a)\right)$. The superscript "+" signifies that $\frac{\partial \bar{\mathbf{K}}^{\mathrm{c}}}{\partial \mathrm{q}_k}$ is computed using the forward difference method. The displacement-dependent stiffness matrix $\bar{\mathbf{K}}\left(\bar{\mathbf{u}}^{\mathrm{PL}} + \mathrm{h}\bar{\mathbf{t}}'_j\right)$ is computed via

$$\bar{\mathbf{K}}(\bar{\mathbf{u}}^{\mathrm{PL}} + \mathrm{h}\bar{\mathbf{t}}'_k) = \bar{\mathbf{K}} + \left.\frac{\partial \bar{\mathbf{f}}^{\mathrm{c}}(\bar{\mathbf{u}})}{\partial \bar{\mathbf{u}}}\right|_{\bar{\mathbf{u}}=\bar{\mathbf{u}}^{\mathrm{PL}}+\mathrm{h}\bar{\mathbf{t}}'_k} \tag{7.86}$$

Recalling Equation (7.2), the stiffness matrix derivative can be simplified to

$$\left(\frac{\partial \bar{\mathbf{K}}^{\mathrm{c}}}{\partial \mathrm{q}_k}\right)^{+} = \frac{\left.\frac{\partial \bar{\mathbf{f}}^{\mathrm{c}}(\bar{\mathbf{u}})}{\partial \bar{\mathbf{u}}}\right|_{\bar{\mathbf{u}}=\bar{\mathbf{u}}^{\mathrm{PL}}+\mathrm{h}\bar{\mathbf{t}}'_k} - \left.\frac{\partial \bar{\mathbf{f}}^{\mathrm{c}}(\bar{\mathbf{u}})}{\partial \bar{\mathbf{u}}}\right|_{\bar{\mathbf{u}}=\bar{\mathbf{u}}^{\mathrm{PL}}}}{\mathrm{h}} \tag{7.87}$$

Perturbation of the preload displacement by $\mathrm{h}\bar{\mathbf{t}}'_k$ is, in general, asymmetric. Stated mathematically,

$$\left.\frac{\partial \bar{\mathbf{f}}^{\mathrm{c}}(\bar{\mathbf{u}})}{\partial \bar{\mathbf{u}}}\right|_{\bar{\mathbf{u}}=\bar{\mathbf{u}}^{\mathrm{PL}}-\mathrm{h}\bar{\mathbf{t}}'_k} \neq -\left.\frac{\partial \bar{\mathbf{f}}^{\mathrm{c}}(\bar{\mathbf{u}})}{\partial \bar{\mathbf{u}}}\right|_{\bar{\mathbf{u}}=\bar{\mathbf{u}}^{\mathrm{PL}}+\mathrm{h}\bar{\mathbf{t}}'_k} \tag{7.88}$$

As such, the stiffness matrix derivative must be computed forwards, according to Equation (7.87), and backwards, according to

$$\left(\frac{\partial \bar{\mathbf{K}}^{\mathrm{c}}}{\partial \mathrm{q}_k}\right)^{-} = \frac{\left.\frac{\partial \bar{\mathbf{f}}^{\mathrm{c}}(\bar{\mathbf{u}})}{\partial \bar{\mathbf{u}}}\right|_{\bar{\mathbf{u}}=\bar{\mathbf{u}}^{\mathrm{PL}}} - \left.\frac{\partial \bar{\mathbf{f}}^{\mathrm{c}}(\bar{\mathbf{u}})}{\partial \bar{\mathbf{u}}}\right|_{\bar{\mathbf{u}}=\bar{\mathbf{u}}^{\mathrm{PL}}-\mathrm{h}\bar{\mathbf{t}}'_k}}{\mathrm{h}} \tag{7.89}$$

where a superscript "−" signifies the backward difference formula. Consequently, Equation (7.81) must be evaluated twice, as

$$\overline{\boldsymbol{\Theta}}_k^{+} = \frac{\partial \overline{\mathbf{T}}'}{\partial \mathrm{q}_k} = -(\overline{\mathbf{K}}^{\mathrm{c}})^{-1}\left(\frac{\partial \overline{\mathbf{K}}^{\mathrm{c}}}{\partial \mathrm{q}_k}\right)^{+}\overline{\mathbf{T}}' \tag{7.90a}$$

$$\overline{\boldsymbol{\Theta}}_k^{-} = \frac{\partial \overline{\mathbf{T}}'}{\partial \mathrm{q}_k} = -(\overline{\mathbf{K}}^{\mathrm{c}})^{-1}\left(\frac{\partial \overline{\mathbf{K}}^{\mathrm{c}}}{\partial \mathrm{q}_k}\right)^{-}\overline{\mathbf{T}}' \tag{7.90b}$$

Similarly, the complete IMD matrix is now

$$\overline{\boldsymbol{\Theta}} = \left[\overline{\boldsymbol{\Theta}}_1^{+} \quad \overline{\boldsymbol{\Theta}}_1^{-} \quad \overline{\boldsymbol{\Theta}}_2^{+} \quad \overline{\boldsymbol{\Theta}}_2^{-} \quad \cdots \quad \overline{\boldsymbol{\Theta}}_{(n_{SCC}+n_a)}^{+} \quad \overline{\boldsymbol{\Theta}}_{(n_{SCC}+n_a)}^{-}\right] \tag{7.91}$$

The step size h is chosen heuristically, such that the structure of interest has a 5% difference in contact area, relative to the preloaded configuration. To explain this, let $\mathrm{CA}(\overline{\mathbf{u}})$ be a function that computes the contact area due to an HCB displacement $\overline{\mathbf{u}}$, as

$$\mathrm{CA}(\overline{\mathbf{u}}) = \frac{\{number\ of\ interface\ node\ pairs\ in\ contact\}}{\{total\ number\ of\ interface\ node\ pairs\}} \cdot 100\% \tag{7.92}$$

The step size should be chosen such that, for $k = 1, 2, \ldots, n_{SCC} + n_a$,

$$|\mathrm{CA}(\overline{\mathbf{u}}^{\mathrm{PL}} + \mathrm{h}\bar{\mathbf{t}}_k') - \mathrm{CA}(\overline{\mathbf{u}}^{\mathrm{PL}})| \approx 5\% \tag{7.93}$$

when computing $\left(\frac{\partial \overline{\mathbf{K}}^{\mathrm{c}}}{\partial \mathrm{q}_k}\right)^{+}$, and

$$|\mathrm{CA}(\overline{\mathbf{u}}^{\mathrm{PL}}) - \mathrm{CA}(\overline{\mathbf{u}}^{\mathrm{PL}} - \mathrm{h}\bar{\mathbf{t}}_k')| \approx 5\% \tag{7.94}$$

when computing $\left(\frac{\partial \overline{\mathbf{K}}^{\mathrm{c}}}{\partial \mathrm{q}_k}\right)^{-}$. This process is a generalization of Witteveen and Pichler's method [22], which can be recovered by setting h = 1. Using h = 1 for all modes and directions (+ or −) ignores the relative degree to which each mode induces nonlinearity in the system, as gauged by contact area change. For example, it is possible that one mode will cause a 1% change in the contact area when scaled by a factor of 20, but another mode will cause a 10% change in the contact area when scaled by a factor of 0.01. Furthermore, a mode can induce different contact area changes when

scaled positively vs. negatively. As a result, using a uniform step size can misrepresent the stiffness matrix derivatives and potentially decrease the overall accuracy of the IMD set. Determining h for each mode and direction requires slightly more upfront computational effort, but generates modal derivatives based on a criterion of consistent nonlinear excitation.

Before further analysis is carried out, each column of $\overline{\boldsymbol{\Theta}}$, denoted $\overline{\boldsymbol{\theta}}_j$, should be normalized by $\left(\overline{\boldsymbol{\theta}}_j\right)^{\mathrm{T}}\overline{\mathbf{K}}^{\mathrm{c}}\overline{\boldsymbol{\theta}}_j$. This ensures that the importance of each mode shape is determined by its direction and not by its magnitude. Using $\overline{\mathbf{K}}^{\mathrm{c}}$ for the normalization is convenient because it is already used in the computation of $\overline{\boldsymbol{\Theta}}$, but is not strictly required. It is theoretically possible to normalize by $\overline{\mathbf{M}}$, for example, but its effect on the present method is not investigated here. Other researchers [23] have converted every modal derivative to a unit vector and then performed a rank-revealing QR decomposition (RRQRD) or singular value decomposition (SVD). In this study, $\overline{\boldsymbol{\Theta}}$ is modified using the proper-orthogonal decomposition (POD) [24], which produces a much smaller set of properly orthogonal interface modal derivatives (POIMDs), denoted by $\breve{\boldsymbol{\Theta}}$. The POIMDs are then combined with the initial SCC transformation matrix shown in Equation (7.3). The final transformation matrix, with SCC modes and POIMDs, is then deflated according to the procedures described in Section 6.3 (magnitude scaling followed by SVD).

The POD begins by computing the eigenvalues of a system defined by

$$(\overline{\boldsymbol{\Theta}}^{\mathrm{T}}\overline{\mathbf{K}}^{\mathrm{c}}\overline{\boldsymbol{\Theta}})\breve{\mathbf{s}}_j = \breve{\lambda}_j\breve{\mathbf{s}}_j \quad ; \quad j = 1, 2, \dots, n_{dc} \tag{7.95}$$

where $\breve{\lambda}_j$ is the j^{th} POD eigenvalue and $\breve{\mathbf{s}}_j$ is its corresponding eigenvector. The POD sorts the eigenvalues in descending order. That is, $\breve{\lambda}_1$ is the largest eigenvalue and $\breve{\lambda}_{n_{dc}}$ is the smallest eigenvalue. Equation (7.95) is considered a weighted POD due to the inclusion of $\overline{\mathbf{K}}^{\mathrm{c}}$, which allows an interface energy criterion ($\breve{\mathrm{E}}$) to be computed as

$$\breve{\mathrm{E}}(n_{dr}) = \frac{\sum_{j=1}^{n_{dr}} \breve{\lambda}_j}{\sum_{j=1}^{n_{dc}} \breve{\lambda}_j} \tag{7.96}$$

where n_{dr} is the number of retained IMDs. According to Witteveen and Pichler [22], n_{dr} should be chosen such that $0.95 \leq \breve{\mathrm{E}}(n_{dr}) \leq 0.9999$. Generally, this is can be accomplished using a small fraction of the computed derivatives. Once n_{dr} is selected, the IMDs are updated according to

$$\breve{\boldsymbol{\theta}}_j = \frac{1}{\sqrt{\breve{\lambda}_j}} \bar{\boldsymbol{\Theta}} \breve{\mathbf{s}}_j \quad ; \quad j = 1, 2, \ldots, n_{dr} \tag{7.97}$$

Finally, the POIMD matrix is assembled via

$$\breve{\boldsymbol{\Theta}} = \begin{bmatrix} \breve{\boldsymbol{\theta}}_1 & \breve{\boldsymbol{\theta}}_2 & \cdots & \breve{\boldsymbol{\theta}}_{n_{dr}} \end{bmatrix} = \begin{bmatrix} \breve{\boldsymbol{\Theta}}_i \\ \breve{\boldsymbol{\Theta}}_r \\ \breve{\boldsymbol{\Theta}}_a \end{bmatrix} \tag{7.98}$$

where $\breve{\boldsymbol{\Theta}}_i$, $\breve{\boldsymbol{\Theta}}_r$, and $\breve{\boldsymbol{\Theta}}_a$ are the POIMD submatrices associated with the fixed-interface DOF (i), interface DOF (r), and active DOF (a), respectively. $\breve{\boldsymbol{\Theta}}$ is concatenated at the end of the original SCC matrix to form the final transformation matrix:

$$\bar{\mathbf{T}} = \begin{bmatrix} \mathbf{I} & \mathbf{0} & \mathbf{0} & \breve{\boldsymbol{\Theta}}_i \\ \mathbf{0} & \bar{\boldsymbol{\Phi}} & \bar{\boldsymbol{\Psi}} & \breve{\boldsymbol{\Theta}}_r \\ \mathbf{0} & \mathbf{0} & \mathbf{I} & \breve{\boldsymbol{\Theta}}_a \end{bmatrix} \tag{7.99}$$

which has $(n_{FI} + n_r + n_a)$ rows and $(n_{FI} + n_{SCC} + n_a + n_{dr})$ columns. The interface reduction derives from the fact that $(n_{SCC} + n_{dr}) \ll n_r$. Equation (7.98) shows the first and only interface reduction matrix with nonzero, non-identity partitions on the top and bottom rows of $\bar{\mathbf{T}}$. As such, a transformation with POIMDs affects the fixed-interface (i) and active DOF (a), as well as the interface DOF (r). A MATLAB function to compute a transformation matrix with POIMDs is shown in Algorithm 7.5.

```
function [T, E, ndr] = POIMD(T, Kc, uPL, h_all, E_targ, idInclude)

% inputs
       % T           =      initial IR transformation matrix
       % Kc          =      sorted HCB stiffness matrix w/ contact contributions
       % uPL         =      sorted HCB preload displacement vector
       % h_all       =      nModex2 matrix of step sizes
       % E_targ      =      target interface energy retention ratio
       % idInclude   =      indices of the columns of T for which IMDs are computed
% outputs
       % T           =      IR transformation matrix with POIMDs
       % E           =      interface energy retention curve
       % ndr         =      number of retained POIMDs
% required subroutines
       % dfcdu(): returns the Jacobian of contact forces with respect to the
       %           input displacement vector

%% IMDs
Tprime  = T(:,idInclude)   ; % truncated IR transformation matrix
nMode   = size(Tprime,2)   ; % number of interface modes
Theta   = []               ; % initialize IMDs
dfcduPL = dfcdu(uPL)       ; % contact force Jacobian at preloaded configuration
for sign = [-1 1]
  for k = 1 : nMode
    h     = h_all(k,(sign+3)/2)                                    ; % step size
    dKcdq = (sign*dfcdu(uPL+sign*h*Tprime(:,k)) - sign*dfcduPL)/h ; % dKc/dq
    Theta = [Theta, dKcdq*Tprime]                                  ; % update IMDs
  end
end
Theta  = -Kc\Theta ; % finalize IMDs

%% POD
[S, lambda]         = eig(Theta'*Kc*Theta)           ; % POD eigenanalysis
[lambda, sortID]    = sort(diag(lambda),'descend')   ; % sorted POD eigenvalues
S                   = S(:,sortID)                    ; % sorted POD eigenmodes

%% POIMDs
E             = cumsum([0;sum(lambda)])/sum(lambda)   ; % energy retention ratio
[~,ndr]       = min(abs(E-E_targ))                    ; % number of POIMDs to retain
S             = S(:,1:ndr)                            ; % first ndr eigenvectors
lambda        = lambda(1:ndr)                         ; % first ndr eigenvalues
Theta         = Theta * S * diag(sqrt(lambda).^-1)    ; % compute POIMDs
T             = [T, Theta]                            ; % add POIMDs to T

%% deflation
T             = T * diag(sqrt(diag(T'*T).^-1))  ; % convert to unit vectors
[T,~,~]       = svd(T, 'econ')                  ; % replace with singular vectors


end % function POIMD
```

Algorithm 7.5. Interface-reduction with POIMDs.

7.4. Application Example: S4 Beam

7.4.1. Overview of the Finite Element Model

Figure 7.1 shows the prototype finite element model that will be used to demonstrate the effectiveness of each interface reduction method. Dubbed the "C beams" [25] or the "S4 beam" [26], this structure has been used extensively to study the nonlinear dynamics of bolted joints [27,28]. Each C beam is 50.8 cm long, 3.2 cm wide, 1.27 cm thick at its ends, and 0.95 cm thick at the midspan gap. All parts of the model are made of linear elastic structural steel, with a Young's modulus of 211 GPa, Poisson's ratio of 0.285, and density of 7,810 kg/m^3.

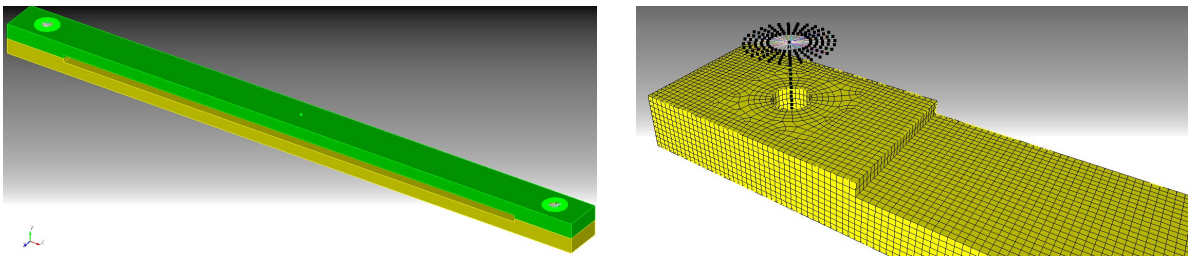

Figure 7.1. *Left*: Finite element model of the S4 beam. *Right*: Close-up view of interface surface with bolt DOF spider.

A single 8-mm diameter bolt at each end of the S4 beam connects the C-shaped substructures. The DOF at the bolt ends are "spidered" to the exterior beam DOF via rigid links, as shown in the right side of Figure 7.1. Rigid spider elements capture the clamping effects induced by a nut-washer-bolt assembly, without having to explicitly model those subcomponents. Moreover, the rigid spiders transfer the preload forces to the contact interfaces, both of which are 3.2 cm wide by 5.0 cm long. The interfaces of each C beam are meshed identically, such that the coordinates of each node pair are initially coincident, but unmerged. This allows for direct

implementation of TD3 contact elements (see Section 6.4) at each node pair. The normal contact stiffness is 5.3E8 N/m, and the tangential contact stiffness is 3.4E8 N/m.

The HCB model of the S4 beam has 16 fixed-interface (FI) modes, with each C beam having 8 FI modal DOF. There are 2,074 node pairs in the model, corresponding to 12,444 interface DOF. The active partition consists of five DOF required for loading the beams: one vertical DOF at each bolt end (four in total), plus an additional DOF to apply a dynamic impulse at the midspan. Table 7.1 summarizes the DOF partitions in the HCB model of the S4 beam.

Table 7.1. DOF partitions in the HCB model of the S4 beam.

DOF Partition	**Physical Meaning**	**Location**	**Number of DOF**
i	Interior	Fixed-interface modes	16 (8 per beam)
r	Interface	Contacting surfaces	12,444 (2,074 node pairs)
a	Active	Bolt ends + dynamic loading node	5 (4 bolt ends, 1 at midspan)
			TOTAL: 12,465

The S4 beam has free-free boundary conditions, with two soft springs added at each end to eliminate rigid body motion (RBM) and allow for time-domain analysis. The springs stiffnesses are selected such that the frequency ratio between the first elastic mode and last pseudo rigid body mode is approximately 10, i.e.

$$\frac{\mathrm{f}_{\mathrm{elastic},1}}{\mathrm{f}_{\mathrm{RBM},6}} \approx 10 \tag{7.100}$$

where $\mathrm{f}_{\mathrm{elastic},1}$is the frequency of the first elastic mode, and $\mathrm{f}_{\mathrm{RBM},6}$ is the frequency of the sixth (i.e. last) pseudo rigid body mode. For the S4 beam, $\mathrm{f}_{\mathrm{elastic},1}$ = 152 Hz, and $\mathrm{f}_{\mathrm{RBM},6}$ = 15.2 Hz was

achieved with a RBM stiffness of 3,065 N/m. Table 7.2 shows the first several frequencies for the undeformed and preloaded HCB model. The undeformed frequencies are computed using $\bar{\mathbf{M}}$ and $\bar{\mathbf{K}}$, while the preloaded frequencies are computed using $\bar{\mathbf{M}}$ and $\bar{\mathbf{K}}^{c}$.

Table 7.2. HCB modal frequencies of the S4 beam.

Mode Number	**Natural Frequency (Undeformed) [Hz]**	**Natural Frequency (Preloaded) [Hz]**
Rigid Body 1	4.78	4.78
Rigid Body 2	8.75	8.75
Rigid Body 3	8.81	8.81
Rigid Body 4	8.83	8.83
Rigid Body 5	8.90	8.90
Rigid Body 6	15.2	15.2
Elastic 1	152	284
Elastic 2	195	289
Elastic 3	398	447
Elastic 4	444	466
Elastic 5	464	777
Elastic 6	480	834

The finite element mesh of the S4 beam was generated in CUBIT [29]. HCB transformations and derivation of the HCB superelement were performed using the Sierra Structural Dynamics codebase [30,31]. All subsequent analyses, including attachment of the node-to-node TD3 elements (see Section 6.4), time integration (Section 6.6), and interface reduction were conducted in MATLAB [9].

7.4.2. Loading

Loading of the S4 beam occurs in two stages. Preloads are applied in the first stage as vertical forces on the bolt DOF. Following this, the preloads are maintained, and a dynamic impulse is applied to the upper C beam.

Preload forces are applied at the vertical bolt DOF, and set equal to 21.2 kN, to be consistent with previous studies of the S4 beam [28]. Preload time variables (see Section 6.5) are $[t_1, t_2, t_3, t_4]$ = [2.5, 5.0, 7.5, 10] ms. The damping coefficient used in the explicit dynamic preload analysis (α) is 1720 sec^{-1}, corresponding to a damping ratio (ξ) of 0.900 and first elastic HCB frequency ($\bar{\omega}_{\text{elastic},1}$) of 955 rad/sec. The HCB frequency is computed using the linear stiffness matrix $\bar{\mathbf{K}}$, because $\bar{\mathbf{K}}^{c}$ is unknown before preloading (requires preload displacement field $\bar{\mathbf{u}}^{\text{PL}}$). The analysis timestep length (Δt_a) is set to one tenth of the critical timestep length (Δt_{cr}) for the preload simulation. The critical timestep length is computed using Equation (6.63), by substituting $\bar{\bar{\omega}}_{\max}$ with $\bar{\omega}_{\max}$, the maximum natural circular frequency of the system defined by $\bar{\mathbf{M}}$ and $\bar{\mathbf{K}}$. A relatively small Δt_a is needed because Δt_{cr} is computed from the linear HCB system matrices, but the simulation itself has significant contact nonlinearities from the TD3 elements.

Figure 7.2 shows the time variation of some energy quantities during the explicit dynamic preload simulation. Figure 7.3. plots the time histories of contact area and slipping area. Contact area is computed using Equation (7.92), and slipping area is computed as a fraction of the contacting nodes, i.e.

$$\text{SA} = \frac{\{number\ of\ interface\ node\ pairs\ classifed\ as\ slipping\}}{\{number\ of\ interface\ node\ pairs\ in\ contact\}} \cdot 100\% \qquad (7.101)$$

Figure 7.2 shows that, by the end of the preload simulation, the kinetic energy is zero and the elastic strain energy remains constant. This indicates that the structure is essentially at-rest at $t = t_4 = 10$ ms, so no initial velocities need to be applied in subsequent analyses. Furthermore, the energy dissipated by viscous damping forces (~0.01 mJ) is very small relative to the frictional dissipation (~2 mJ), so the inclusion of time-dependent damping may not be necessary to reduce unwanted transient oscillations.

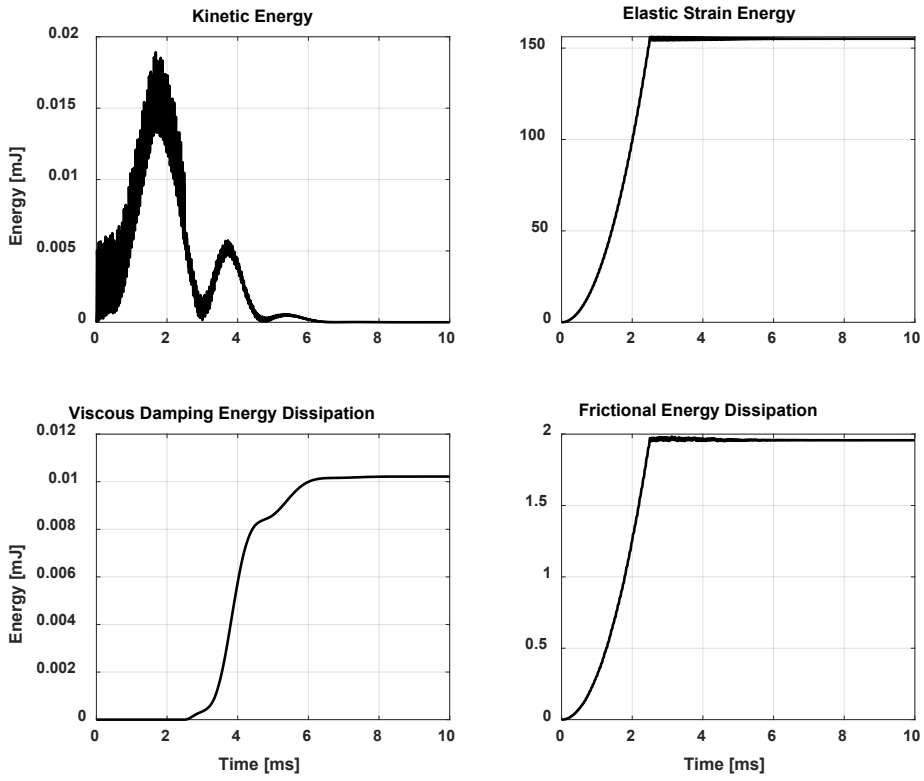

Figure 7.2. Energy quantities during explicit dynamic preload simulation.

Figure 7.3 indicates that the contact interfaces rapidly reach their at-rest conditions during dynamic preloading. The contact area reaches 54% at $t = 0.040$ ms and remains steady for the remainder of the simulation. The slipping area peaks at 1.4% when $t = 0.13$ ms, and then oscillates between 0% and 0.2% until $t = 6.6$ ms, after which it remains at 0%. This is consistent with the

findings of Dundurs [32] and Ahn and Barber [33], who found that contact areas do not change under monotonic loading.

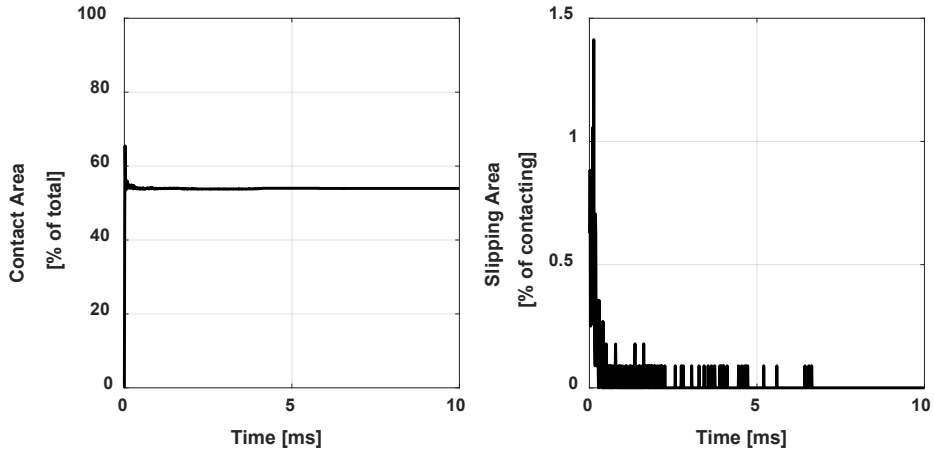

Figure 7.3. Contact area and slipping area time histories during explicit dynamic preload simulation.

Once the preload analysis is complete, dynamic loading is applied as a haversine pulse (see Figure 7.4) with a duration of 1 ms and an amplitude of 10 N, 100 N, or 250 N. The loading amplitudes are intended to illicit dynamic behavior that is, respectively, essentially linear, moderately nonlinear, and strongly nonlinear. The pulse is applied to an active DOF node at the midspan of the upper C beam. The simulations shown here are 10 ms long, in order to observe both forced and free vibration behavior of the S4 beam. In the dynamic loading phase, analysis timestep lengths are computed as one-fourth or one-half of the critical timestep lengths, depending on the model, to provide sufficient stability and accuracy. In this case, the preload configuration is known, so the critical timestep length for the HCB model is computed using the $\bar{\omega}_{\max}$ from $\bar{\mathbf{M}}$ and $\bar{\mathbf{K}}^{\mathrm{c}}$. Critical timestep lengths for IR models are computed according to Equation (6.63), i.e. using $\bar{\bar{\omega}}_{\max}$. Figure 7.5. shows the successive loadings applied to the S4 beam.

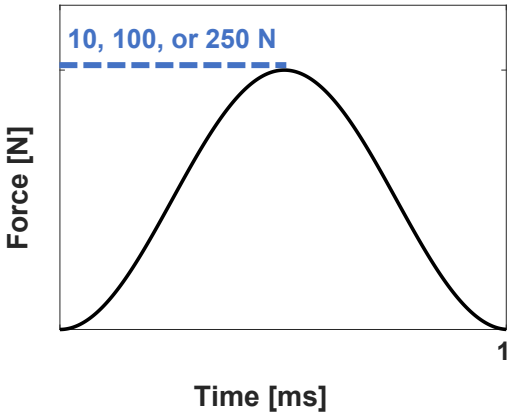

Figure 7.4. Haversine pulse applied to S4 beam. The duration is 1 ms and the amplitude is either 10 N (essentially linear), 100 N (moderately nonlinear), or 250 N (strongly nonlinear).

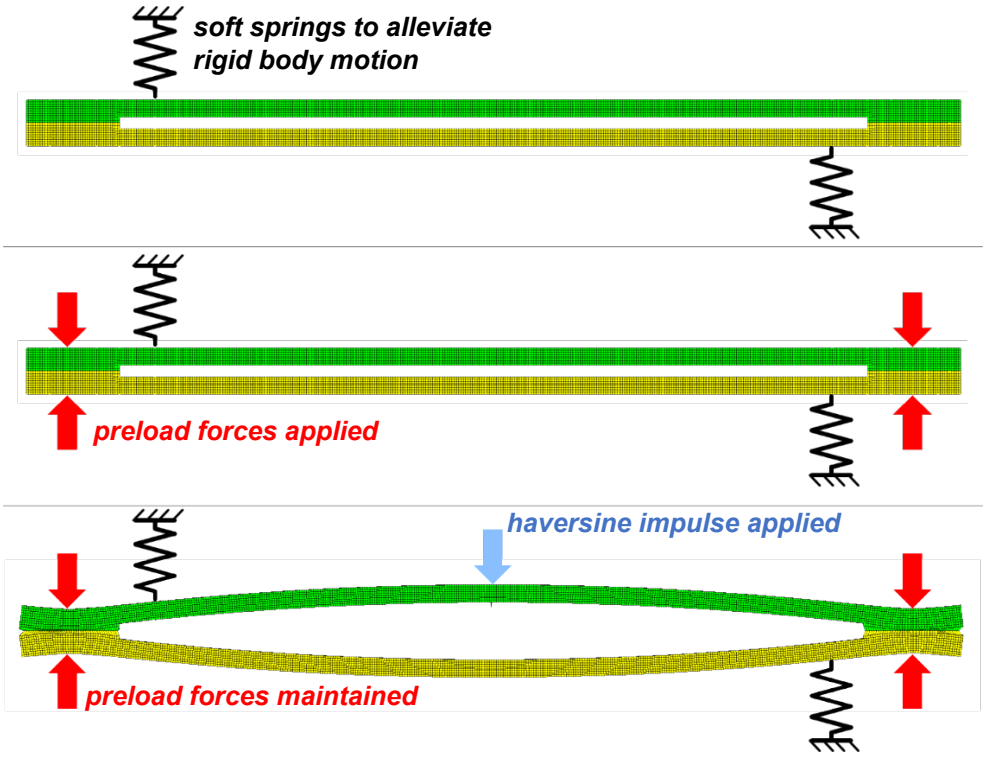

Figure 7.5. Successive loading of the S4 beam. *Top:* undeformed. *Middle:* preload forces applied. *Bottom:* preloads maintained and haversine impulse applied (preload displacements scaled by 2,000).

7.4.3. Damping

Modal viscous damping is applied during the dynamic loading phase. Frequencies less than 1 kHz are assigned damping ratios of 1%, and frequencies greater than 10 kHz are assigned damping ratios of 10%. Frequencies between 1 kHz and 10 kHz are assigned damping ratios that vary linearly between 1% and 10%. All frequencies are computed with contact contributions (i.e. using $\bar{\mathbf{K}}^{c}$). Once the distribution of damping ratios has been determined, an HCB modal damping matrix ($\bar{\mathbf{C}}^{*}$) is computed via

$$\bar{\mathbf{C}}^{*} = \begin{bmatrix} 2\xi_1\bar{\omega}_1 & & & \\ & 2\xi_2\bar{\omega}_2 & & \\ & & \ddots & \\ & & & 2\xi_n\bar{\omega}_n \end{bmatrix} \tag{7.102}$$

where $\xi_1, \xi_2, \ldots \xi_n$ are the modal damping ratios and $\bar{\omega}_1, \bar{\omega}_2, \ldots, \bar{\omega}_n$ are the modal frequencies. If $\bar{\mathbf{\Phi}}$ is a matrix whose columns are the eigenvectors corresponding to $\bar{\omega}_1, \bar{\omega}_2, \ldots, \bar{\omega}_n$, then the HCB damping matrix ($\bar{\mathbf{C}}$) is computed via

$$\bar{\mathbf{C}} = \bar{\mathbf{\Phi}}^{-\mathrm{T}}\bar{\mathbf{C}}^{*}\bar{\mathbf{\Phi}}^{-1} \tag{7.103}$$

Transform the HCB damping matrix using $\breve{\mathbf{T}}$ (see Section 6.3) to obtain the IR damping matrix:

$$\breve{\mathbf{C}} = \breve{\mathbf{T}}^{\mathrm{T}}\bar{\mathbf{C}}\breve{\mathbf{T}} \tag{7.104}$$

7.5. Performance of the Interface Reduction Bases

Multiple analyses of interface-reduced models are conducted, in order to see the convergence behavior of each method. All told, five different IR methods are considered here, implementing (1) SCC modes, (2) SCC modes with GSI modification (i.e. GSI modes) (3) JI modes, (4) SCC modes with ARI mode enrichment, and (5) SCC modes augmented with POIMDs.

Methods 1-4 consider 12 different truncation limits, with 10, 20, 30, 40, 50, 100, 200, 300, 400, 500, 1000, or 1435 retained interface modes. Method 5 includes modal derivatives, so the initial basis size is limited to 10, 20, 30, 40, or 50 interface modes. The 1435 mode case for methods 1-4 is chosen such that the highest-fidelity models of each IR method have the same number of DOF. A total of 53 different IR models are studied, summarized in Table 7.3. Considering the HCB model and the three loading amplitudes, 162 nonlinear dynamic time history analyses were conducted using a custom MATLAB repository.

Table 7.3. Comparison of interface-reduced models.

Method	**Interface Basis Type**	**Basis Enrichment**	**Number of Models**	**Number of Retained Interface Modes**	**Number of DOF**	$\frac{\Delta t_a}{\Delta t_{cr}}$	Δt_a **[sec]**
HCB	-	-	1	-	12,465	0.50	1.7E-8
IR1	SCC	none	12	10 – 1435	31 – 1456	0.25	9.8E-8 – 3.8E-6
IR2	GSI	none	12	10 – 1435	31 – 1456	0.50	6.8E-8 – 2.1E-6
IR3	JI	none	12	10 – 1435	31 – 1456	0.25	5.5E-8 – 3.2E-6
IR4	SCC	ARI modes	12	10 – 1435	31 – 1456	0.25	9.8E-8 – 4.3E-6
IR5	SCC	POIMDs	5	10 – 50	233 – 1456	0.50	1.8E-8 – 4.7E-8

In Table 7.3, the number of retained interface modes, total number of DOF, timestep factor ($\Delta t_a/\Delta t_{cr}$), and timestep lengths (Δt_a) are given as range. Models with fewer retained interface modes have fewer overall DOF and a larger timestep length. For example, the SCC model with 10 retained interface modes has 31 total DOF and a timestep length of 3.8E-6 sec. Similarly, the SCC model with POIMDs and 50 retained interface modes has 1,456 total DOF and a timestep length of 1.8E-8 sec. IR methods 1 (SCC), 3 (JI), and 4 (SCC + ARI) require the analysis timestep length (Δt_a) to be one-fourth of the critical timestep length (Δt_{cr}), while only one-half is required for

methods 2 (GSI) and 5 (SCC + POIMDs). The HCB reference model has 12,465 DOF and an analysis timestep length of 1.7E-8 sec. HCB models tend to produce small critical timesteps due to the localized deformations associated with the static constraint modes. Interface-reduced models avoid this problem by truncating the higher frequency content, but can still suffer from increasingly smaller timesteps as more modes are added to the reduction basis.

Sections 7.5.1 through 7.5.5 summarize the key results for HCB model, as well as the various interface-reduced models. In this case, the HCB model is considered to be the "truth" model, against which all IR models will be compared. Previous studies of the S4 beam concluded that 16 fixed-interface modes is sufficient to demonstrate convergence in the HCB solution [25]. The behavior of every model is analyzed using two global response metrics and two local response metrics. The global response metrics are drive point displacement (i.e. vertical displacement at the node where the haversine pulse is applied), and total kinetic energy in the system. The first local response metric is the total contact area, reported as the percentage of the joint areas with contacting node pairs, as computed in Equation (7.92). The second local response metric is the slipping area, computed according to Equation (7.101).

In the subsequent sections, the HCB response is plotted with a thick grey line, and the IR models are plotted with thin colored lines, varying from blue to red with an increasing number of retained interface modes. That is, a blue line corresponds to the fewest number of retained interface modes, and a red line corresponds to the greatest number of retained interface modes. Sections 7.5.1 through 7.5.4 show the response time histories of the first four IR methods, without commentary. Section 7.5.5 details the computational procedures involved in POIMD generation, followed by response time histories for the last IR method. Finally, Section 7.5.6 compares the relative performance of each interface reduction method.

7.5.1. SCC Modes

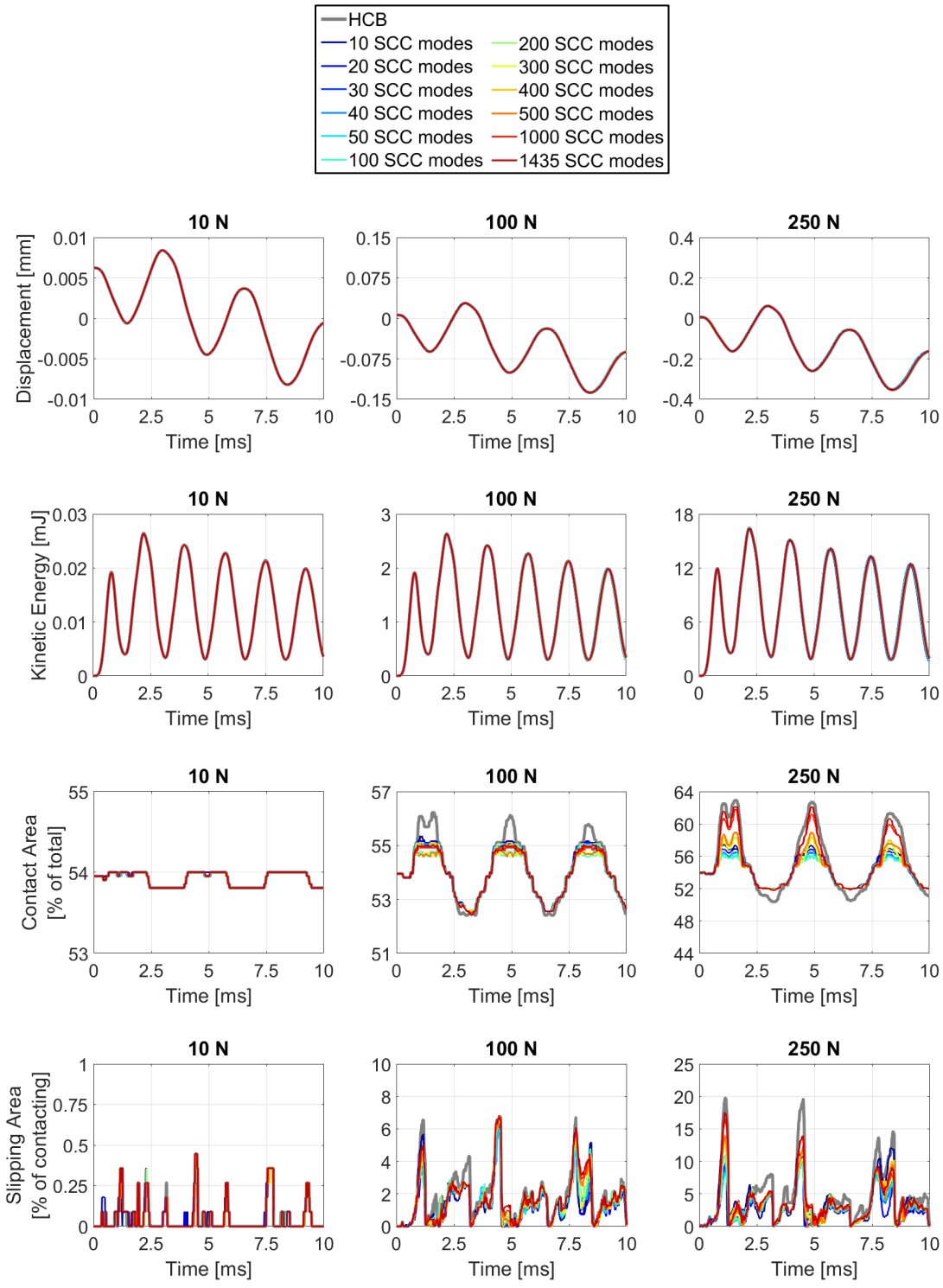

Figure 7.6. Response comparison: HCB (grey) vs. SCC (increasing modes from blue to red).

7.5.2. GSI Modes

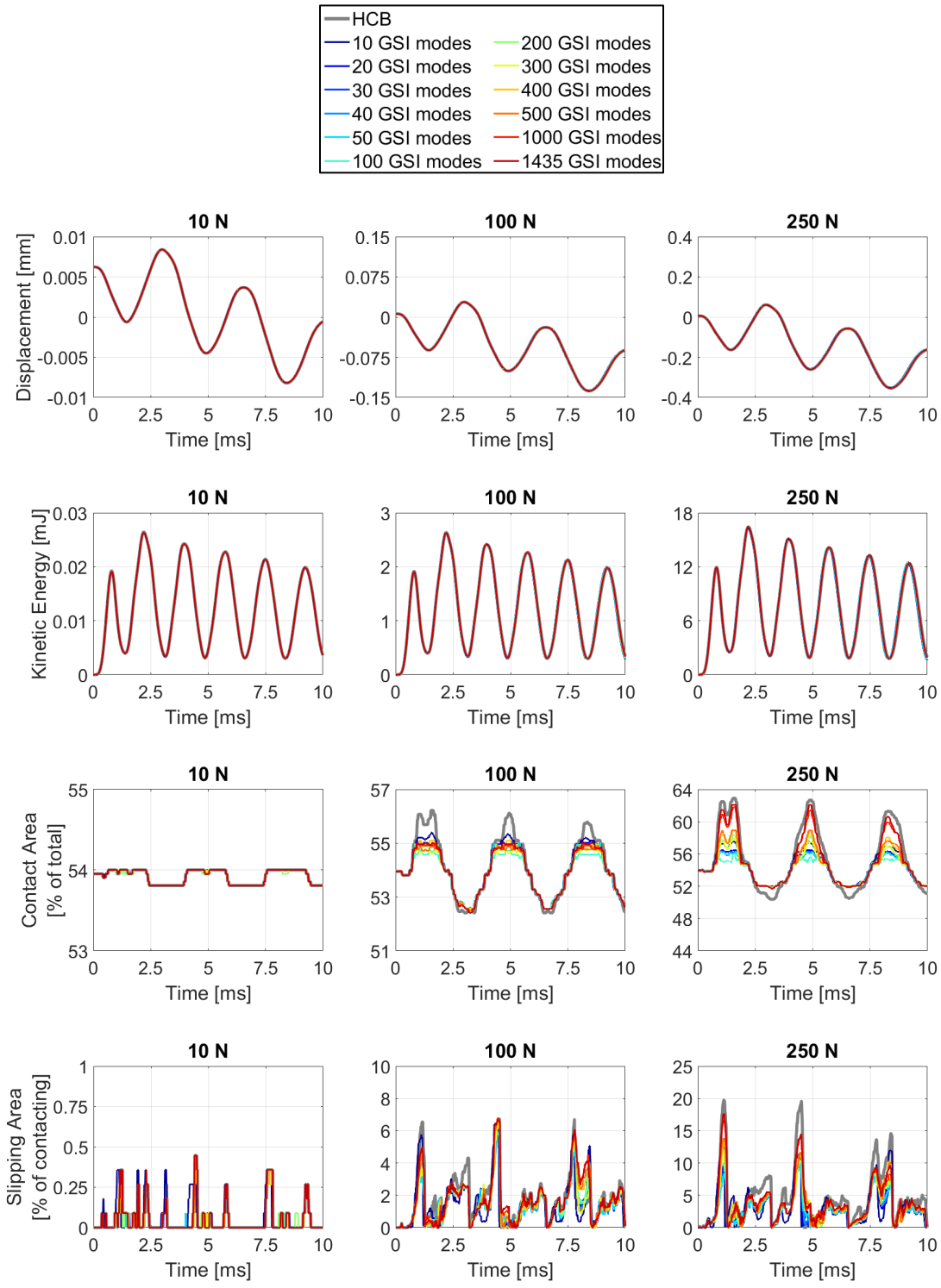

Figure 7.7. Response comparison: HCB (grey) vs. GSI (increasing modes from blue to red).

7.5.3. JI Modes

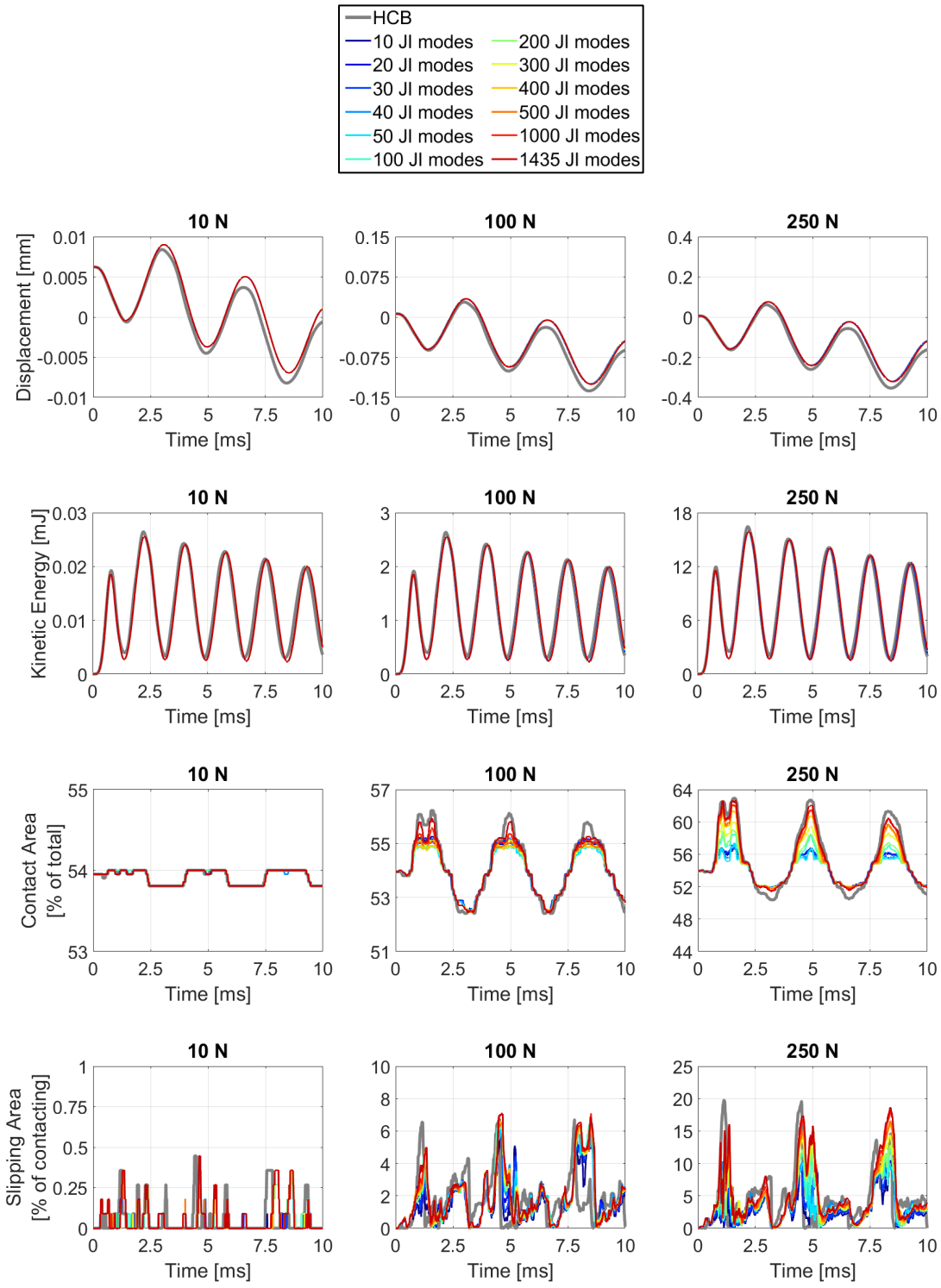

Figure 7.8. Response comparison: HCB (grey) vs. JI (increasing modes from blue to red).

7.5.4. SCC + ARI Modes

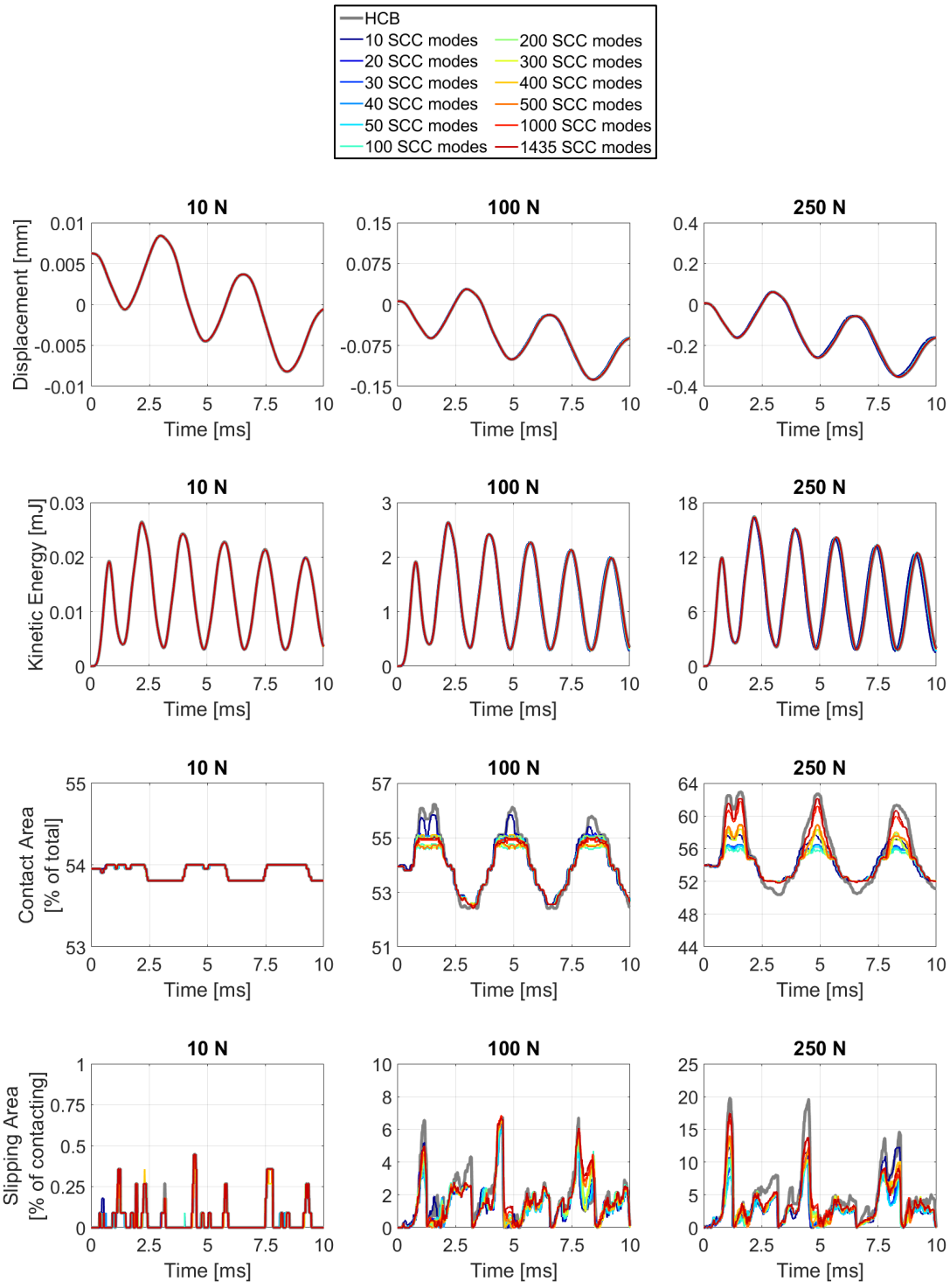

Figure 7.9. Response comparison: HCB (grey) vs. SCC + ARI modes (increasing modes from blue to red).

7.5.5. SCC Modes + POIMDs

Figures 7.10 and 7.11 summarize the intermediate steps in the development of a basis with POIMDs. The left side of Figure 7.10 plots the energy retention ratio, computed using Equation (7.96), as a function of the number of retained POIMDs. Each line in this figure represents the behavior of a particular IR model. Between 23% and 44% of all the POIMDs are necessary to obtain an energy retention ratio of 0.9999, meaning that a majority of the modal derivatives are discarded during basis construction. This is reinforced by the righthand side of Figure 7.10, which plots the number of modal derivatives versus the size of the original basis (i.e. number of SCC modes). The number of computed IMDs is two to five times greater than the number of POIMDs ultimately retained in the model.

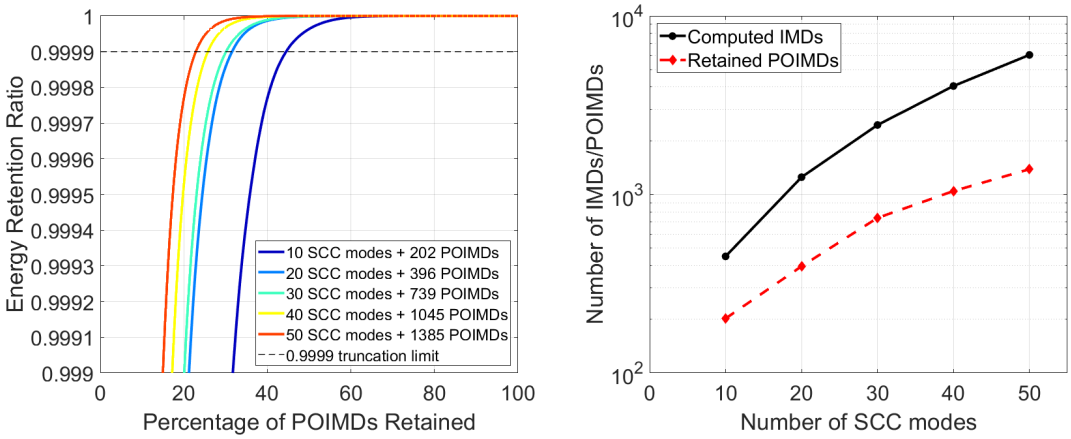

Figure 7.10. Computation of IMDs/POIMDs. "Energy retention ratio" refers to the quantity in Equation (7.96).

Figure 7.10 examines how each SCC mode changes the contact area, relative to the preloaded configuration, when scaled by a variable step size h. It is essentially a visualization of

the intermediate calculations of Equations (7.93) and (7.94). Values of h varied between the user-defined cutoff values of 1E-10 and 1E+10. A step size of 1E-10 or 1E+10 implies that the contact area is insensitive to the mode in question – any arbitrarily large or small scaling of the mode will cause marginal changes in the contact state. The first 50 modes are the SCC eigenmodes, and the last five are the SCC constraint modes corresponding to the five active DOF. For both backward and forward difference methods, the interface modes are capable of inducing the targeted 5% change in contact area, with a few exceptions: modes 7, 23, 31, 32, 40, 41, 42, 43, and 49 were unable to achieve the target contact area change. The last five modes (i.e. the constraint modes) are all able to produce an approximate contact area change of 5%. Figure 7.12 shows the response time histories of the SCC model with POIMD enrichment.

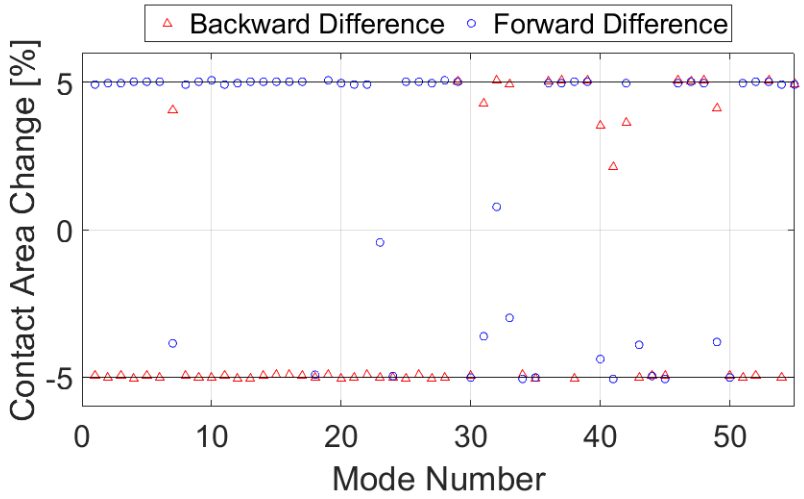

Figure 7.11. Contact area change induced by each mode (50 interface eigenmodes + 5 interface constraint modes), using a variable step size h. See Section 7.3.2, Equations (7.93) and (7.94).

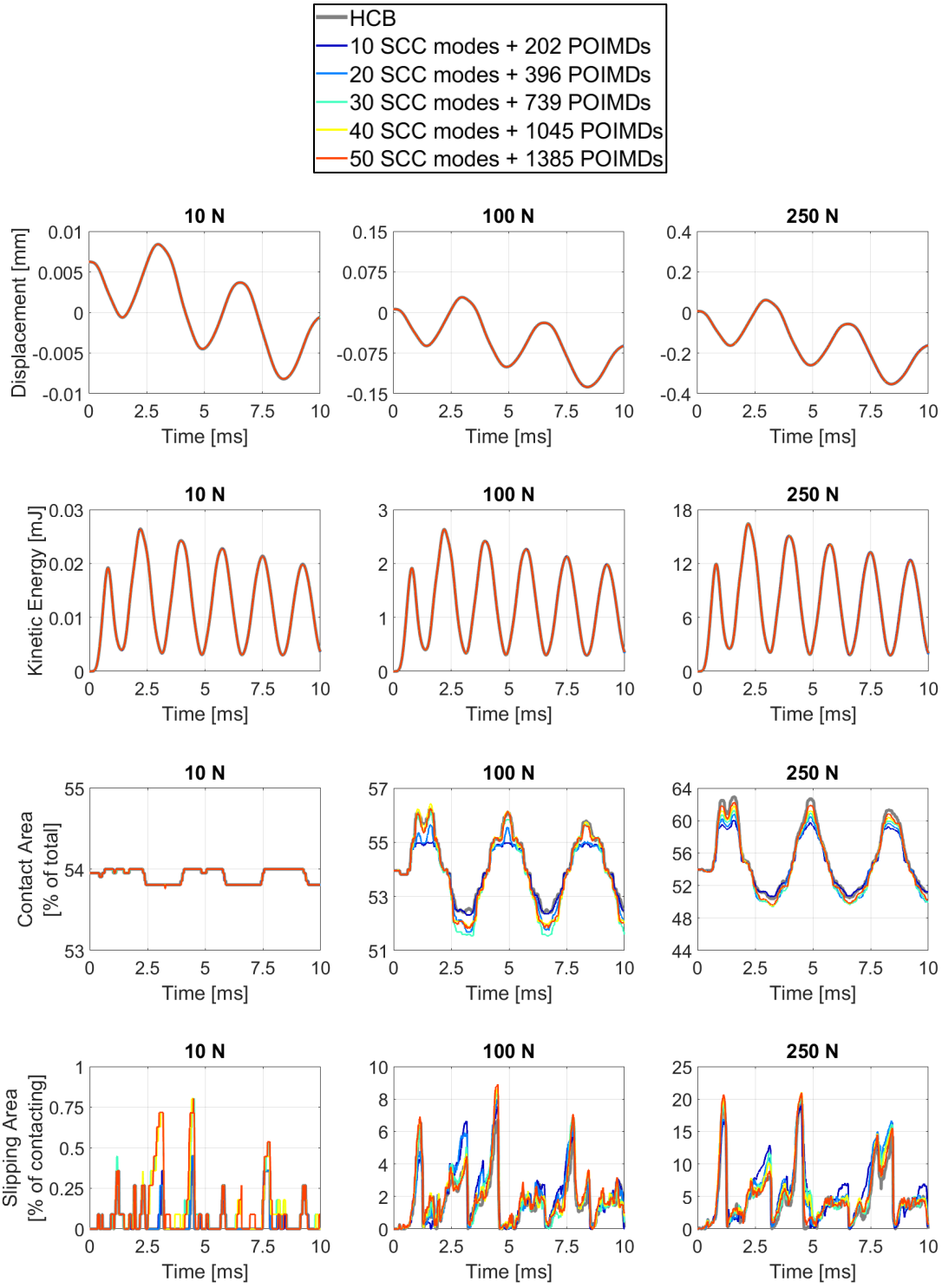

Figure 7.12. Response comparison: HCB (grey) vs. SCC + POIMDs (increasing modes from blue to red).

7.5.6. Interface Basis Comparison

Several common traits can be observed from the response time histories in Figures 7.6, 7.7, 7.8, 7.9 and 7.12. The global metrics – drive point displacement and kinetic energy – are accurately captured with any of the IR models shown here. The smallest IR models, which only have 31 total DOF, immediately converge to the HCB displacement and kinetic energy. This observation holds for the 10 N, 100 N, and 250 N loading cases. The exception to this trend is the JI model, which exhibits slight error in both frequency and amplitude.

The local response metrics, however, are visibly more difficult to resolve. For the first four IR methods in particular, contact area and slipping area generally agree with the HCB reference solution at 10 N loading, but converge slowly at 100 N and 250 N loadings. Under 10 N loading, the S4 beam has almost no contact area change (± 0.1% about the preload value) and only 0.5% change in the slipping area, so the behavior can be described as essentially linear. The 100 N and 250 N loadings, however, produce more significant changes in contact area (± 2% and ± 6%, respectively) and slipping area (8% and 20%, respectively). In these cases, the S4 beam exhibits nonlinear behavior, with many nodes coming in and out of contact throughout the simulation. Consequently, the IR methods match the HCB results at 10 N loading with relatively few modes, but require many more modes at 100 N and 250 N loadings. The JI method once again shows the poorest performance, with a visible time lag in the slipping area response, relative to the HCB solution.

The fifth IR method, which employs SCC modes with POIMD enrichment, does show a mostly convergent solution in terms of contact area and slipping area. The highest-fidelity model of this type (with 1,456 DOF) shows excellent agreement with the HCB reference model (with 12,465 DOF). Periods of high contact area (e.g. 250 N loading at $t = 1$ ms) are well-captured, with

less than 0.5% difference between the IR and HCB models. The SCC + POIMD model does visibly deviate from the HCB solution at periods of low contact area (e.g. at $t = 3$ ms), but the difference is no greater than 2% across all loading magnitudes. Under 250 N loading, the IR slipping area shows similar behavior to the HCB solution, with the largest deviation occurring at $t = 4.6$ ms. At this point in time, the HCB model drops to nearly zero slipping area, and the interface is completely stuck. The IR solution also drops during this period, but it takes slightly longer, getting closest to zero at $t = 4.9$ ms. As a result, the IR prediction of slipping area is in error by 4%. Still, the SCC + POIMD model with 1,456 total DOF shows the best performance by far.

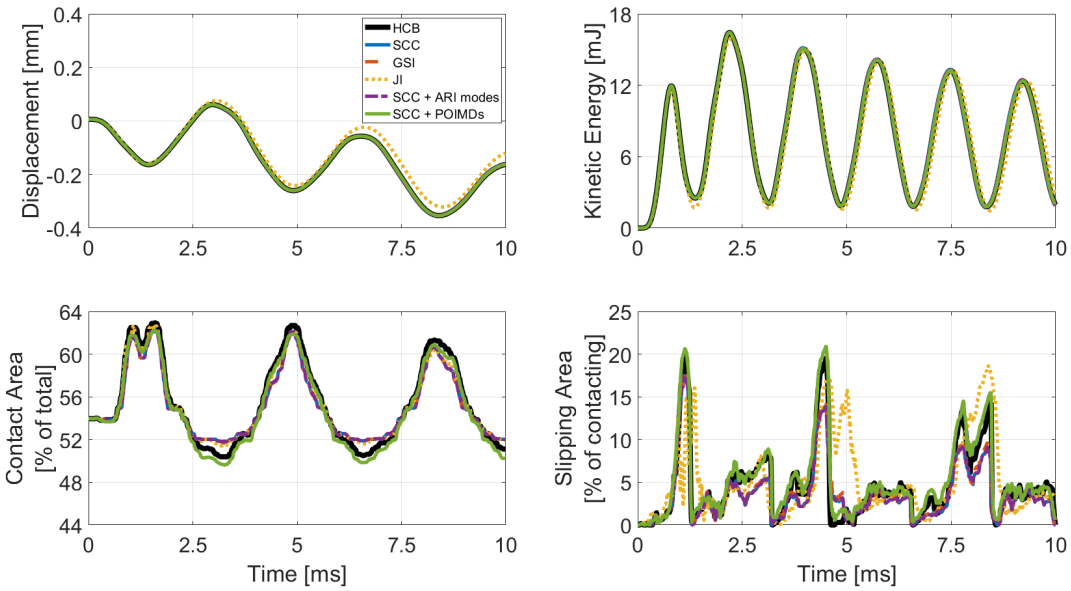

Figure 7.13. Response comparison of the HCB model and highest-fidelity IR models, under 250 N loading.

Figure 7.13 compares the response time histories for the highest-fidelity models of each IR method, subjected to 250 N loading. Methods 1-4 are shown with 1,435 retained interface modes, and Method 5 is shown with 50 SCC modes and 1,385 POIMDs. This serves as a "best-case"

comparison between five different IR models with the same number of DOF. Notably, Figure 7.13 shows that methods 1 (SCC), 2 (GSI), and 4 (SCC + ARI) produce virtually identical results. Computational savings notwithstanding, each of these methods can be considered interchangeable – using one over the other will not produce appreciably different results. Method 3 (JI) shows the most visible errors, even for drive point displacement and kinetic energy. Method 5 (SCC + POIMDs) exhibits the overall highest accuracy, particularly in the slipping area. Methods 1-4 show the greatest discrepancy in contact area, at around $t = 3.2$ ms, 6.5 ms, and 10 ms (when contact area is lowest).

Thus far, there has been no quantitative estimate of accuracy in the IR methods. In general, computing time domain errors in high-frequency signals can give misleading results, or otherwise requires sophisticated reliability metrics [34]. As such, accuracy discussions are limited to the coarse discussion given above, which still indicate which methods perform the best (SCC + POIMDs) and worst (JI). Computational savings, however, can be robustly investigated.

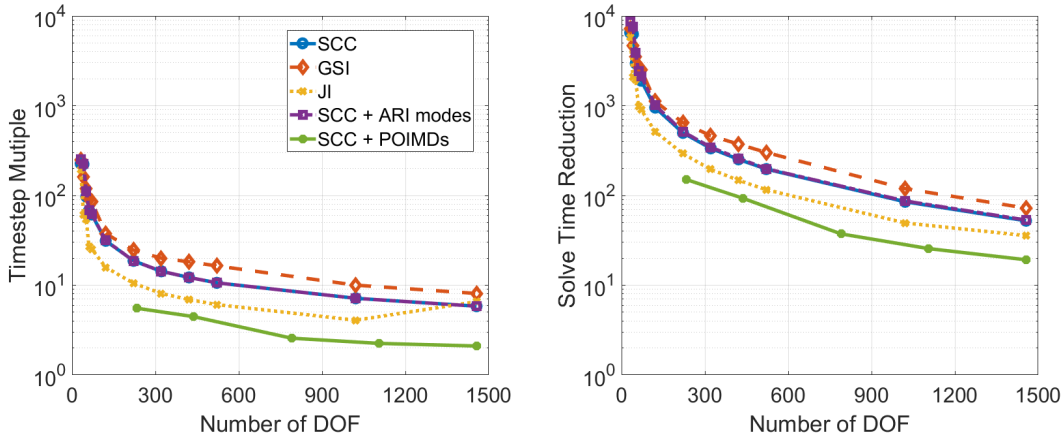

Figure 7.14. Timestep multiple (ratio of IR timestep length to HCB timestep length) and solve time reduction (ratio of HCB solve time to IR solve time) for all IR models.

Figure 7.14 shows how each IR method increases the analysis timestep length (left) and decreases the analysis solve time (right), relative to the HCB solution. Timestep multiples range from 254, for the smallest IR models, to 1.3, corresponding to the SCC + POIMD method. Solve time reduction also varies greatly between the methods. The SCC, GSI, JI, and SCC + ARI methods all reduce the simulation time by a factor of approximately 8,600 for the smallest models, and between 36 and 72 for the larger models. The GSI models run slightly faster than the SCC models because the GSI method was stable with $\Delta t_a = \Delta t_{cr}/2$, while the SCC method required $\Delta t_a = \Delta t_{cr}/4$. The SCC + POIMD method has smaller reduction factors, ranging between 19 and 151.

The traditional SCC method with minimal interface modes is likely the best option for a very quick analysis that can still accurately predict system-level responses. It is relatively straightforward in construction and provides computational speed-ups on the order of several thousand. On the other hand, if interface-level metrics are critical, then the SCC + POIMD method is recommended. With sufficient interface modes and modal derivatives, this method can accurately predict slipping area, while providing modest speed-ups on the order of 10-20. Slipping area is closely tied to frictional energy dissipation, so it is expected that the SCC + POIMD method will provide the most accurate estimation of nonlinear damping. Based on the results presented, the GSI, JI, and ARI approaches do not provide significant accuracy advantages in comparison to the SCC and SCC + POIMD methods.

7.6. Summary and Conclusions

This chapter developed five methods of reducing nonlinear interface DOF in Hurty/Craig-Bampton (HCB) superelements with preloaded bolted joints. The first method employed system-level characteristic constraint (SCC) modes, combining interface eigenmodes and static interface constraint modes. Gram-Schmidt interface (GSI) modes made a modification to the SCC method by performing Gram-Schmidt orthogonalization on the interface partition of full-boundary eigenmodes. Joint interface (JI) modes computed static and dynamic mode shapes from a system pre-constrained to obey Newton's third law at its interfaces. Approximate residual interface (ARI) modes extended the enhanced HCB method to interface reduction, by approximating residual interface eigenmodes without increasing the size of the basis. Finally, interface modal derivatives (IMDs), which through orthogonalization become properly orthogonal interface modal derivatives (POIMDs), were derived as a way to consider the perturbation of basis vectors about some preloaded configuration.

All five nonlinear interface reduction (IR) methods were tested on the S4 beam - an assembly of two C-shaped beams connected by a bolted lap joint at each end. The HCB superelement of the system was preloaded in an explicit dynamics environment, after which it was loaded with a haversine impulse. Using the HCB solution as a baseline "truth" model, multiple instances of every IR method were analyzed and compared.

A number of conclusions can be drawn from the results of the 162 nonlinear dynamic time history analyses. Firstly, the methods shown here represent a family of IR methodology that is highly tunable. That is to say, the analyst can tailor the method to their desired level of accuracy and computational effort. For a so-called "quick and dirty" simulation, the SCC method will provide the analyst with a dynamic model that is straightforward to generate, and provides

simulation speed-up factors in the thousands. Depending on the problem, the lightweight SCC model can provide highly accurate results at the system-level, while making some accuracy sacrifices at the interface level. If interface response metrics are important to the analyst, however, they might "upgrade" the method to include POIMDs, which can accurately predict interface mechanics and still provide moderate computational savings.

Another important conclusion applies to the GSI and JI bases, as well as basis enrichment via ARI modes. These methods require a nontrivial amount of upfront computational effort, which ideally, would result in commensurate savings or accuracy improvement during time integration. As shown in Section 7.5, however, none of these methods show significant differences with the SCC method, which is much less complicated in its construction. The GSI method may allow for slightly larger analysis timestep lengths, but this effect should be investigated further. Consequently, these methods are not recommended in their current form.

In future studies, the robustness of the most accurate method – SCC modes with POIMD enrichment – should be examined further. Numerous questions still remain. How is IMD computation affected by the differentiation step size, h? What can be done to improve the overall process of modal derivative computation? After applying the proper orthogonal decomposition, 50% or more of the final set of POIMDs are discarded – an obvious area for improvement. Moreover, how well does the method perform for different types of structures. Different mesh sizes? Can it accurately capture interface mechanics when different contact models are used? This research is a survey of a new family of interface reduction techniques. The SCC + POIMD method revealed itself as a contender in the tapestry of nonlinear interface reduction, but more work must be done if it is to confidently remain there.

References

1. Hurty W. Vibrations of Structural Systems by Component Mode Synthesis. *Transactions of the American Society of Civil Engineers* 1960.

2. Hurty WC. Dynamic analysis of structural systems using component modes. *AIAA Journal* 1965. DOI: 10.2514/3.2947.

3. Craig RR, Bampton MCC. Coupling of substructures for dynamic analyses. *AIAA Journal* 1968. DOI: 10.2514/3.4741.

4. Craig RR, Chang CJ. *Substructure Coupling for Dynamic Analysis and Testing*. 1977.

5. Castanier MP, Tan YC, Pierre C. Characteristic Constraint Modes for Component Mode Synthesis. *AIAA Journal* 2001; **39**(6): 1182–1187.

6. Krattiger D, Wu L, Zacharczuk M, Buck M, Kuether RJ, Allen MS, Tiso P, Brake MR. Interface reduction for Hurty/Craig-Bampton substructured models: Review and improvements. *Mechanical Systems and Signal Processing* 2019; **114**: 579–603. DOI: 10.1016/j.ymssp.2018.05.031.

7. Witteveen W, Irschik H. Efficient Mode-Based Computational Approach for Jointed Structures: Joint Interface Modes. *AIAA Journal* 2009; **47**(1): 252–263. DOI: 10.2514/1.38436.

8. Battiato G, Firrone CM, Berruti TM, Epureanu BI. Reduction and coupling of substructures via Gram–Schmidt Interface modes. *Computer Methods in Applied Mechanics and Engineering* 2018; **336**: 187–212. DOI: 10.1016/j.cma.2018.03.001.

9. MathWorks. Matlab Documentation 2020. DOI: 10.1201/9781420034950.

10. Kim JG, Lee PS. An enhanced Craig-Bampton method. *International Journal for Numerical Methods in Engineering* 2015. DOI: 10.1002/nme.4880.

11. Boo SH, Kim JH, Lee PS. Towards improving the enhanced Craig-Bampton method. *Computers and Structures* 2018; **196**: 63–75. DOI: 10.1016/j.compstruc.2017.10.017.

12. Idelsohn SR, Cardona A. A load-dependent basis for reduced nonlinear structural dynamics. *Computers and Structures* 1985. DOI: 10.1016/0045-7949(85)90069-0.

13. Idelsohn SR, Cardona A. A reduction method for nonlinear structural dynamic analysis. *Computer Methods in Applied Mechanics and Engineering* 1985. DOI: 10.1016/0045-7825(85)90125-2.

14. Weeger O, Wever U, Simeon B. On the use of modal derivatives for nonlinear model order reduction. *International Journal for Numerical Methods in Engineering* 2016; **108**: 1579–1602. DOI: 10.1002/nme.5267.

15. Varona MC, Gebhart R, Bilfinger P, Lohmann B, Rixen DJ. A novel derivation for modal derivatives based on Volterra series representation and its use in nonlinear model order reduction. *COMPDYN Proceedings* 2019; **2**(June): 2376–2394.

16. Stewart GW. *Matrix Algorithms: Volume II: Eigensystems*. SIAM; 2001.

17. O'Callahan J. A procedure for an improved reduced system model. *Proceedings of the 7th International Modal Analysis Conference (IMAC VII)*, Las Vegas, Nevada, USA: 1989.

18. Witteveen W, Pichler F. Efficient model order reduction for the nonlinear dynamics of jointed structures by the use of trial vector derivatives. *Conference Proceedings of the Society for Experimental Mechanics Series*, 2014. DOI: 10.1007/978-3-319-04501-6_13.

19. Pichler F, Witteveen W, Fischer P. A complete strategy for efficient and accurate multibody dynamics of flexible structures with large lap joints considering contact and friction. *Multibody System Dynamics* 2017; **40**: 407–436. DOI: 10.1007/s11044-016-9555-2.

20. Pichler F, Witteveen W, Fischer P. Reduced-order modeling of preloaded bolted structures in multibody systems by the use of trial vector derivatives. *Journal of Computational and Nonlinear Dynamics* 2017. DOI: 10.1115/1.4036989.

21. Mottershead JE, Friswell MI. Model updating in structural dynamics: A survey. *Journal of Sound and Vibration* 1993. DOI: 10.1006/jsvi.1993.1340.

22. Witteveen W, Pichler F. Efficient model order reduction for the dynamics of nonlinear multilayer sheet structures with trial vector derivatives. *Shock and Vibration* 2014; **2014**: 147–155. DOI: 10.1155/2014/913136.

23. Varona MC, Gebhart R, Bilfinger P, Lohmann B, Rixen DJ. A novel derivation for modal derivatives based on Volterra series representation and its use in nonlinear model order reduction. *COMPDYN Proceedings* 2019; **2**(June): 2376–2394. DOI: 10.7712/120119.7081.19178.

24. Kerschen G, Golinval JC, Vakakis AF, Bergman LA. The method of proper orthogonal decomposition for dynamical characterization and order reduction of mechanical systems: An overview. *Nonlinear Dynamics* 2005; **41**(1–3): 147–169. DOI: 10.1007/s11071-005-2803-2.

25. Hughes PJ, Scott W, Wu W, Kuether RJ, Allen MS, Tiso P. Interface reduction on hurty/craig-bampton substructures with frictionless contact. *Conference Proceedings of the Society for Experimental Mechanics Series* 2019; **1**: 1–16. DOI: 10.1007/978-3-319-74280-9_1.

26. Singh A, Scapolan M, Saito Y, Allen MS, Roettgen D, Pacini B, Kuether RJ. Experimental characterization of a new benchmark structure for prediction of damping nonlinearity. *Nonlinear Dynamics, Volume 1* 2019: 57–78.

27. Singh A, Wall M, Allen MS, Kuether RJ. Spider Configurations for Models with Discrete Iwan Elements. *Nonlinear Structures and Systems, Volume 1. Conference Proceedings of the Society for Experimental Mechanics Series*, 2020. DOI: https://doi.org/10.1007/978-3-030-12391-8_4.

28. Wall M, Allen MS, Zare I. Predicting S4 Beam Joint Nonlinearity Using Quasi-Static Modal Analysis. *Nonlinear Structures and Systems, Volume 1. Conference Proceedings of the Society for Experimental Mechanics Series*, Springer, Cham.; 2020. DOI: https://doi.org/10.1007/978-3-030-12391-8_5.

29. Blacker TD, Bohnhoff WJ, Edwards TL. CUBIT mesh generation environment. Volume 1: User's manual. *SAND-94-1100*, Sandia National Laboratories. Albuquerque, New Mexico, USA and Livermore, California, USA: 1994.

30. Shaw RP, Agelastos AM. Guide to using Sierra. *SAND2015-1642*, Sandia National Laboratories. Albuquerque, New Mexico, USA and Livermore, California, USA: 2015.

31. Reese GM. Sierra/SD - Theory Manual. *SAND2017-11104*, Sandia National Laboratories. Albuquerque, New Mexico, USA and Livermore, California, USA: 2016.

32. Dundurs J. Properties of elastic bodies in contact. *The Mechanics of the Contact between Deformable Bodies* 1975: 54–66.

33. Ahn YJ, Barber JR. Response of frictional receding contact problems to cyclic loading. *International Journal of Mechanical Sciences* 2008; **50**(10–11): 1519–1525. DOI: 10.1016/j.ijmecsci.2008.08.003.

34. Ao D, Hu Z, Mahadevan S. Dynamics Model Validation Using Time-Domain Metrics. *Journal of Verification, Validation and Uncertainty Quantification* 2017; **2**(1). DOI: 10.1115/1.4036182.

Chapter 8 Concluding Remarks

8.1. Summary of Research and Novel Contributions to the Body of Knowledge

Inter-component contact in multi-body systems can significantly influence the overall dynamic characteristics. Analysis of multi-body systems is largely undertaken using the finite element method (FEM), which has grown in popularity with the increasing power and accessibility of computing resources. Each component of a structure, and the numerous contact interfaces that join them, can be modeled in rich detail. Despite the significant strides made in the dynamic modeling of multi-body systems, the handling of contact in a finite element environment is a lingering research problem.

This dissertation examined state-of-the-art contact models using base-isolated buildings and preloaded mechanical joints as case studies. Base-isolation is a proven seismic protection strategy for building structures, which reduces floor accelerations at the expense of increased displacements at the isolation plane. Under intense ground shaking, the base mat of the

superstructure has the potential to displace beyond the allowed clearance and collide with the surrounding moat wall. This is a case of vibroimpact, where two nominally separate structures (i.e. the base-isolated building and moat wall), come into contact for a short duration and vibrate as a single entity. Due to the large size of building structures, moat wall pounding is typically modeled using macro elements, which reduce the entire contact surface to a series of uniaxial springs and dashpots.

Chapter 3 of this dissertation examined how different macro elements affect the response of base-isolated buildings subjected to impact-inducing ground motions. Five common state-of-the-art macro elements were implemented into a finite element model that was previously calibrated to experimental data from moat wall pounding tests. Results of this study indicate that the system-level behavior of the isolated building is generally insensitive to the analyst's choice in contact model. Swapping one contact model for another induced moderate changes in the pounding forces and base mat accelerations, but upper floor accelerations and interstory drift ratios were utterly unaffected. This was the first study of its kind to compare contact models in a calibrated, nonlinear finite element model. Three uniaxial material models used in this study are in the process of being added to a future release of OpenSees, an open-source finite element software.

Chapters 4 and 5 reconstructed different moat wall pounding experiments using high-fidelity finite element models. Chapter 4 focused on predicting the pounding force time histories in a simulation limited to a single, unidirectional impact event. Dynamic conditions were gradually ramped up to their pre-impact values, after which the contact duration was simulated using an initial velocity or prescribed displacement approach. Both of these approaches failed to accurately estimate the peak impact force or contact duration, but effectively predicted the overall shape of

the force-time curves. Furthermore, this study revealed that inter-component contact and friction significantly affected the pounding forces, and that the experimental measurements during an impact event may be unreliable. Chapter 5 studied a full-scale base-isolated building model subjected to three-dimensional ground motion and moat wall pounding. In this case, consideration of the entire earthquake record, as well as detailed models of the isolation hardware and damping devices, lead to accurate predictions of the seismic response. These models show, for the first time, how to effectively model moat wall pounding using high-fidelity finite elements. Localized simulations focusing solely on the contact duration, such as those shown in chapter 4, may not contain enough dynamic information to accurately capture the pounding response. Alternatively, modeling the isolation devices and simulating the entire earthquake record, as shown in chapter 5, can predict superstructure and moat wall responses with sufficient accuracy.

Chapters 6 and 7 shifted the focus to analyzing projection-based reduced order models (ROMs) of structures with mechanical joints. Jointed structures are often approximated as Hurty/Craig-Bampton (HCB) superelements, which greatly reduce the number of interior DOF while retaining all nonlinear DOF at the interfaces. In many cases, the HCB superelement may still be too large, necessitating a secondary reduction of the interface DOF. Chapter 6 laid the theoretical groundwork for a new family methods specifically designed to reduce the number of interface DOF in HCB superelements with contact nonlinearities. This chapter summarized the HCB transformation, demonstrated a generalized form of projection-based interface reduction, introduced a novel contact element, and explained how to conduct a nonlinear dynamic time history analysis of a preloaded structure with modally-reduced interfaces.

Chapter 7 developed a new family of interface reduction procedures that only require the mass and stiffness matrices of the HCB superelement. Included in this family of methods is a novel

extension of the enhanced HCB method to interface modes, as well as a new procedure for computing modal derivatives based on consistent nonlinear engagement at the contact areas. The performance of five different interface reduction methods is judged on the basis of time-domain accuracy and computational savings, using a preloaded beam assembly as a case study. All methods shown in this chapter increase the critical timestep length and reduces the overall computation time. With a few exceptions, every method can also accurately predict system-level responses with only a few interfaces modes. Accurate resolution of interface responses like contact area and slipping area, however, require additional interface modes with basis enrichment via modal derivatives.

8.2. Recommendations for Future Research

This dissertation enhances the understanding of high-fidelity and reduced-order models of contacting structures, but leaves ample opportunity for future development. The findings shown here can be complemented with additional research in the following areas:

- The parametric study of uniaxial contact models in chapter 3 can be extended to full-scale buildings subjected to three-dimensional ground shaking. Ground motion directionality strongly influences the overall seismic response of base-isolated buildings, and the degree to which macro contact elements affect this response is uncertain. It is recommended that the macro elements be arranged in series and out-of-plane, to form a multi-dimensional wall structure. Model parameters should also be updated to reflect stiffness and damping quantities per unit length of wall.
- The next generation of impact macro models may not require an explicit constitutive law at all, but rather may be estimated using machine learning algorithms. Long short-

term memory (LSTM) networks, for example, are capable of simulating dynamic systems, and may be an effective simulation tool in seismic pounding analysis.

- A robust methodology is needed for *a posteriori* correction of uncertain measurements recorded during a moat wall pounding test. The dynamic equilibrium approach in chapter 4, as well as the measured moat wall accelerations in chapter 5, indicate that the accelerometer recordings may be erroneous during an impact event. Spectral analysis of the recorded signals, with source location and time history reconstruction, may be a fruitful path forward.
- The high-fidelity moat wall impact model shown in chapter 5 should be modified to include backfill soil, to represent the moat walls in a more realistic fashion. The presence of backfill soil adds damping and inertia, which can significantly affect both the superstructure and moat walls.
- The three-dimensional time domain (TD3) contact element (see Section 6.4) was developed as a necessary interim step for the present research, but more investigation into its physical behavior and computational performance is warranted.
- Numerous questions persist regarding chapter 7's most promising interface reduction method, which employed system-level characteristic constraint (SCC) modes with properly orthogonal interface modal derivatives (POIMDs). Computation of the modal derivatives involves many parameters, such as the finite difference step size and nonlinear excitation criteria (e.g. $\pm$5% contact area change). How these parameters affect the final ROM is unknown. Furthermore, a significant portion of the computed derivatives are discarded after the proper orthogonal decomposition (POD) stage. The source of this redundancy, and possible remedies, merits further investigation.

- Leveraging component mode synthesis (CMS) for moat wall pounding simulation would be an interesting and unique addition to body of knowledge. Despite their proven accuracy and efficiency, CMS techniques like the HCB method are rarely used in analyses of civil structures. The finite element model shown in chapter 5, however, is a prime candidate for HCB reduction because all nonlinearities are concentrated at the moat walls. The linear elastic superstructure, which contains roughly half of the degrees of freedom in the model, could be approximated with relatively few fixed-interface modes. Interface nodes, as well as the bulk of the moat wall nodes, would have to remain in the physical domain due to contact and material nonlinearities.

Appendix

A1. Derivation of the contact force Jacobian for the three-dimensional time domain (TD3) contact model

The Jacobian matrix of contact forces with respect to nodal displacements is necessary to generate interface reduction vectors, as described in Chapter 7. This appendix derives the Jacobian matrix for a three-dimensional time domain (TD3) contact element, which acts between a single node pair. Derivations are shown for initially coincident nodes, but the final results apply to noncoincident nodes as well, because the contact forces are not a function of the initial coordinates. First, consider a system of two initially coincident nodes. Node 1 has a displacement vector equal to

$$\mathbf{u}^{(1)} = \begin{Bmatrix} u_N^{(1)} \\ u_{T1}^{(1)} \\ u_{T2}^{(1)} \end{Bmatrix} \tag{A1.1}$$

where the superscript (1) refers to the node number, and the subscripts N, T1, and T2 refer to the normal direction, first tangential direction, and second tangential direction, respectively. Similarly, node 2 has a displacement vector given by

$$\mathbf{u}^{(2)} = \begin{Bmatrix} u_N^{(2)} \\ u_{T1}^{(2)} \\ u_{T2}^{(2)} \end{Bmatrix} \tag{A1.2}$$

The displacement vector for the entire node pair is

$$\mathbf{u} = \begin{Bmatrix} \mathbf{u}^{(1)} \\ \mathbf{u}^{(2)} \end{Bmatrix} = \begin{Bmatrix} u_N^{(1)} \\ u_{T1}^{(1)} \\ u_{T2}^{(1)} \\ u_N^{(2)} \\ u_{T1}^{(2)} \\ u_{T2}^{(2)} \end{Bmatrix} \tag{A1.3}$$

The TD3 model also employs a slider displacement vector, which has two tangential components:

$$\mathbf{w} = \begin{Bmatrix} w_{T1} \\ w_{T2} \end{Bmatrix} \tag{A1.4}$$

The generalized contact force vector for the node pair is

$$\mathbf{f} = \begin{Bmatrix} \mathbf{f}^{(1)} \\ \mathbf{f}^{(2)} \end{Bmatrix} = \begin{Bmatrix} f_N^{(1)} \\ f_{T1}^{(1)} \\ f_{T2}^{(1)} \\ f_N^{(2)} \\ f_{T1}^{(2)} \\ f_{T2}^{(2)} \end{Bmatrix} = \begin{Bmatrix} f_N^{(1)} \\ f_{T1}^{(1)} \\ f_{T2}^{(1)} \\ -f_N^{(1)} \\ -f_{T1}^{(1)} \\ -f_{T2}^{(1)} \end{Bmatrix} \tag{A1.5}$$

Note that the forces applied to node 2 are equal and opposite to the forces applied to node 1, i.e.

$$\mathbf{f}^{(2)} = -\mathbf{f}^{(1)} \tag{A1.6}$$

The general form of the Jacobian matrix is

$$\mathbf{J} = \frac{\partial \mathbf{f}}{\partial \mathbf{u}} = \begin{bmatrix} \dfrac{\partial \mathbf{f}^{(1)}}{\partial \mathbf{u}^{(1)}} & \dfrac{\partial \mathbf{f}^{(1)}}{\partial \mathbf{u}^{(2)}} \\ \dfrac{\partial \mathbf{f}^{(2)}}{\partial \mathbf{u}^{(1)}} & \dfrac{\partial \mathbf{f}^{(2)}}{\partial \mathbf{u}^{(2)}} \end{bmatrix} = \begin{bmatrix} \dfrac{\partial f_N^{(1)}}{\partial u_N^{(1)}} & \dfrac{\partial f_N^{(1)}}{\partial u_{T1}^{(1)}} & \dfrac{\partial f_N^{(1)}}{\partial u_{T2}^{(1)}} & \dfrac{\partial f_N^{(1)}}{\partial u_N^{(2)}} & \dfrac{\partial f_N^{(1)}}{\partial u_{T1}^{(2)}} & \dfrac{\partial f_N^{(1)}}{\partial u_{T2}^{(2)}} \\ \dfrac{\partial f_{T1}^{(1)}}{\partial u_N^{(1)}} & \dfrac{\partial f_{T1}^{(1)}}{\partial u_{T1}^{(1)}} & \dfrac{\partial f_{T1}^{(1)}}{\partial u_{T2}^{(1)}} & \dfrac{\partial f_{T1}^{(1)}}{\partial u_N^{(2)}} & \dfrac{\partial f_{T1}^{(1)}}{\partial u_{T1}^{(2)}} & \dfrac{\partial f_{T1}^{(1)}}{\partial u_{T2}^{(2)}} \\ \dfrac{\partial f_{T2}^{(1)}}{\partial u_N^{(1)}} & \dfrac{\partial f_{T2}^{(1)}}{\partial u_{T1}^{(1)}} & \dfrac{\partial f_{T2}^{(1)}}{\partial u_{T2}^{(1)}} & \dfrac{\partial f_{T2}^{(1)}}{\partial u_N^{(2)}} & \dfrac{\partial f_{T2}^{(1)}}{\partial u_{T1}^{(2)}} & \dfrac{\partial f_{T2}^{(1)}}{\partial u_{T2}^{(2)}} \\ \dfrac{\partial f_N^{(2)}}{\partial u_N^{(1)}} & \dfrac{\partial f_N^{(2)}}{\partial u_{T1}^{(1)}} & \dfrac{\partial f_N^{(2)}}{\partial u_{T2}^{(1)}} & \dfrac{\partial f_N^{(2)}}{\partial u_N^{(2)}} & \dfrac{\partial f_N^{(2)}}{\partial u_{T1}^{(2)}} & \dfrac{\partial f_N^{(2)}}{\partial u_{T2}^{(2)}} \\ \dfrac{\partial f_{T1}^{(2)}}{\partial u_N^{(1)}} & \dfrac{\partial f_{T1}^{(2)}}{\partial u_{T1}^{(1)}} & \dfrac{\partial f_{T1}^{(2)}}{\partial u_{T2}^{(1)}} & \dfrac{\partial f_{T1}^{(2)}}{\partial u_N^{(2)}} & \dfrac{\partial f_{T1}^{(2)}}{\partial u_{T1}^{(2)}} & \dfrac{\partial f_{T1}^{(2)}}{\partial u_{T2}^{(2)}} \\ \dfrac{\partial f_{T2}^{(2)}}{\partial u_N^{(1)}} & \dfrac{\partial f_{T2}^{(2)}}{\partial u_{T1}^{(1)}} & \dfrac{\partial f_{T2}^{(2)}}{\partial u_{T2}^{(1)}} & \dfrac{\partial f_{T2}^{(2)}}{\partial u_N^{(2)}} & \dfrac{\partial f_{T2}^{(2)}}{\partial u_{T1}^{(2)}} & \dfrac{\partial f_{T2}^{(2)}}{\partial u_{T2}^{(2)}} \end{bmatrix} \tag{A1.6}$$

Furthermore, differentiating Equation (A1.6) with respect to $\mathbf{u}^{(1)}$ and $\mathbf{u}^{(2)}$ yields

$$\frac{\partial \mathbf{f}^{(2)}}{\partial \mathbf{u}^{(1)}} = -\frac{\partial \mathbf{f}^{(1)}}{\partial \mathbf{u}^{(1)}} \tag{A1.8a}$$

$$\frac{\partial \mathbf{f}^{(2)}}{\partial \mathbf{u}^{(2)}} = -\frac{\partial \mathbf{f}^{(2)}}{\partial \mathbf{u}^{(2)}} \tag{A1.8b}$$

Thus, only the first three rows of $\mathbf{J}$ (the derivatives of $\mathbf{f}^{(1)}$) must be computed. As explained in Section 6.4, the TD3 element may be in a state of gapping (out of contact), sticking, or slipping. Consequently, $\mathbf{J}$ is computed differently when gapping ($\mathbf{J}^{\text{gap}}$), sticking ($\mathbf{J}^{\text{stick}}$), or slipping ($\mathbf{J}^{\text{slip}}$). The following sections derives the Jacobian matrix at each contact state.

A1.1. Gapping

When the node pair is gapping (i.e. out of contact), there are no contacting forces, i.e.

$$\mathbf{f} = \begin{Bmatrix} f_N^{(1)} \\ f_{T1}^{(1)} \\ f_{T2}^{(1)} \\ f_N^{(2)} \\ f_{T1}^{(2)} \\ f_{T2}^{(2)} \end{Bmatrix} = \begin{Bmatrix} 0 \\ 0 \\ 0 \\ 0 \\ 0 \\ 0 \end{Bmatrix} \tag{A1.9}$$

The corresponding Jacobian matrix $\mathbf{J}^{gap}$ is trivial, with

$$\mathbf{J}^{gap} = \begin{bmatrix} 0 & 0 & 0 & 0 & 0 & 0 \\ 0 & 0 & 0 & 0 & 0 & 0 \\ 0 & 0 & 0 & 0 & 0 & 0 \\ 0 & 0 & 0 & 0 & 0 & 0 \\ 0 & 0 & 0 & 0 & 0 & 0 \\ 0 & 0 & 0 & 0 & 0 & 0 \end{bmatrix} \tag{A1.10}$$

A1.2. Sticking

The sticking force vector is given by

$$\mathbf{f} = \begin{Bmatrix} f_N^{(1)} \\ f_{T1}^{(1)} \\ f_{T2}^{(1)} \\ f_N^{(2)} \\ f_{T1}^{(2)} \\ f_{T2}^{(2)} \end{Bmatrix} = \begin{Bmatrix} k_N\left(u_N^{(1)} - u_N^{(2)}\right) \\ f_{T1}^{stick} \\ f_{T2}^{stick} \\ -k_N\left(u_N^{(1)} - u_N^{(2)}\right) \\ -f_{T1}^{stick} \\ -f_{T2}^{stick} \end{Bmatrix} \tag{A1.11}$$

where

$$f_{T1}^{stick} = k_T\left(u_{T1}^{(1)} - u_{T1}^{(2)} - w_{T1}\right) \tag{A1.12a}$$

$$f_{T2}^{stick} = k_T\left(u_{T2}^{(1)} - u_{T2}^{(2)} - w_{T2}\right) \tag{A1.12b}$$

are the components of the 2×1 sticking force vector $\mathbf{f}^{\text{stick}}$. The normal and tangential contact stiffnesses are given by k_N and k_T, respectively. Compute the derivatives of the normal force components as

$$\frac{\partial f_N^{(1)}}{\partial u_N^{(1)}} = -\frac{\partial f_N^{(1)}}{\partial u_N^{(2)}} = \frac{\partial\left[k_N\left(u_N^{(1)} - u_N^{(2)}\right)\right]}{\partial u_N^{(1)}} = k_N \tag{A1.13}$$

$$\frac{\partial f_N^{(1)}}{\partial u_{T1}^{(1)}} = \frac{\partial f_N^{(1)}}{\partial u_{T2}^{(1)}} = \frac{\partial f_N^{(1)}}{\partial u_{T1}^{(2)}} = \frac{\partial f_N^{(1)}}{\partial u_{T2}^{(2)}} = 0 \tag{A1.13b}$$

Derivatives of the first component of tangential force $\left(f_{T1}^{(1)}\right)$ are

$$\frac{\partial f_{T1}^{(1)}}{\partial u_{T1}^{(1)}} = -\frac{\partial f_{T1}^{(1)}}{\partial u_{T1}^{(2)}} = \frac{\partial f_{T1}^{\text{stick}}}{\partial u_{T1}^{(1)}} = k_T \tag{A1.14a}$$

$$\frac{\partial f_{T1}^{(1)}}{\partial u_N^{(1)}} = \frac{\partial f_{T1}^{(1)}}{\partial u_{T2}^{(1)}} = \frac{\partial f_{T1}^{(1)}}{\partial u_N^{(2)}} = \frac{\partial f_{T1}^{(1)}}{\partial u_{T2}^{(2)}} = 0 \tag{A1.14b}$$

Similarly, the derivatives of $f_{T2}^{(1)}$ are

$$\frac{\partial f_{T2}^{(1)}}{\partial u_{T2}^{(1)}} = -\frac{\partial f_{T2}^{(1)}}{\partial u_{T2}^{(2)}} = \frac{\partial f_{T2}^{\text{stick}}}{\partial u_{T2}^{(1)}} = k_T \tag{A1.15a}$$

$$\frac{\partial f_{T2}^{(1)}}{\partial u_N^{(1)}} = \frac{\partial f_{T2}^{(1)}}{\partial u_{T1}^{(1)}} = \frac{\partial f_{T2}^{(1)}}{\partial u_N^{(2)}} = \frac{\partial f_{T2}^{(1)}}{\partial u_{T1}^{(2)}} = 0 \tag{A1.15b}$$

Thus, the stick-state Jacobian is

$$\mathbf{J}^{\text{stick}} = \begin{bmatrix} k_N & 0 & 0 & -k_N & 0 & 0 \\ 0 & k_T & 0 & 0 & -k_T & 0 \\ 0 & 0 & k_T & 0 & 0 & -k_T \\ -k_N & 0 & 0 & k_N & 0 & 0 \\ 0 & -k_T & 0 & 0 & k_T & 0 \\ 0 & 0 & -k_T & 0 & 0 & k_T \end{bmatrix} \tag{A1.16}$$

Equation (A1.15) shows that, while sticking, the TD3 element is equivalent to a three-dimensional spring with uncoupled stiffnesses in the normal and tangential directions.

A1.3. Slipping

The slip-state contact force vector is

$$\mathbf{f} = \begin{Bmatrix} f_N^{(1)} \\ f_{T1}^{(1)} \\ f_{T2}^{(1)} \\ f_N^{(2)} \\ f_{T1}^{(2)} \\ f_{T2}^{(2)} \end{Bmatrix} = \begin{Bmatrix} k_N\left(u_N^{(1)} - u_N^{(2)}\right) \\ f_{T1}^{slip} \\ f_{T2}^{slip} \\ -k_N\left(u_N^{(1)} - u_N^{(2)}\right) \\ -f_{T1}^{slip} \\ -f_{T2}^{slip} \end{Bmatrix} \tag{A1.17}$$

where f_{T1}^{slip} and f_{T2}^{slip} are the components of the 2×1 slip force vector ($\mathbf{f}^{slip}$). Recall from Section 6.4 that the slipping force acts in the same direction as $\mathbf{f}^{stick}$, but with a magnitude equal to the Coulomb limit, computed as

$$f^{CL} = \mu k_N \left| u_N^{(1)} - u_N^{(2)} \right| \tag{A1.18}$$

where μ is the friction coefficient. Thus, f_{T1}^{slip} and f_{T2}^{slip} are given by

$$f_{T1}^{slip} = \frac{f_{T1}^{stick}}{\|\mathbf{f}^{stick}\|} f^{CL} \tag{A1.19a}$$

$$f_{T2}^{slip} = \frac{f_{T2}^{stick}}{\|\mathbf{f}^{stick}\|} f^{CL} \tag{A1.19b}$$

or, in expanded form,

$$f_{T1}^{slip} = \frac{\mu k_N k_T \left| \left(u_N^{(1)} - u_N^{(2)}\right) \right| \left(u_{T1}^{(1)} - u_{T1}^{(2)} - w_{T1}\right)}{\sqrt{\left[k_T\left(u_{T1}^{(1)} - u_{T1}^{(2)} - w_{T1}\right)\right]^2 + \left[k_T\left(u_{T2}^{(1)} - u_{T2}^{(2)} - w_{T2}\right)\right]^2}} \tag{A1.20a}$$

$$f_{T2}^{slip} = \frac{\mu k_N k_T \left| \left(u_N^{(1)} - u_N^{(2)}\right) \right| \left(u_{T2}^{(1)} - u_{T2}^{(2)} - w_{T2}\right)}{\sqrt{\left[k_T\left(u_{T1}^{(1)} - u_{T1}^{(2)} - w_{T1}\right)\right]^2 + \left[k_T\left(u_{T2}^{(1)} - u_{T2}^{(2)} - w_{T2}\right)\right]^2}} \tag{A1.20b}$$

The normal components of **f** are identical while sticking and slipping, so Equation (A1.13) also holds for the sticking state. The slip-state derivatives of $f_{T1}^{(1)}$ are

$$\frac{\partial f_{T1}^{(1)}}{\partial u_N^{(1)}} = -\frac{\partial f_{T1}^{(1)}}{\partial u_N^{(2)}} = \frac{\partial f_{T1}^{slip}}{\partial u_N^{(1)}} = -\frac{\mu k_N k_T \left(u_{T1}^{(1)} - u_{T1}^{(2)} - w_{T1}\right)}{\sqrt{\left[k_T\left(u_{T1}^{(1)} - u_{T1}^{(2)} - w_{T1}\right)\right]^2 + \left[k_T\left(u_{T2}^{(1)} - u_{T2}^{(2)} - w_{T2}\right)\right]^2}} \tag{A1.21a}$$

$$\frac{\partial f_{T1}^{(1)}}{\partial u_{T1}^{(1)}} = -\frac{\partial f_{T1}^{(1)}}{\partial u_{T1}^{(2)}} = \frac{\partial f_{T1}^{slip}}{\partial u_{T1}^{(1)}} = \frac{\mu k_N k_T^3 \left|u_N^{(1)} - u_N^{(2)}\right| \left(u_{T2}^{(1)} - u_{T2}^{(2)} - w_{T2}\right)^2}{\left\{\left[k_T\left(u_{T1}^{(1)} - u_{T1}^{(2)} - w_{T1}\right)\right]^2 + \left[k_T\left(u_{T2}^{(1)} - u_{T2}^{(2)} - w_{T2}\right)\right]^2\right\}^{3/2}} \tag{A1.21b}$$

$$\frac{\partial f_{T1}^{(1)}}{\partial u_{T2}^{(1)}} = -\frac{\partial f_{T1}^{(1)}}{\partial u_{T2}^{(2)}} = \frac{\partial f_{T1}^{slip}}{\partial u_{T2}^{(1)}} = -\frac{\mu k_N k_T^3 \left|u_N^{(1)} - u_N^{(2)}\right| \left(u_{T1}^{(1)} - u_{T1}^{(2)} - w_{T1}\right)\left(u_{T2}^{(1)} - u_{T2}^{(2)} - w_{T2}\right)}{\left\{\left[k_T\left(u_{T1}^{(1)} - u_{T1}^{(2)} - w_{T1}\right)\right]^2 + \left[k_T\left(u_{T2}^{(1)} - u_{T2}^{(2)} - w_{T2}\right)\right]^2\right\}^{3/2}} \tag{A1.21c}$$

Equation (A1.22) can be rewritten in compact form as

$$\frac{\partial f_{T1}^{(1)}}{\partial u_N^{(1)}} = -\frac{\partial f_{T1}^{(1)}}{\partial u_N^{(2)}} = -\mu \frac{f_{T1}^{stick}}{\|\mathbf{f}^{stick}\|} k_N \tag{A1.22a}$$

$$\frac{\partial f_{T1}^{(1)}}{\partial u_{T1}^{(1)}} = -\frac{\partial f_{T1}^{(1)}}{\partial u_{T1}^{(2)}} = \frac{f^{CL}\left(f_{T2}^{stick}\right)^2}{\|\mathbf{f}^{stick}\|^3} k_T \tag{A1.22b}$$

$$\frac{\partial f_{T1}^{(1)}}{\partial u_{T2}^{(1)}} = -\frac{\partial f_{T1}^{(1)}}{\partial u_{T2}^{(2)}} = -\frac{f^{CL} f_{T1}^{stick} f_{T2}^{stick}}{\|\mathbf{f}^{stick}\|^3} k_T \tag{A1.22c}$$

To simplify these expressions further, define coefficients α_1, β_2, and γ as

$$\alpha_1 = \mu \frac{f_{T1}^{stick}}{\|\mathbf{f}^{stick}\|} \tag{A1.23a}$$

$$\beta_2 = \frac{f^{CL}\left(f_{T2}^{stick}\right)^2}{\|\mathbf{f}^{stick}\|^3} \tag{A1.23b}$$

$$\gamma = \frac{f^{CL} f_{T1}^{stick} f_{T2}^{stick}}{\|\mathbf{f}^{stick}\|^3} \tag{A1.23c}$$

such that Equation (A1.22) can be rewritten as

$$\frac{\partial f_{T1}^{(1)}}{\partial u_N^{(1)}} = -\frac{\partial f_{T1}^{(1)}}{\partial u_N^{(2)}} = -\alpha_1 k_N \tag{A1.24a}$$

$$\frac{\partial f_{T1}^{(1)}}{\partial u_{T1}^{(1)}} = -\frac{\partial f_{T1}^{(1)}}{\partial u_{T1}^{(2)}} = \beta_2 k_T \tag{A1.24b}$$

$$\frac{\partial f_{T1}^{(1)}}{\partial u_{T2}^{(1)}} = -\frac{\partial f_{T1}^{(1)}}{\partial u_{T2}^{(2)}} = -\gamma k_T \tag{A1.24v}$$

Derivatives of $f_{T2}^{(1)}$, while slipping, are computed as

$$\frac{\partial f_{T2}^{(1)}}{\partial u_N^{(1)}} = -\frac{\partial f_{T2}^{(1)}}{\partial u_N^{(2)}} = \frac{\partial f_{T2}^{slip}}{\partial u_N^{(1)}} = -\frac{\mu k_N k_T \left(u_{T2}^{(1)} - u_{T2}^{(2)} - w_{T2}\right)}{\sqrt{\left[k_T\left(u_{T1}^{(1)} - u_{T1}^{(2)} - w_{T1}\right)\right]^2 + \left[k_T\left(u_{T2}^{(1)} - u_{T2}^{(2)} - w_{T2}\right)\right]^2}} \tag{A1.25a}$$

$$\frac{\partial f_{T2}^{(1)}}{\partial u_{T1}^{(1)}} = -\frac{\partial f_{T2}^{(1)}}{\partial u_{T1}^{(2)}} = \frac{\partial f_{T2}^{slip}}{\partial u_{T1}^{(1)}} = -\frac{\mu k_N k_T^3 \left|u_N^{(1)} - u_N^{(2)}\right| \left(u_{T1}^{(1)} - u_{T1}^{(2)} - w_{T1}\right)\left(u_{T2}^{(1)} - u_{T2}^{(2)} - w_{T2}\right)}{\left\{\left[k_T\left(u_{T1}^{(1)} - u_{T1}^{(2)} - w_{T1}\right)\right]^2 + \left[k_T\left(u_{T2}^{(1)} - u_{T2}^{(2)} - w_{T2}\right)\right]^2\right\}^{3/2}} \tag{A1.25b}$$

$$\frac{\partial f_{T2}^{(1)}}{\partial u_{T2}^{(1)}} = -\frac{\partial f_{T2}^{(1)}}{\partial u_{T2}^{(2)}} = \frac{\partial f_{T2}^{slip}}{\partial u_{T2}^{(1)}} = \frac{\mu k_N k_T^3 \left|u_N^{(1)} - u_N^{(2)}\right| \left(u_{T2}^{(1)} - u_{T2}^{(2)} - w_{T2}\right)^2}{\left\{\left[k_T\left(u_{T1}^{(1)} - u_{T1}^{(2)} - w_{T1}\right)\right]^2 + \left[k_T\left(u_{T2}^{(1)} - u_{T2}^{(2)} - w_{T2}\right)\right]^2\right\}^{3/2}} \tag{A1.25c}$$

As before, Equation (A1.26) can be restated in terms of known force quantities:

$$\frac{\partial f_{T2}^{(1)}}{\partial u_N^{(1)}} = -\frac{\partial f_{T2}^{(1)}}{\partial u_N^{(2)}} = -\mu \frac{f_{T2}^{stick}}{\|\mathbf{f}^{stick}\|} k_N \tag{A1.26a}$$

$$\frac{\partial f_{T2}^{(1)}}{\partial u_{T1}^{(1)}} = -\frac{\partial f_{T2}^{(1)}}{\partial u_{T1}^{(2)}} = -\frac{f^{CL} f_{T1}^{stick} f_{T2}^{stick}}{\|\mathbf{f}^{stick}\|^3} k_T \tag{A1.26b}$$

$$\frac{\partial f_{T2}^{(1)}}{\partial u_{T2}^{(1)}} = -\frac{\partial f_{T2}^{(1)}}{\partial u_{T2}^{(2)}} = \frac{f^{CL}\left(f_{T1}^{stick}\right)^2}{\|\mathbf{f}^{stick}\|^3} k_T \tag{A1.26c}$$

Define new coefficients α_2 and β_1 as

$$\alpha_2 = \mu \frac{f_{T2}^{stick}}{\|\mathbf{f}^{stick}\|} \tag{A1.28a}$$

$$\beta_1 = \frac{f^{CL}\left(f_{T1}^{stick}\right)^2}{\|\mathbf{f}^{stick}\|^3} \tag{A1.28b}$$

such that

$$\frac{\partial f_{T2}^{(1)}}{\partial u_N^{(1)}} = -\frac{\partial f_{T2}^{(1)}}{\partial u_N^{(2)}} = -\alpha_2 k_N \tag{A1.29a}$$

$$\frac{\partial f_{T2}^{(1)}}{\partial u_{T1}^{(1)}} = -\frac{\partial f_{T2}^{(1)}}{\partial u_{T1}^{(2)}} = -\gamma k_T \tag{A1.29b}$$

$$\frac{\partial f_{T2}^{(1)}}{\partial u_{T2}^{(1)}} = -\frac{\partial f_{T2}^{(1)}}{\partial u_{T2}^{(2)}} = \beta_1 k_T \tag{A1.29c}$$

With all necessary derivative terms computed, the slip-state Jacobian can be concisely stated as

$$\mathbf{J}^{slip} = \begin{bmatrix} k_N & 0 & 0 & -k_N & 0 & 0 \\ -\alpha_1 k_N & \beta_2 k_T & -\gamma k_T & \alpha_1 k_N & -\beta_2 k_T & \gamma k_T \\ -\alpha_2 k_N & -\gamma k_T & \beta_1 k_T & \alpha_2 k_N & \gamma k_T & -\beta_1 k_T \\ -k_N & 0 & 0 & k_N & 0 & 0 \\ \alpha_1 k_N & -\beta_2 k_T & \gamma k_T & -\alpha_1 k_N & \beta_2 k_T & -\gamma k_T \\ \alpha_2 k_N & \gamma k_T & -\beta_1 k_T & -\alpha_2 k_N & -\gamma k_T & \beta_1 k_T \end{bmatrix} \tag{A1.30c}$$

Note that $\mathbf{J}^{slip}$ is not a symmetric matrix. While slipping, a change in the normal displacements will induce a change in the tangential contact forces. This is readily observed from Equation (A1.20), in which f_{T1}^{slip} and f_{T2}^{slip} are both proportional to $\left|u_N^{(1)} - u_N^{(2)}\right|$. A change in the tangential displacements, however, will not affect the normal contact force, hence the asymmetry. $\mathbf{J}^{slip}$ also reveals the coupling between the two tangential contact force components, brought on by their mutual dependence on the norm of the sticking force.

The Jacobian matrices presented here describe the differential change in contact force with respect to interface nodal displacements, for a single node pair. In a real system, like the beam assembly shown in Chapter 7, $\mathbf{J}^{gap}$, $\mathbf{J}^{stick}$, or $\mathbf{J}^{slip}$ must be computed at every node pair, depending on its own contact state, and then mapped to the correct global degrees of freedom.